AN INVESTIGATION INTO THE USE OF CHARGE-COUPLED DEVICES FOR DIGITAL MAMMOGRAPHY

Laurence Edward Court

UNIVERSITY COLLEGE LONDON

ProQuest Number: 10016722

ProQuest 10016722

ABSTRACT

This thesis describes the design, optimisation, construction and evaluation of a laboratory based digital mammography system which uses phosphor coated charge-coupled devices (CCDs) for x-ray detection. The size mismatch between the breast and the CCD is overcome by operating the CCD in time delay and integration (TDI) mode and scanning across the breast.

Multiparameter optimisations have been carried out for a wide range of digital mammography system configurations and requirements, with the aim of optimising the image quality for a given patient dose. The influence of slot width, exposure time, focal spot size, detector resolution and noise level, dose restrictions, patient thickness and x-ray tube target on the system configuration to give optimum image quality is examined.

The system is fully characterised in terms of responsivity, dark current, modulation transfer functions (MTFs), noise power spectra (NPS) and spatial frequency dependent detective quantum efficiency (DQE(f)). Direct interactions of x-rays with the CCD are shown to give a significant increase in the high frequency values of the MTF. These interactions also act as a source of noise and act to significantly reduce the DQE(f) at all frequencies. A subjective comparison of images produced with the optimised prototpye system with those produced using a conventional film-screen detector shows that these interactions must be removed if the prototype system is to produce images of equal quality to those currently produced using film-screen combinations. Other improvements to the system are suggested.

CONTENTS

FIGURES

TABLES

ACKNOWLEDGEMENTS

There are so many people that I would like to thank for their friendship and support that I am in danger of exceeding the University of London word limit, not to mention missing someone out. I have, therefore, decided to shy away from specific acknowledgements and would like to start by thanking everyone who has helped me reach this stage in my studies and career.

That said, I would like to thank a number of people who have been specifically involved in this project. I would like to acknowledge the help of Dr Robert Speller and Dr David Miller from UCL and Dr Gordon Hopkinson and Dr Mike Cutter from Sira Ltd for their supervision throughout the last three years. I would also like to thank Ian Ho who is working on a parallel project, Mark Skipper from Sira Ltd and Brian Allan from EEV Ltd, as well as all my friends and colleagues at UCL, Sira and beyond.

Special thanks must go to all my family for their encouragement, support and guidance in reaching this goal, specifically my parents and sister, Tony, Jenny and Vicky Court, and my grandparents.

Last, but definitely not least, I would like to thank Parveen Akther for sharing the joys and stresses of the last few years.

Errata

p17	line 8	IPSM 1989 appears in the reference list as Fitzgerald et al
p18	line 4	for 'hydroxyapetite' read 'hydroxyapatite'
p19	line 18	for 'dE' read 'dE$_{ab}$'
p26	line 12	for 'used of' read 'use of'
p26	line 21	for 'Cunningham 1994' read 'Cunningham et al 1994'
p33	line 9	for 'passed through Z' read 'passes through Z'
p37	line 8	for 'form a moving platform' read 'from a moving platform'
p45	line 7	for 'theses systems' read 'these systems'
p51	lines 3,4	refers to figure 2.1
p53	line 9	refers to figure 2.4
p55	line 14	refers to figure 2.4
p56	equation 2.1	for 'V$_{nosie}$' read 'V$_{noise}$'
p57	line 5	refers to figure 2.4
p66	line 17	for 'Ne,p' read 'N$_{e,p}$'
p73	line 11	for 'full fell' read 'full well'
p79	line 7	for 'Burke 1991' read 'Burke and Gajer 1991'
p89	figure 3.11	for 'Relatice' read 'Relative'
p98	line 7	for 'direction of the can' read 'direction of the scan'
p127	figure 4-17	for 'silt length' read 'slit length'
p133	line 18	for 'independent' read 'dependent'
p135	line 19	delete 'using the assumption that W$_{direct}$ is independent of frequency'
p138	line 2	for 'accounts of' read 'accounts for'
p143	line 10	for 'then be described' read 'then described'
p152	equation 5-5	for '(x$_p$ + A' read '(x$_p$ + A)'
p154	line 9	for 'figures 3(a) and 3(b)' read 'figures 5.4(a) and 5.4(b)'
p155	figure 5.4	for 'equation 15' read 'equation 5.8'
p189	line 21	for 'current of film-screen based systems' read 'current film-screen based systems'
p205	figure 6.12	for 'colimated' read 'collimated'
p211	line 8	for 'sterio' read 'stereo'
p211	line 13	for 'Hsu et al 1994 and 1995' read 'Hsu et al 1995'
p224	line 17	for 'Sones 1984' read 'Sones and Barnes 1984'
p224	line 23	for 'Ganzales' read 'Gonzales'
p225	line 6	for 'Reichenbach 1991' read 'Reichenbach et al 1991'
p237	line 1	for 'where is' read 'where φ_{75} is'
p243	reference 12	refers to p417-27
p251	reference 3	year of reference is 1991
p251	reference 5	year of reference is 1988

1. INTRODUCTION TO CONVENTIONAL AND DIGITAL MAMMOGRAPHY

1.1 Introduction

Breast cancer is the commonest form of cancer to affect females in the UK, with 24000 new cases and 15000 deaths each year. Such a high incidence rate - it affects one woman in twelve - is considered an epidemic (Roebuck 1994).

In 1985, when nearly half the health districts within the National Health Service had no mammographic facilities whatsoever, the Minister of Health set up a working group, chaired by Professor Sir Patrick Forrest, to investigate all information available on breast cancer screening, to examine any appropriate changes in the UK policy on mammographic screening, to suggest a range of policy options and to assess the costs and benefits involved. The working group issued its final report, known as the Forest Report, in 1986, in which it recommended breast screening every three years for women between 50 and 64 years of age. Their findings were strongly influenced by the results of two randomised controlled trials: The New York Health Insurance Plan (HIP) trial and the Swedish 'two counties' trial, both of which identified a 30% reduction in mortality of screened women compared with control groups. Results of other trials have since been published (Alexander et al 1994, Wald et al 1991), which also indicate that screening can reduce breast cancer mortality rates.

Conventional mammography is currently seen as the most efficient technique for the early detection of breast cancer, and is used by breast screening programmes throughout the world, including the now well established United Kingdom National Health Service Breast Screening Programme (NHSBSP). In spite of its success, the effectiveness of film-screen combinations for imaging the breast is limited by several technical problems which it hoped can be overcome by replacing the film-screen combination with a digital detector.

This theses is an investigation into the use of one specific digital imaging detector, the charge-coupled device (CCD), for digital mammography. The first chapter serves as an introduction to conventional mammography and also to some elementary x-ray imaging concepts such as film response curves and patient dose. The limitations of film-screen combinations are discussed, and the advantages of digital detectors are described. Various digital detectors are then considered for mammography, and the reasons for choosing CCDs are discussed. The design and operation of charge-coupled devices is then described in some detail.

The construction of a prototype digital mammography system based on charge-coupled devices is detailed in chapter 2. Chapter 3 describes the initial calibration of this system, including evaluation of characteristics such as gain and dark current in the CCD. Chapter 4 then describes resolution (modulation transfer function) and noise (noise power spectra) measurements as well as detective quantum efficiency. The theoretical optimisation of this system for use in mammography is detailed in chapter 5. Chapter 6 then uses breast phantom images to evaluate the image quality, both subjectively and quantitatively, as well as providing some validation of the model used for the theoretical optimisation in chapter 5. Chapter 7 describes the use of CCDs for stereo-mammography, including an initial evaluation of such a system. Finally, chapter 8 discusses improvements which could be made to the present system, and gives some suggestions for future work.

1.2 Anatomy of the female breast

The female breast is a mixture of adipose and glandular tissue. It "exhibits a continuous flow of transitional forms between the extremes of abundant parenchyma and practically no parenchyma at al" (Craigmyle 1984). The mammary gland contains 15-18 lobes, each of which has a main duct opening in the nipple. Each main duct branches out to form the terminal ductal lobular unit (TDLU) which is made up of the extralobular terminal duct

(ELTD) and the lobule, as illustrated in Figure 1-1. As well as large ranges in composition, breasts also range enormously in size, with one study (Fife 1991) finding a range of compressed breast thickness from 2.5 to 8.6cm and a range of breadths (chest wall to nipple distance) from 1.4 to 17.4cm.

To allow quantitative comparison of breast doses the Institute of Physical Sciences in Medicine (IPSM) has adopted a definition of a 'standard' breast with standard composition (IPSM 1989). This 'standard' breast has a central region comprising a 50:50 mixture by weight of adipose and glandular tissue, surrounded by a 0.5cm thick layer of adipose tissue. It is 4.5cm thick and has a semi-circular cross-section in the horizontal plane with a diameter of 16cm, giving a cross-sectional area of approximately 100cm^2. The huge variation in composition and size of real breasts means that, although this 'standard' breast is useful for quantitative comparisons it is important to remember that this is only a generalisation.
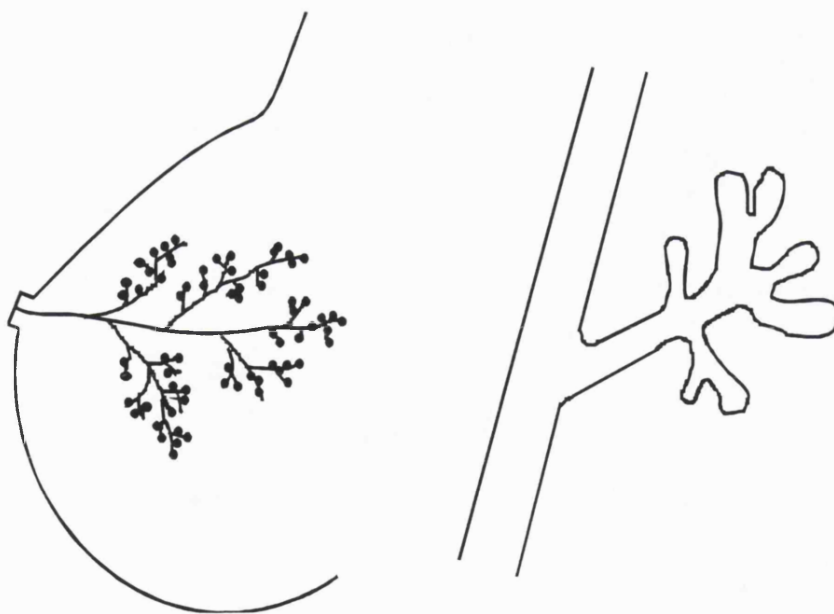
Figure 1-1 Schematic of a lobe in a breast and the Terminal Ductal Lobular Unit, TDLU

1.3 Mammographic indicators of breast cancer

Tabar and Dean 1985 identify four distinct classifications of lesion which may exist individually or in any combination: calcifications, circumscribed lesions, stellate lesions and thickened skin syndrome.

Calcifications

Calcifications are composed of calcium hydroxyapetite or calcium phosphate. They are formed by either active cellular secretion or by the calcification of intraluminal debris. Histological examination shows that 60-80% of breast carcinomas have associated microcalcifications but conventional film-screen mammography only detects microcalcifications in 30-50% of cases (Sickles 1982).
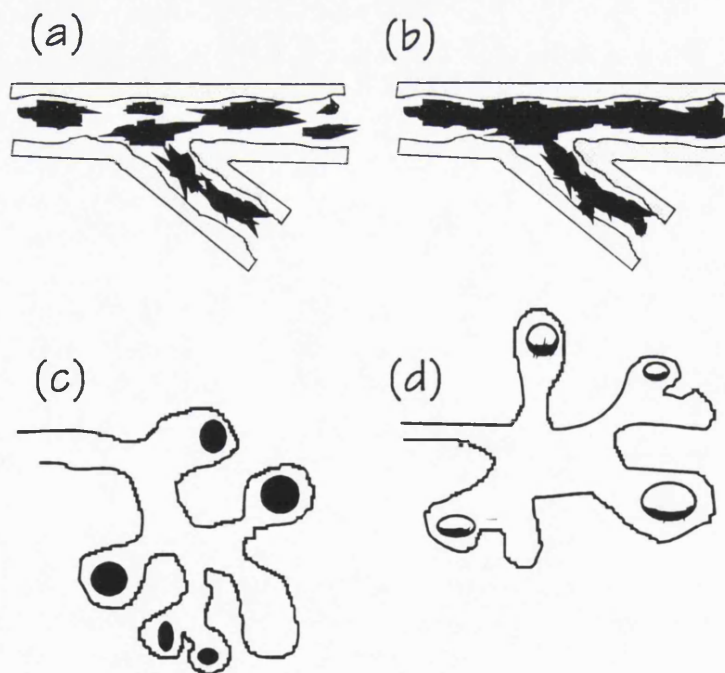
Figure 1-2 schematic of calcifications (a) granular type, (b) casting type, (c) lobular type and (d) lobular type in large cavities

Detailed analysis of the form, size, density, number and distribution of the detected microcalcifications can lead to a very high level of diagnostic accuracy (Tabar and Dean 1985), although the number detected is highly dependent of the mammographic technique used. It should also be noted that 80% of biopsied clusters of calcifications represent benign processes (Tabar and Dean 1985). Different classifications of calcifications which can be identified by mammography are illustrated in Figure 1-2.

Circumscribed and stellate lesions and thickened skin syndrome

Circumscribed and stellate lesions are identified by their structure, shape and density. Definite diagnosis is not always possible and histologic examination may be necessary. For further details of the mammographic characteristics of these lesions and of thickened skin syndrome the reader is referred to Tabar and Dean 1985.

1.4 Patient dose

Any examination using ionising radiation has an associated risk of radiation-induced carcinogenesis although in mammography,. with modern equipment and techniques, this risk is generally considered low compared with the benefit of the examination (NCRP 1986, Law 1987, IPSM 1989). The female breast is, however, considered to be a particularly sensitive organ for the induction of cancer and patient dose must be carefully monitored.

Absorbed dose is defined as (ICRU 1980, Johns and Cunningham 1983)

$$Absorbed\ dose = \frac{d\overline{E_{ab}}}{dm}$$

Equation 1-1

where dE is the mean energy imparted by the ionising radiation to a mass dm. It has units of gray (Gy), defined as $1Gy=1\ J\ kg^{-1}$. In the breast it is believed that it is the

glandular tissues (IPSM 1989) which are most sensitive to radiation induced carcinogenesis. That is, the mean dose to the glandular tissues (the mean glandular dose) is considered to be more closely related to patient risk than mean dose to the entire breast.

1.5 Conventional mammography

Figure 1-3 shows a schematic of a conventional mammography system. Each of the elements seen in this figure are subject to reasonably strict guidelines and requirements, as issued by bodies such as the National Health Service Breast Screening Programme, The Department of Health and the Commission of the European Communities. Typical specifications considered as 'good practice' are (CEC 1990) reproduced below.

Diagnostic requirements

- Visually sharp reproduction of the whole glandular breast
- Visually sharp reproduction of the cutis and subcutis
- Nipple should be parallel to the film

Criteria for good imaging performance

- Important image details: round details   :   3mm diameter

                             microcalcifications   :   0.2mm

- Patient dose per film with grid: 2mGy average glandular dose (CEC 1995)

Example of good radiographic technique

- Specially dedicated equipment, molybdenum anode

- Focal spot size ≤ 0.6mm

- Total filtration: 0.03 mmMo or 0.5mmAl equivalent

- Anti-scatter grid: Specially designed moving grid. Not necessary for breasts < 4cm

- Film-screen combination: High resolution mammography combination with dedicated processing

- Source-to-detector distance ≥ 60cm

- Radiographic voltage: 25 - 35kV

- Exposure time < 2s

- Breast compression: to a level which the patient can tolerate
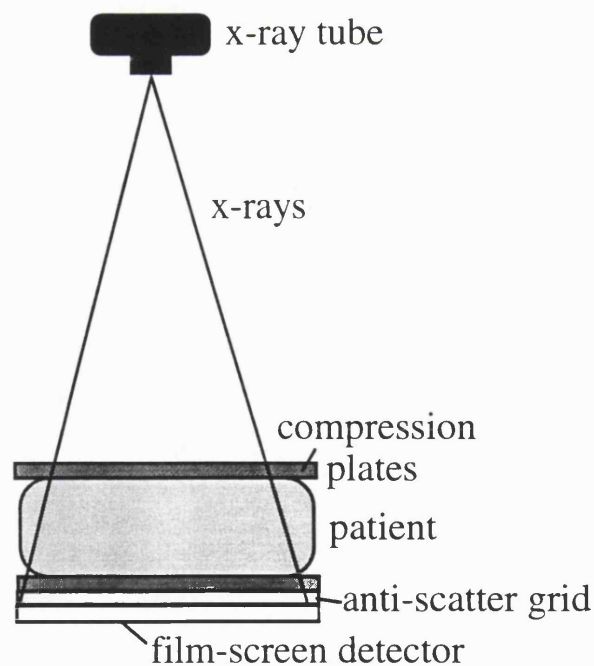
Figure 1-3 Schematic of a typical mammography system

1.5.1 Film-screen combination

The film-screen combination consists of a radiographic film in contact with an intensifying screen which has a high x-ray absorption efficiency. It converts the absorbed x-ray energy to visible photons which are then detected by the film. The combinations used in mammography are specially designed to meet the resolution and dose requirements of the examination and have been the subject of much research and improvements. Aspects of this combination which are relevant to this work are the x-ray response curve, reciprocity failure, system resolution and system noise. These are discussed below, including some discussion on possible advantages of digital detectors and the relevance of guidelines for film-screen systems when applied to digital technology.

X-ray response curve

The relationship between the x-ray exposure and the optical density of the exposed film is given by a graph called the Hurter-Drifield curve (H-D curve), an idealised illustration of which is given in Figure 1-4.
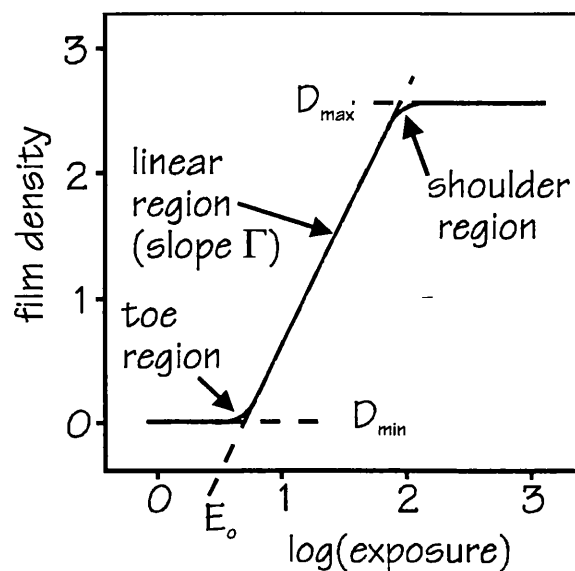
Figure 1-4 An idealised film characteristic curve

For maximum display contrast the radiographic information must be contained in the linear region. Under-exposure of the film results in lost information. Some important results of this curve are:

- Preventing radiation scattered in the breast (which reduces contrast and signal-to-noise ratio) from reaching the detector can results in under-exposure of the film. This means that the use of anti-scatter techniques, such as a grid or air gap between the patient and the detector, typically necessitates an increase in patient dose.

- Magnification techniques, in which the energy flux of the x-rays is spread out over an increased area, can result in under-exposure of the film unless accompanied by an increase in patient dose.

- Low contrast objects may not be particularly well displayed, particularly when they are located in thin and thick or dense regions of the breast for which the film exposure may be near the toe or shoulder region of the H-D curve.

These problems, which are primarily a results of the film being used for image capture, display *and* storage, may be overcome by the use of an appropriate digital detector, particularly if it is linear and has a large dynamic range. For such a detector the display contrast is not adversely affected by the removal of the scattered x-rays and the full benefit of scatter rejection techniques can be experienced.

Reciprocity failure, where a given x-ray exposure gives an optical density dependent on the intensity of the radiation and the exposure time (rather than their product), can be important for very high and very low radiation intensities. This may hinder the use of magnification techniques for which the intensity level can be relatively low. This is not a problem experienced with many digital detectors.

Resolution

Film-screen systems used in mammography are designed to optimise the resolution whilst still providing sufficient x-ray responsivity for such a dose limited examination. For example, these systems typically use a single emulsion film with a single intensifying

screen, compared with double emulsion - double screen combinations used for other radiographic examinations. Current guidelines require a limiting resolution of better than 10 line pairs per mm ($lpmm^{-1}$). Since most digital detectors suitable for use in mammography use an intensifying screen in front of the digital detector it is unlikely that digital systems, which have the additional degrading effect of the pixel structure, will be able to better the resolution achievable with current film-screen systems. With small enough pixels it should be possible to nearly equal that currently available.

There is, however, some argument in the literature about the resolution really needed for diagnosis in mammography. The results of Karssemeijer 1993 suggest that storage phosphor plates with a limiting resolution of only $5lp\ mm^{-1}$ ($100\mu m$ pixels) are adequate for mammographic imaging. Chan et al 1994, however, demonstrate that for optimal computer detection of subtle microcalcifications in digitised mammograms, pixel sizes at least as small as $35\mu m$ square are needed. But, Freedman et al 1995 are of the opinion that there is minimal advantage in using $50\mu m$ pixels rather that $100\mu m$ pixels. It is clear that the necessary pixel size is far from decided. The policy of this work is to aim to match all current guidelines, including those for resolution, with the proposal that, for example, small pixels can always be binned to make large pixels as required by, for example, limited storage space.

Noise

The main sources of noise in a film-screen system are:

- Quantum noise due to fluctuations in both the number of x-rays reaching the detector per unit area and the number of visible photons produced and detected per x-ray
- Quantum mottle, which is a result of the discrete nature of the detected x-ray photons (Barrett and Swindell 1981). It is seen when the average spacing between incident quanta is large compared to the characteristic dimension of the point spread function. It is most significant for high speed systems
- Screen structure mottle, caused by fluctuations in phosphor thickness
- Film granularity, caused by variations in the number of grains per unit area in the film

Film granularity is the most significant source of noise in mammographic film-screen systems (Nishikawa and Yaffe 1987) and can make it difficult to detect microcalcifications. Film granularity and screen structure mottle can both be regarded as fixed pattern noise. That is, if the same combination could be re-used the signal variations would always appear at the same place. For a digital detector with linear response, which is re-used for each exposure, these sources of noise can be removed by applying a flat fielding algorithm in software after image detection. This algorithm applies a weight to each pixel value to account for pixel-to-pixel variations in responsivity as caused by fluctuations in factors such as phosphor thickness. Thus, in principle digital detectors can produce images with less noise than film-screen combinations. This algorithm is discussed further in section 1.8.7.

Image area

Typical film-screen combinations used in mammography are 24 x 18 cm^2. This area presents a problem for some digital detectors, particularly CCDs which are only available in much smaller sizes.

1.6 Digital mammography

The effectiveness of film-screen mammography for the early detection of breast cancer is limited by a number of problems, as discussed above. In summary, film-screen combinations are limited by the shape of the film-response curve which necessitates a compromise between display contrast and system latitude, and the presence of film granularity which can hinder the detection of microcalcifications and small lesions. A digital detector with sufficiently wide dynamic range should be able to overcome these limitations. This is primarily because digital systems have separate image capture, display and storage stages, and each process can therefore be separately optimised. Because the detector is re-used it may also be possible to remove fixed pattern type noise, similar to film granularity, by applying appropriate compensation factors.

As well as overcoming some of the technical limitations experienced with film-screen combinations, digital mammography has a number of other advantages. These include the use of computer algorithms to aid diagnosis by, for example, highlighting microcalcifications in the image, and the use of tele-diagnosis where images can be transferred between screening sites to allow radiographers to obtain advice from more experienced colleagues. Numerous methods which have been used to classify and detect masses in digital mammograms (obtained by digitising film images) including thresholding (Nishikawa et al 1994), matched Fourier filtering (Brettle et al 1994), wavelet analyses, neural networks (Nishikawa et al 1994) and fractals (Lefeburre et al 1995). This research into computer classification and detection of lesions and microcalcifications is very popular The success of these algorithms places an increased need to produce a clinical digital mammography system. It is hoped that the used of computer aided diagnosis may reduce the number of false-positives and, therefore, reduce the number of patients undergoing unnecessary biopsy.

The main advantage of film-screen combinations over digital mammography is their high contrast resolution or Modulation Transfer Function (MTF). This apparent advantage may not be realised in real imaging situations, however, as high frequency response is often strongly degraded by the noise transfer characteristics of the system. For example poor optical coupling efficiency between the screen and the detector increases noise at all frequencies, with the most noticeable effect at high frequencies (see, for example, Cunningham 1994).

Current expectations regarding the potential impact of digital mammography on the diagnosis and management of breast cancer are generally high. Indeed, in North America a National Digital Mammography Development Group which includes radiologists, medical physicists, engineers, telecommunications experts, computer scientists and epidemiologists, representing academia, Government and private industry, has been set up (Anderson 1994).

1.7 Choosing a digital detector

There are a number of detectors available which could be used for digital mammography, including film, which can be digitised after image collection. Table 1-1 compares several detectors and their characteristics which are relevant to mammography. These include:

- Is the detector available in a sufficiently large area? Alternatively, can it be operated is such a way to image the entire breast area?

- Is the digital image immediate? This has important consequences for its use in a breast screening programme where high patient turn around is important.

- What are the main noise sources? (except x-ray quantum noise and digitisation noise, which are unavoidable).

- What is the smallest pixel size readily available?

- Has the detector previously been used in a mammography context? How successful was it?

The small pixel size available with CCDs means that they potentially have comparable resolution to mammographic film-screen systems. They also have the advantage over digitising film, xeroradiographic plates and storage phosphor plates that the image is immediately available. That is, there is no intermediate stage between detecting the image and producing a digital image, thus giving the potential for a system which is extremely simple and quick to operate. This may be a significant advantage considering the high throughput that is required of screening units in the UK Breast Screening Programme. The main disadvantage of CCDs compared with the other detectors is their small size. This does not impose a fundamental limit on the image size as either a large number of CCDs can be butted together to give an increased imaging area, or a row of CCDs can be scanned across the breast, options which are considered in more detail below where the construction and operation of CCDs are described.

If resolution requirements are relaxed some time in the future then it is probable that both storage phosphor plates and amorphous silicon detectors will make excellent detectors for use in mammography, particularly amorphous silicon arrays as they require

Detector	Large area available?	Immediate digital image?	Expected noise sources
Storage phosphor	yes	no	• secondary quantum noise • reader system noise • screen structure noise
Amorphous silicon thin-film arrays	yes	yes	• thin-film transistor switching noise • amplifier noise • screen structure noise
Xeroradiographic plates	yes	no	• scorotron charging noise • readout noise (laser power fluctuations, electron shot noise...) • system noise (probe-distance non-uniformities, scanning speed variations) • structural noise
CCD	yes (can scan across object, or but several together)	yes	• dark current noise • screen structure and CCD response noise • readout noise
Film-screen	yes	no	• film granularity • screen structure

Table 1-1 Comparison of characteristics of various detectors

Typical pixel size	Use in mammography	References
100	Clinical evaluations at Leeds. Diagnostic quality found to be comparable with film-screen.	• Cowen et al 1993 • Dance 1994
127	Not yet.	• Schiebel et al 1994 • Antonuk et al 1994
50	Popular in UK 10 years ago due to edge enhanced images and good spatial resolution. No longer used because of higher patient dose compared with film-screen.	• Dance 1988 • Papin and Huang 1987 • Rowlands et al 1991
20	Prototype scanning system built in Toronto found to compare well with film-screen. Two reasonably successful commercial preoperative localisation and needle biopsy systems are currently available.	• Maidment et al 1990 • Beynon and Lamb 1980 • Holdsworth et al 1990 • Janesick 1991
digitiser dependent	Various studies to evaluate necessary pixel size, but no consensus as such.	• Barrett and Swindell 1981 • Nishikawa and Yaffe 1987 • Dance 1994 • Karssemeijer et al 1993 • Chan et al 1994 • Freedman et al 1995

no secondary stage of digitisation. The relatively poor resolution of these detectors can also be overcome by operating the system in a magnification geometry together with a smaller focal spot, a possibility which is explored further in chapter 5.

On the basis of the small pixel sizes available and the immediate availability of the image, CCDs are the detector of choice. This chapter now moves on to discuss the design and operation of CCDs, including further details regarding solutions to the breast/CCD area mismatch.

1.8 Theory and operation of charge-coupled devices

Charge-coupled devices (CCDs) were first introduced in 1970 by Boyle and Smith as a memory device, designed in an attempt to electrically mimic magnetic bubble devices. It was not long before scientists and engineers realised the huge potential of CCDs in the field of imaging:

- High quantum efficiency (for optical wavelengths)
- Broad spectral range
- Low readout noise
- Good geometric stability and fidelity
- Solid-state construction
- High resolution capabilities
- Large dynamic range
- Linear response

The two processes which are fundamental to the operation of the CCD - charge storage and charge coupling - are described below. The different architectures used by two-dimensional imaging CCDs are discussed.

1.8.1 Charge storage

Figure 1-5 shows a single CCD electrode, a metal-oxide-semiconductor (MOS) structure. Initially, when there is no bias applied to the electrode there is a uniform distribution of holes - the majority carriers - in the p-type semiconductor.
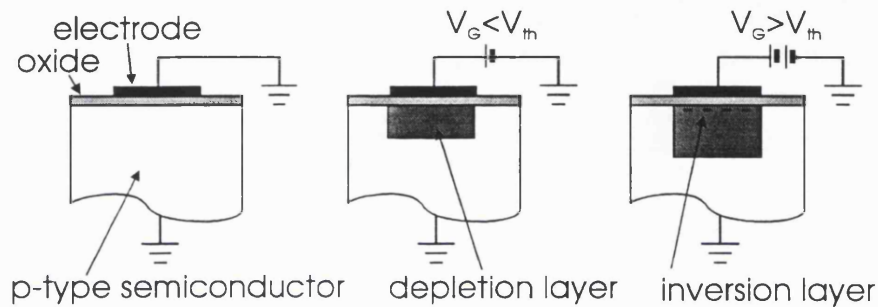
Figure 1-5 Schematic of a single CCD electrode

If a positive voltage, V_G, is applied to the electrode the holes are repelled away from the volume of the semiconductor which is directly below the electrode, creating a depletion layer. As the gate bias is increased the potential at the semiconductor/insulator interface - known as the surface potential, ϕ_s - becomes increasingly positive, and the depletion region extends further into the semiconductor. If the gate bias is further increased, eventually it reaches a threshold voltage, V_{th}, where the surface potential is so positive that electrons are attracted to the surface to form a very thin, very dense inversion layer. This is how a conducting channel is established in MOS transistors (MOST). Unlike MOSTs, which have a ready supply of minority carriers from the transistor's source and sometimes its drain, CCDs have no such supply. If no inversion layer can be formed, the depletion layer extends much further into the semiconductor. Most of the potential difference between the gate and the substrate is dropped across this depletion layer. If minority carriers then become available - perhaps light becomes incident on the CCD and releases electron-hole pairs by photoelectric interaction - the depletion layer will shrink and the surface potential fall as the inversion layer charge increases. In this way, charge is stored in the CCD as an inversion layer.

CCDs with the structure described above are known as surface channel CCDs, SCCDs. These CCDs store the charge packets very close to the interface between the semi-conductor and the overlying insulator. In 1972 a different CCD structure was developed in which charge packets are stored some distance below the surface of the semiconductor. CCDs with this structure are known as buried, or bulk, channel CCDs, BCCDs.

The differences in structure of BCCDs and SCCDs can be seen by comparing Figure 1-6 and Figure 1-5. The substrate of a BCCD is lightly doped with one type of dopant, on top of which there is a thin layer which is more heavily doped with dopant atoms of the opposite type.
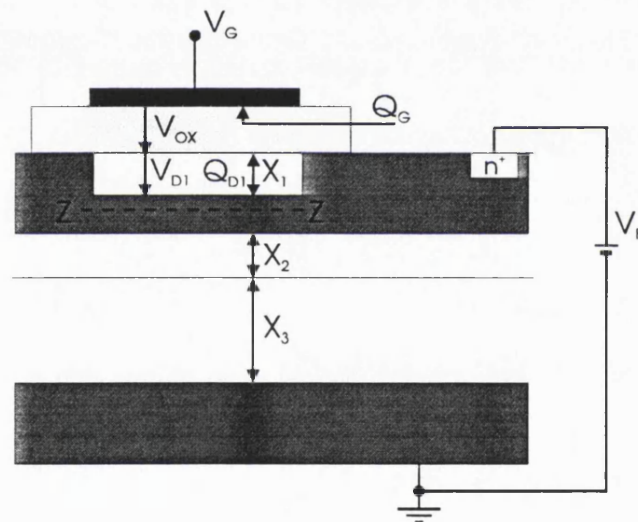
Figure 1-6 Schematic of a BCCD

As with SCCDs, the semiconductor is covered with an insulator and a series of metallic electrodes. Consider both the gate voltage and the substrate set at ground potential, and increase the potential of the n-type layer by increasing the bias voltage, V_B. This results in a depletion layer of thickness X_1 being formed in the n layer directly below the gate. This is equivalent to varying the gate voltage of Figure 1-5 except that, in this case, the gate voltage is kept constant and it is the potential of the semiconductor which is varied. As well as the depletion layer which is formed directly below the gate, a second depletion

layer of thickness $X_2 + X_3$ is formed at the reverse biased p-n junction in the bulk semiconductor. If the bias voltage is further increased, eventually the two depletion layers meet at point Z in a condition known as 'pinch-off'. Prior to pinch-off the potential at Z, V_Z, was equal to V_B. At pinch-off Z becomes separated from the applied bias, and any further increase in V_B does not affect V_Z. A typical potential profile is shown in Figure 1-7.
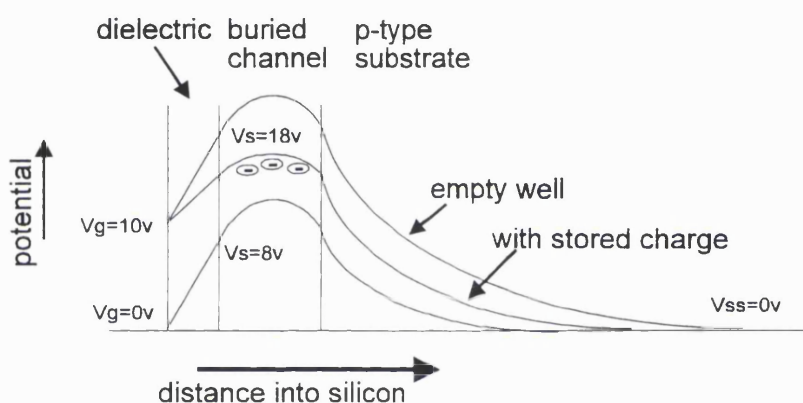
Figure 1-7 Potential profile across a BCCD

For any bias above pinch-off, the potential at Z is the most positive in the semiconductor beneath the electrode. This means that electrons in the CCD are attracted to a plane which is parallel to the surface and passed through Z, where their potential energy is at a minimum. In a manner which is analogous to that used by the SCCD, the BCCD can therefore, store charge at a certain point in the semiconductor beneath an electrode. It should be noted, however, that in a SCCD the electrons carrying the information are minority carriers, whereas in BCCDs the electrons carrying the information are the majority carriers.

A disadvantage of increasing the gate-channel distance (i.e. when using BCCDs rather than SCCDs) is the associated reduction in the effective gate-channel capacitance, which

means that the charge handling capability of BCCDs is significantly less than that of SCCDs. This advantage, however, is offset by the increased charge transfer efficiency, CTE, found with BCCDs. This is discussed further below.

1.8.2 Charge coupling

Charge-coupling is best introduced using the hypothetical concept of a potential well, the depth of which is related to the potential applied to the gate, V_g, and by representing charge as water. This is demonstrated in Figure 1-8, showing 4 electrodes - three at 0v and one at 10v.
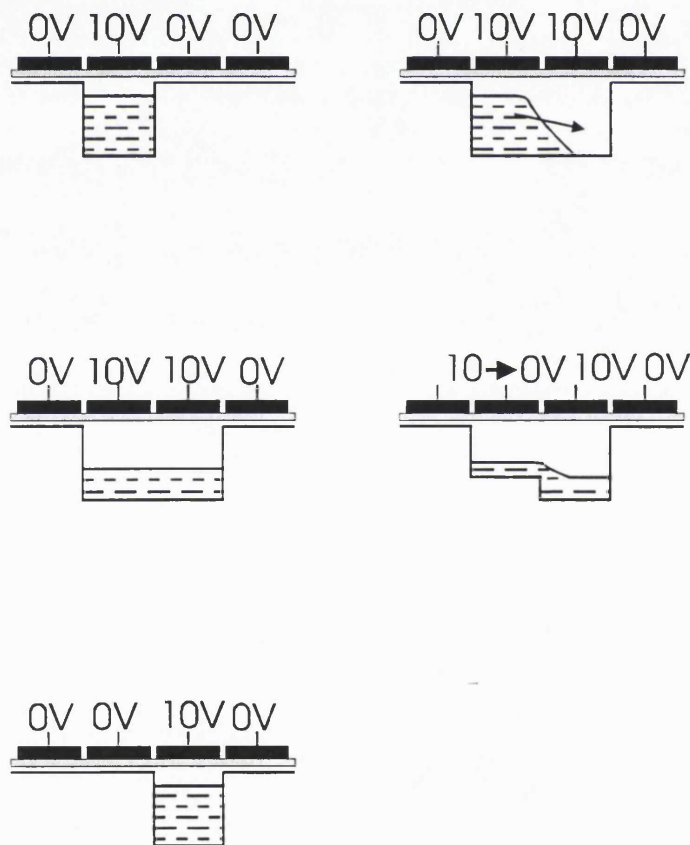
Figure 1-8 Charge-coupling

The charge is collected under the second electrode. If the bias on the third electrode is increased to 10v, and if the electrodes are close enough together, their potential wells

will merge together and the charge becomes shared between the wells of electrodes two and three. If the bias on the second electrode is then biased to 0v, all the charge is transferred to the well under the third electrode. In this way, the charge has been moved from one place to another. Commonly each pixel is composed of three parallel electrodes and charge is moved using a three-phase clocking scheme (see chapter 2).

A major problem found with SCCDs is that charge became trapped in traps at the silicon - silicon dioxide interface. This typically limits the efficiency with which charge can be transferred across the CCD from pixel to pixel to 98%. This can severely degrade the system resolution and is much too low for scientific devices. In BCCDs, where the charge packets are stored some distance beneath the silicon surface where there is a significantly reduced number of traps, the CTE is greatly increased, typically to values greater than 99.999%.

1.8.3 The second dimension

The discussion above has shown how the pixels can be defined, in one dimension, by applying appropriate potentials to the electrodes. The standard technique for confining the charge to a well defined channel (and defining the second dimension in a 2-dimensional imaging array) is the use of a channel stop diffusion, as illustrated in Figure 1-9. Typically, these are heavily doped p regions, which act to lower the potential energy profile in their vicinity, and therefore serve to define columns in the CCD.
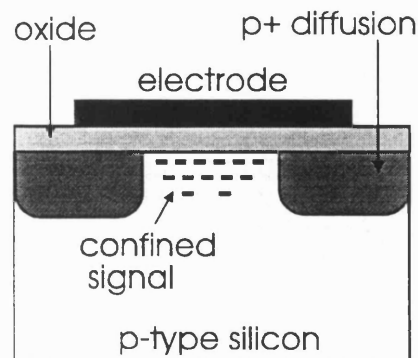
Figure 1-9 Channel stops

1.8.4 Detection of optical photons and x-rays

Optical photons are absorbed in the silicon by interacting photo-electrically with electrons in the valence band. The electrons are excited from the valence band to the conduction band, a gap of approximately 1.14eV, where they can move freely in the silicon, and are collected at the potential minima. A single electron is released for each visible photon absorbed, and an image is produced because the number of electrons stored is, therefore, proportional to the intensity of the incident radiation.

As with film, bare CCDs have a poor x-ray absorption efficiency and, for x-ray examinations where patient dose is important, should be used with a phosphor screen. This screen can be in direct contact with the CCD or, alternatively, the light photons produced in the phosphor can be directed towards the CCD by appropriate optics. For examinations where dose is less important it is possible to detect the x-rays directly in the CCD, giving a high resolution image.

1.8.5 Output circuitry of CCDs

Once the charge can be moved through the CCD to some detection point, it must then be converted into a useful signal. This can be done in many ways, the most common of which is to use a floating diffusion circuit, as illustrated in Figure 1-10. the readout operation is as follows:

1. Turn reset FET 'on' to charge the capacitance at the gate of the output FET to the potential of Vrd. As well as a contribution from the reverse biased output diode, the capacitance has some contribution from any stray capacitance in the output circuit
2. Turn reset FET 'off'
3. Clock charge onto the output node. This partially discharges the capacitance, causing the potential on it to drop by an amount proportional to the charge transferred from the CCD. i.e. $\Delta V = Q / C$
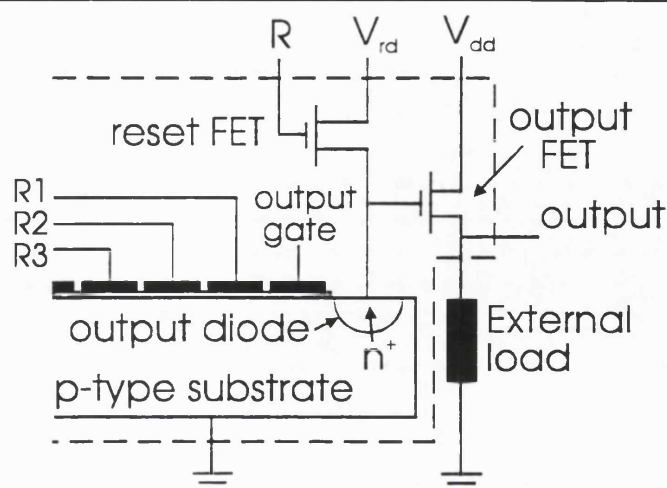
Figure 1-10 Typical CCD output structure

When the reset FET is turned on, charge from a previous pixel drains out through a resistor at V_{rd}. It is useful for calibration of the system if the camera design allows the potential across V_{rd} to be monitored, as it is directly related to the average number of electrons per pixel. This technique is used in chapter 3 for system calibration.

1.8.6 Design of area imaging CCDs

This section describes various ways in which CCDs can be used to produce area (i.e. two-dimensional) images. The first two - frame transfer arrays and interline transfer arrays - are alternative two-dimensional structures. The third - time delay and integration - is a technique for producing 2-dimensional images form a moving platform.

Frame transfer arrays

A schematic of a frame transfer array is shown in Figure 1-11. The vertical columns are defined by channel stop diffusions and the horizontal lines are supplied by electrodes.
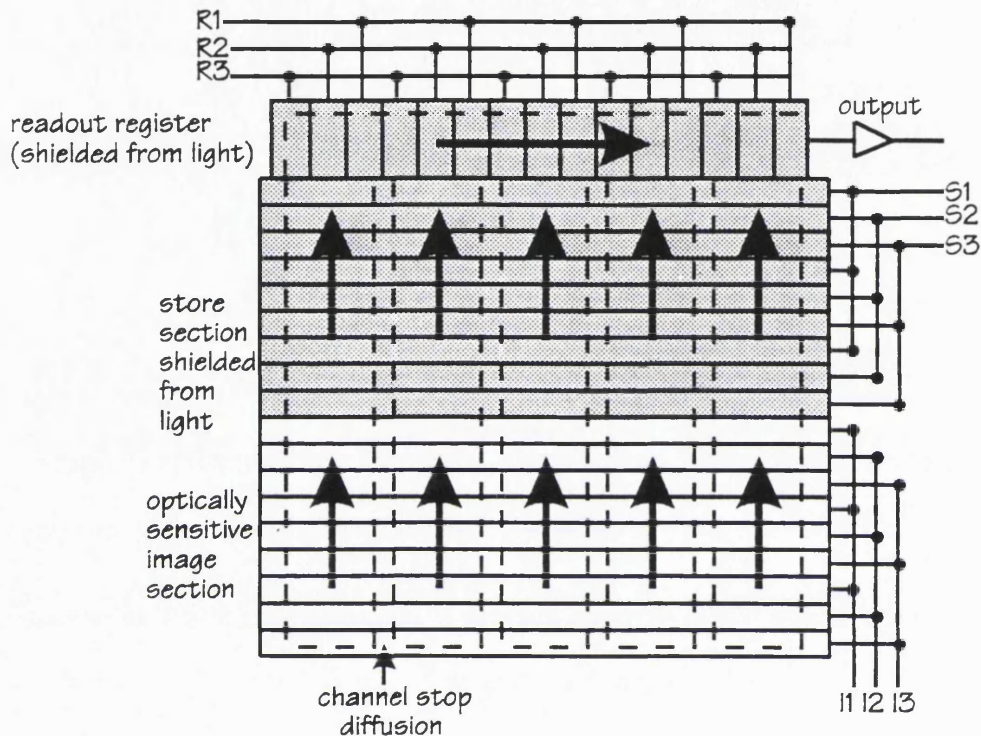
Figure 1-11 Schematic of a CCD frame transfer array

The electrodes in frame transfer arrays are divided into three sections: the integration section, the image storage section and the readout register. An image is incident on the integration section, where one or two of the electrode phases are held at a suitable bias (say, 10V) to store the photo-generated charge. This sensing element is bounded by electrodes (biased at, say, 0V) and the channel stop diffusions, thus giving the array its spatial resolution. At the end of the integration period (that is, the designated time for which the image is collected on the image region) appropriate clocking waveforms are applied to the gates in the integration and storage regions, and all collected charge is moved from the integration section to the store which is shielded from incident radiation.

This frame of information is then moved, by applying appropriate clocking to the electrodes of the store and readout register, one line at a time into the serial readout register and transferred horizontally to the output stage of the CCD. While this is happening, a second image frame is being collected in the integration section. If radiation is still incident on the imaging area when the charge collected in the integration section is moved into the store section, then there will be some image smear, caused by the finite time taken by charge transfer. The faster that charge is transferred between the two sections, the less the smearing.

Interline transfer arrays

A schematic of an interline array is shown in Figure 1-12.
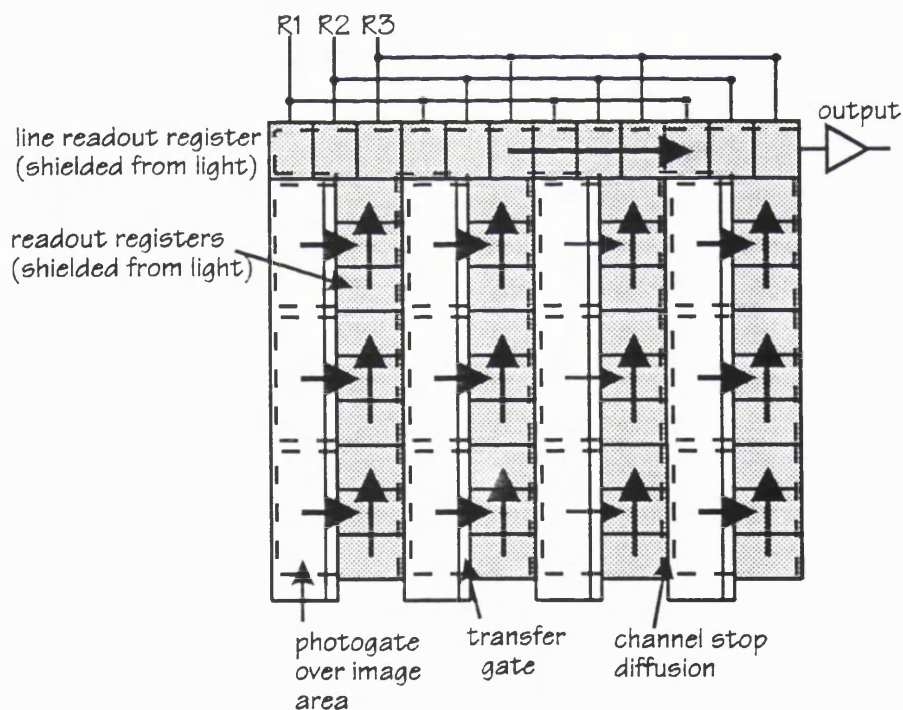
Figure 1-12 Schematic of a CCD interline transfer array

As for the frame transfer device, interline transfer devices have an integration section, store section and readout register. The difference between the two schemes is the

location of the store section. Also, each sensing element is defined by a single photogate, rather than by three electrodes. The photogates in each column are separated by channel stop diffusions. After the integration period, during which charge signals are collected beneath the photogates, the charge is transferred horizontally in one step to the storage register, which are shielded from light by, for example, a metal overlay. This frame is then read out line by line in a similar manner to that used in the frame transfer array. The transfer of the collected image from the integration section to the storage section is very fast ($\sim 1\mu s$) and, therefore, the use of interline transfer arrays virtually eliminates image smear. The readout regions, however, introduce some optically dead regions into the imaging area, which will affect the optical coupling between the CCD and any scintillator coating.

Time delay and integration

Time delay and integration (TDI) is a technique which is used to take images using CCDs which are positioned on moving objects. For example, groups such as the airforce use TDI to take images from fast moving aeroplanes. The technique is based on a CCD which has an integration section, but no storage section. If such a CCD is stationary and no shuttering mechanism is employed to overcome the lack of a storage region, it will only produce a one-dimensional image of a two-dimensional object, as information in the column direction is lost due to smearing as the charge is clocked down the columns. However, the TDI technique allows a 2-dimensional image to be produced by introducing a relative motion between the image and the CCD. That is, the charge is moved down the columns with a velocity V_C, and the CCD is translated with the same velocity, but in the opposite direction. Charge produced at a certain point in the CCD by the image can therefore remain the same position (in the image frame) and integrate until this point reaches the readout register of the CCD. This line of the image is then read out. The length of an image produced by a TDI system is therefore not limited by the size of the CCD.

TDI: The chosen technique

Using CCDs in scanning mode for mammography has a number of potential advantages over butting a large number of CCDs together to give a full area detector:

- The smaller breast volume irradiated at any one moment gives a significant reduction in the amount of scattered radiation reaching the detector. A slot is preferable over a grid as slots stop none of the primary radiation

- Fewer CCDs are needed

- Less problems with butting CCDs together

- Scanning the x-ray tube across the breast removes the common problem of varying effective focal spot size across the breast area. e.g. a nominal 0.4mm focus may have an effective size of 0.9mm close to the chest wall (Law 1993)

Disadvantages include:

- Mechanically more complex

- Slot scanning systems only use a small fraction of the available x-ray flux. X-ray tube power limitations may mean that this is a problem resulting in an increased exposure time

In the context of this prototype system the advantages of TDI seem to overcome the disadvantages and, therefore, this is the technique of choice. Note that a TDI system can also, potentially, be operated in a pseudo-full area mode.

1.8.7 Details of noise sources in CCDs

Noise is introduced into the signal from a CCD from various sources, including input quantum noise, dark current noise, fixed pattern noise, charge transfer noise, background electronic noise, readout noise and digitisation noise. These are discussed below.

Dark current

All semi-conductor imaging devices experience dark current resulting from the thermal generation of charge carriers. This charge fills the potential wells, effectively reducing the dynamic range of the detector. It also introduces background shot noise, which adds to the shot noise of the detected image. Dark current and its associated noise can be reduced using various techniques, from cooling the CCD to using 'clever' clocking techniques, and, except in applications with very low signal levels or long integration times, should not pose a fundamental restriction.

Fixed pattern noise

Fixed pattern noise (FPN) in the image is due to non-uniformities in both dark current production and responsivity. In many ways it is equivalent to screen structure mottle and film granularity found in film-screen systems. FPN can be the dominant noise source at high signal levels but is easily corrected using a simple algorithm which take advantage of the system linearity.

In a two-dimensional frame transfer or interline transfer device, two two-dimensional arrays (look-up tables or files) are needed to describe the non-uniformities in the CCD. The first describes the dark current non-uniformities, and consists of a two-dimensional dark image which should be subtracted from any optical (or x-ray) image. The second array describes variations in the visible or x-ray response of the detector. It is calculated by placing the CCD in a flat field (i.e. uniform intensity) of visible photons or x-rays. A correction factor is then found for each pixel to bring its signal level to be equal to the average. For example, a pixel which detects 10% more photons than the average has a correction factor of 1/1.1 to bring its value to the average. The corrected image is therefore given by:

$$P_{i,j}^C = C_{i,j}(P_{i,j}^D - D_{i,j})$$

Equation 1-2

where $P_{i,j}^C$ is the corrected pixel value corresponding to pixel co-ordinates i and j, $P_{i,j}^D$ is

the detected intensity value at the given pixel, $D_{i,j}$ is the average dark current expected

to be collected by the pixel and $C_{i,j}$ is the correction factor to bring the pixels

responsivity in line with the average. For TDI systems non-uniformities down a given

column average out and only column to column variations are important.

Readout noise

As described above, once the charge from a given pixel has been detected by the output

circuitry, the output node is reset by turning the reset FET 'on' so that the signal charge

flows away to the V_{rd} connection. There is an uncertainty in the potential to which the

output node is reset, giving an rms. variation of (Holdsworth et al 1990):

$$\sigma_{reset} = \frac{\sqrt{kTC}}{q}$$

Equation 1-3

where C is the output node capacitance (typically 0.2pF), k is the Boltzman constant, T

is the absolute temperature and q is the charge on the electron.

This source of noise can be eliminated from the signal using a technique called correlated

double sampling (CDS), in which the reset level and the level after charge transfer are

both sampled and the results subtracted, leaving the component due to the signal charge.

Charge transfer noise

This source of noise comes from fluctuations in the number of charge carriers which are

successfully transferred through the CCD to the output circuitry. If the signal charge

makes N transfers, the total amount of charge lost is approximately ϵnN, where n is the

number of electrons in the charge packet, and ϵ is the charge transfer inefficiency. The

variance on this is given by $(\epsilon nN)^{0.5}$. The charge transfer efficiency of modern BCCDs is

extremely high - typically 99.9995%. This source of noise is, therefore, generally negligible.

Background electronic noise

Background electronic noise can come from two main sources. The first is the electronic noise produced by components and power supplies of the camera board (which drives the CCD) and analogue-to-digital converter. Secondly, CCD preamplifiers can be very susceptible to external electrical interference (EMI) and care is needed to screen all signal cables and the detector. Background electronic noise can often be the most significant source of noise after input quantum noise (see, for example, Holdsworth et al 1990).

Digitisation noise

The quantisation error of a digitiser is given by (Holdsworth et al 1990):

$$\sigma_{dig} = \frac{\Delta E}{\sqrt{12}}$$

Equation 1-4

where ΔE is the number of electrons represented by 1 ADU. If 12bits are used to represent the full well of a CCD published systems indicate that this source of noise is small compared with dark current noise and background electronic noise (see, for example, Holdsworth et al 1990, Beynon and Lamb 1980...)

1.8.8 The use of CCDs in mammography

CCDs have been used in a number of configurations for digital radiography including mammography (Maidment et al 1993), angiography (Roehrig et al 1987 and 1988) and dental imaging (Cox et al 1994, Spiekerman et al 1994). In North America work on the use of CCDs in digital mammography is at an advanced stage, with one screening unit being ready for clinical tests. Two commercial units have also become available: the

Fischer MammoVision and LoRad SM. A schematic of the Fischer system shown in Figure 1-13. Both of these are designed for use in stereotactic breast needle biopsies and preoperative needle localisations. The use of CCDs for such a procedure has allowed radiologists to be introduced to the technology without having some of the technical problems associated with imaging the larger area required of a screening unit.
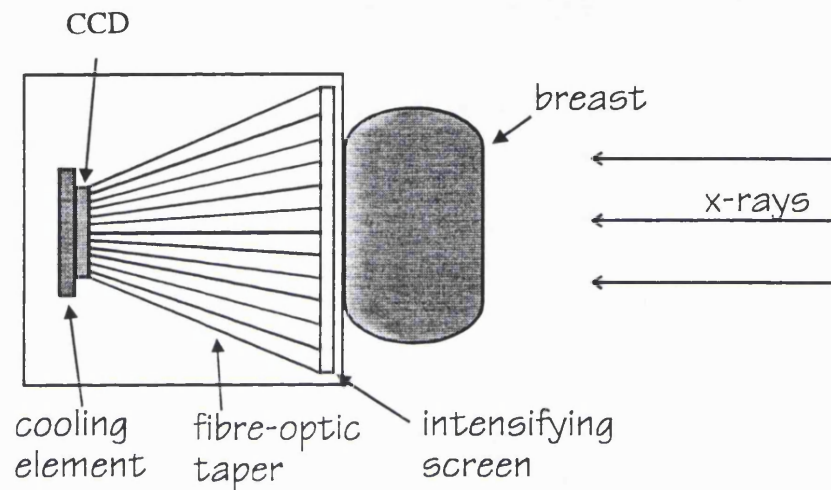
Figure 1-13 Schematic of a commercially available CCD based system

These systems are considered a success (Roehrig 1994), not least in reducing the average procedure time from 45 minutes to 20 minutes. Disadvantages of theses systems compared with film-screen detectors include the relatively small field-of-view of only 5x5 cm^2; the larger area available with film gives a better perspective of the breast anatomy adjacent to the target area. Another concern is the spatial resolution of the systems, which is limited by the pixel size and the demagnification between the screen and the CCD (0.3 - 0.5) to 50μm pixels at the intensifying screen. The worry is that this may be inadequate for the small number of localisations which involve very small calcifications (Roehrig 1994).

The most advanced digital mammography system which is appropriate for screening and is based on CCDs is a prototype clinical scanned-slot digital mammography imaging system developed by a group in Toronto (Maidment et al 1993). This system, which is currently ready for clinical tests, consists of a $Gd_2O_2S{:}Tb$ phosphor screen coupled via a 2:1 demagnifying fibre-optic taper to a series of TDI CCD detectors. The detector's top

surface is a slot and is scanned in an arc across the breast using a swing arm, which also rotates the x-ray tube. Advantages of pivoting the x-ray tube as well as the detector are that variations in x-ray flux due to the heel effect are avoided and that the effective focal spot size is invariant with scan position. The chosen slot width gives a measured scatter-to-primary ratio of 0.005, significantly less than the value of approximately 0.5 typically found at the exit plane of the breast. The CCDs used in this system have 27μm pixels, equivalent to approximately 50μm pixels in the mid-plane of the breast. Published MTF data for this system give a limiting resolution (5%MTF values) as 8.7mm^{-1} and 5.7mm^{-1} in the slot and scan directions respectively. This can be compared with sampling frequencies of 9.6mm^{-1} and 8.1mm^{-1} in the two directions (the sampling frequencies differ in the two directions because of anisotropy in the demagnifying fibre-optic). The x-ray tube used has a tungsten target with 0.3mm nominal focal spot size and Al filtration of half-value layer (HVL) 0.95mm. A 60cm source to image distance is used. The system has been tested using the American College of Radiology (ACR) accreditation phantom (RMI, Model 156), with a mean glandular breast dose of 0.85mGy, and found to exceed the image quality requirements of the ACR.

1.9 Summary and discussion

This chapter has described the advantages of using digital detectors in place of the film-screen combination currently used in mammography. These include the separate image capture, image display and image storage stages, computer aided diagnosis and tele-radiography. The advantages of CCDs over other digital detectors were indicated, in particular their small pixel size which should allow the high resolution achieved with film-screen systems to be maintained. The theory of the design and operation of charge-coupled devices was then described and the use of time delay and integration techniques to overcome the size mismatch between the breast and the CCD was discussed. Finally, current uses of CCDs in mammography were described. It was noted that a CCD based mammography system has been built by a Toronto research team, and it is appropriate to indicate the reasons for building a second prototype:

- To investigate the use of directly coated CCDs, compared to the fibreoptically coupled devices used in Toronto

- To investigate the use of different alternative coatings for use in TDI CCD scanning systems (i.e. CsI(Tl))

- To theoretically and experimentally investigate the optimisation of digital mammography systems

- To gain experience in the design and construction of such a system

- To separately investigate sources of degradation of resolution and noise

2. A CCD BASED MAMMOGRAPHY SYSTEM

2.1 Introduction

This chapter describes the implementation of a prototype scanning digital x-ray imaging system. The design of the prototype was kept as simple as possible while allowing the feasibility of using such a system in a clinical environment to be assessed. The main example of this was the use of only one CCD in the prototype system to avoid the complication of butting several CCDs together, but still allowing factors such as modulation transfer function (MTF) and noise power spectrum (NPS) to be measured, and also providing a large enough image to allow evaluation of sections of breast phantom images. The camera board was designed to allow easy access to the CCD to facilitate easy exchange of CCDs.

The prototype system can be considered as seven interconnected blocks: the camera, the timing generator, the correlated double sampling (CDS) unit, the scanning gantry, the framegrabber, the personal computer (PC) and the x-ray tube. The flow of information between these blocks is illustrated in Figure 2-1.

2.2 Charge coupled devices and camera board

The CCDs used in this work are EEV CCD15-11s. These CCDs, which were originally designed for use in high performance scientific spectroscopy, are front illuminated and consist of an array of 1024 columns x 256 rows x 27µm square pixels, giving an imaging area of 27.6 x 6.9 mm^2. Five CCDs were available, three of which had a CsI(Tl) coating and one which had a fibreoptic stud with high lead content on its imaging surface (Schott high-trans. 32AS). These are listed in Table 2-1. The values of the phosphor thicknesses were provided by the manufacturer and are accurate to within 15%

(Martinez 1994). With the exception of CCDe, all these CCDs are fronted with a glass protective plate.
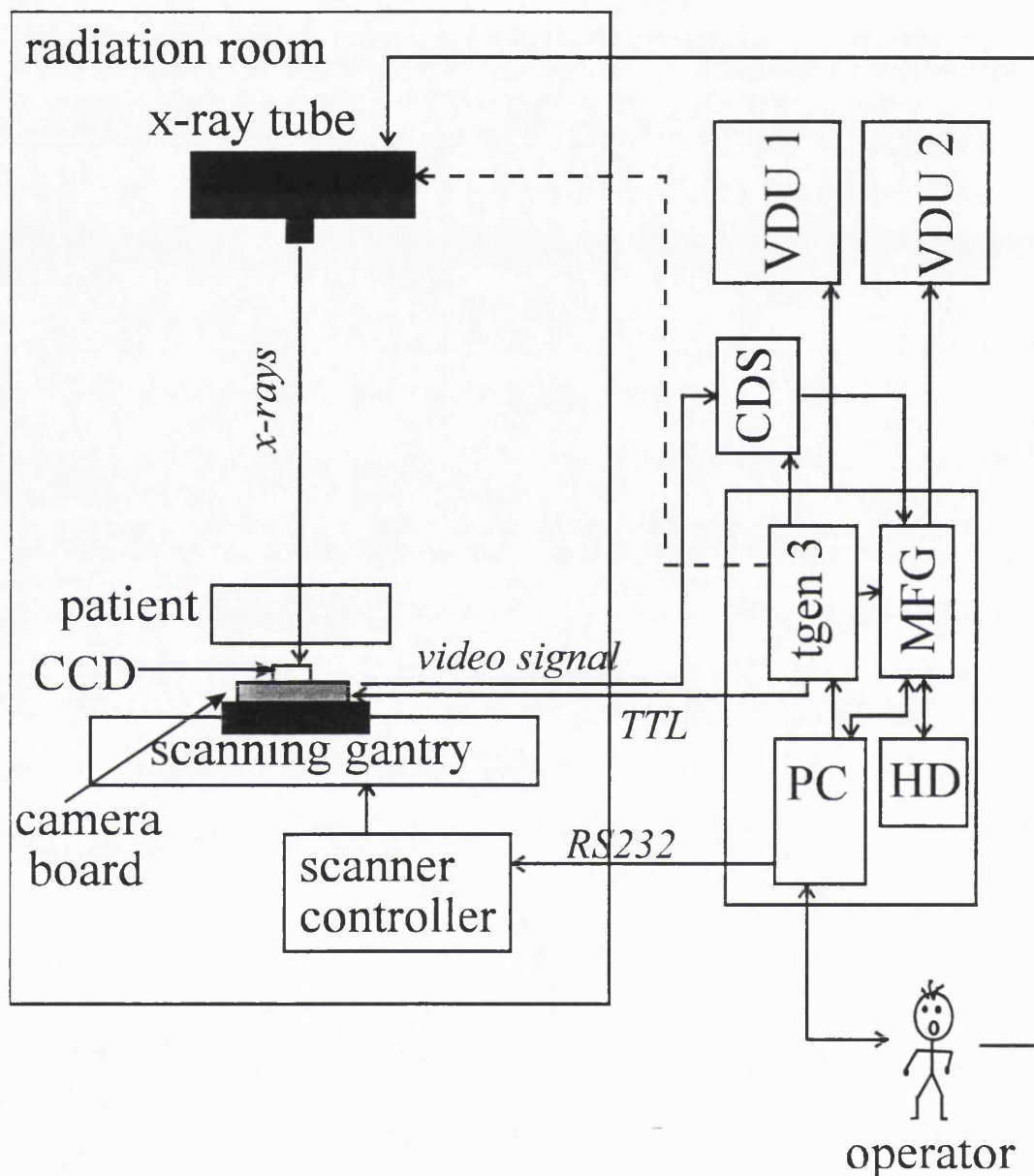
Figure 2-1 Schematic showing information flow in the prototype imaging system. A dotted line indicates a route not used at present. Other abbreviations are: HD (hard drive), tgen3 (timing generator v3), MFG (Modular Frame Grabber) and CDS (correlated double sampling unit)

Device	Serial number	Details
CCDa	A2179-20-15	bare device
CCDb	A2072-18-17	43μm CsI(Tl) coating
CCDc	A0922-4-8	67μm CsI(Tl) coating
CCDd	A2154-16-15	120μm CsI(Tl) coating
CCDe	unknown	5mm fibreoptic stud on imaging surface

Table 2-1 CCDs available for this work

CsI(Tl) has a broad emission spectrum which is well matched to the sensitivity of silicon photodiodes and most front illuminated CCDs (see chapter 3). The structure of the coating used here is shown in the scanning electron microscope (SEM) images of Figure and Figure , which were taken for this work. The detectors in these images were provided by EEV Ltd for a previous project (Martinez 1994). The characteristics of the CsI layers are known to be strongly dependent on the types of substrate and its temperature at the time of deposition. In principle, the cracks and columnar structure seen in these figures can help to channel light down towards the CCD and, therefore, improve the resolution of the system (see, for example, Martinez 1994).

CCD 15-11s are packaged in a 20 pin DIL ceramic package. All operating voltages were set at EEVs normal specification (EEV 1993), with the exception of the substrate voltage which was kept at 8V (normal spec. 6V) to reduce dark current (see chapter 3 for details of this). The camera board provides the appropriate voltages to the CCD, some of which are constant and some of which are determined by applied locking signals. It acts as a buffer between the clocking signals from the timing generator and the CCD and also provides some initial signal amplification. The camera board was purpose built using a "quickwire" board, thus allowing it to be easily adapted to accept a different CCD pin architecture if necessary. The video output is connected to the correlated double sampling (CDS) unit via co-axial cable.
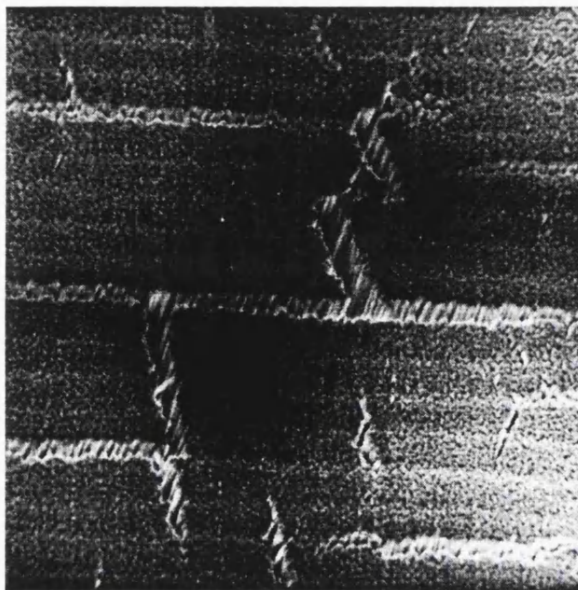
Figure 2-2 SEM image of CsI(Tl) structure. The width of this image is 180μm

Figure 2-3 SEM image of CsI(Tl) structure. The width of this image is 18μm

Clocks supplied by the timing generator to the CCD (via camera board) are i1, i2, i3, r1, r2, r3 and the reset pulse:

- i1, i2 and i3 give the three-phase clocking waveform to move the charge down the columns of the CCD.

- r1, r2 and r3 give the three-phase clocking waveform to move the charge along the readout register

- The reset pulse turns the reset FET in the output circuitry of the CCD on and off to prepare for the next charge packet, as described in chapter 1.

These drive waveforms (as used for TDI clocking) are shown in Figure . The cycle 'line-move' moves the charge one row down the CCD; 'pixel-readout' moves the charge one pixel along the readout register. Each 'line-move' is followed by 1040 'pixel-readouts'. This is 1024 CCD pixels and 16 blank pixels which can be used to give a zero reference level. This group of 'line-move' and 1024 'pixel readout' is repeated 1024 times to give a complete image.

CCD 15-11s are not designed for use in integration mode as there is no masked region, but can be used in this mode by keeping all clocks stationary (for example, integrating the charge under phase 1) for a set integration time and then quickly reading out the charge. The preferred technique is to set the integration time to be significantly longer than the illumination time. e.g. an integration time of 2s with an illumination time of 1s or less. This helps overcome any problems with interfacing the illumination source (x-ray or optical) and the frame grabber. Additional problems associated with using the 15-11 in this way include the increased dark current, although this was not found to significantly degrade the image, although there was an increased need for efficient flat fielding.

Solid arrows show the movement of the charge

CYCLE 'line-move': Move imaging area down one line
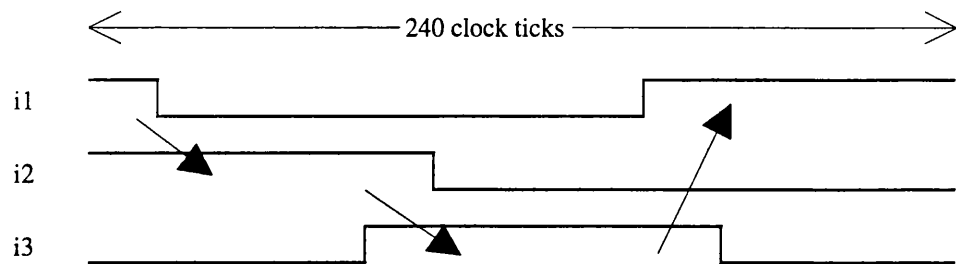
**CYCLE 'pixel readout': Pixel readout into amp using unequal clock intervals
to prevent switching spikes**
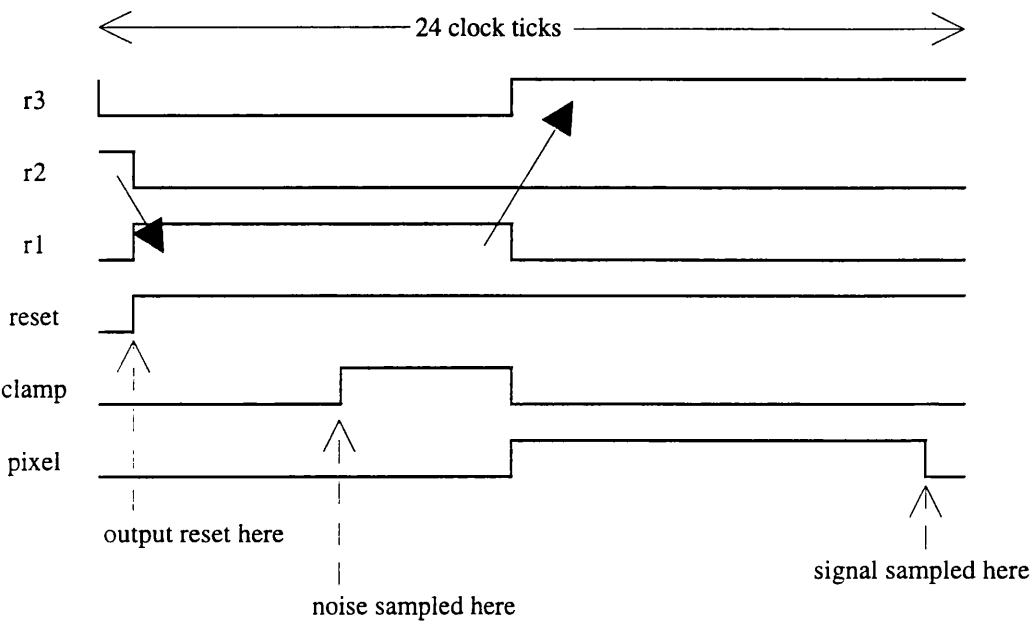
Figure 2-4 Typical TDI clocking waveforms

2.3 Timing generator

The timing generator provides all the clocks for the CCD (via the camera board), CDS unit and frame grabber:

- i1, i2 and i3 to move charge down the columns of the CCD
- r1, r2 and r3 to move charge along the readout register of the CCD
- Reset pulse to CCD
- Pixel and clamp signals for the CDS
- New line signal for the framegrabber
- New frame signal for the framegrabber

The timing generator used in this work was designed at Sira Ltd. It is a PC AT expansion board which can be programmed to generate up to 128 clock sequences on 23 outputs (TTL connections), with clock rates up to 50Mhz. The timing generator is programmed by means of an initialisation file and a timer description file. Once initiated, the timing generator runs continuously. A typical example of timings used in this work is shown pictorially in Figure . In the waveforms of Figure it takes 240 clock pulses to move the image area down one line (12µs for a clock rate of 20Mhz) and 24 clock pulses to move the charge one pixel along the readout register (1.2µs), giving a line rate of 777 s^{-1} (for a clock rate of 20Mhz)

2.4 Correlated Double Sampling Unit

The correlated double sampling (CDS) unit provides the analogue-to-digital conversion. CDS is a technique used to eliminate noise generated in the output structure of the CCD. Before a signal packet of electrons can be transferred into the output structure of the CCD, which converts the signal electrons to an output voltage, it must be cleared of the previous packet. This reset is carried out by pulsing an MOS gate high so that the electrons are drained away into an adjacent diode, as described in chapter 1. There is a

thermal noise component associated with the reset, V_{noise}. The same noise component is present on valid video as on the reset level. That is,

$$V_{reset} = V_{dark} + V_{noise}$$
$$V_{valid} = V_{signal} + V_{nosie}$$

<div align="right">Equation 2-1</div>

where V_{reset} is the measured output voltage at the output transistor source of the CCD during reset, V_{valid} is the OS voltage during the valid video period and V_{dark} is the reset noise-free output voltage with no incident light or x-rays. This is only true if V_{reset} and V_{valid} are sampled within a certain minimum time. Correlated double sampling works by taking the difference of these two samples to eliminate the reset noise:

$$V_{CDS} = V_{reset} - V_{valid}$$
$$= V_{dark} + V_{signal}$$

<div align="right">Equation 2-2</div>

One disadvantage of this technique is that it results in double sampling of the off-chip amplifiers, resulting in a doubling of the noise power added to the signal (see, for example, Holdsworth et al 1990).

The CDS unit used in this work was previously designed at Sira Ltd. The unit has the following features which are relevant to this system:

- A top sample rate of 10.10^6 samples per second (10MSPS)
- Three gain levels which are set by using appropriate resistors
- Variable zero offset

The CDS requires the following inputs:

- Video signal from camera board
- Pixel clock from timing generator to show when to sample V_{valid}
- Clamp clock from timing generator to show when to sample V_{reset}

The relative positions of the pixel and clamp clocks are illustrated in Figure .

2.5 Frame grabber

Digital data from the CDS unit is temporarily stored in the frame grabber before being transferred to the hard drive of the PC. The frame grabber used in this work was Imaging Technology's Modular Frame Grabber (MFG) with 3Mb memory board and digital variable scan acquisition module. This is a plug-in PC card which combines a flexible memory architecture, a programmable Texas Instruments TMS34020 graphics system processor and a VGA chip to display the collected image on a second monitor. In this work the MFG image memory was configured as 2 x 1k x 1k x 12bit, allowing two 1k x 1k TDI images to be stored at any one time. The MFG also has a 1k x 1k x 4bit overlay memory, which can be used to annotate images - this is useful, for example, when identifying events above a given threshold. Simple image processing was carried out with the image stored in the framegrabber memory. External inputs to the MFG are the data line from the CDS and pixel clock, frame enable and line enable from the timing generator. All frame grabber initialisation, such as memory architecture initialisation, and functions, such as image grabbing (where the frame grabber constantly grabs images) or image snapping (where the frame grabber snaps a single frame) were controlled by purpose written C programs.

2.6 Scanning gantry and controller

The prototype unit uses a linear stage (M424.21) and motor controller (C808.20), both produced by Physik Instrumente, Berlin. The C808 controller is programmed by the PC via RS-232 communications. It can control the position and velocity of up to two d.c. motors with a final position accuracy and repeatability of 1μm. For each axis the C808 has registers containing information such as actual position, target position, velocity, gain, torque and dynamic error, with variables like target position, and gain which are programmed from the P.C.

Of particular importance for a TDI scanning system is the accuracy to which a constant velocity can be maintained. The M242.41 controls the velocity of the linear stage by keeping it on the position-time line calculated from the programmed values for velocity, acceleration and deceleration, with the difference in actual and calculated positions stored in the dynamic error register. Any deviation from the position-time line results in a proportional increase, or decrease, in motor voltage, updated every 4ms. For example, if at time=4s the gantry should be 5cm from its starting point, but has actually only moved 4.9cm then the controller will react to this dynamic error of 0.1cm and increase the velocity of the gantry. The 'stiffness' of this control loop is set by dynamic gain. Too high or too low a dynamic gain can result in excessive motor vibrating during motion.

One problem experienced with this system is that exact velocity information is not available. Also, time overheads in the RS-232 communications between the controller and the PC and 'time jitter' in the internal loops of the gantry means that there is uncertainty in the exact point in time when a position is taken. Although this is not a problem during normal operation, it complicates experimental attempts to quantify effects like velocity stability and alternative methods must be used. These are described in chapter 4, where the system resolution is evaluated. The distributors claim a top speed of 18cm s^{-1} (personal communication, K Grimley 1993), although, when using the CCD 15-11, the TDI scanning speed used here was typically 21mm s^{-1} (this is limited by the pixel rate of the CCD EEV15-11)

Figure 2-5 shows the scanning gantry with the camera board in position. The camera board is attached via a single bolt. The angle between the scanner and the camera board is controlled by two positioning screws.
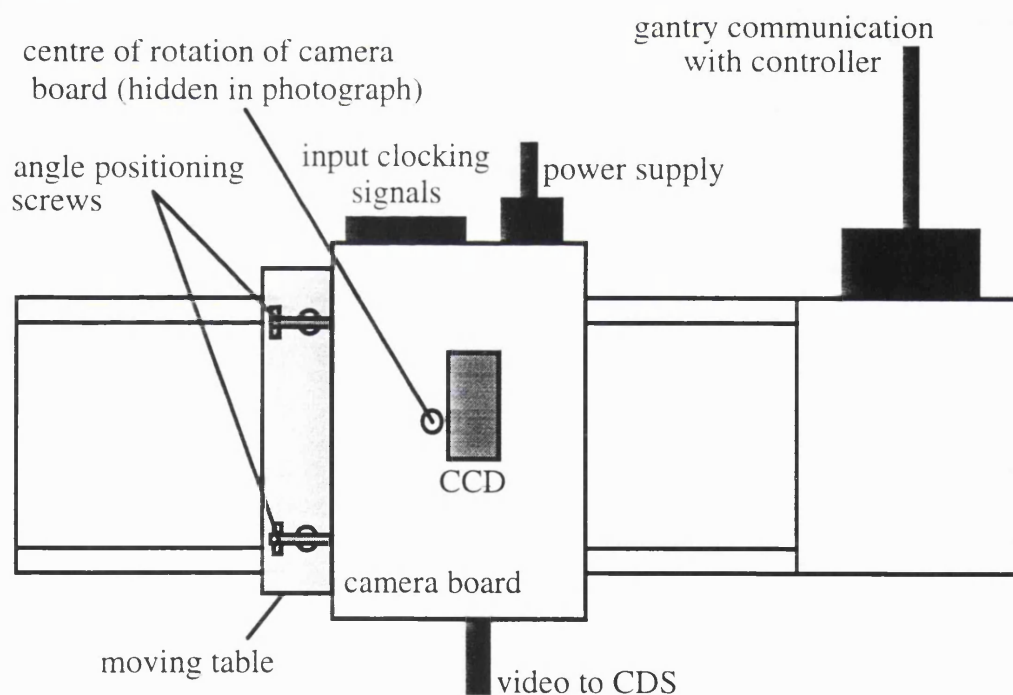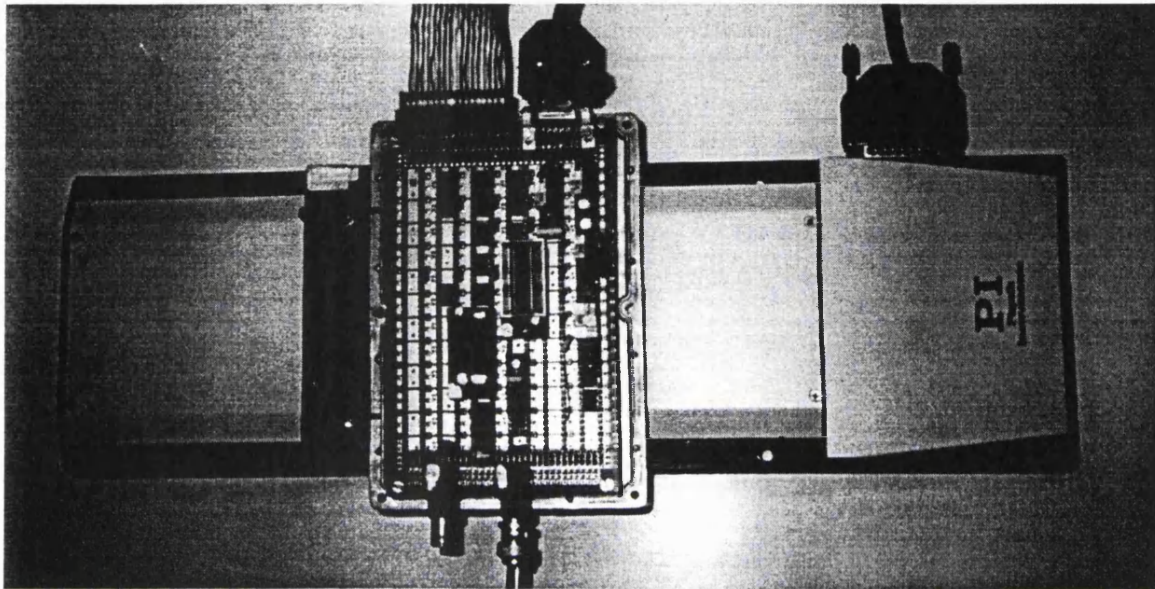
Figure 2-5 Photograph and schematic of the scanning gantry with camera board

2.7 Personal Computer

Overall control of the imaging process is achieved by a C program. This program provides initialisation of the frame grabber, timing generator and scanning gantry as well as a number of imaging and image processing functions, some of which are listed in Table 2-2.

Function	Details
grab	Continuously grab images from the CCD
snap	Store the image which immediately follows the next new frame pulse
scan	Scan across the object and snap an image at a user defined point
flatfield	prepare flat fielding data (1-D for TDI or 2-D for integration)
correct	Correct image with flat fielding data
adjust	Adjust image ADU values to give maximum display contrast. i.e. adjust image in a linear fashion such that $ADU_{min}=0$ and $ADU_{max}=4095$.
line	Draw a cross-section of the image along a user defined row or column
SNR	Evaluate SNR of a defined object (see chapter 6 for various methods)
save	Save image in user determined format
restore	Restore image from disk

Table 2-2 Examples of functions performed by control software

Separate programs were also written to evaluate MTF and NPS.

To take a TDI image the following steps are taken:

- Initialise timing generator (i.e. load waveforms)
- Initialise motor controller (i.e. set velocity, acceleration etc.)
- Start scanning gantry moving
- Continuously ask motor controller for position of gantry until it reaches a predetermined position
- Snap image

Other functions, such as flat fielding, are performed as required.

2.8 X-ray tubes

Two x-ray tubes were available for use in this project: a Mullard Guardian 125 tungsten target x-ray tube with an AED generator (model 44) and a Siemens Mammomat mammography screening unit with molybdenum target x-ray tube (P 50 mA 0.4). The Guardian/AED combination has a minimum tube voltage of 36kV and 45kV for radiographic and fluoroscopic mode respectively. This is slightly high for mammographic applications but tube voltages higher than 36kVp have been used successfully in similar mammography systems (Maidment et al 1993). It has a reasonably constant tube current throughout its exposure time and, therefore, is appropriate for use with the scanning system, although it was necessary to account for current variations when calculating noise power spectra (NPS) and signal-to-noise ratios (SNRs) as discussed in chapters 4 and 6 respectively. It has a nominal focal spot size of 1mm, which is larger than most modern mammography systems. It was possible to vary the amount of filtration by placing 0.5mm thick layers of 99.9995% pure aluminium in front of the tube. The inherent filtration was estimated by measuring the half value layer, HVL, (Johns and Cunningham 1983) from which the filtration can be calculated using, for example, the results of Wachsmann and Drexler 1976 or HPA 1976. which relate HVL to total filtration. For this tube the total inherent filtration was estimated at 0.8mm.

The Mammomat has a 0.4mm nominal focal spot and tube voltage settings of 28, 30, 35 and 40kVp. It can be used with either aluminium or molybdenum inherent filtration, although only the molybdenum filtration was used in this case. The HVL of this tube was measured as 0.4mmAl (28kVp), giving an estimated inherent filtration of 0.7mmAl.

The image detection system and x-ray tube were not interfaced - the x-ray tube exposure was controlled manually. It is reasonably straight forward to interface with the x-ray tube control by, for example, starting the exposure at a pulse from the timing generator,

but this was not considered necessary for this project. This may be carried out in future work, but it is likely that the equipment will first be upgraded to use several CCDs and to take clinical, or near-clinical, size images.

2.9 Summary

The prototype system uses EEV CCD15-11s in either TDI mode, with a scanning rate of 21mm s^{-1} or stationary mode with a typical integration time of 2s. The maximum scanning rate is limited by the maximum readout rate of the CCDs. Five different CCDs are available, three with CsI(Tl) coating, one bare and one with a 1:1 fibreoptic stud on its imaging surface. In TDI mode each image is 1024 x 1024 pixels (27.6 x 27.6 mm^2); in stationary mode the image produced is 1024 x 256 pixels (27.6 x 6.9 mm^2). With the exception of the x-ray exposure, which is controlled manually, all imaging processes are fully controlled via the PC. Two x-ray tubes were available - a general purpose tungsten target x-ray tube with a nominal 1 mm focal spot and minimum tube voltage of 36kVp (in radiographic mode) and a dedicated mammography unit with a nominal 0.4mm focal spot and a range of tube voltages in the mammographic energy range (28-40kVp).

3. CCD PERFORMANCE PARAMETERS

3.1 Introduction

Initial calibration of the system involved evaluation of the following parameters:

- System gain in electrons per ADU
- Gain of the output amplifier in terms of μV per electron
- Quantum detective efficiency (QDE) of the CCD (optical and x-ray)
- Linearity of the system's response to optical and x-radiation
- Pixel-to-pixel response variations to give data for the flat fielding algorithm
- Full well capacity of the CCD
- Dark current
- Evaluation of the signal fraction due to direct x-ray interactions in the CCD

Optical measurements were taken for several reasons:

- Continuous x-ray measurements are difficult because of the risk of overheating the x-ray tube. Optical systems do not suffer from this and are therefore ideal for evaluation of factors such as system gain (analogue-to-digital units per electron, ADU electron^{-1})
- Comparison of optical and x-ray measurements can allow some evaluation of the effect of the scintillator
- The optical response of CCDs is well documented. Comparison between published and experimental results gives confidence in the present results and techniques.

Many of these measurements require a flat field illumination. That is, one which is uniform across the imaging area. This chapter therefore starts by describing the optical and x-ray equipment used to produce the necessary flat field.

The first three of the parameters listed above, and described in sections 3.3.1, 3.3.2 and 3.3.3, give different measures of the system gain and must be known if the digital signal, in analogue-to-digital units (ADUs), is to be understood in terms of electrons in the CCD and number of incident x-rays or visible photons. These relationships are subsequently used in the evaluation of a number of system parameters including full well capacity, dark current, noise magnitude and noise power spectra. The reliability of these results is, to some extent, dependent on an assumption of system linearity, and this is tested in section 3.3.4. If the system is non-linear this may also have a significant effect on the effectiveness of the flat fielding algorithm to reduce fixed pattern noise. The extent of this fixed pattern noise is indicated in section 3.3.5, where the pixel to pixel response variations are measured. Measurements of the full well capacity are reported in section 3.3.6. The available full well capacity can be significantly reduced by the presence of dark current in the CCD. Dark current, which also acts as a source of noise, is fully characterised in section 3.4. This includes an evaluation of various ways to minimise the dark current. Another source of noise is caused by x-rays which pass through the CsI coating and are absorbed in the silicon of the CCD. The influence of this effect on the signal is evaluated in section 3.5. The influence of these direct interactions on the measured signal and noise transfer characteristics (MTF and NPS) is described in chapter 4.

3.2 Calibration equipment

A schematic diagram of the optical apparatus used for these measurements is shown in Figure 3-1. The reasonably large distances between the CCD and the light source , and the use of two diffusers, was necessary to produce a flat field at the input surface of the CCD. A green filter was used to approximate the spectrum emitted from CsI(Tl) screens, as shown in Figure 3-2 where it is compared with the typical response of a CCD.

The x-ray flat field was produced using a Mullard Guardian 125 tungsten target x-ray tube with 1.8mmAl total filtration placed 150cm away from the CCD.
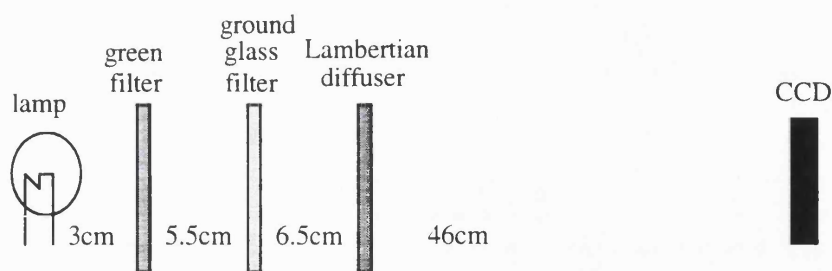
Figure 3-1 Apparatus used for producing an optical flat field

The quality of the optical flat field was evaluated by positioning the camera board on the linear scanner such that the columns of the CCD were perpendicular to the scanning direction. The average signal (ADU) along a set column was calculated. The scanner was then moved on by 27μm and the average signal along the same column calculated. This was repeated across all the flat field to find any intensity variations. The reason for averaging the data along the same column for all measurements, was that this removes the effect on the data of any response variations in the CCD.
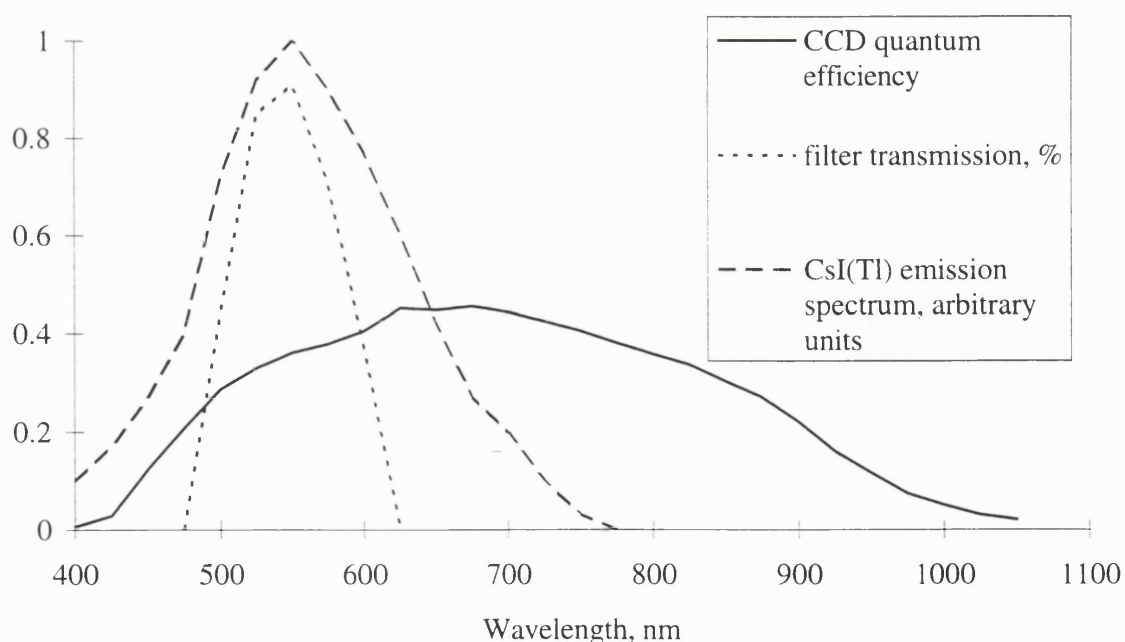
Figure 3-2 Comparison of quantum efficiency of CCD, filter transmission used and emission spectrum of CsI(Tl)

With some experimentation, the apparatus geometry was finally optimised to give a central 5cm wide flat field with peak-to-peak and rms. intensity variations of 0.9% and 0.4% respectively. The x-ray flat field was evaluated in a similar way, with the x-ray system in fluoroscopic mode, and found to be slightly less uniform, with peak-to-peak and rms. variations across the central 5cm region of less than 1.5% and 1% respectively, although this was difficult to measure because of variations in x-ray tube current.

In the optical case the average irradiance at the CCD was measured using a United Detector Technology optometer (S370) with a silicon detector (model 248). The x-ray irradiance was measured using a Keithley electrometer (35050A) with a Keithley ion chamber (15cc, model 96035).

3.3 Experimental techniques and calibration results

3.3.1 System gain in terms of electrons per ADU

After charge has been detected in the output circuitry of the CCD, it flows out through the V_{rd} connection, through the reset resistor. The average charge on a pixel can therefore be directly measured by monitoring the potential across this resistor: If V_{reset} is the potential measured across the reset resistor, R is the resistance of the reset resistor, $N_{e,T}$ is the total number of electrons collected in the integration time, Δt is the integration time, q is the charge on an electron and Ne,p is the average number of electrons per pixel, <ADU> is the average ADU per pixel, and I is the average current flowing through the reset resistor, then for the CCD 15-11:

$$I = \frac{V_{reset}}{R} = \frac{qN_{e,T}}{\Delta t} = qN_{e,P}\frac{1024\times256}{\Delta t}$$

$$N_{e,ADU} = \frac{V_{reset}}{\langle ADU\rangle}\frac{\Delta t}{q\,R\,(1024\times256)}$$

Equation 3-1

V_{reset} and ADU. were measured for a range of light levels, and a straight line graph of V_{reset} vs <ADU> drawn, with gradient (V_{reset}/<ADU>). The number of electrons per ADU was then calculated from Equation 3-1. This was repeated for each gain setting on the CDS, and for each available CCD. The results are given in Table 3-1. In summary, the conversion factor varied from 20 to 300 electrons per ADU depending on the gain of the CDS. With the exception of CCDa, all the CCDs gave similar results. CCDa has a substrate short, which introduces a large number of electrons into one region of the CCD and saturates several columns. This means that the average ADU is not representative of the average number of electrons in the CCD at any one time, and a lower value of electrons per ADU is found. In other work it will be assumed that this is caused by the short, and CCDa will be assumed to have the same conversion factor as the other CCDs. The errors on these results are +/- 2%.

CCD	low gain	medium gain	high gain
a	246	32.8	19.2
b	308	40.5	23.7
c	319	42.3	24.8
d	310	40.7	23.6
e	301	40.0	23.0

Table 3-1 Gain of each CCD (electrons per ADU) for different CDS gain settings

3.3.2 Gain of the output circuitry of the CCD

The gain of the output circuitry of the CCD is calculated by first removing the CCD from the camera board and connecting a square wave source (produced by a piece of specially built circuitry) to the output transistor source pin (pin 13) of the camera board. The square wave is a scaled version of r3. The amplitude of the square wave is typical of that obtained from CCD output circuitry and is fully controllable. The gain of the camera board and CDS can be calculated, in units of ADU per mV, by plotting amplitude against average ADU. Knowledge of the system gain in electrons per ADU then allows simple calculation of the gain of the CCD in μV per electron, the results of

which are given in Table 3-2. These are all within 15% of EEV's published value of 3µV per electron. This difference is attributed to the sensitivity of the CCD gain to the applied potentials, particularly the voltage at the output drain. The errors on these results are ±0.08. These results, together with the results of section 3.3.1 can be used to calculate the gain of the electronics in terms of ADU/µV for the three different CDS gains. These were evaluated, neglecting the results for CCDa which were severely affected by a pixel short, and found to be 0.001220±0.000002, 0.0092±0.0001 and 0.017±0.002 ADU/µV for the low, medium and high gain settings respectively.

CCD	gain
a	2.74
b	2.66
c	2.56
d	2.64
e	2.72

Table 3-2 Gain of each CCD (µV/electron)

3.3.3 Response of the CCD

The quantum efficiency, η, is the fraction of incident photons which contribute to the output of the detecting system (Barrett and Swindell 1981). Using the measured system gain the number of electrons in the CCD was measured for a range of light levels and x-ray flux levels.

To estimate η, the incident light is assumed to be monoenergetic, with wavelength, λ, 570nm. The number of optical photons incident on the imaging face of the CCD is given by:

$$N_\gamma = \frac{E\Delta t}{hc/\lambda}$$

Equation 3-2

where E is the incident irradiance, h is Planck's constant and c is the speed of light. The number of electrons generated in the CCD is given by:

$$N_e = \frac{I\Delta t}{q} = \frac{V_{reset}\Delta t}{Rq}$$

<div align="right">Equation 3-3</div>

where Δt, I, V_{reset} and R are defined in section 3.3.1.

One electron is produced per optical photon absorbed (Beynon and Lamb 1980) and, therefore, η can be described by:

$$\eta = \frac{N_e}{N_\gamma} = \frac{V_{reset}}{E}\frac{1}{Rq}\frac{hc}{\lambda}$$

<div align="right">Equation 3-4</div>

The quantum efficiency is calculated using Equation 3-4 and from the gradient of a straight line graph of V_{reset} vs E. The results of optical quantum efficiency for the different CCDs are given in Table 3-3. The optical QE was measured at 27-39% (for $\lambda=570$nm), with the coated CCDs having an experimental value of approximately 30% and the bare and fibreoptic devices having higher values of 36-38%. These higher values agree with published results (see Figure 3-2). This variation between devices is attributed to several sources including absorption of light in the CsI and reflection of light at the interface between the air and the phosphor coating, which can be significant.

The response of the CCDs to x-rays was calculated in terms of electrons per incident exposure for a 45kVp spectrum with 1.8mm aluminium filtration by plotting a straight line graph of average ADU against exposure and then converting the ADU values to number of electrons using conversion factors determined above. For known exposure and spectra it is possible to calculate the number of incident x-ray photons by the use of appropriate conversion factors (Johns and Cunningham 1983, Birch et al 1979) and, therefore, calculate the number of electrons per incident photon. The results of these

calculations are given in Table 3-3. Some of the signal is due to interactions in the CsI and some is due to interactions of x-rays direct with the silicon of the CCDs. This effect is discussed further in section 3.5. The errors on the values for QE and x-ray response (electrons pixel^{-1} C^{-1} kg) are approximately ±4%. Errors on the response in electrons photon^{-1} are higher, as these rely on the data of Birch and Marshall 1979 and are dependent on the shape of the spectrum.

These measurements were taken with the protective glass plate in place in front of the upper surface of the CCD. For this spectrum this plate was found to reduce the signal by approximately 20%. Without this plate the responsivities are 25% higher.

CCD	QE (λ=570nm)	Response to x-ray spectrum (electrons/pixel/(C kg^{-1}))	Response to x-ray spectrum (electrons/photon)
a	36.5	-	-
b	29.3	19.01 10^9	86.8
c	30.8	31.40 10^9	142.5
d	27.1	42.95 10^9	194.9
e	38.7	-	-

Table 3-3 Response of CCDs to visible light and x-rays.

These results indicate that the coupling efficiency of this system is well above the 10 electrons per x-ray interaction which Maidment and Yaffe 1994 shown is the minimum required to ensure that images are x-ray quantum noise limited at high, as well as low, spatial frequencies.

3.3.4 An evaluation of system linearity

If the mean output signal of the CCD, in ADUs, can be described by:

$$<ADU> = k + gE^{\gamma}$$

<div align="right">Equation 3-5</div>

where k is some offset (including dark current), g is the system gain, E is the input irradiance in W cm^{-2}, and γ is a measure of the linearity of the system. Equation 3-5 was fitted to the data from section 3.3.2, which gives the number of electrons produced for a range of incident fluxes. The values of γ found are given in Table 3-4. All the CCDs showed good linearity for both visible and x-irradiation, with γ found to be close to unity in all cases.

CCD	γ (visible radiation)	γ (x-rays)
a	1.01±0.01	-
b	0.99±0.01	1.03±0.05
c	1.05±0.01	0.97±0.05
d	1.01±0.01	1.04±0.05
e	1.02±0.01	-

<div align="center">Table 3-4 Linearity of the CCDs to visible and x-radiation</div>

3.3.5 Response variations

In high intensity images, fixed pattern noise, due to pixel-to-pixel variations in dark current and responsivity can be the dominant source of noise. Since in a TDI device each charge packet is integrated down an entire column, there are no row-to-row variations; only column-to-column variations are important. The flat field algorithm described in chapter 1, therefore, only needs a one-dimensional array describing these column-to-column variations. This is achieved by illuminating the CCD under the flat field and, after removing the contribution due to dark current, calculating the correction factor needed to make the signal in each column equal to the average signal across the entire CCD. It is interesting to compare the rms. and peak-to-peak response variations for the different CCDs. These parameters were evaluated for the entire width (i.e. all columns) of the CCDs, and also for arbitrary regions 50 and 100 columns wide. The results are given in Table 3-5, where the response variations are expressed as a percentage.

CCD (v: visible x: x-ray)	peak-to-peak (total area)	σ (total area)	peak-to-peak (over 100 columns)	σ (over 100 columns)	peak-to-peak (over 50 columns)	σ (over 50 columns)
a (v)	10.1	1.4	2.6	0.5	1.6	0.5
b (v)	11.7	1.7	1.3	0.3	1.0	0.2
b (x)	11.5	3.9	3.5	0.4	3.0	0.3
c (v)	4.0	0.6	1.3	0.2	1.0	0.2
c (x)	10.0	2.7	3.0	0.4	2.9	0.3
d (v)	13.6	2.1	1.4	0.3	1.1	0.3
d (x)	15.0	2.4	3.2	0.3	2.9	0.3
e (v)	11.0	2.3	1.5	0.3	1.1	0.2

Table 3-5 Response variations for the different CCDs, expressed as a percentage

In summary, across the whole CCD, column to column peak-to-peak and rms. variations in optical response were typically 10% and 2% respectively, falling to 1% and 0.3% for a 50 column wide region. Variations in x-ray response were slightly larger at 15% and 3% for the entire CCD and 3% and 0.3% over 50 pixels. After applying the flat fielding algorithm the effective peak-to-peak x-ray response variations were measured at less than 0.2% across the entire CCD (for incident air kerma of 0.5mGy, evaluated as in IPSM 1989).

3.3.6 Full well capacity

A pixel can only store a certain amount of charge - the full well capacity. If more charge is generated than the potential well can hold, the excess carriers spread sideways into adjacent pixels - a phenomenon known as blooming. Blooming provides a reasonably simple method for estimating full fell capacity. A thin slit, as used in the MTF experiments, is focused onto a row or column, and the light intensity is gradually increased, until the charge carriers bloom into adjacent pixels. This method estimated a full well capacity for all the CCDs as approximately 750k +/- 50k electrons, a value which agrees well with the nominal specification provided by EEV.

3.4 Dark current

Dark current in CCDs is caused by the generation of electron-hole pairs at defects in the semiconductor, with the most significant contribution in non multi pinned-phase, MPP, (see section 3.4.5 for a discussion of MPP chips) BCCDs coming from generation due to interface states at the oxide-silicon interface (Burke 1991). The large number of pixels in the EEV CCD 15-11 (1024 columns x 256 rows), and its slow output circuitry, means that the fastest it can be read out, using a top pixel-rate of 1 MHz, is a quarter of a second. Operating the chip in TDI mode means that all the pixels will collect quarter of a second worth of dark current. For room temperature operation, using no dark-current reducing techniques, this has been measured at approximately 30k electrons per pixel - that is of the order of 6% of the full well capacity. Dark current, therefore, can reduce

the dynamic range of the system. It also acts as a source of Poisson shot noise which can be significant compared with other noise sources, such as amplifier noise. It is, therefore, both interesting and useful to examine ways of reducing dark current. Also, the dark current increases linearly with integration time, and any application requiring a slower readout - e.g. if the scanning gantry is to be moved at a slower rate - will soon become completely swamped in dark charge. The three main ways to reduce dark current - cooling the CCD, increasing the substrate voltage, and using a clocking technique known as dithering - are each described below.

3.4.1 Cooling the CCD to reduce dark current

Dark current in the CCD is strongly temperature dependent; the rate of thermal charge generation from surface states is given by (Blouke et al 1987)

$$J_{SS} = aT^{3/2} \exp(\frac{-E_g}{2kT})$$

Equation 3-6

where a is some device dependent constant (A cm^{-2} K$^{-3/2}$), T is the absolute temperature, k is the Boltzman constant and E_g is the silicon band gap. The band gap is also temperature dependent, given by (Blouke et al 1987):

$$E_g = 1.1577 - [(0.0007021T^2) / (1108 + T)]$$

Equation 3-7

where E_g is given in eV. The dark signal, in electrons, is given by:

$$S_{dark} = \frac{J_{ss} A_{pixel} t_{exp}}{q}$$

Equation 3-8

where A_{pixel} is the pixel area, t_{exp} is the exposure (i.e. integration) time and q is the charge on the electron). The amount of noise produced by this dark signal is given by:

$$\sigma_{thermal} = \sqrt{S_{dark}} = \sqrt{q^{-1} J_{SS} A_{pixel} t_{exp}}$$

Equation 3-9

Imaging CCDs used in astronomy are cooled by either positioning the chip in a liquid nitrogen cooled dewier, or using Peltier coolers. At temperatures below the dew point, if the CCD is in moist air, water will condense onto the CCD and cause corrosion, although this can be prevented by placing the CCD in a container purged with dry nitrogen gas. The working temperature of the CCD can be estimated by comparing the dark signal when the power is first switched on - i.e. when the CCD is at transient room temperature - and when the CCD has warmed up to its operating temperature. The temperature can then be estimated using Equation 3-8. In this way, the CCD's operating temperature was estimated at 30°C for a room temperature of 23°C. A significant problem with this heating up of the CCD during operation is the time that it takes before it stabilises - typically 30-40 minutes.
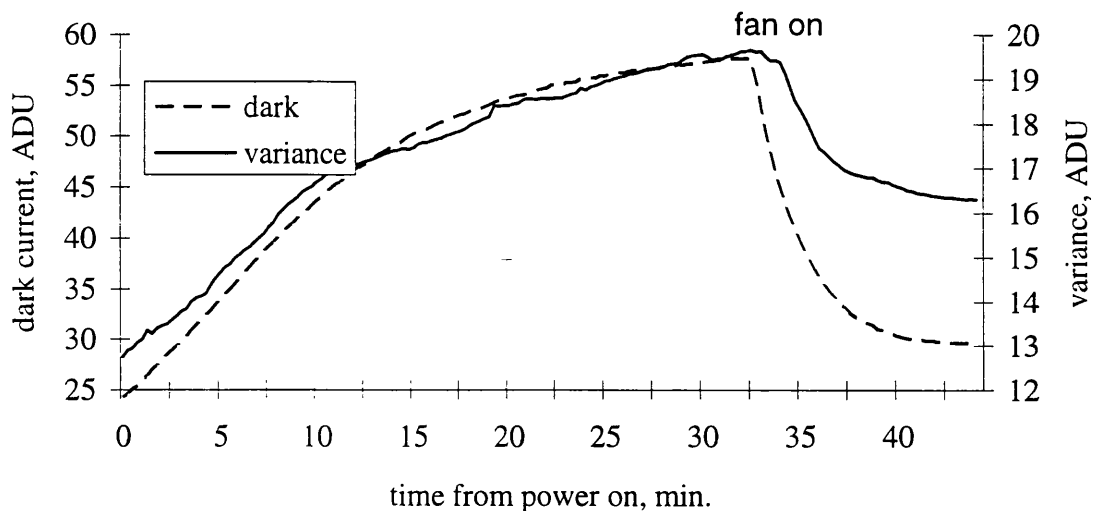
Figure 3-3 Effect of cooling fan on dark current

Dark current can not be adequately corrected for in the flat fielding algorithm until it has stabilised. It was found that the use of a small electric fan positioned approximately 15cm away from the CCD surface was sufficient to keep the CCD temperature to only slightly above room temperature, and, therefore, to reduce the initial stabilisation time to less than 5 minutes.

A potential complication is caused by the susceptibility of the output circuitry of CCDs to external electrical interference, although interference due to the fan was found to be small compared with the benefit of the reduction in dark current. The influence of the fan on the dark current and system noise is shown in Figure 3-3. To obtain these results the dark current was allowed to increase from 'power on', as the CCD heated up and, when stabilised, the fan was turned on, and the dark current and system noise is seen to decrease. These results indicate that a second generation system should include Peltier cooling.

3.4.2 Increasing the substrate voltage to reduce dark current

EEV buried channel CCDs show a significant decrease in dark current when the substrate voltage, Vss, is increased to 8 or 9 volts (EEV 1993). Experimental evidence of this for the 15-11 is shown in Figure 3-4. For each position on this graph it was necessary to recalibrate the system, as the gain of the CCD increases slightly with increasing Vss. The rate of electron-hole generation by interface states is strongly dependent on the density of free carriers at the interface; introducing a high density of carriers at the interface, as in accumulation or inversion, can significantly decrease the rate of thermal generation.
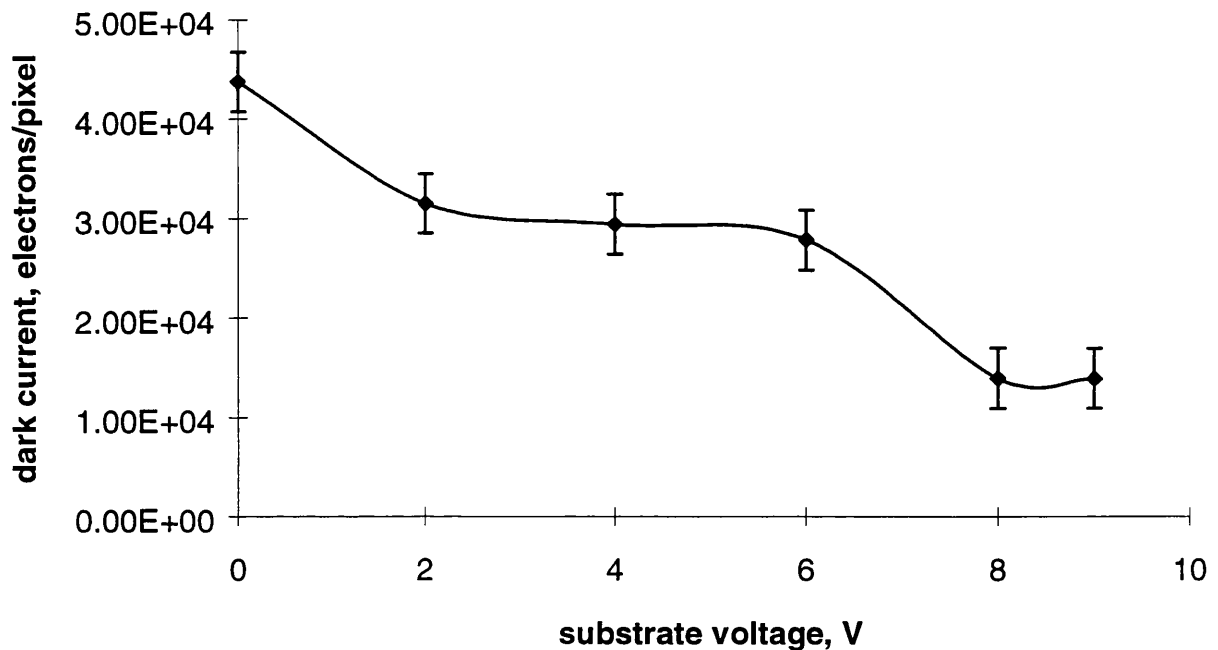
Figure 3-4 Effect of substrate voltage on dark current

This is because the thermal generation of free carriers at the silicon-oxide surface is a two step process: firstly, an electron is excited from the valence band to levels in the mid-gap (an equivalent process is the emission of a hole to the valence band); secondly the electron is excited to the conduction band. During normal operation (Vss ~ 6V) the silicon-oxide interface is clear of free carriers and the rate of thermal generation is at its maximum value. As Vss is initially increased from 0V, the depth of the depletion band beneath the electrodes is increased. When Vss reaches 8-9 volts it now equals the potential at the silicon surface below the low level electrodes (i.e. those at 0V) and holes flow from the p-type channel stops that form the CCD's columnar structure, to the surface region, as shown in Figure 3-5; the surface is effectively inverted from n to p type and dark charge generation is suppressed as the mid-gap levels are emptied of electrons by recombination with holes. This is only true for the low level electrodes (i.e. those at 0V); the surface potential under the high level electrodes (i.e. those at 10V) is still higher than Vss. It is not possible to increase Vss further to simultaneously invert this third phase to reduce dark current still further because once the surface is inverted Vs

becomes 'pinned' to Vss, and any further increase in Vss simply increases the maximum potential in the buried channel, Vc, by a similar amount. This will eventually reduce the difference between the high and low level channel potentials, giving a reduced full-well capacity. This effect is shown in Figure 3-5. Increasing the substrate voltage can decrease the dark current by 50-60%, depending on the clocking waveforms used.
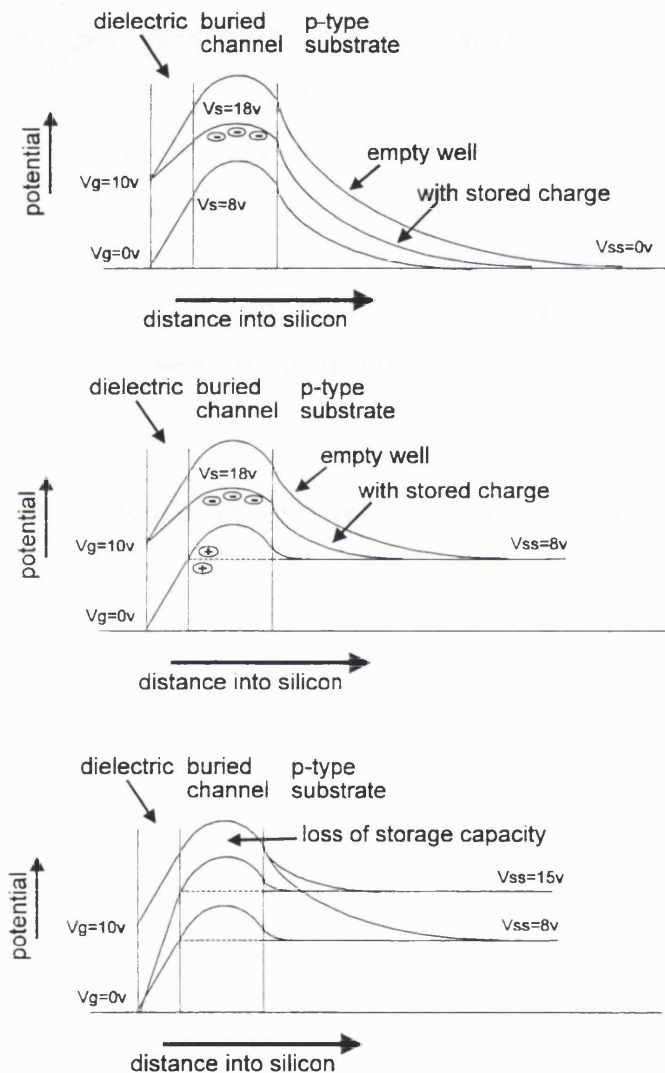
Figure 3-5 Effect of substrate voltage on potentials in a CCD

3.4.3 Dithering to reduce dark current

As discussed above, with conventional clocking at least one of the pixel electrodes must be in the non-inverted (high) state, as this is where the signal charge is collected. With a slightly different clocking scheme, however, it is possible to dynamically suppress the dark current generation even further. When a surface has been depleted, the mid-levels must be repopulated before the generation of dark current can resume. If the surface is inverted again before the mid-levels have had a chance to repopulate, dark charge generation can be suppressed in this third phase (Burke 1991). The use of this technique, known as dithering or charge pumping, is experimentally demonstrated in Figure 3-6. These results are for CCDa with medium gain, such that 1ADU is equivalent to 40 electrons per pixel. In this experiment a line of pixels is clocked down the CCD as normal, with the charge ending up under phase 1. A line of data is then read out from the readout register, whilst periodically swapping the charge in the integration region between phases 1 and 2. Phase three must be kept low to prevent charge mixing between the integration region and the readout register. The x-axis in Figure 3-6 shows the number of pixels which are readout between each transfer of charge from i1 to i3, or vice versa. As the charge is swapped between clocks at increasing rates, the mid-levels have less time to repopulate, and less dark charge is collected.

The problem with using this sort of technique on with the CCD 15-11 used in TDI mode, is that moving the i clocks when simultaneously reading out a pixel gives a series of distorted columns in the image, due to interference between the two processes - a large number of dithers in each line will give a very distorted image. This effect is significantly reduced by pausing pixel readout whilst the i clocks are swapped, and then resuming readout. When the system is being clocked at its maximum rate, these pauses result in an increase in the integration time and, therefore, prevent the use of higher dither rates and prevents further reduction of the dark current.
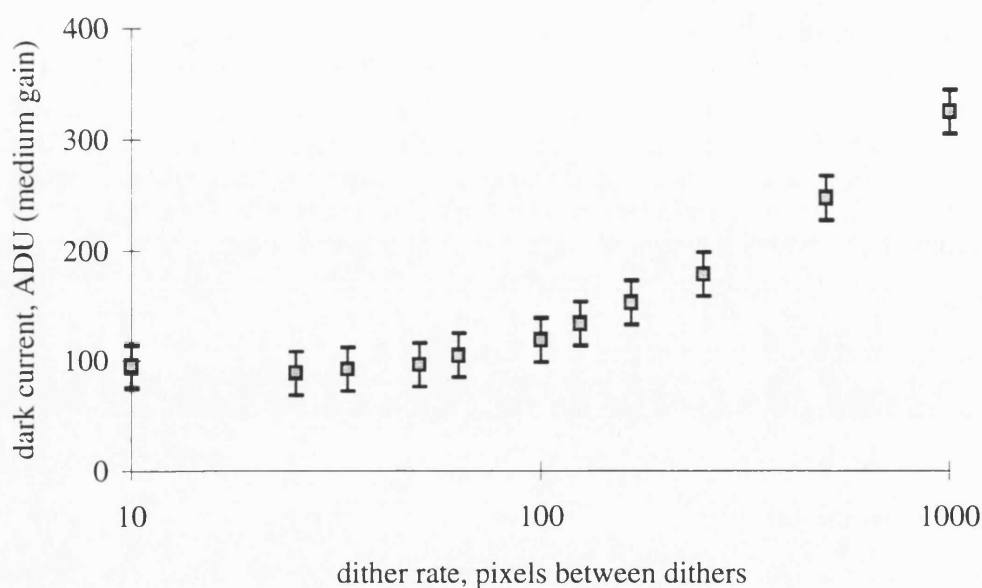
Figure 3-6 Effect of dithering on dark current

The large reduction in dark current when dithering is applied can be accompanied by an increase in rms. noise. This increase in noise is caused by pixel-to-pixel variations in the effectiveness of dithering, possibly due to variations in the inversion voltage, and is reduced by flat-fielding. Thus, dithering is worth while, but only if accompanied by efficient flat-fielding.

3.4.4 Spatial variations in dark charge generation

Figure 3-7 and Figure 3-8 show dark images for integration and scanning modes, clearly showing that some pixels produce more dark charge than others. Note that variations between pixels in a given column are averaged out when the CCD is operated in TDI mode. It is interesting to examine the effects of these non-uniformities on the statistics of the pixel values. Figure 3-9 and Figure 3-10 show log-log graphs of the standard deviation of the pixel value against the average pixel value for both a single column and a single row. For a single column, where, in TDI mode, the pixel-to-pixel variations are insignificant the gradient is 0.5, as would be expected from Poisson shot statistics. For a single row, the pixel to pixel variations are seen to dominate over Poisson noise, giving a

gradient of 1. The same effect can be demonstrated using illuminated images, where the pixel-to-pixel variations are caused by response variations instead of variations in the rate of dark current generation.
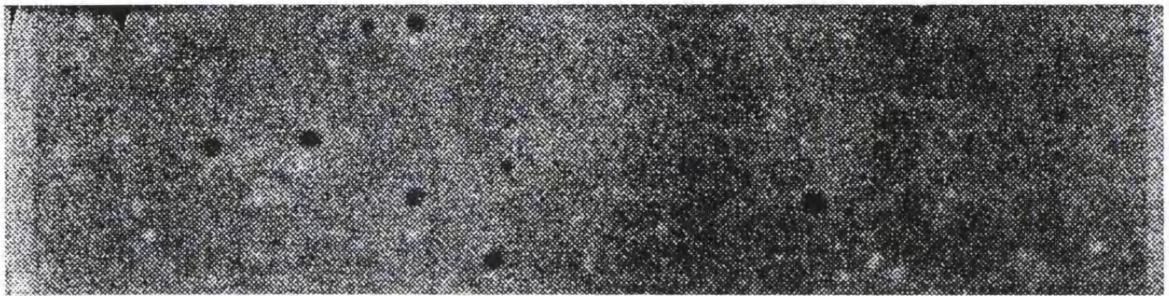
Figure 3-7 Dark image when in integration mode

Figure 3-8 Dark image when in TDI mode
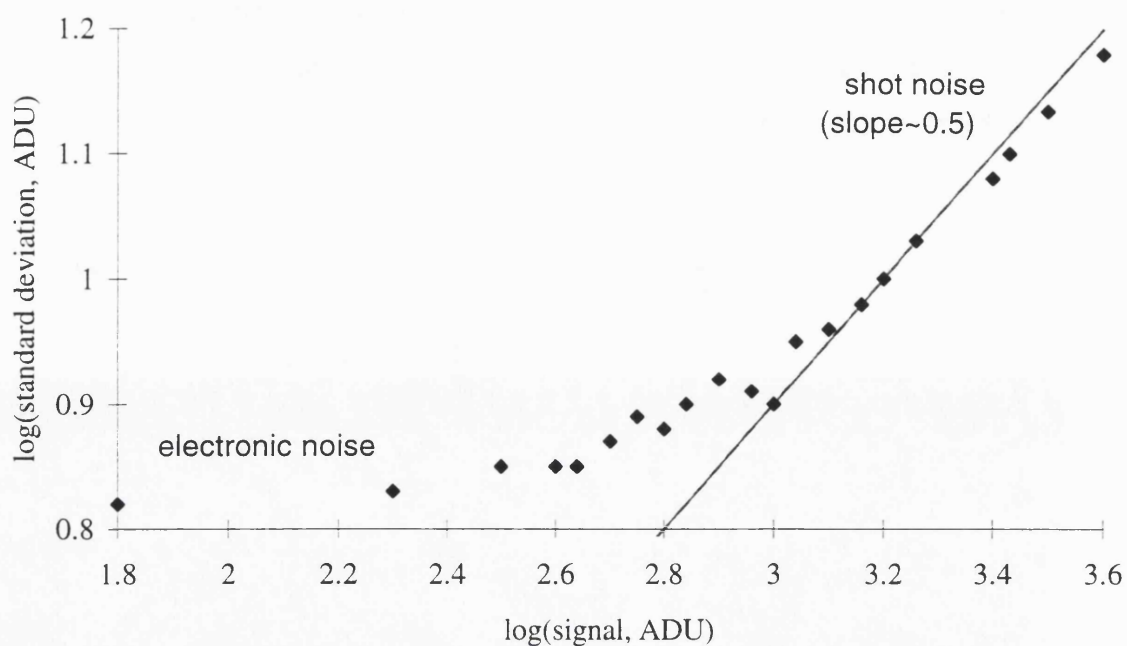
Figure 3-9 Noise as a function of dark current for a column of pixels
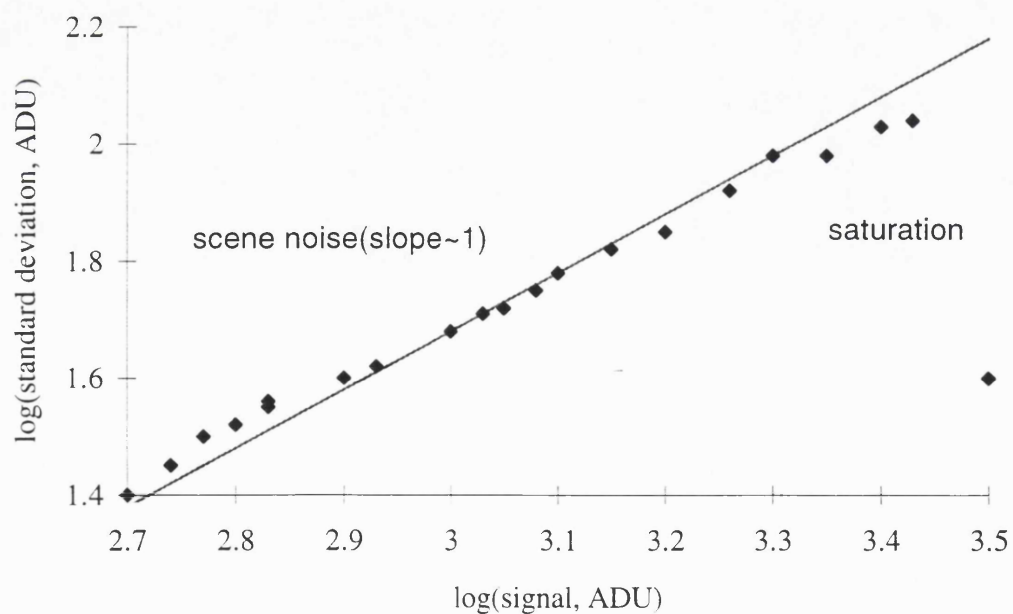
Figure 3-10 Noise as a function of dark current for a row of pixels

3.4.5 Multi pinned-phase CCDs

The technique of dithering was introduced in 3.4.3. to dynamically reduce the dark current. This was necessary because it is not possible to fully invert all phases of a conventional CCD, as this would result in the potential wells beneath each phase being equivalent and there being no collecting well. More recent CCD designs, including newer 15-11s and their replacement, the 30-11s, are available which overcome this limitation. These chips, known as multi pinned-phase (MPP) CCDs can operate totally inverted to achieve ultra-low dark current generation rates. For a three phase CCD this is achieved, for example, by doping the silicon beneath phase three such that when all phases are biased into inversion charge will collect under phases one and two, and be confined by phase three, known as the barrier phase. The full well capacity of a MPP CCD is determined by the MPP built in potential and, depending on pixel size, may be as much as 2-3 times lower than when only 1 or 2 of the three phases are inverted (Janesick 1991). EEVs data sheet for the CCD30-11 gives the typical maximum peak charge storage as 500k electrons per pixel, compared with 750k for the 15-11s used here. This reduction in full well capacity means that MPP CCDs are not suitable for all x-ray examinations, for which the above techniques should be used.

3.4.6 Summary of dark current reduction techniques

The following table shows the methods used, and an indication of their efficiency, to reduce dark current and dark current noise; for a pixel rate of 800kHz (equivalent to a TDI scan rate of approximately 21mm/s). Dark current reduction has the effect of maximising the dynamic gain of the CCD, and minimising dark current and associated noise.

The dark current, with dark current reduction, for all the available CCDs was measured. Typical values are given in Table 3-7. Note that variations in room temperature can have a significant effect on these values.

Method	Details	Typical dark current for CCDa (electrons per pixel)
none	no dark current reduction	30000
fan	keep CCD temp close to room	20000
increase V_{ss} to 8v	temp	7000
use dither clocking	100 dithers per line	4000

Table 3-6 Effect of dark current reduction techniques

CCD	Minimum dark current (electrons per pixel)
CCDa	4000
CCDb	7000
CCDc	15000 (see text)
CCDd	8000
CCDe	8000

Table 3-7 Typical dark currents for all measured CCDs

Dithering was not possible with CCDc, as it has a large pixel short in one column, which introduces a large number of electrons into the image at that point. When charge from this saturated column is transferred along the readout register, it was found that, if the i clocks were swapped, some of the charge would escape into the image region (as i2 is closer to the readout register than i1), thus ruining the image.

It is suggested that a second generation system should use Peltier cooling to both reduce dark current ant reduce the 'warm-up' time.

3.5 Direct x-ray interactions with the CCD

X-rays which pass through the phosphor coating may interact with the silicon of the CCD. This introduces a number of complications particularly as x-ray absorptions in the silicon produce many more electrons per absorbed x-ray than absorptions in the scintillator. These interactions, known as *direct hits*, act as an additional source of noise as well as acting to reduce the dynamic range of the CCD. In this section a simple theory to predict the fraction of total signal which is due to direct hits is constructed and shown to give reasonable agreement with experimental results. This theory is used in chapter 4 to estimate the influence of direct hits on the measured resolution (MTF) and noise (NPS).

3.5.1 Theory to predict signal fraction due to direct hits

The number of electrons produced in the silicon due to x-ray interactions in the phosphor layer can be approximated as:

$$N_e^{CsI} = \int_E \int_\lambda \phi_{x-ray}(1 - e^{-\mu_{CsI}(E)d_{CsI}})E f(\lambda)T(\lambda)\eta(\lambda)\,d\lambda\,dE$$

Equation 3-10

where $\phi_{x-ray}(E)$ is the incident x-ray flux at energy E, $\mu_{CsI}(E)$ is the linear attenuation coefficient of the phosphor coating, d_{CsI} is the thickness of the phosphor coating, $f(\lambda)$ is the emission function of the screen normalised such that

$$\int f(\lambda)d\lambda = n$$

Equation 3-11

where n is the number of light photons emitted per energy E (52 photons keV^{-1} for CsI(Tl), Knoll 1989), $\eta(\lambda)$ is the wavelength dependent detective quantum efficiency of

the CCD and $T(\lambda)$ is the transmission of the phosphor to the visible photons. It is assumed that all x-ray interactions in the screen are photoelectric interactions. Above the K-edge of CsI a significant fraction of the absorbed energy is re-radiated by K-shell fluorescence and, unless it is reabsorbed, this energy is lost to the conversion process. In the graphs below it is assumed that, for energies above the CsI K-shell, the amount of energy absorbed in the CsI is reduced by 50% because of escaping fluorescent photons. This value is a very approximate estimate based on Monte Carlo work of Martinez 1995. The influence of fluorescent photons absorbed in the silicon is neglected in this simple treatment.

If it is assumed that the transmission characteristics of the phosphor to visible photons are independent of wavelength then for CsI(Tl) Equation 3-10 simplifies to

$$N_e^{CsI} = \int_E \phi_{x-ray} 22.6 (1 - e^{-\mu_{CsI}(E)d_{CsI}}) E \, T \, dE$$

Equation 3-12

where the factor of 22.6 accounts for the integration over optical wavelength of the CsI emission spectrum multiplied by the wavelength dependent quantum efficiency of the CCD. The number of electrons produced in the CCD due to x-ray interactions in the silicon can be approximated by:

$$N_e^{Si} = \int_E \phi_{x-ray}(E) e^{-\mu_{CsI}(E)d_{CsI}} \frac{\mu_{Si}^{pe}(E)}{\mu_{Si}(E)} (1 - e^{-\mu_{Si}d_{Si}}) \frac{E}{3.65} dE$$

Equation 3-13

where $\mu_{Si(E)}$ is the linear attenuation coefficient of silicon at x-ray energy E, $\mu^{pe}_{Si}(E)$ is the photoelectric linear attenuation coefficient of silicon for x-ray energy E, d_{Si} is the active thickness of the silicon, typically 20µm. The factor $(E/3.65)$ gives the number of electron-hole pairs generated per x-ray absorption (Lumb 1987). It is assumed that all energy is transferred from the x-ray to the signal when an x-ray interacts

photoelectrically with the silicon, and that all the charge is collected. It is also assumed that energy transfer during Compton events is negligible compared with photoelectric events and can therefore be neglected. This is a reasonable assumption for the low energy x-rays used in mammography, but will introduce increasing errors as the incident x-ray energy is increased.

3.5.2 Experiment to find signal fraction due to direct hits

It is also possible to measure experimentally the approximate relative signals due to x-rays absorbed in the CsI and direct hits in the silicon. This is done by comparing pixel values taken under a number of different illumination conditions using both a CsI coated CCD and a bare CCD. The method used in this work is as follows. First, the total dark signal for 30 images was found, where the total number of electrons due to dark current is given by

$$N^{dark}_{coated} = \sum_{all\ images} \sum_{all\ pixels} n_{electrons}$$

<div align="right">Equation 3-14</div>

where $n_{electrons}$ is the number of electrons in a given pixel. The coated CCD was then illuminated with an Am-241 source placed a distance δ_{coated} from the surface of the CCD. The Am-241 source was heavily filtered, giving a near mono-energetic spectrum with energy 60keV. The total signal for 30 images was then found using

$$N^{\gamma+dark}_{coated} = \sum_{all\ images} \sum_{all\ pixels} n_{electrons}$$

<div align="right">Equation 3-15</div>

The total signal due to gamma events in both the CsI and the silicon for the coated device is then given by

$$N_{coated}^{\gamma} = N_{coated}^{dark+\gamma} - N_{coated}^{dark}$$

<div align="right">Equation 3-16</div>

The Am-241 source was then removed and the coated CCD replaced with a bare CCD, and the number of electrons due to dark current over 30 images, N_{bare}^{dark} was calculated as before. The Am-241 was then placed a distance δ_{bare} from the surface of the CCD and N_{bare}^{γ} calculated. The distance δ_{bare} was calculated such that the number of x-rays incident of the surface of the CCD (as opposed to the surface of the CsI) was equivalent in both the coated and bare case. That is,

$$\left(\frac{\delta_{coated}}{\delta_{bare}} \right)^2 = \exp(-\mu_{CsI} d_{CsI})$$

<div align="right">Equation 3-17</div>

The fraction of the total signal due to gamma events is then given by

$$f = \frac{N_{bare}^{\gamma}}{N_{coated}^{\gamma}}$$

<div align="right">Equation 3-18</div>

This technique was repeated using the near monoenergetic spectra from a secondary cadmium target illuminated with a collimated 60kVp tungsten target x-ray spectrum, and also using spectra from a tungsten target x-ray tube.

3.5.3 Comparison of theoretical and experimental estimates of direct hits

Figure 3-11 compares the predicted fraction of the total signal due to direct hits with experimental results. The theory is seen to agree reasonably well with the experimental results.
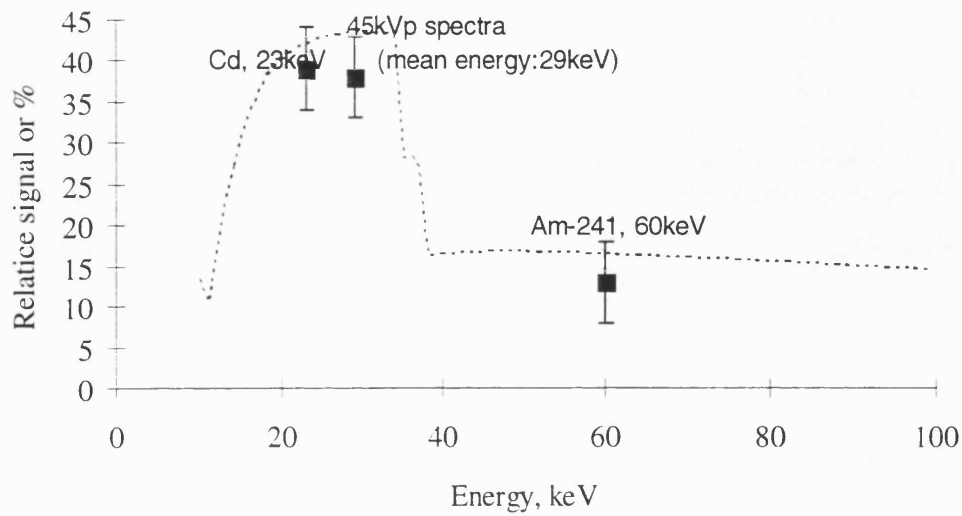
Figure 3-11 Fraction of signal due to direct hits in the silicon
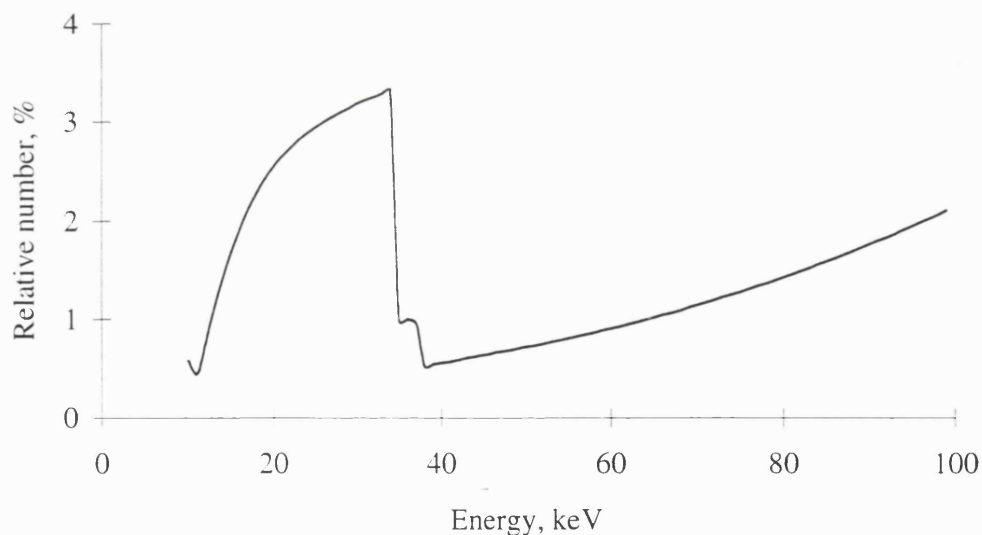
Figure 3-12 Predicted fraction of x-ray interactions due to interactions in the silicon

Figure 3-12 shows the predicted fraction of x-ray interactions with both the CsI(Tl) and the silicon that is due to interactions with the silicon, based on the theory detailed above. These fractions are small, indicating that noise will be significant compared to the noise due to interactions in the phosphor.

3.5.4 Discussion

The simple theory of section 3.5.1 has been found to give reasonably accurate predictions of the significance of direct hits in the silicon. Since such a large proportion of the signal is due to these events, it is inevitable that they will have a significant effect on the system resolution (MTF) and noise (NPS). The effect on the noise characteristics of the system is particularly important as such a significant amount of the signal is produced by such a small fraction of the interactions. This is discussed further in chapter 4.

One method of reducing the number of direct hits in the silicon is to place a fibreoptic stud between the CsI and the CCD. This could be used in such a manner that the CCD is no longer in the path of the x-rays and, therefore, completely eliminate direct hits. Alternatively, the stud could be placed between the CsI and the CCD as for CCDe used in this work. By comparing the signal from this CCD when illuminated with x-rays with that from a bare CCD in a manner similar to that described above, it was estimated that the stud reduced the signal due to direct hits in the silicon by 99.5%.

3.6 Summary of CCD performance parameters

The gain and quantum efficiency have been measured, and found to agree well with published values (where available). The coupling efficiency was found to be significantly higher that the 10 electrons per x-ray interaction needed to ensure that the images are x-ray quantum noise limited at all frequencies (see Maidment and Yaffe 1994) . The system has been shown to have a linear response to both visible radiation and x-rays, which means that the flat fielding algorithm can be applied to reduce pixel to pixel response variations from more than 10% to less than 0.2%.

The dark current has been evaluated and various ways of reducing it have been described. Typically, it was possible to reduce the dark current to 8000 electrons per pixel when operated in TDI mode (833kHz pixel rate).

Finally, the signal fraction due to direct x-ray interactions in the silicon of the CCD was investigated. A simple theory was described which gave predictions of the fraction of the total signal which is due to these direct hits, and was found to agree well with experimental measurements. These hits contribute significantly to the total signal and will, therefore, have a significant effect on measurements of resolution (MTF) and noise (MTF), as discussed in the next chapter.

4. SIGNAL AND NOISE TRANSFER CHARACTERISTICS

4.1 Introduction

This chapter describes the signal transfer and noise performance characteristics of the TDI CCD mammography system detailed in previous chapters. Both theory and experimental results are discussed. Calculations of the spatial frequency dependent detective quantum efficiency are detailed.

4.2 Spatial resolution of a TDI CCD system: theory

When an object is imaged by a radiographic system its spatial resolution is degraded by the resolution properties of the system. The Modulation Transfer Function (MTF) of an imaging system provides a characterisation of its resolution properties which is useful for comparison with other detectors. An accurate estimation of the system MTF is also required by many digital image processing algorithms (Reichenbach 1991), such as algorithms for image enhancement, spatial registration and geometric transformation, which involve a process known as restoration - that is, the removal of the effects of the imaging system.

General modulation transfer function theory, including the use of an angled slit to measure the presampling MTF, is described in Appendix A. This section starts by describing the theoretical MTF of a TDI CCD system, followed by experimental results.

The MTF of a TDI CCD imaging system is due to a number of individual degradations:

1   Pixel structure

2   Sideways diffusion of charge carriers once generated in the silicon

3   Charge transfer inefficiency

4   Inappropriate scanning speed and variations in scanner speed

5   Clocking waveforms used

6   Poor angular alignment of CCD with respect to the scanning direction

7   Scatter of x-rays and spreading of light photons in the scintillator

8   Fluorescence lifetime of the scintillator

9   Direct interactions of x-rays with the silicon of the CCD

4.2.1 Pixel structure

Pixel structure can be a significant cause of degradation of the detector MTF. If it is assumed that the pixel has a uniform response across its entire area then the ideal pixel MTF is given by

$$MTF_{pixel}(u) = \text{sinc}(uW)$$

<div align="right">Equation 4-1</div>

where $sinc(x)=sin(\pi x)/(\pi x)$ and W is the effective width of the pixel structure. Because the pixel's potential profile is dependent on how much charge is stored, the pixel MTF is fill factor dependent (Tzannes and Mooney 1993). For systems such as the phosphor coated TDI CCD used in this work, however, this variation of MTF$_{pixel}$ with fill factor is negligible compared with other factors.

4.2.2 Carrier diffusion

Once charge has been created in the silicon it is accelerated towards the collection channel. The finite time taken to reach this channel means that the charge can diffuse

laterally from its creation point, thus giving a degradation in the resolution. This effect is generally negligible compared with other sources of degradation. Seib 1974 calculated the MTF degradation due to carrier diffusion and found that the carrier diffusion MTF for 600nm light incident on a typical front illuminated CCD is virtually flat and is still above 0.95 at a spatial frequency of 50mm^{-1}. (The broad emission spectrum of CsI(Tl) peaks at around 570nm, see chapter 3). Carrier diffusion is significant, however, when deep depletion CCDs are used to directly detect x-rays, a technique used by some dental imaging systems (Cox and Williams 1994). For these CCDs there is an increased time during which the carriers can diffuse laterally. More importantly, charge produced in the field-free region, located beyond the depletion region, randomly diffuses until it is either reabsorbed or reaches the depletion region where the electric field accelerates it towards the collection region. This is discussed further below where the diffusion of charge produced when x-rays interact with the silicon of the CCD is specifically discussed.

4.2.3 Charge transfer inefficiency

The influence of charge transfer inefficiency (CTI), ε, on the MTF has been found to be significant for some infrared cameras (Tzannes and Mooney 1993). It is caused when some fraction, ε, of the charge stored in a pixel is lost in each transfer and picked up by the trailing pixel. The influence of this effect depends not only on the value of ε but also on how many transfers are made. The CTI for the CCD 15-11 is very low at 0.0007-0.0001%. Simulation work of Tzannes and Mooney 1993 indicates that the MTF degradation due to charge transfer inefficiency when ε has such a low value is negligible, especially in the face of more serious degradations such as light spreading in the phosphor

4.2.4 Inappropriate scanning speed

The gantry velocity and the velocity with which charge is transferred from pixel to pixel should be identical, but opposite directions, if the image pixel is to be kept in the same place. Any differences in these velocities will cause a blurring of the image. First the

influence of a constant difference in velocity throughout the scan will be considered. Secondly, the influence of variations in the velocity differences, which occur as the controller attempts to maintain a constant velocity, will be discussed.

The time for 1 pixel to read all the way down a column of the CCD and then be read out is given by:

$$t = \frac{m \Delta y}{V_c}$$

<div align="right">Equation 4-2</div>

where m is the number of rows in the CCD (256 for an EEV CCD15-11), Δy is the pixel size in the scan direction and V_C is the average velocity at which charge is moved from pixel to pixel. For a constant velocity difference, $\Delta V = V_C - V_s$ where V_s is the constant velocity of the scanning gantry, the signal spread can be described by a 'rect' function whose width is given by:

$$s = \Delta V t = \Delta V \frac{m \Delta y}{V_C}$$

<div align="right">Equation 4-3</div>

This 'rect' function describes the PSF due to velocity variation. The MTF is found Fourier transform of this, giving

$$MTF_{\Delta V}(u) = sinc(u \; \Delta V \; m \; \Delta y \; / \; V_C)$$

<div align="right">Equation 4-4</div>

More realistically, the stage does not have a constant velocity throughout time t, but has an ever changing velocity about a mean velocity of $<V_s>$. This means that there will be some degradation in the MTF due to scanning velocity mismatch, even when the mean velocities are equal. The extent of the blurring depends on how well V_C stays close to $<V_C>$.

4.2.5 Clocking waveform used

The effect of the clocking waveform of a TDI CCD system upon the MTF can be divided into two generalisations. Which generalisation a particular waveform fits into depends on which is the slower: the serial readout of a single line, or the transfer of charge down one pixel in the column. The two extremes will be considered separately.

MTF degradation due to slow serial readout

This discussion concerns the MTF degradation due to clocking waveforms when the time taken to transfer charge one pixel down the column is negligible compared with the time to read out an entire line from the readout register. This is the case experienced by the CCD 15-11 when the image scanning rate is approximately 21mm s^{-1}: The maximum pixel readout rate of the 15-11 means that it typically takes a minimum a 125ms to readout an entire line; charge is moved down a pixel in the columns in 12μs. While a line is being readout, the clocks in the integration region are stationary, but the detector is being continuously moved. By the time the complete line has been read out, the pixels in the integration region have moved 'up' the image a distance equal to one pixel width. The detected image is therefore blurred in the y (column) direction by a 'rect' function of width Δy. The MTF degradation due to this effect is given by:

$$MTF_{y,clk}(u) = \text{sinc}(u\,\Delta y)$$

<div align="right">Equation 4-5</div>

MTF degradation due to slow charge transfer down a column

If the time taken to read an entire line out from the readout register is negligible compared with the time taken to transfer charge one pixel down the column then the clocking waveform degradation of the MTF is not as severe as in the above case. This is the case experienced in many TDI CCDs (see Holdsworth et al 1990) and could be the case for the CCD 15-11 when used for very slow scans. In this case, resolution loss is

caused because charge is transferred from electrode to electrode in discrete steps, while the detector motion is continuous. If charge transfer occurs within a small fraction of the clock cycle then the charge is moved one electrode distance along the image before being transferred to the next electrode. The MTF due to charge clocking is then given by

$$MTF_{y,clk}(u) = \mathrm{sinc}(u\,\Delta y\,/\,n)$$

<div align="right">Equation 4-6</div>

where n is the number of phases in the clocking scheme. The CCD 15-11 uses a common three phase clocking scheme, as described in chapter 2.

4.2.6 Angular alignment

If the columns of the CCD are not parallel to the direction of the can, then some degradation of resolution in the x (row) direction will result. This will occur if the camera board is not correctly aligned on the scanning gantry. If the columns are at an angle θ with respect to the scanning direction, as illustrated in Figure 4-1, a given point in the image will fall into several columns as the CCD is scanned across it. For a TDI CCD with m rows, the image will be displaced in the x-direction by an amount given by:

$$\Delta x = \Delta y\, m \tan\theta$$

<div align="right">Equation 4-7</div>

where Δy is the pixel to pixel spacing in the y (column) direction. Thus the image is blurred in the x-direction by a 'rect' function of width Δx, and the MTF due to misalignment is, therefore, given by:

$$MTF_{x,align}(u) = \mathrm{sinc}(u\,\Delta y\, m \tan\theta)$$

<div align="right">Equation 4-8</div>

Careful alignment is necessary as, for the 15-11, which has 256 rows, a misalignment angle of only 0.2° will displace the image across a complete pixel.
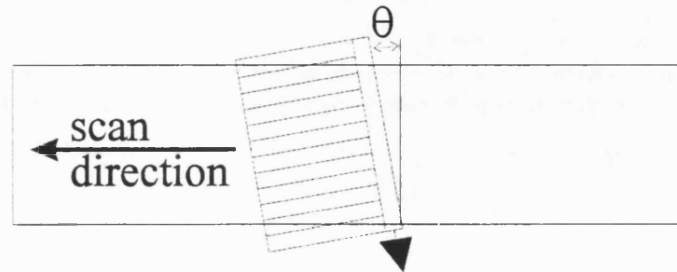
Figure 4-1 Schematic showing poor angular alignment

4.2.7 Spreading of light photons in the scintillator

Spreading of light photons in the scintillator generally gives the most serious degradation of MTF. There are many fluorescent screens currently available for use with film or other optical detectors, some of which attempt to reduce the spreading of light photons in the scintillator by using a light absorbing dye in the phosphor or using a structured screen such as the CsI screens found in some image intensifiers. Other screens maximise the amount of collected light to give a film-screen combination with increased speed by, for example, placing a reflective backing onto the screen.

The significance of this source of MTF degradation is reflected in the number of published models which simulate the various conditions described above (see, for example, Swank 1973, Westmore and Cunningham 1993...). One of the simplest, is that of Barrett and Swindell 1981. In their treatment they make the following assumptions:

- The phosphor layer is assumed to be optically transparent
- The phosphor layer is taken to have a non-reflecting surface
- Optical photons are take to be emitted with an isotropic distribution at the point of absorption

- The phosphor layer is assumed to be sufficiently thin that the probability of an x-ray being absorbed is independent of the depth in the screen at which the x-ray is absorbed
- Circular symmetry is assumed

With these assumptions and assuming that the phosphor is directly placed on the detecting surface of the optical detector (e.g. the CCD) the screen MTF can be modelled as:

$$MTF(u) = \frac{1 - e^{-2\pi u d}}{2\pi u d}$$

Equation 4-9

where d is the screen thickness. When there is a protective layer between the phosphor and the detector, as is the case here, Equation 4-9 is multiplied by a factor $\exp(-2\pi u d_2)$ where d_2 is the thickness of this extra layer.

4.2.8 Fluorescence lifetime of the scintillator

Scintillation light emitted some time after the absorption of the incident x-ray will cause blurring of the image when the system is used in TDI mode and may restrict the choice of scintillator material. For example, the fluorescence from Gd_2O_2S:Tb has a typical lifetime of 0.9ms (Maidment et al 1993) which is close to the top line rate of the CCD 15-11. If the temporal decay of the light output of the phosphor screen is described by an exponential decay with a lifetime λ and the scanner is moving at a constant velocity, v, the MTF degradation due to the fluorescence lifetime of the scintillator is given by

$$MTF_{lag}(u) = (1 + (\lambda v u)^2)^{-1/2}$$

Equation 4-10

When using CsI(Tl) this effect can generally be neglected as its fluorescence has a lifetime of only 1μs (Knoll 1989). This could only become important for very fast scans not achievable with the present equipment. There is also some concern that extended tails on the temporal emission of the phosphor may be significant (B P Allen, EEV Ltd, verbal communication 1994). This effect was not evaluated in this work, as the MTF and noise transfer were found to be dominated by other sources. This may be a problem with different (faster) detector combinations and, therefore, is an effect which should be studied further in the future.

4.2.9 Interactions of x-rays in the silicon

X-rays which pass through the phosphor coating can interact within the silicon of the CCD itself. As discussed in chapter 3, although the number of x-rays absorbed in the silicon compared with the number absorbed in the phosphor coating is generally small, the signal due to these events is much more significant and, therefore, the direct absorptions can contribute significantly to the measured MTF.

Figure 4-2 shows the possible regions of a CCD where the x-rays may interact. When x-rays interact with the silicon a charge cloud is produced. Charge produced in the depletion region is swept to the collection well, whilst simultaneously diffusing outwards. Charge produced in the field-free region diffuses randomly until it is either reabsorbed or reaches the depletion region boundary from where it is swept to the collection channel. The surface between the substrate and the field free region is often totally reflecting (e.g. with a p-type epitaxial layer/p$^+$ substrate), such that charge produced in the field-free region which diffuses to this boundary is reflected back towards the depletion region. For a p$^+$ substrate the diffusion length is typically 10μm (Hopkinson 1983) and recombination is significant in this region. Although models of the effect of charge diffusion in the substrate are available (Hopkinson 1983) here it will be assumed that interactions in the substrate can be neglected. Recombination is much less significant in the depletion region, although the extended paths taken in the field-free region mean that it can be significant in this region. Diffusion in the depletion region is not significant

compared with the initial cloud diameter for the energies used here and will also be neglected. There are, therefore, two main contributions to the average PSF due to direct interactions in the CCD: the initial cloud diameter and diffusion in the field-free region.
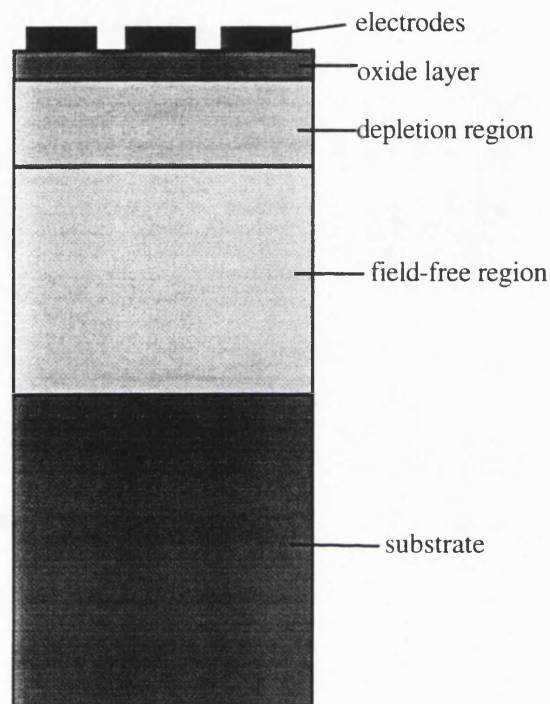
Figure 4-2 Cross section through a typical CCD

The average distribution of the charge cloud is estimated from electron-beam-induced current experiments to be Gaussian with 2σ diameter given by (Everhart and Hoff 1971)

$$C_i = 0.0171E^{1.75}$$

Equation 4-11

where E is the absorbed energy in keV. For example, when one 25keV x-ray is absorbed it produces a charge cloud with a 2σ diameter of 4.8μm. In a more complete treatment the influence of collecting the radially distributed charge in the plane of the buried channel should also be included (Lumb 1987).

Janesick et al 1987 provide an empirical formula based on Monte Carlo results modelling diffusion in the field-free region. They give the cloud diameter at the field-free/depletion region boundary as

$$C_{ff} \approx 2x_{ff}\left[1 - \left(\frac{x_a}{x_{ff}}\right)^2\right]^{\frac{1}{2}}$$

Equation 4-12

for $0 < x_a < x_{ff}$., where x_a is the distance from the field-free depletion interface at which the x-ray interacts. Janesick et al 1987 did not include recombination, but this approach is adequate for a simple approximation.

A full description of the average collected charge distribution can be constructed from Equation 4-11 and Equation 4-12. An approximation considered adequate for this work involves the quadrature sum of the individual cloud diameters. For an x-ray interactions in the field-free region the diameter of the collected charge cloud is estimated from (Janesick et al 1987)

$$C_D \approx \sqrt{(C_i^2 + C_{ff}^2)}$$

Equation 4-13

where C_i and C_{ff} are defined in above. For an event in the depletion region $C_D = C_i$.

The average PSF is given by finding the average over the total thickness of the CCD, including a term for the exponential attenuation of the x-rays. For the energies of interest here, however, the x-ray intensity can be considered as constant through the thickness of the CCD: at 15keV the x-ray intensity variation across 20μm of silicon is only 5%, falling to less than 1% at 30keV. An MTF based on these for various incident x-ray energies is shown in Figure 4-3 where it is assumed that the CCD consists of a 5μm depletion layer and a 15μm field-free layer.
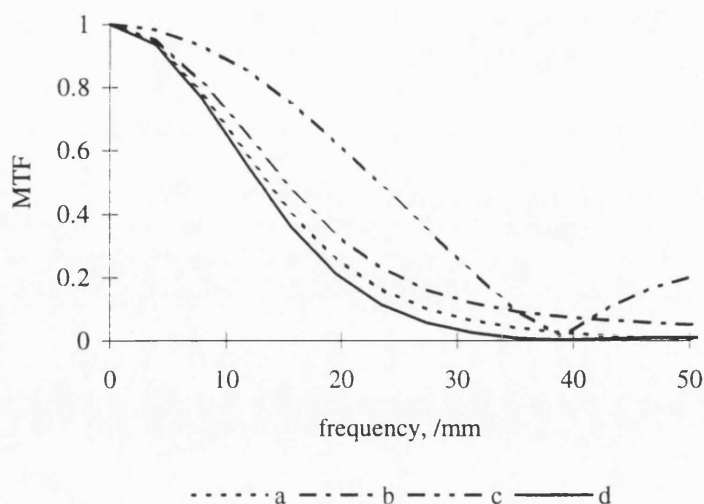
Figure 4-3 Predicted MTF due to x-ray interactions with the silicon for (a) 50keV and (b) 25keV photons and (c) the pixel MTF giving (d) the total MTF for 25keV photons

4.3 Experimental evaluation of the modulation transfer function

4.3.1 Method of MTF evaluation

The system MTF was measured for optical and x-radiation. In this way it was possible to demonstrate the various sources of degradation of the MTF discussed above. The use of optical radiation allowed the MTFs due to factors such as velocity mismatch to be evaluated without the issue being complicated by the extra contributions to the MTF that must be included when using x-rays.

The optical arrangement used to calculate the system MTF consisted of a tungsten bulb, green filter, 50µm slit and a x10 microscope objective lens to focus the slit onto the CCD array. A C program was specially written to control the scanner and frame grabber and to calculate the MTF using the algorithm given in Table 4-1. It is based on the angled slit technique described in appendix A. The slit was focused by adjusting the focusing until the full-width-half-maximum (FWHM) of the image of the slit was minimised.

1. Take image of slit

2. Correct response and dark current variations in the image by flat fielding

3. Identify the slit by thresholding

4. Estimate the centre of the slit by centroiding

5. Apply least squares fit to the centroiding results to accurately determine position of slit

6. Calculate angle of slit and number of samples per pixel distance

7. Register LSF data in super-resolution LSF

8. Calculate full-width-half-maximum (FWHM) of super-resolution LSF

9. Fourier transform the LSF to give the OTF

10. Divide the MTF by the transfer function of the slit

N.B. Steps 9 and 10 are omitted when initially focusing the slit

Table 4-1 Algorithm for calculating the optical MTF and for optimising the system resolution

Once the slit was focused, the influence of factors such as camera angle and scanner velocity were investigated.

The system MTF for x-ray irradiation was investigated in a similar manner but, instead of a slit image, an image of an edge was used. This gives the edge response function, which must then be differentiated to give the line spread function (see appendix A for further details of this). If numerical differentiation is used, a correction factor is necessary to compensate for the frequency pass-band of the finite-element differentiation (Cunningham and Fenster 1987). If MTFe(f) is the estimated MTF, then the corrected MTF is given by

$$MTF(f) = \frac{MTF(f)_e}{\text{sinc}(f / (2f_N))}$$

Equation 4-14

where f_N is the Nyquist frequency associated with the sampled data. Another problem with differentiation of the ERF is that it amplifies the high frequency components of the scans where the SNR is lower. One method of overcoming this is to assume a parametric form for the LSF. This has the disadvantage that it forces the MTF to have a fixed form, but has been found to work well both in this work and also by previous authors (see, for example, Tzannes and Mooney 1993). A function which was found to work well for CCD based imaging systems (Tzannes and Mooney 1993) is the Fermi function of the form

$$f(x) = \frac{a}{e^{(x-b)/c} + 1}$$

Equation 4-15

where a, b and c are constants. Since ESFs are not necessarily symmetric about the midpoint of the rising or falling edge, in common with the work of Tzannes and Mooney 1993, a summation of N Fermi functions was used to improve the fit. That is, the ERF was fitted to F(x) where

$$F(x) = D + \sum_{i=0}^{N} \frac{a_i}{e^{(x-b_i)/c_i} + 1}$$

Equation 4-16

where D, a_i, b_i and c_i are constants. The fit was carried out using the curve-fitting function in Sigma Plot v1.02. Sigma Plot uses the Marquardt-Levenberg algorithm to find the values of the constants to minimise the sum of the squared differences between the values of the experimental ERF(x) and predicted values of F(x). This is not a particularly fast procedure and, therefore, the value of N was varied depending on the significance of the given results. For example, N=2 was used when evaluating the influence of the scanner velocity, for which a relatively large number of ERFs were calculated, and a value of N=6 used when evaluating the optimum system edge response function. Other authors who have used a computerised fit of some analytic formula to

experimentally measured data in their calculations of MTF include Yin et al 1990 and Boone et al 1994.

4.3.2 Effect of velocity mismatch on the experimental MTF

The effect of scanning velocity of the system resolution was evaluated both optically and using x-rays. Figure 4-4 shows the value of the x-ray MTF at $8.8mm^{-1}$ for CCDd ($120\mu m$ CsI coating) with pixel rate of 800kHz.
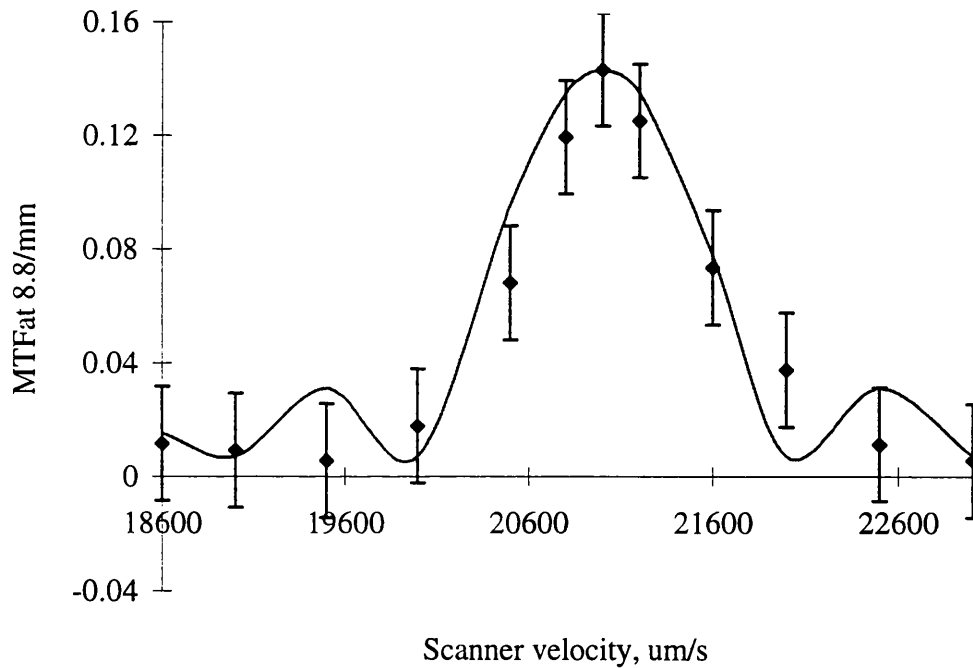
Figure 4-4 Effect of velocity mismatch on MTF

The scanning gantry was set with a dynamic gain of 60 (see chapter 2 and 'Dynamic gain' on page 110). The experimental results are compared with the predictions of Equation 4-4, for which it is assumed that the MTF for a velocity of $21mm\ s^{-1}$ equates to zero velocity mismatch. Values for other velocities are predicted by degrading the MTF for $v=21mm\ s^{-1}$ with Equation 4-4. Figure 4-5 shows the variation of the FWHM of the image of the slit produced with the optical apparatus described above. This also gives

the optimum velocity as 21mm s^{-1}, and shows that evaluation of the FWHM is adequate in optimising the velocity. In both cases the errors were estimated by repeating the 21mm s^{-1} results five times.
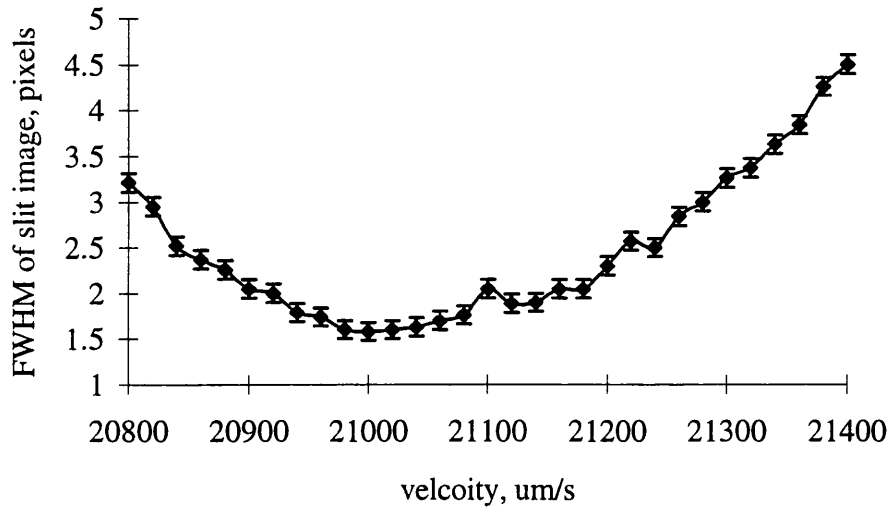
Figure 4-5 Effect of velocity mismatch on FWHM of slit image

This technique of minimising the FWHM of the slit image may be useful as it is much faster than evaluating the x-ray MTF for each velocity and, therefore, provides a relatively quick and simple method of optimising the scanner velocity, as is necessary when, for example, different clocking schemes are used.

Both these sets of measurements indicate that the velocity of the scanning gantry must be correct to within 100μm s^{-1} to prevent significant degradation of the MTF.

4.3.3 Effect of velocity variations on the experimental MTF

If the scanning gantry does not move at a constant rate then this will degrade the resolution, an effect which can be calculated from the scanner velocity variations, if known. Unfortunately, as described in chapter 2, exact velocity (or position in time) information is not available as there is a varying time delay between the PC requesting

information from the scanner controller and the controller responding. It is possible to estimate the influence of velocity variations on the PSF, however, by collecting information on the variations in dynamic error during a scan (set at constant velocity). Dynamic error gives the difference in the position where the scanner should be according to the set values of acceleration, deceleration and velocity, and were it really is (as detailed in chapter 2). Typical variations in dynamic error with time for a set velocity of 21mm s^{-1} are shown in Figure 4-6. The point spread function due to velocity variations can be estimated by, for each measured point in a data set like that of Figure 4-6, scoring the difference in dynamic error between this point and each following points within 0.3s (which is the time for charge to move all the way across the CCD) as a histogram. This histogram, an example of which is shown in Figure 4-7, is the PSF due to velocity variations.
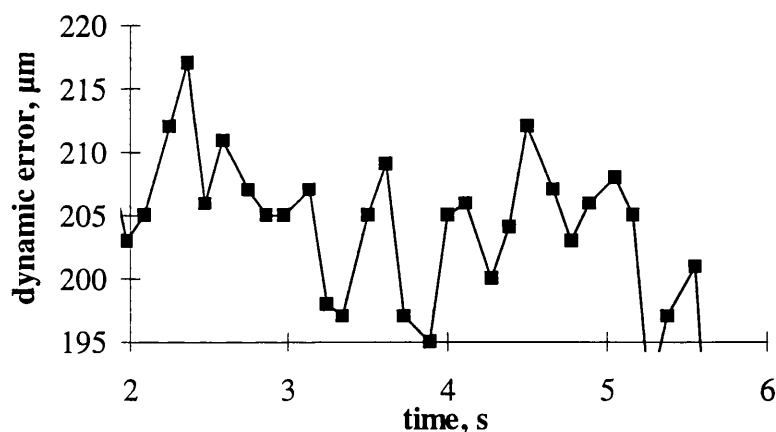
Figure 4-6 Dynamic error variations with time

This evaluation was repeated for various gain settings and the results fitted to a Gaussian function. These gave a typical variation in position PSF as a Gaussian with σ of 7μm for a typical dynamic gain setting of 50-70, increasing rapidly for higher and lower settings. (The dynamic gain is the gain of the feed back loop which controls the velocity. See chapter 2 for further details).
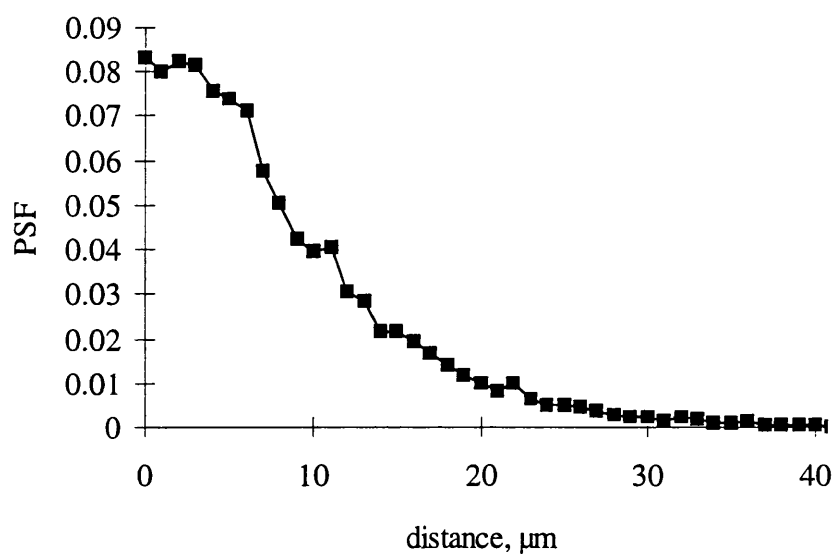
Figure 4-7 Average PSF due to velocity variations in the scanning stage

4.3.4 Effect of the dynamic gain of the scanning gantry on the experimental MTF

The Full-Width-Half-Maximum, FWHM, of the image of the optical slit was evaluated for a range of dynamic gains.
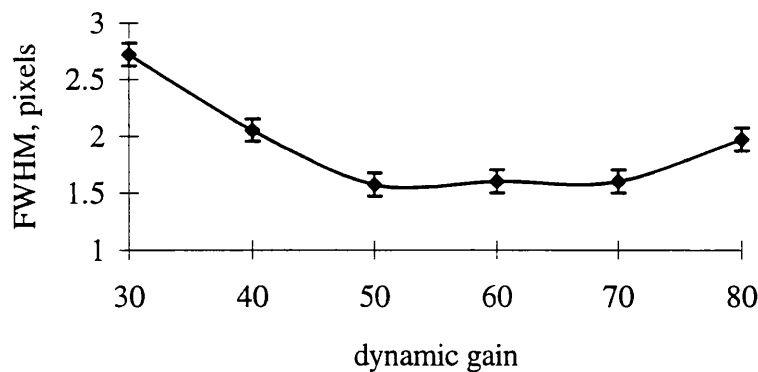
Figure 4-8 Effect of scanner dynamic gain on the FWHM

The results, shown in Figure 4-8, agree with the above prediction, where it was indicated that there was a wide range of dynamic gain values for which the effect of velocity

mismatch on the resolution is minimised, with severe degradation for extreme high or low values.

4.3.5 TDI waveform degradations on the MTF

Figure 4-9 shows the optical MTF for the bare CCD (CCDa) operated in integration mode, where it is compared with the optical MTF when operated in TDI mode, with the optimum velocity and dynamic gain set as determined above. Errors on these points are approximately ±0.005. It can be seen the TDI MTF is accurately predicted when the stationary MTF is degraded by the blur due to the TDI clocking and the blur due to scan jitter (Gaussian, with σ taken as 7μm). The predicted scan MTF is almost directly under the experimental points for the scan MTF.
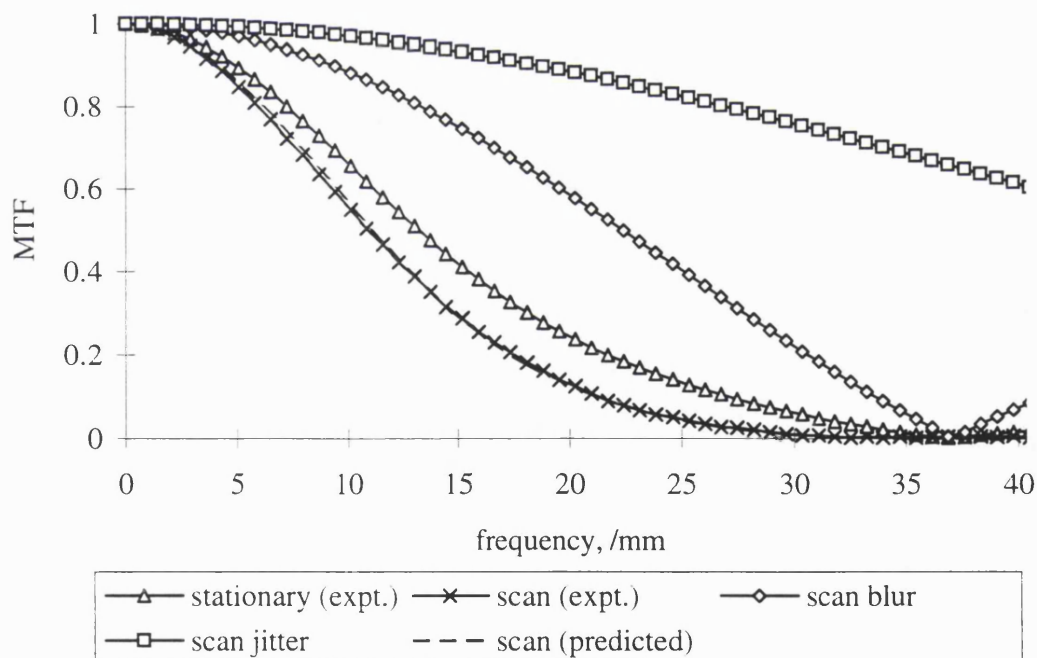
Figure 4-9 Degrading effects in the scanning direction

The optimum x-ray MTFs in the scanning direction are shown in Figure 4-10. The high frequency response is mainly due to x-ray interactions in the silicon of the CCD. The

small number of these resulted in a significant amount of noise at these frequencies. For example, for the 67μm CsI coated device, less than 2% of the x-ray interactions were due to absorptions in the silicon. So that the LSF was fully described during the scanning process it was, therefore, necessary to average several ERFs before fitting the curve to the formulae described in section 4.3.1. For these measurements 10 ERFs were averaged. Errors on these points are approximately ±0.02 at low frequencies. Errors in the tails of the MTFs are larger, particularly for the thicker phosphor coatings. The errors on the points above a spatial frequency of 15mm^{-1} for the 43μm CsI coated device were estimated at ±0.05.
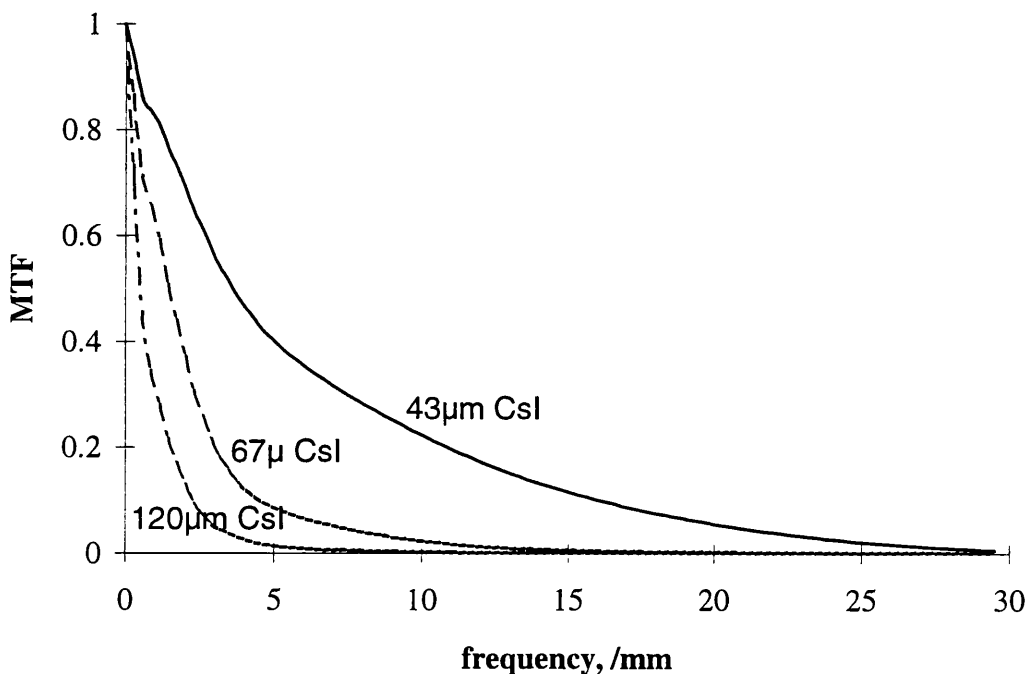
Figure 4-10 X-ray MTFs in the scanning direction

4.3.6 The influence of scanning gantry angular mismatch on the experimental MTF

The effect of the scanning angle on the MTF was evaluated both optically and using x-rays. The angular mismatch was varied using the adjusting screws described in chapter

2.   The screw position was then converted to angular mismatch, with the angular mismatch for the optimum MTF taken as the zero position. The experimental MTF values at a spatial frequency of 21mm^{-1} are shown in Figure 4-11, where they are compared with theoretical predictions described above.
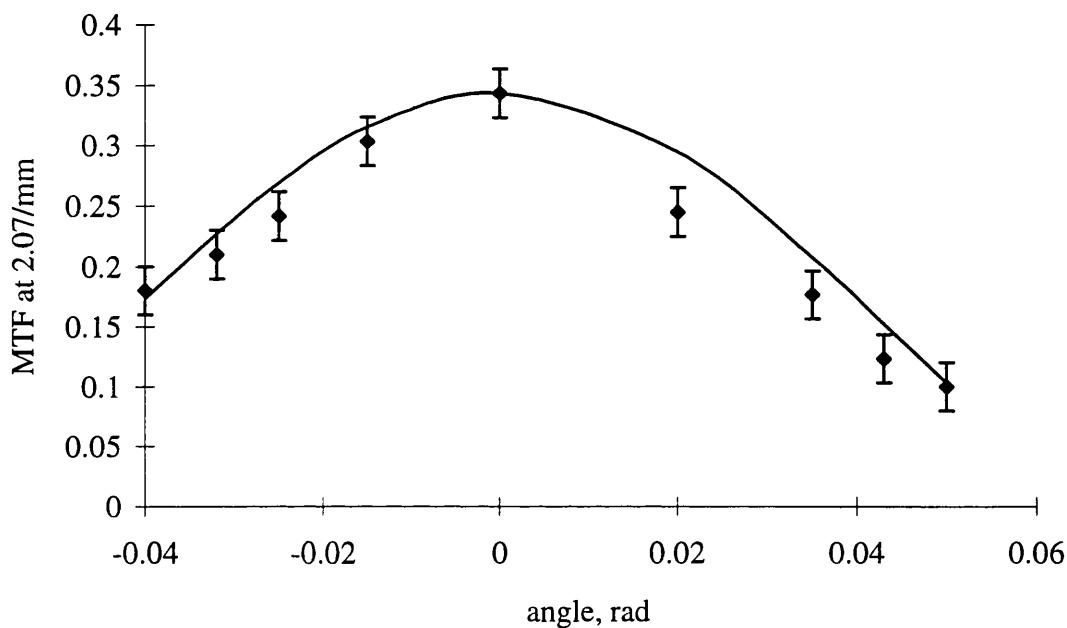
Figure 4-11 Influence of angle mismatch on MTF

As with the scanning velocity measurements it was found that the FWHM of the image of the optical slit was sufficient to evaluate the optimum position. The scanning MTF is slightly worse than the stationary MTF, an effect attributed to sideways movement in the scanning gantry.

4.3.7 Scintillator coating and direct hits in the silicon

The stationary MTF was evaluated for the three CsI coatings (CCDb, CCDc and CCDd), the results of which are given in Figure 4-12. As expected the MTF gets worse as the coating thickness increases. The MTF due to direct hits in the silicon was evaluated

using the bare CCD (CCDa), the results of which are also shown in Figure 4-12. It can be seen that the experimental MTFs for the 43μm CsI coated chip and the bare chip come together at high frequencies and actually cross at approximately 20 mm^{-1}. This is not expected and is attributed to the influence of noise at higher frequencies on the efficiency of the curve fits, which is can be significant, especially for the edge technique used here (Cunningham and Reid 1992). The errors on the high frequency tails of the coated MTFs are ±0.05. Errors on the bare MTF are slightly less at ±0.03.

A comparison of Figure 4-12 with the theory of Figure 4-3 it can be seen that this agrees reasonably well with the predicted results.
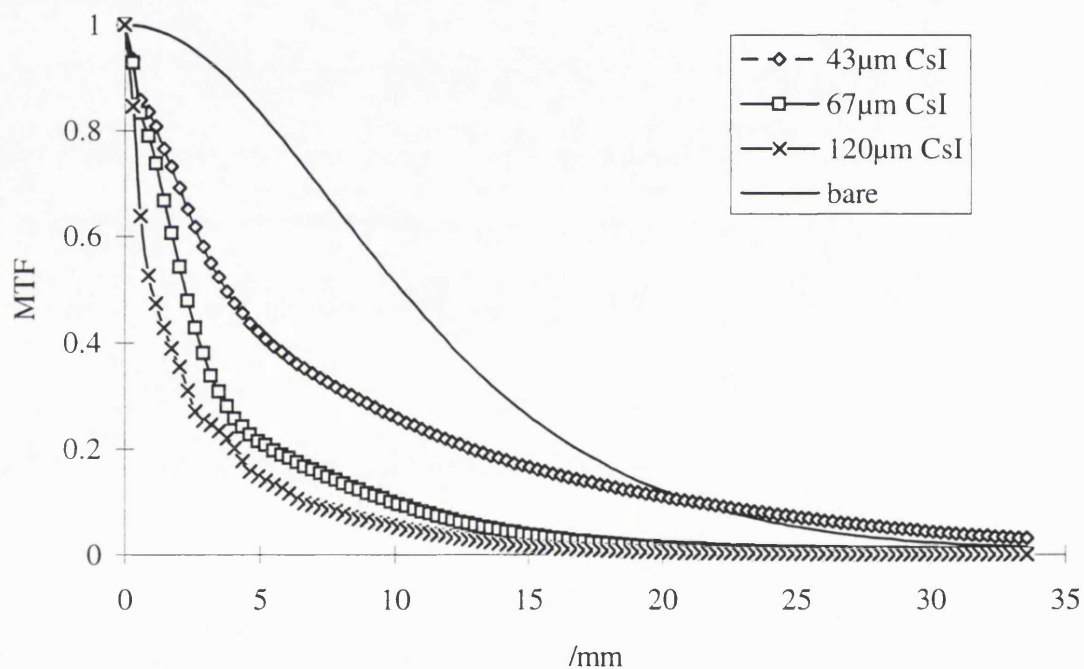
Figure 4-12 MTF for three coated CCDs and a bare device

Using the theory of chapter 3 it can be estimated that the fractions of the total signal which is due to direct absorptions of x-rays (tungsten target, 45kVp, 1.8mmAl total filtration) in the silicon are 36%, 24% and 12% for the 43μm, 67μm and 120μm coatings respectively. Since the MTFs of the two processes (i.e. absorptions in the scintillator and absorptions in the silicon) are summed with weights equal to their relative signal

strengths, it is possible to estimate the MTF due to the scintillator alone. The results of this calculation, after re-normalising the zero frequency values to unity, are given in Figure 4-13.
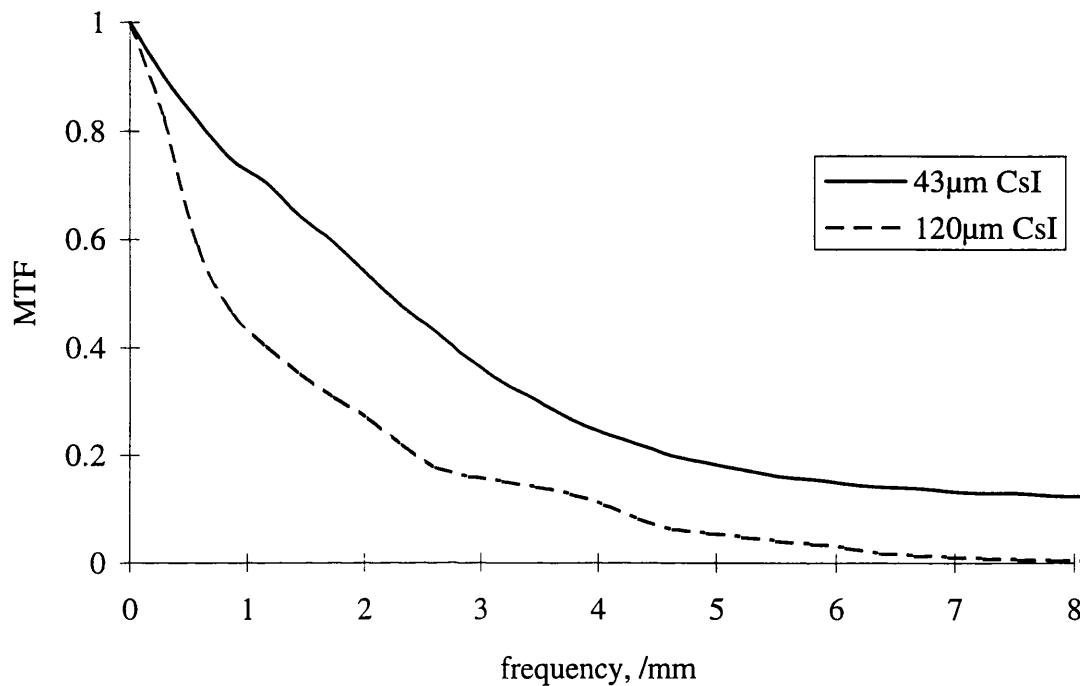
Figure 4-13 Estimated MTFs due to phosphor alone

These estimated results for the MTF of the phosphor can only be regarded as estimates, as the calculations are plagued with possible sources of error, some of which can have a significant influence on the resulting MTFs. These include the thickness of the phosphor layer, which is only known to ±15%, and the fraction of signal due to direct hits in the silicon, the estimation of which may have a significant error, and errors in the experimental evaluation of the constituent MTFs. As discussed above, these errors are most significant at high frequencies.

These estimated phosphor MTFs agree reasonably well with experimental measurements of Martinez 1994 who measured MTFs for CCDs (EEV CCD02-06s) with a fibreoptic faceplate and fibreoptic taper couplings and for CsI thickness from 70 - 130μm.

There are two important conclusions that can be drawn from these results. The first is that the measured resolution has a significant contribution from direct absorptions of x-rays in the silicon of the CCD. It will be shown below that these also act as a significant contribution to the noise. This means that the 10% or 5% points of the MTF do not give reasonable estimates of limiting resolution. A second conclusion which can be drawn, based on Figure 4-13 is that the CsI coating does not seem to give the high frequency response that would be expected if its columnar structure acted to (efficiently) channel the light down to the CCD surface.

4.3.8 Summary of experimental MTF results

Measurements of MTF for both scanning and stationary operation have been presented. It has been shown that the experimental scanning MTFs can be realistically modelled, with the most serious degradations of MTF being light spread in the phosphor and TDI waveforms degradations. It should be possible to significantly reduce the TDI waveform degradations by using a CCD with faster output circuitry (such as the newer EEV CCD30-11) and, therefore, bring the scanning MTF closer to the stationary MTF.

The significance of 'direct hits' has been demonstrated. It has been shown that these interactions give a significant contribution to the high frequency response.

4.4 Experimental investigation of the magnitude of noise

All images are subject to noise. This can be quantified in various ways. Two methods used here are measurement of the standard deviation of the measured intensity values (ADU values) and measurements of the noise power spectrum (NPS).

Typical measured noise values for no incident radiation are given in Table 4-2.

CDS gain setting	σ^2 (ADU^2)	σ^2 (electron^2)	σ (electron)
low (~300 electron ADU^{-1})	11.7	1053000	1026
medium (~40 electron ADU^{-1})	65	104000	322
high (~22 electron ADU^{-1})	162	78408	280

Table 4-2 Measured noise for different gain settings

These values varied from day to day, giving a typical uncertainty on these values of ±50%. As the gain is changed the significance of different sources of electronic noise changes. For a simple treatment consider Figure 4-14.

Figure 4-14 Schematic showing noise sources in the prototype system

σ_{CCD} is the standard deviation, in number of electrons, due to noise sources in the CCD and camera board, σ_{CDS} is the noise due to sources in the CDS unit in number of electrons. Let G_1 be the gain of the camera board and CDS and G_2 the gain of the CDS in ADU/electrons. If G_2 is taken as unity, then the total background noise in the image is given by

$$\sigma^2_{total} = G_1^2 \sigma^2_{CCD} + \sigma^2_{CDS} \qquad (ADU^2)$$

<div align="right">Equation 4-17</div>

To express σ_{total} in electrons, this should be divided by G_1^2:

$$\sigma^2_{total} = \sigma^2_{CCD} + \frac{\sigma^2_{CDS}}{G_1^2} \qquad (electron^2)$$

<div align="right">Equation 4-18</div>

Thus the decrease in equivalent electrons with increased gain is to be expected, as σ^2_{CDS} becomes less significant. The theoretical significance of CCD and digitisation noise sources are given in Table 4-3. These values are calculated using theoretical expressions given in chapter 1.

Noise source	σ (electron)
quantisation noise	87 (low gain), 12 (medium gain), 6 (high gain)
charge transfer noise	51 (assuming η=0.999993 and N=5.10^5 electrons)
dark current shot noise	89-122 (for dark current = 8000 - 15000 electrons)

<div align="center">Table 4-3 Theoretical significance of various noise sources</div>

Table 4-4 gives the theoretical noise values for various dark current levels, assuming noise free electronics. These values are based on those of Table 4-3.

	Dark	current		(electrons)
Gain	**4000**	**8000** –	**12000**	**16000**
low	120	135	149	162
medium	82	103	121	137
high	81	103	121	137

<div align="center">Table 4-4 Theoretical noise (s.d.) for noise free electronics</div>

Comparison of Table 4-4 and Table 4-2 indicates that although dark current is significant, particularly at high gain, it is not always the dominant source of noise. For

the higher gain settings dark current is significant and can be the dominant source of noise, whereas for the low gain setting the noise is generally dominated by electrical interference and other sources of noise in the electronics.

In summary, the most significant sources of background noise are dark current shot noise, electrical pickup and other electrical noise and (for the low gain setting) quantisation noise. The reduction of noise with increased gain at the CDS shows the advantage of using the highest gain setting possible while still being able to contain the whole image in 12bits.

4.5 Noise power spectrum: experimental details

The pixel rms. noise has already been used to describe the magnitude of the noise and also to indicate the main sources of noise. This sort of analysis, however, does not show the texture of the noise. Background noise is typically uncorrelated ('white'), although electrical pick-up can have a definite frequency. Also, the x-ray detection process, described by the OTF and efficiency of the detector, can cause the initial quantum noise to become spatially correlated ('coloured') due to blurring. The noise power spectrum, also called the noise power spectrum (NPS), of an imaging system can be used to show the structure of the system noise, and can also help in the identification of the source of any pickup by identifying its frequency. The theory of noise power spectra is detailed in Appendix B.

The optical arrangement used for obtaining a uniform field of light at the CCD surface is described in chapter 3, as is the arrangement for producing a uniform field of x-rays. Other relevant details regarding the experimental techniques used here are described below.

4.5.1 Slit length

If the approximation of equation B-6 (see appendix B) is to be true, the chosen slit must be sufficiently long. This can be checked by measuring the NPS for a given slit length, and comparing this with the measured NPS for a longer slit. If the NPS at a given frequency is seen to increase as the slit length increases then the chosen slit length is not long enough, and a longer slit should be used (see, for example, Goldman L W 1992). There is no advantage in using the longest slit possible from a given image. In fact there are several disadvantages: first a long slit means that less independent spectra can be obtained from each image (see below); secondly, a long slit can increase the influence of fixed frequency interference on the NPS. The effect of fixed frequency interference is discussed in more detail in section 4.4. In this work a slit length of 256 pixels (6.9mm) was used.

4.5.2 Number of quantisation levels

It has already been shown that the different noise sources vary in significance, depending on the CDS gain setting. Giger et al (1984) showed that an inadequate number of quantisation levels can affect the shape and level of the measured NPS. The influence of this was investigated by measuring the NPS due to x-ray detection, $W_Q(u)$, for each gain setting, with an incident air kerma of 0.5mGy. $W_Q(u)$ was found to be independent of gain, with the conclusion that all settings quantise the noise sufficiently well not to affect the measured NPS.

4.5.3 Finding the fluctuation function $\Delta D(x,y)$

After acquiring an image, the flat fielding algorithm was applied. The mean signal level (in ADU), $\langle S \rangle$, was calculated from the individual pixel values:

$$\langle S \rangle = \frac{\displaystyle\sum_{x=0}^{N-1}\sum_{y=0}^{M-1} S(x,y)}{NM}$$

<div align="right">Equation 4-19</div>

where $S(x,y)$ is the spatial distribution of the signal, expressed in ADU. The difference fluctuation function is then calculated using:

$$\Delta D(x,y) = S(x,y) - \langle S \rangle$$

<div align="right">Equation 4-20</div>

An alternative to flat fielding the image is to subtract two images. It will be shown below that this method can be useful for removing fixed frequency interference from the measured NPS and, therefore, this is the method generally used here. Note that when two images are subtracted the measured NPS must be divided by two, as subtraction effectively doubles the noise power (Fu and Roehrig 1984). When used in scanning mode with the tungsten target x-ray tube variations in tube current act as an additional source of noise. This was overcome by fitting the pixel data from a selected column to a polynomial (3rd order) and then normalising the image appropriately. This method of fitting the data to a polynomial has been used previously by Giger et al 1986.

4.5.4 Improving the estimate of the ensemble average

A large number of spectra are needed to give a reasonable estimate of the NPS. The speed of the experiment can be improved by obtaining more than one spectra from each image (see, for example, Maidment et al 1993). In this study, 4 spectra were obtained from each image when used in scanning mode, or two when used in integration (stationary) mode. This was achieved by dividing the image into four regions, which are then considered independent. Each region was 256×256 pixels^2; an overlap between regions of 20 pixels was necessary to fit these regions into the image area. Broad comparisons of the effects of light level and CDS gain on the measure NPS were

obtained using spectra from 10 images. This gave a typical standard error on the mean for each point in the NPS of 8%.

4.5.5 Details of the purpose written program

A C program was written to collect fresh dark current data for the flat-fielding algorithm (if necessary), collect the images, subtract two images or perform the flat-fielding algorithm, calculate the fluctuation function, calculate the measured NPS and, finally, to correct this for the length of the slit.

4.5.6 The influence of aliasing on the measure NPS

As discussed in section appendix A in the context of MTFs, NPS with contributions at frequencies above the Nyquist frequency, defined as the reciprocal of twice the pixel size, are subject to aliasing. This gives a false increase to values below the Nyquist frequency and care must, therefore, be taken when interpreting the NPS results. This is particularly true when investigating the NPS due to x-ray interactions in the silicon of the CCD, which can have significant high frequency contributions. This effect must be born in mind when considering the results.

4.6 An investigation into the effects of fixed frequency interference on the measured NPS

Set frequency artefacts can occur in the image and, therefore, in the measured noise power spectra, due to either fixed frequency electrical interference or interactions between the readout electronics and the signal acquisition electronics (Boreman 1987). Any lack of synchronisation between the pixel readout clock frequency and the digitisation rate can result in beating frequencies in the image. These effects should, whenever possible, be corrected for in the hardware by changing the frame grabber sampling rate. In the system currently under investigation all clocks originate from the same PC card and, therefore, there should be no frequency synchronisation problems. Electrical interference can, however, be a problem. Although much effort was invested into reducing any electrical interference, there were a number of persistent interferences which gave peaks of varying height in the NPS. An example of an NPS with fixed frequency interference peaks can be seen below .
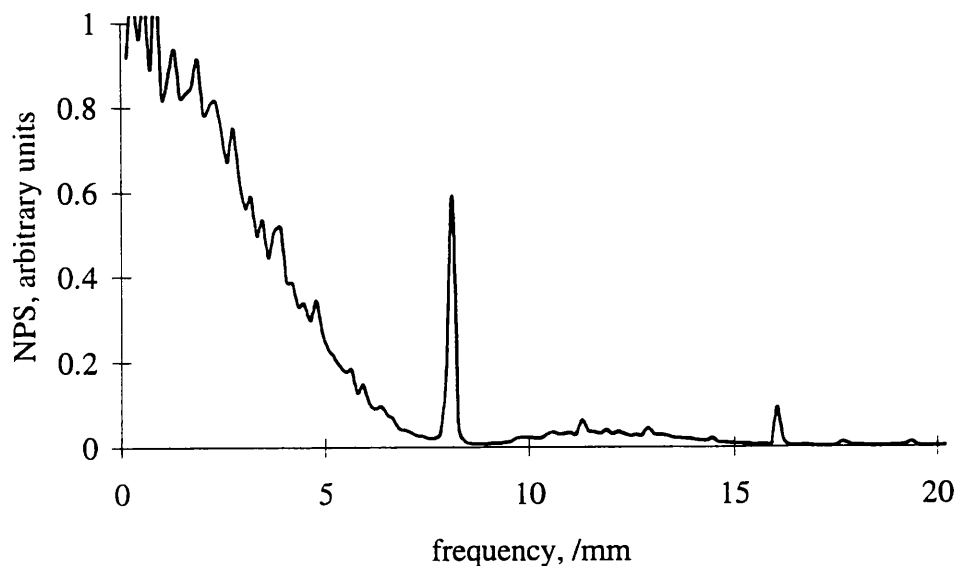
Figure 4-15 Typical NPS with fixed frequency interference

Unfortunately the fixed frequency peaks caused by electrical interference are not delta-function peaks and noise on the signal results in the peaks having some finite width, possibly giving some difficulty in using and interpreting the measured NPS. The peak height is, however, dependent on (amongst other things) the slit length and, in some cases, it may be possible to adjust the slit length to minimise these effects. Subtraction of two images can also reduce the effect of this interference, particularly if the interference on the two images is in phase.

A number of simulations have been carried out to determine the influence of different types of interference on the measured NPS, and of the influence of the slit length on this. The effect of subtracting two images has also been simulated to determine the usefulness of this technique in reducing the significance of fixed frequency interference on the measured NPS. These simulations will first be described, followed by some experimental results and a discussion of the ways of reducing the effect of fixed frequency interference on the measured NPS.

4.6.1 Simulation of a noisy image

A noisy image was simulated by first producing an image with Gaussian pixel-to-pixel variations, with an arbitrary variance of 10000ADU. This was then convolved with the following kernel to simulate the influence of the scintillator on the noise:

$$\begin{vmatrix} 1 & 1 & 1 & 1 & 1 \\ 1 & 2 & 2 & 2 & 1 \\ 1 & 2 & 3 & 2 & 1 \\ 1 & 2 & 2 & 2 & 1 \\ 1 & 1 & 1 & 1 & 1 \end{vmatrix} \cdot \frac{1}{2^5}$$

This has the effect to give some structure to the NPS, in the same way the light spreading in the scintillator gives structure to the NPS. Two different interference types were investigated: sine wave and pulsing types. This interference was added to each line using the algorithm of Figure 4-16. Each line was taken to be 1050 pixels long to

include the time taken to move charge one row down the chip. The sine wave had a peak-to-peak amplitude of 36 ADU and a wavelength of 16.1 pixels. The pulsing interference had a peak of 18 ADU and a wavelength of 16.1 pixels. These values are arbitrary; the wavelength was set to a value not an exact multiple of pixels as this will be the general case. Note that interference would normally be expressed in frequency terms; here it is expressed in pixels to indicate its relationship to interference structure seen in the images. For example, for a pixel rate of 800kHz an interference wavelength of 8 pixels is equivalent to an interference frequency of 100kHz.

The NPS for both types of interference was calculated for various slit lengths, the results for the pulsing case are shown in Figure 4-17. In the sin wave interference case all fixed frequency peaks were seen to fall with increasing slit length. In the pulsing case some fixed frequency peaks decrease with increasing slit length and some increase.
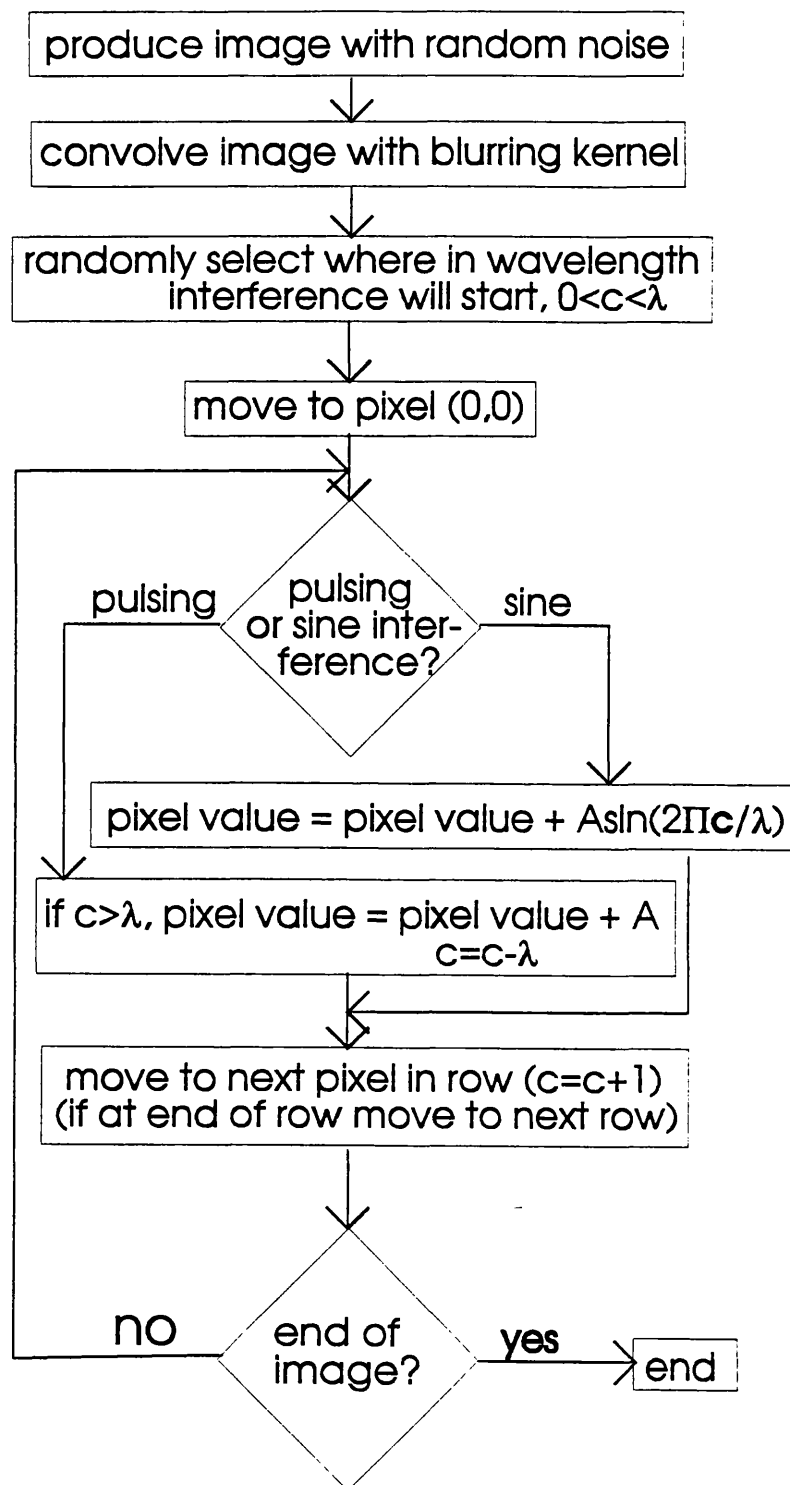
Figure 4-16 Algorithm used to add interference to random image
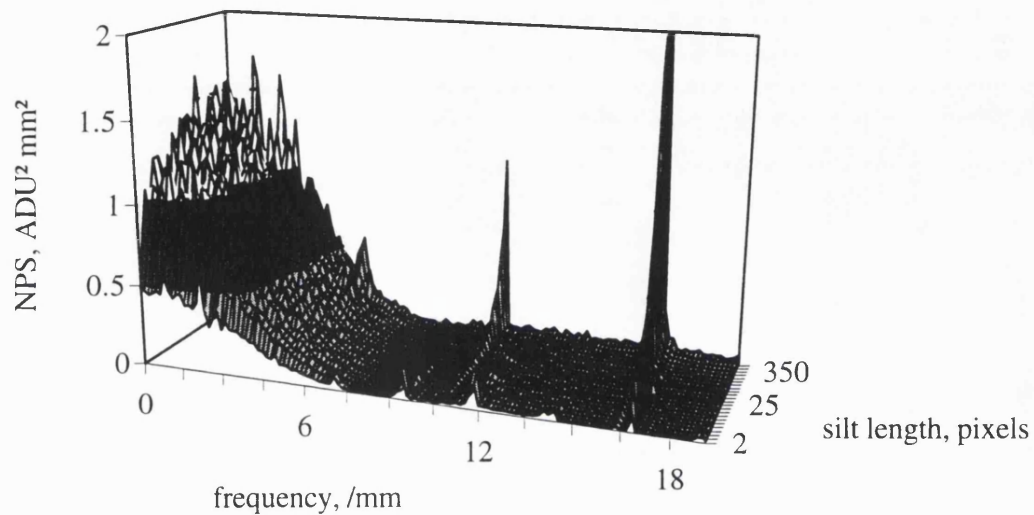
Figure 4-17 Effect of slit length on NPS

The influence of subtracting two images with pulsing interference (random phase) before calculating the NPS was also simulated, the results of which for one of the fixed-frequency peaks are shown in Figure 4-18. The errors on these points are ±8%. In the simulation carried out here all frequency peaks were found to reduce with increase in slit length.
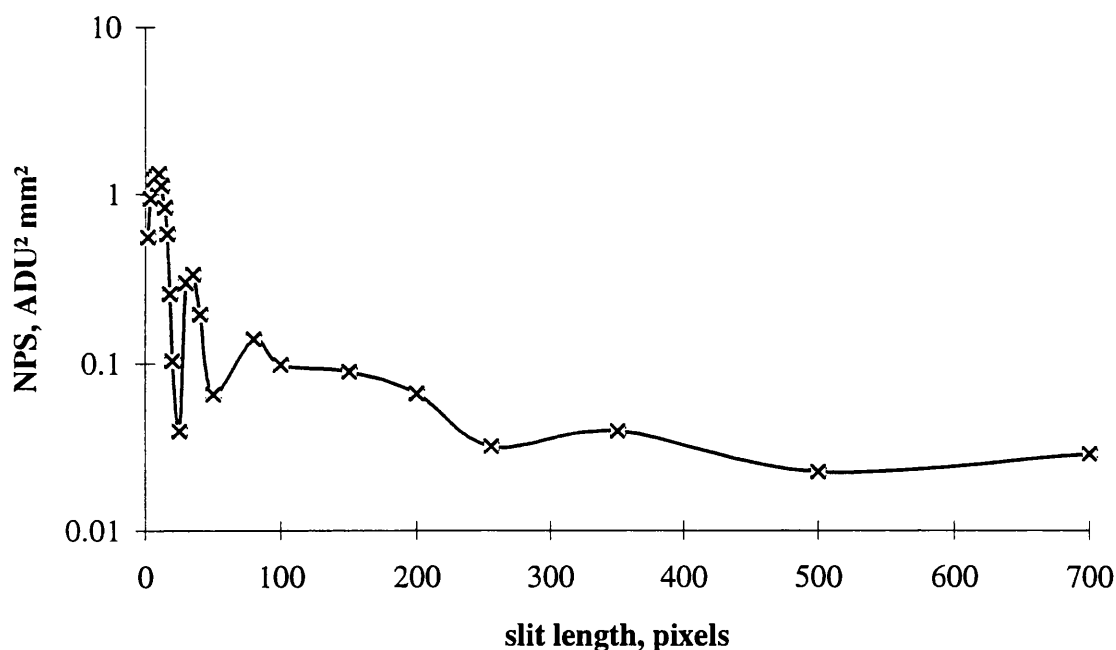
Figure 4-18 Effect of slit length on NPS value at an interference peak for subtracted images

Some structure is seen for small slit lengths which are of similar lengths to the interference wavelength.

4.6.2 Discussion of the simulation results

The frequency of the peaks in the NPS is dependent not only on the interference wavelength, but also on the line (row) length. Unless the wavelength fits exactly into the line length, each sequential line will be slightly out of phase and it is this phase difference which causes peaks in the NPS. A schematic of an image with somewhat excessive interference, showing the line-to-line phase difference is shown in Figure 4-19.

When the slit length used for calculating the NPS is less than the interference wavelength the peak height is a function of how well the wavelength fits into the slit length (this does not affect the frequency). As a simple example, for a slit which is 1 pixel long the

peak measured will be close to the amplitude of the interference. If the slit is 2 pixels long the average height at the peak will be reduced as it is averaged out along the slit, and so on.
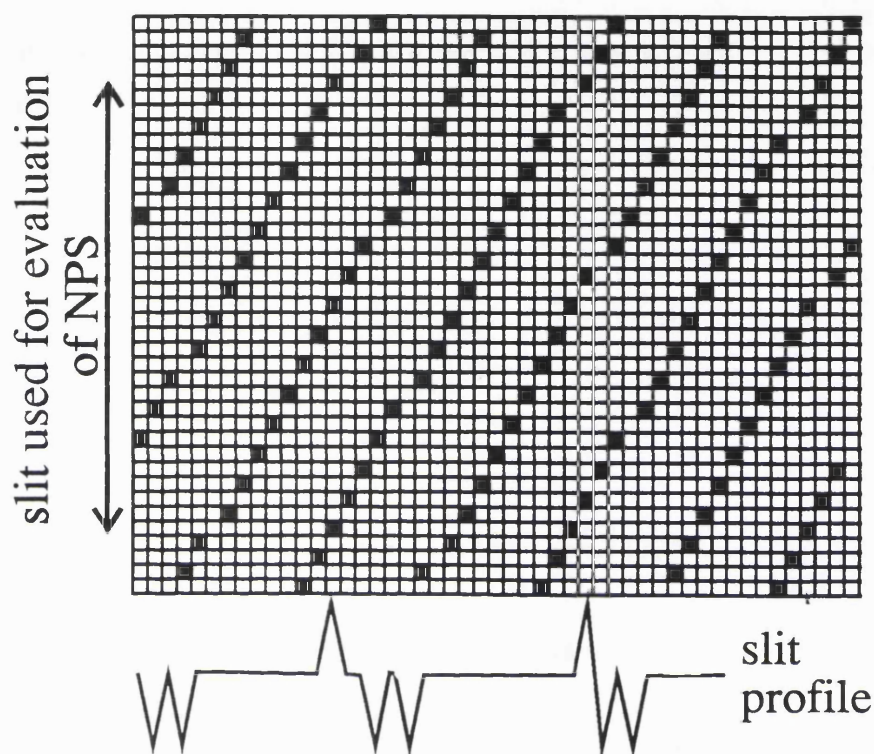
Figure 4-19 Schematic of an image with pulsing interference

In the sine wave case it is only the fraction of the wavelength that is left after removing any whole wavelengths from the slit which contribute to the peak, as whole wavelengths average to zero. As the slit length is increased the contribution of the interference to the signal stays the same (i.e. no greater than the amplitude) and is therefore proportionally reduced when dividing by the length of the slit (see equation B-7 in appendix B).

The pulsing case is slightly more complicated and increasing the slit lengths does not necessarily reduce the height of these interference peaks. As for the sine case for slit lengths less than the interference wavelength some structure is seen. For slit lengths larger than the interference wavelength different sources of fixed frequency interference

can be identified. A schematic of an image with fixed frequency pulsing interference is shown in Figure 4-19 together with the profile found from a given slit length. Frequencies are found in the profile due to variations in the number of pulses contained in the slit due to the effective slope (y/x) of the interference lines and also due to 'dislocations' in this pattern caused because the interference wavelength is not an integer number of pixels. Increasing the slit length results in an increase in the number of pulses per slit, giving an increase in the mean value of the pixels in each slit. This results in an increase in the zero frequency value of the NPS, an effect seen in the experimental results of Figure 4-20.

If perfectly in-phase images are subtracted then no interference is seen. If however, the subtracted images are not exactly in phase, then, depending on the interference type and wavelength, the peak heights may decrease as the slit length is increased. When averaging along a slit much of the pulsing will average to zero thus giving no interference peaks if the interference wavelength is an integer number of pixels (i.e. 1 positive pulse + 1 negative pule = 0).

4.6.3 Experimental investigation of fixed frequency interference

Figure 4-20 shows an experimental dark current NPS for the system currently under investigation (CCDb, high gain). This NPS was calculated as previously described by subtracting two images. It can be seen from that some frequency peaks increase with slit length and some decrease with slit length. This means that, in this case, there is no simple 'optimum' slit length which gives the minimum amount of fixed frequency interference on the measured NPS. To reduce the influence of this interference on the measure NPS a reasonably long slit (300 pixels) was used to remove some of the interference peaks from the NPS. Also one of the images was displaced (down a column) relative to the second image such that the interference of the two images was in phase. Two techniques were investigated to achieve this. In the first, the images were positioned such that the square of the corresponding pixel-to-pixel variations between the images was minimised.
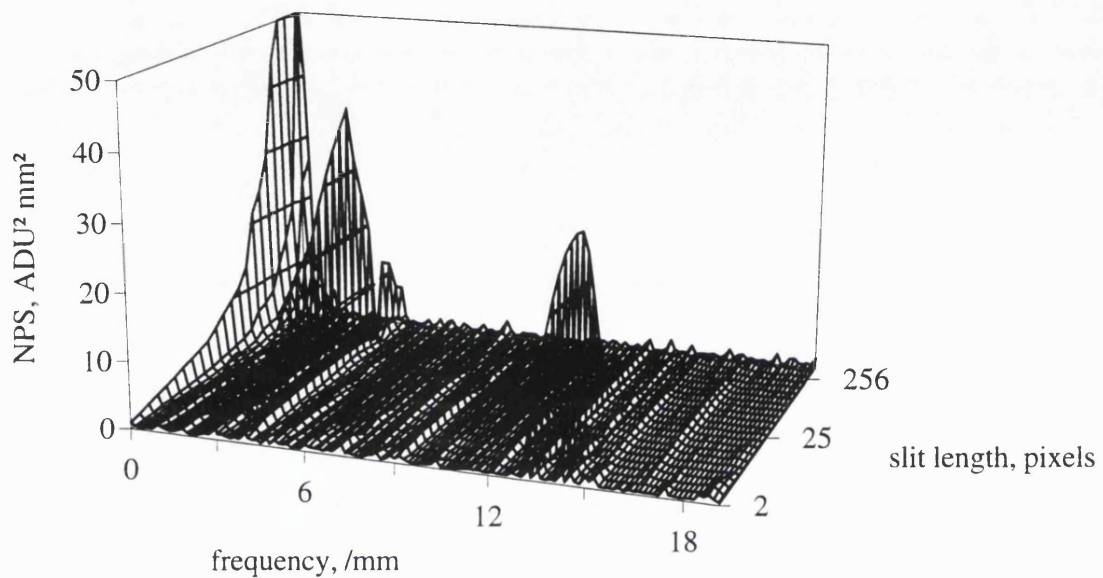
Figure 4-20 Experimental dark NPS showing various fixed frequency interference peaks

This technique was found to be inadequate in this case as these variations were dominated by a small sine-type wavelength interference whose peak in the NPS was already negligible due to using a long slit. In the second technique the NPS was calculated for a number of displacements and the one for which the area under the given interference peak was smallest, was used. This was found to work well in removing all interference peaks from the measured NPS. It did, however, result in an increase in the time taken to calculate the NPS but, by only calculating the frequencies at and immediately surrounding the peaks, this time increase was reduced such that the time taken was only a factor of two greater than simply subtracting randomly phased images. It should be noted that displacing two images down a column when the system is

operating in TDI mode still removes fixed pattern noise, as only column-to-column variations in response and dark current are important.

The simulations described above assume that the interference is noiseless. This is obviously not the case in real experiments. Noise on the interference will tend to blur out the interference peaks, thus affecting a larger surrounding region of frequencies.

4.6.4 Summary of the effects of fixed frequency interference on the measured NPS

Fixed frequency interference can cause peaks in the measured NPS which, in extreme cases, may interfere with the interpretation of these NPS. The height of these peaks is dependent not only on the amplitude of the interference, but also on the length of the slot used in measuring the NPS, on the method of subtracting two images and also on the type of interference (pulsing or sin-type). The frequency of the peaks is dependent on the relationship between the interference wavelength and the CCD line length, including the time taken to read a line down the CCD. Although it is not possible to remove the noise caused by variations in the amplitude of the interference, it is often possible to significantly reduce the size of all interference peaks in the NPS by using an appropriate slit length (i.e. long enough, but not too long) and by subtracting two images using an appropriate algorithm to bring the images into phase before subtraction. Although interference peaks can be removed manually by the investigator, this investigation has shown possible ways of automatically removing them. Often authors use image subtraction as a method of removing the effect of fixed pattern noise on the NPS. This will still work if one image from a TDI system is displace down a column relative to the second image before subtraction as the response and dark current variations average over a column.

4.7 Experimental NPS results

The total NPS is made up from the following contributions which, as described in Appendix B, sum to give the total NPS:

- $W_Q(u)$, the NPS due to x-ray detection in the phosphor. This includes variations in the number of light quanta produced and also the effects of the spreading of the light.

- $W_{SQ}(u)$, the NPS due to secondary quantum fluctuations (i.e. light photons), including the detection of these quanta.

- $W_X(u)$, the NPS due to direct x-ray interactions with the silicon of the CCD

- $W_D(u)$, the NPS due to inherent detector system fluctuations .e.g. noise due to dark current and any electrical noise

Firstly the NPS due to secondary quanta, W_{SQ}, was calculated, as described in section 4.5 and Appendix B, for a range of incident light intensities. The results are shown in Figure 4-21. As expected W_{SQ} was found to be independent of frequency (each photon produces only one electron and so there is no correlation of the noise) and, therefore, Figure 4-21 only shows the variation of average value with intensity. The NPS value is directly proportional to the intensity for quantum limited detection.

As discussed previously, direct x-ray absorption in the silicon of the CCD produces a significant fraction of the total signal. The NPS due to this was calculated for a range of incident x-ray intensities and, within experimental error, was found to be independent of frequency. When an x-ray is absorbed in the CCD it produces a cloud of electrons (nearly 7000 electrons for a 25keV x-ray) and the noise is, therefore, correlated. The electrons only spread slightly giving an MTF with significant high frequency response. The variation of the measured average NPS value with intensity for a spatial frequency of $15mm^{-1}$ is shown in Figure 4-22. This was evaluated by irradiating the bare CCD (CCDa) with a uniform field of x-rays and calculating the NPS as before. The shape of this spectrum (after smoothing to reduce noise) can be seen in figures 4-23 and 4-24.
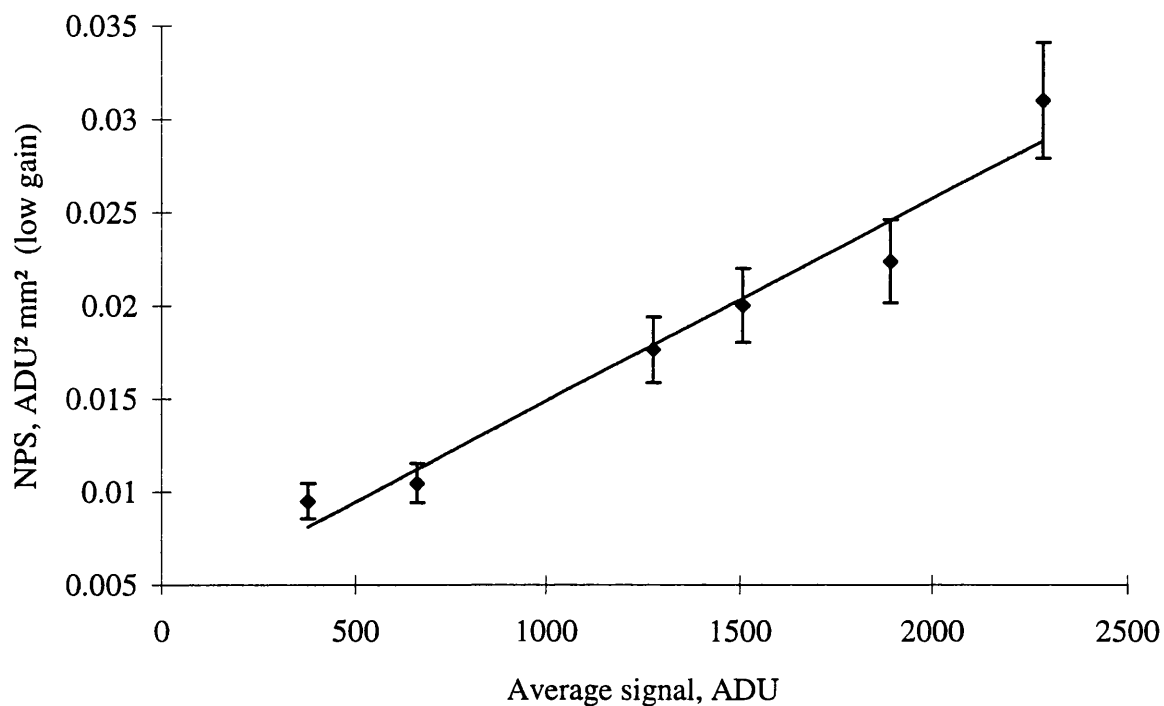
Figure 4-21 NPS value for secondary quanta
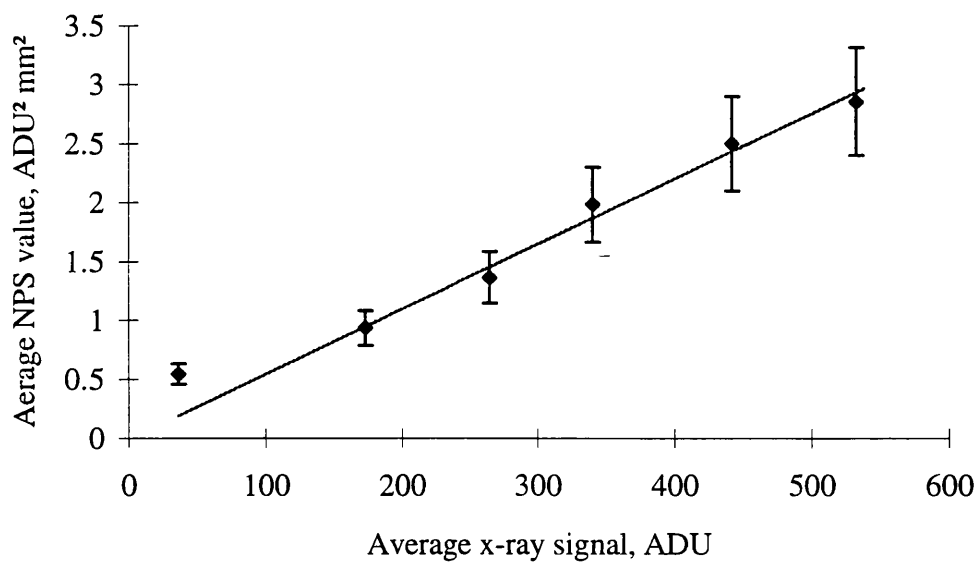
Figure 4-22 Variation of direct hit NPS with signal level (low gain)

The spectrum used was obtained using the tungsten target tube described in chapter 3, set at 45kVp with 4.3mmAl total filtration, to approximate the spectrum with 45kVp and 1.8mm Al after passing through the CsI(Tl) coating. This extra amount of 2.5mmAl filtration is between that necessary for 43μm CsI and that for 120μm CsI, which are approximately equivalent to 1.5mmAl and 3.5mmAl respectively, and the NPS results should, therefore, be considered as estimates rather than exact values. They indicate that this source of noise is significantly larger than that due to visible light, to the extent that W_{SQ} can almost be considered negligible.

During calculation of the above results it was necessary to measure the dark NPS, $W_D(u)$. This was found to be approximately flat, with a typical value of 0.012 ± 0.008 ADU^2mm^2 for low gain. (CCDb and CCDd) using all dark current reduction techniques described in chapter 3. With no dark current reduction techniques (and approximately four times the dark current) this was measured at 0.015 ± 0.008 ADU^2mm^2. This is a smaller increase than expected, and indicates the significance of noise other than dark current, such as amplifier noise and electrical pickup.

Finally the total NPS was calculated for the 43μm and 120μm CsI coated CCDs (CCDb and CCDd), the results of which are shown in Figure 4-23 and Figure 4-24 respectively. Also shown are the individual contributions to the NPS calculated from the above results using the assumption that W_{direct} is independent of frequency. The size of each individual contributions in these figures is based on the theory presented in chapter 3, which predicts that the fraction of the signal due to direct hits is 14% and 40% for 43μm and 120μm CsI coatings respectively. These results of Figure 4-23 and Figure 4-24 are for incident air kerma of 0.53mGy and 0.71mGy respectively.

Several conclusions can be drawn from these results. Of particular importance is the significance of direct hits in increasing system noise, even for the 120μm CsI coating. It is clear that removal of these events by, for example, using a fibreoptic stud with high lead content between the phosphor and the CCD will significantly reduce the noise. Once these events have been prevented the NPS due to x-ray detection will dominate. Background noise, as illustrated in $W_D(u)$ is not significant at these exposures.
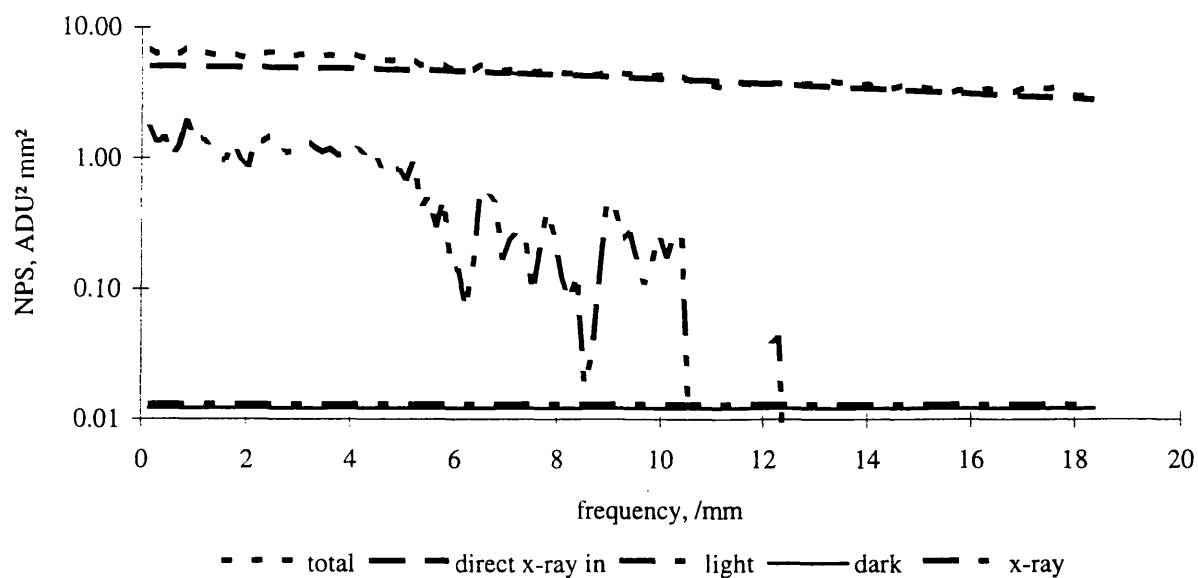
Figure 4-23 Total NPS for CCDb
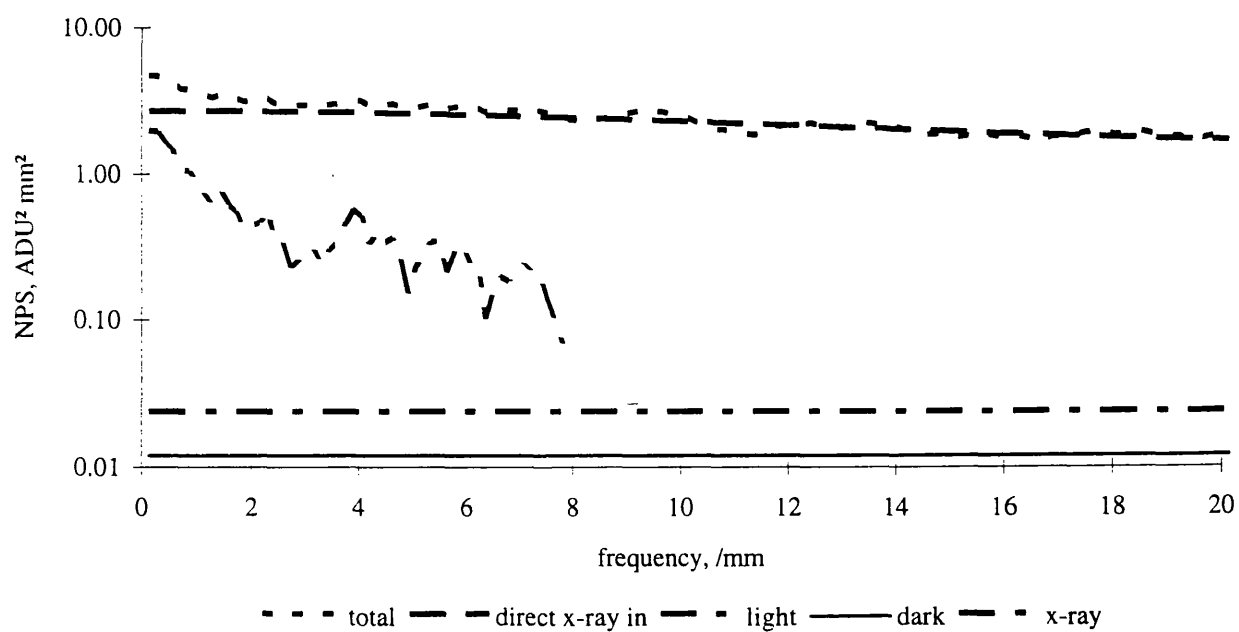
Figure 4-24 Total NPS for CCDd

4.8 Summary of NPS results

Various methods of reducing the influence of fixed frequency interference on the NPS have been investigated, including the use of different slit lengths and subtracting images. It has been shown that noise due to direct x-ray interactions in the silicon of the CCD are significant, even for the thickest CsI coating used (120μm), and a second generation system must, therefore, prevent these interactions.

4.9 Detective quantum efficiency

4.9.1 Introduction

The spatial frequency dependent detective quantum efficiency, DQE(f), describes the transfer of signal to noise ratio from the input to the output of the detector. It provides a combined description of both the signal and noise transfer characteristics of the detector and, therefore, gives a more complete measure of the system's imaging capabilities than, say, the MTF alone. Radiographic systems which use a phosphor screen coupled to an optical detector have a characteristic DQE(f) which decreases with increasing frequency (Nishikawa and Yaffe 1990), an effect which has two major causes. First the x-ray quantum noise may be transferred more efficiently than the signal and, secondly, the presence of other noise sources, such as fluctuations in the number of light photons emitted by the screen and background noise in the detector, serves to reduce the DQE(f).

The basic theory of spatial frequency dependent detective quantum efficiency is described in Appendix C.

4.9.2 Evaluation of DQE(f)

The zero frequency DQE is the produce of the quantum efficiency and the Swank factor. As detailed in Appendix C, the Swank factor accounts of fluctuations in the number of photons emitted per absorbed x-ray. When direct interactions in the CCD are included the process is somewhat complicated and there is a much larger variation in the signal produced in the CCD per x-ray interaction. This is equivalent to a significant reduction of the Swank factor which consequently reduces the zero-frequency DQE. In this case, using Equation C-4 of Appendix C, the zero frequency DQE has been estimated at 0.04 ± 0.02 and 0.22 ± 0.02 for the 43μm and 120μm CsI coatings. Most of the errors in this measurements are due to experimental errors in evaluation of the NPS, and errors in estimates in the number of incident photons. Removal of the glass plate in front of the CCD housing would increase these values by (1/0.8), as this plate stops approximately 20% of the x-rays reaching the phosphor. These zero frequency values are at the bottom of the low frequency DQE values reported for mammography film-screen systems of 0.1 - 0.3 (Nishikawa and Yaffe 1985) and are significantly lower than predicted values where direct x-ray interactions in the CCD are neglected. The spatial frequency dependent DQE for the 120μm CsI coated device, CCDd, and the 43μm coated device, CCDb, is shown in Figure 4-25.
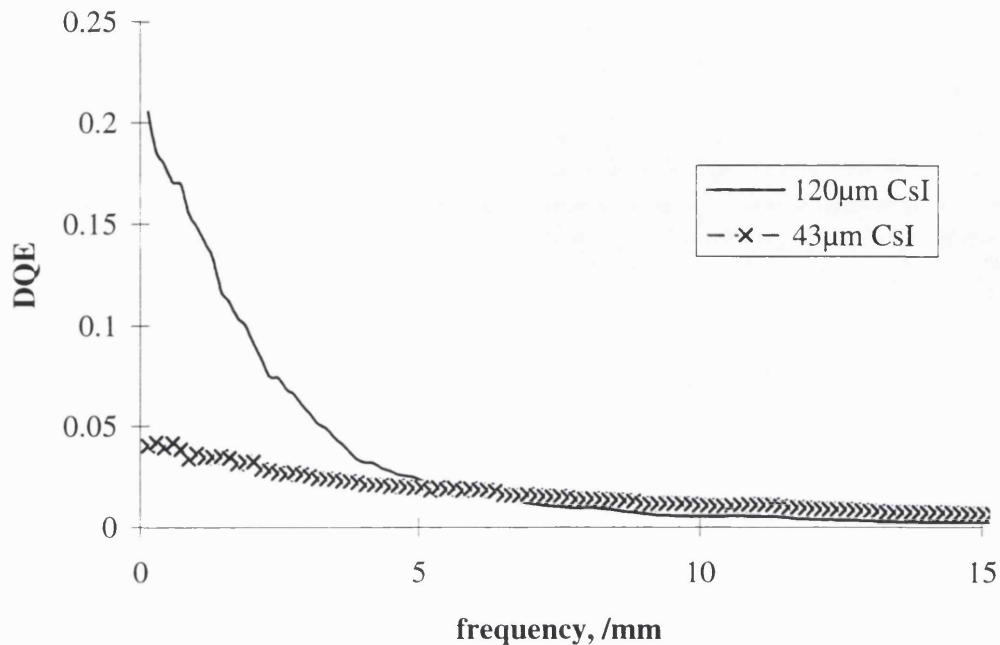
Figure 4-25 Experimental DQE(f) for CCDb and CCDd

Figure 4-26 shows the DQE(f) for these detectors, as calculated from Equation C-8 of Appendix C, where direct hits are neglected. The MTFs used are those estimated above for the phosphor alone. The average number of visible photons produced per x-ray interaction, m, is taken as the product of the average energy of the 45kVp spectra (29kVp) and the number of photons per keV (52, Knoll 1981). The Swank factor, I_X, is taken as 0.8 (Martinez 1994), the product of η_{op} and η_λ is taken as 0.175 and η_Q is taken as 0.31 and 0.61 for the 43µm and 120µm coatings respectively. These were calculated for a 45kVp spectrum with 1.8mm aluminium filtration. The shapes and trends agree broadly with those of Westmore and Cunningham 1993. It should be noted that these curves are only approximate and do not include factors such as dark current and consideration of the depth dependent MTF. They are also dependent on errors in estimating the MTF due to the phosphor alone.
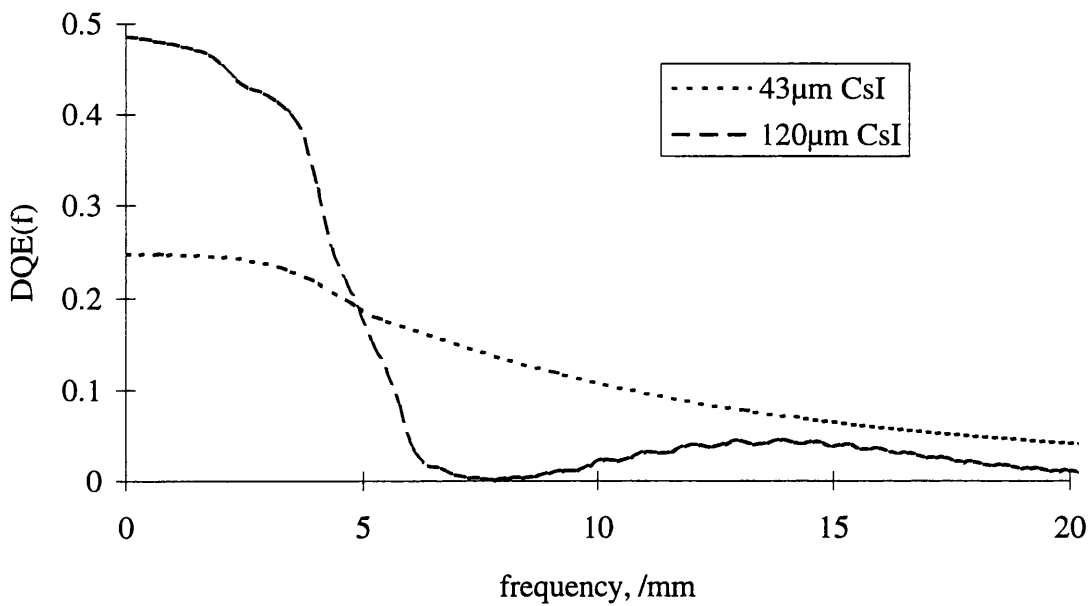
Figure 4-26 Estimated DQE without direct x-ray interactions in the CCD

Comparison of Figure 4-26 and Figure 4-25 indicates two important results: Firstly, as already mentioned, direct hits in the CCD reduce the zero frequency DQE. Secondly, the system DQE at frequencies above zero will be higher if these direct hits can be prevented. That is, the high frequency response due to direct hits as shown in the MTF is not reflected in the DQE(f) because of the high level of noise at the higher frequencies. These detectors, as they stand, are, therefore, not optimised for this application. The suitability of various coatings and fibreoptic arrangements is investigated further in Ho _ 1996.

4.9.3 Summary of DQE results

Direct interactions of x-ray in the CCD act to significantly reduce the DQE(f) at all frequencies. DQE(f) without this effect have been estimated and found to have significantly higher values at all frequencies, with the conclusion that the use of a fibreoptic taper or stud with high lead content between the scintillator and CCD is

extremely advantageous, particularly for a dose limited system where the magnitude of the DQE is important.

4.10 Conclusions

The main conclusions of this chapter are related to the effects of direct x-ray interactions with the silicon of the CCD. These interactions have been found to give increased high frequency response for the MTF measurements, but also to significantly increase noise, as illustrated in the NPS measurements. In particular, these interactions increase the variation in signal size per x-ray interaction and, therefore, significantly reduce the DQE(f) at all frequencies. These results indicate that if the system is to be optimally used in mammography then these interactions must be removed or significantly reduced by, for example, using a fibreoptic stud with high lead content between the phosphor and the CCD or using some sort of light guide such that the CCD can be removed from the direct path of the x-rays.

Other conclusions are that the use of a CCD with faster output circuitry than available with the CCD 15-11 would be advantageous in increasing the MTF, as TDI waveform degradation is the most significant factor in degrading the MTF after light spread in the phosphor. Other effects, such as velocity variations in the scanner, have been shown to be less significant.

5. A MULTIPARAMETER OPTIMISATION OF DIGITAL MAMMOGRAPHY[#]

5.1 Introduction

This chapter describes an investigation of the system parameters, such as tube voltage and source-to-patient distance, needed to maximise the image quality for a minimum patient dose. First the requirements and constraints of a mammography system are discussed. Although some of these have already been listed in chapter 1, a number of them are now discussed in more detail, particularly those which are somewhat arbitrary, such as exposure time and source-to-patient distance. A Monte Carlo study aimed at finding a simple method of predicting the amount of radiation scattered in the patient is then described. These results are then used in a model of the mammographic imaging process. After detailing the optimisation technique, the results of a large number of theoretical optimisations are then be described. The influence of detector width, exposure time, focal spot size, detector resolution and noise on the optimum settings of tube voltage, source-to-patient distance (SPD), filtration and target magnification are examined.

In order to maintain the generality of the results presented the influence of these factors are examined by using trends in the optimisation. For example, optimisation results are described for 10 focal spot sizes from 80μm to 800μm, and the trends in SPD, tube potential, filtration and magnification as the focal spot increases are shown graphically as trend surfaces. This use of trends avoids any absolute values, which can be misleading as they are only true for the specific case described. It also allows factors like cost and ease of use, which are not included in the optimisation, to be separately considered by equipment designers and allows the use of simple models to describe factors like scatter

---

[#] A significant proportion of the work presented in this chapter has been submitted to Phys. Med. Biol. as 'A Multiparameter Optimisation of Digital Mammography' with R Speller as co-author. The results in this chapter are those of L E Court.

in the breast. An understanding of the trends involved in the optimisation of a digital mammography system will also help in the design of a strategy for experimentally optimising the system after it has been set up with initial predictions. Finally, the application of these results to a TDI CCD mammography system are discussed.

5.2 Requirements and constraints of a mammography system

This section supplements the discussion of 'good imaging practice' in chapter 1. It discusses the arbitrary constraints of exposure time and source-to-patient distance It also discusses constraints imposed by present technology: scanning rate and x-ray tube power limits.

5.2.1 Exposure time

Haus 1990 suggests that the exposure time should be kept below 1s in order to minimise blurring of the image caused by patient movement. The Commission of the European Communities suggests a similarly short maximum exposure time of 2s (CEC 1990). It should be noted, however, that patient blurring is less of a problem for slot scanning systems as the image of a single part of the breast (usually a strip) is collected in a much shorter time than for a full area detector for which the whole image is integrated for the whole exposure time. A second limitation on exposure time is imposed by the pain experienced by the patient during breast compression. This pain has been identified as significant (Vaile et al 1993) and should, therefore, be minimised. The importance of these two effects is not well defined and, therefore, a range of exposure times between 1 and 10s have been considered, where the short exposure times may be more appropriate for large area imagers, while the longer exposure times may be used for scanning systems.

5.2.2 Source-to-patient distance

Slit scanning systems only use a small fraction of the available x-ray flux. One way of increasing the available flux is to move the x-ray source closer to the patient. This can influence the imaging system in a number of ways, including increased influence of the heel effect, increased variations in focal spot size across the image, increased variations in object magnification across the breast thickness which may give a distorted image and an increase in patient dose caused by x-rays scattered in the filter material. A Monte Carlo analysis using the general purpose EGS4 code (Nelson et al 1985, and Appendix E), found that another possible effect - increased variations in patient dose across the breast thickness due to $1/r^2$ flux variations - was small compared with exponential attenuation of the x-rays for source-to-patient distances (SPDs) down to at least 15cm. The results of this study, for a water phantom, are illustrated in Figure 5-1 where the variation of absorbed dose across the breast thickness is seen to vary very little as the source to patient distance is altered from 15cm to 60cm. The absorbed energy was binned into 0.5cm thick slabs. These measurements were for 10^7 incident photons, giving approximate errors (standard deviations) of less than 0.1% in the first 0.5cm slab increasing to 0.3% in the last 0.5cm slab.

It will be shown later that flux limitations are generally only a problem for slit scanning systems. In these systems it should be possible to overcome variations in focal spot size and increased heel effect by rotating the x-ray tube to follow the detector in the manner used by Maidment et al 1993. The significance of x-rays scattered in the filter material subsequently being absorbed by the patient depends on the filter material and on the detector size (i.e. slit scanning or full area). A Monte Carlo analysis has shown that for 20keV x-rays using 2mm aluminium filtration and an SPD of 15cm and no collimation between the filtration and the patient these scattered x-rays can increase patient dose by approximately 6%. The results for a more realistic SPD of 30cm with a large area detector (i.e. no collimation) with various filter thicknesses are given in Figure 5-2. This effect becomes negligible for slot scanning systems.
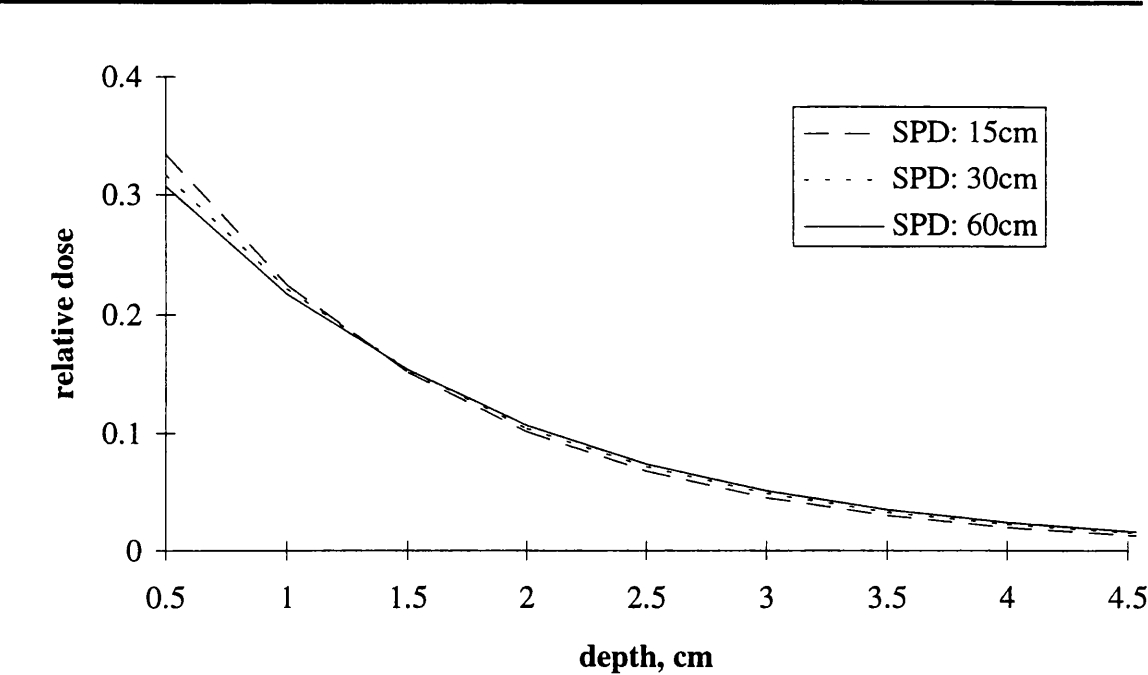
Figure 5-1 Variation of absorbed energy across the breast thickness for different values
of SPD

Note that the higher values of filtration shown here are somewhat unrealistic, but are
included to shown the continuing trend of dose increase.   Errors of these points,
estimated by repeating the 4mm results five times are, ±1%.
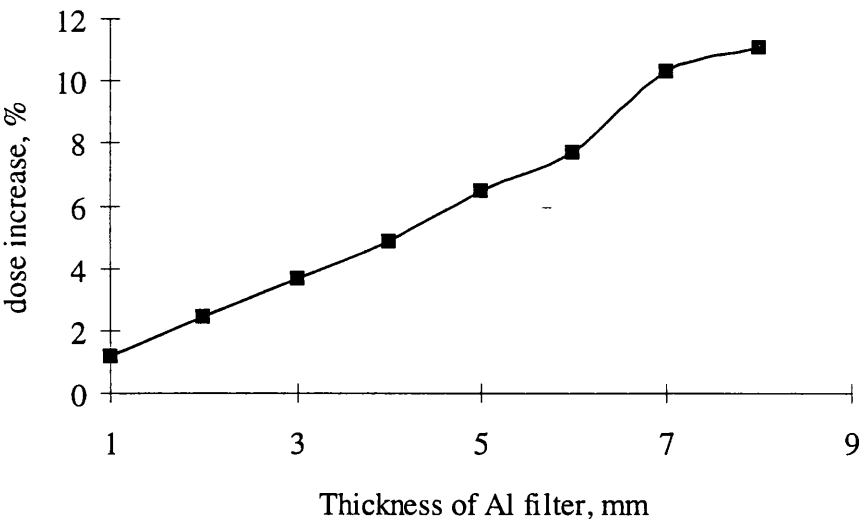
Figure 5-2 Effect of radiation scattered from filter material on patient dose (20keV,
SPD:30cm)

Possibly the most significant of the effects listed above is the effect of the variation in magnification across the breast thickness. For example, for a SPD of 15cm the variation in magnification across a 6cm thick breast is close to 30%. This can results in a large variation in both the perceived object size and also the resolution. The effect of this on the diagnostic quality of the image is unclear and needs further work, but in this work a totally arbitrary minimum SPD of 30cm has been imposed, as this limits the magnification variations across a 6cm breast to 17%. The use of trends in the optimisation means that it is reasonably simple to estimate the effect of using a larger, or smaller, minimum SPD. This may be necessary if, for example, the resolution for objects near the top of the breast is found to be insufficient.

5.2.3 Scanning rate

In a TDI scanning system the scanning rate is fundamentally limited by the rate of transfer of signal electrons in the CCD, although the practical limit is often set by difficulty in generating and transmitting the drive waveforms. Burt 1991 has given an approximate expression for the maximum rate at which charge can be transferred through the readout register, whilst maintaining a high charge transfer efficiency of 99.999% as

$$f_{max} = \frac{5.10^{11}}{L_P^3} \qquad (pixels\,/\,second)$$

Equation -5-1

where L_P is the length of the CCD pixel in microns. The numerical constant comes from considering typical parameters for buried channel CCDs such as the oxide thickness and diffused channel depth. This expression predicts that a CCD with 27μm pixels and 1024 pixels perpendicular to the scan direction (i.e. 1024 columns) can scan approximately 60cm in 1s. This fundamental limitation can, therefore, be neglected. Commonly CCDs are not limited by the rate of transfer of electrons through the CCD but by the speed of the output circuitry of the CCD. For example, EEV CCD 15-11s have a maximum readout rate of 800-1000kHz, limiting the scan rate to less than approximately 2.5cms[-1]. Since these are the CCDs used in this work this poses a limit on the scan speed of the

prototype. It does not, however, limit the speed of operation of a second-generation system as CCDs are available with significantly faster operating frequencies.

Another limit of the scan speed is the blurring effect of the screen fluorescence decay. As discussed in chapter 4, this is insignificant when using CsI(Tl).

The final limitation on the scanning speed is the top speed of the scanning gantry. This is not considered a fundamental constraint and will not be discussed further. Indeed, for the system constructed in this work the maximum speed of the gantry gantry (18cms^{-1}, see chapter 2) is 8-9 times faster than allowed by the readout circuitry of the CCD (approx. 2.1cms^{-1}).

5.2.4 X-ray tube power limitations

Details of the relationship between tube voltage, exposure time and maximum current for individual tubes is provided by the manufacturers in the form of rating charts (nomograms). For lower tube voltages the rate of electrons reaching the target material is limited because the negative space charge inhibits the extraction of further electrons from the filament and blocks any increase in tube current. The relationship between the maximum achievable current , I_{lim}, and the tube voltage, V, is given by (Ballu 1980):

$$I_{\text{lim}} = c_1 V^{3/2}$$

Equation 5-2

where c_1 is a constant which depends on the geometry of the electron optics. For higher values of tube potential and/or longer exposure times the tube power is limited by the temperature of the focal track. An empirical formula which fits data in this region is:

$$P_{\text{lim}} = c_2 \left[-\ln\left(\frac{t_{\text{exp}}}{c_3}\right) \right]^{\frac{1}{2}}$$

<div align="right">Equation 5-3</div>

where P_{lim} is the power limit, t_{exp} is the exposure time and c_2 and c_3 are empirical constants. The maximum permitted tube current for a given tube potential and t_{exp} is calculated from Equation 5-2 or Equation 5-3, whichever is the most limiting.

X-ray tubes with molybdenum targets typically have a lower power rating than tungsten target tubes and the above equations are not appropriate. For molybdenum tubes the power limit is constant, and the maximum permitted tube current can be calculated from

$$P_{\text{lim}} = VI$$

<div align="right">Equation 5-4</div>

The tungsten target x-ray tube used in this theoretical study is the Philips SRM 03 10. This is a high load unit, with a nominal focal spot size of 0.3mm. The values of c_1, c_2 and c_3, based on nomogram data for this tube, are 0.367 ± 0.007 mA $kV^{2/3}$, 4279 W and 36.2 s^{-1} respectively. The molybdenum target x-ray tube is the Philips ROM20 ROT206 (Philips 1988), for which P_{lim} is 3kW for a nominal focal spot size of 0.3mm. In both cases the power rating for other (hypothetical) tubes with different focal spot sizes are estimated assuming that the power limit is proportional to the focal spot area. Although the accuracy of this assumption depends on specific x-ray tube designs, it should be a reasonable assumption. The use of trends, rather than absolute values, when considering the optimisation results means that inaccuracies in this assumption, and any inaccuracies in the algorithm of Birch and Marshall 1979 should not invalidate the conclusions.

5.3 Scatter in mammography

It has been known for many years that scattered radiation can seriously degrade the image quality in mammography (Barnes 1979). This is because it reduces contrast, and acts as an additional source of noise (see Appendix D). Therefore, a number of techniques have been proposed to reduce the amount of scattered radiation which reaches the detector. These include grids, air gaps and slit scanning devices, with the anti-scatter grid dominating in the field of mammography. It has already been mentioned (see chapter 1) that digital detectors present excellent opportunities for scatter rejection as, typically and unlike film, no associated increase in patient exposure is needed. In order that this potential be realised, reliable predictions of the amount of detected scatter are needed. There are various approaches for this, including Monte Carlo techniques (Dance and Day 1984, Chan and Doi 1983), radiation transfer equations based on Monte Carlo results and empirical formulae based on experimental results (Sorenson 1985). The method used here is to fit empirical formulae to Monte Carlo results. The advantage of such a method is that the results can immediately, and simply, be applied to numerous system geometries and incident x-ray spectra. This method does not provide details such as the angular distribution of the scattered x-rays, as might be included in a more rigorous description (see, for example, Bernstein 1986); as will be discussed below, the use of trends in the optimisation approach used here means that a very detailed model is not necessary.

The model used to describe the scatter flux is described in section 5.3.1. The Monte Carlo simulation is described in section 5.3.2, and the results given in section 5.3.3. The Monte Carlo model is then evaluated by comparing some of its predictions with results from the available literature. Finally, after describing techniques of predicting the energy (rather than number of quanta) of the scattered radiation, a brief discussion on the implications of the results of this model.

Throughout, emphasis is placed on the use of scanning slits and/or air gaps.
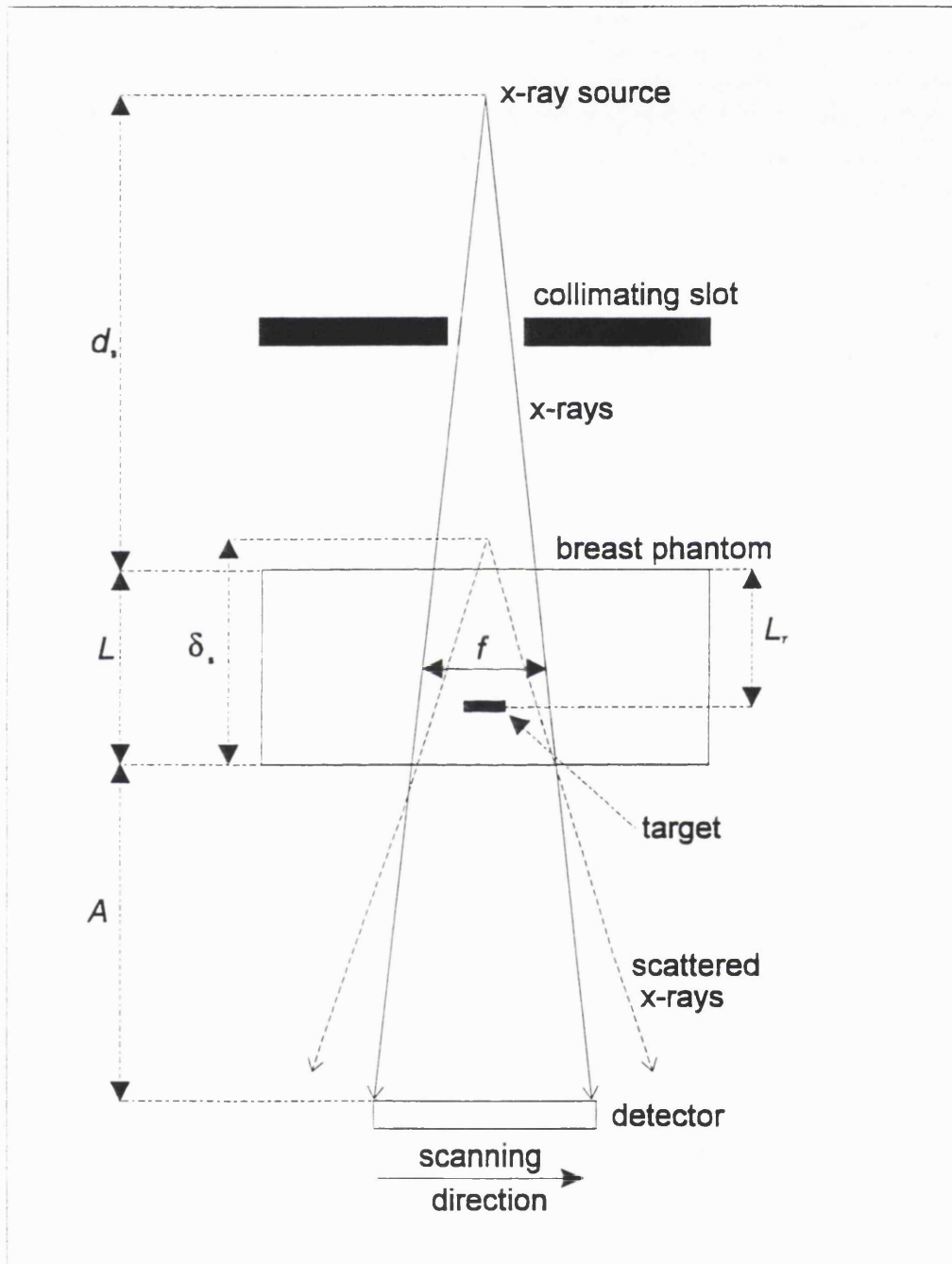
Figure 5-3 Schematic of a scanning mammography system

5.3.1 The effective scatter point source (ESPS) model

The use of the effective scatter point source (ESPS) model to simulate scattered radiation as if it originates from some virtual source a distance δ_S from the patient exit plane is illustrated in Figure 5-3. It was first suggested by Muntz, and has since been used for a variety of applications including chest examinations (Muntz 1979), mammography (Muntz 1979, 1981, 1982, 1985) and digital radiography (Neitzel 1992).

If the scatter is assumed to originate from a point a distance δ_S from the exit plane of the patient, the scatter-to-primary ratio, S/P, at a detector a distance A from the patient can be shown (Sorenson et al, 1984) to be:

$$\frac{S}{P} = \left(\frac{S_0}{P_0}\right)\left[\left(\frac{\delta_s}{x_p}\right)\frac{(x_p + A)}{\delta_s + A}\right]^2$$

Equation 5-5

where x_p is the distance from the x-ray source to the exit plane of the patient ($=d_s + L$). The scatter to primary ratio is defined as the ratio of the number of scattered quanta to the number of primary quanta detected by a perfect, totally absorbing, photon counter. Equation 5-5 simplifies to:

$$\sqrt{\frac{P}{S}}\frac{(x_p + A)}{x_p} = \sqrt{\frac{P_o}{S_o}}\frac{(\delta_s + A)}{\delta_s}$$

Equation 5-6

Therefore, a plot of

$$\sqrt{\frac{P}{S}}\frac{(x_p + A)}{x_p}$$

Equation 5-7

versus air-gap, A, will give a straight line with y intercept $\sqrt{P_o/S_o}$ and x intercept $-\delta_s$. This is found to be the case in both experimental (Sorenson 1984) and Monte Carlo

(present work) treatments. The values of $\sqrt{P_o/S_o}$ and δ_S are both dependent on x_p and source to patient distance, patient size, input x-ray energy and the dimensions of the field-of-view.

5.3.2 Monte Carlo simulation to estimate scatter-to-primary ratios

The Monte Carlo code used in this scatter study is the general purpose EGS4 v2.2 code (Nelson 1985). In common with much published Monte Carlo work EGS4 v2.2 calculates the coherent scattering form factor using an independent atoms assumption. This assumption has been shown (Johns and Yaffe 1983) to over estimate the differential cross-section for scattering angles close to $0°$, but this should result in only a slight overestimate of S/P and δ_S, with larger errors for small slot widths.

The geometry used in this simulation is given in Figure 5-3. The breast phantom considered is a rectangular approximation of the average breast shape (Fife 1993) with an upper surface area of 10×15 cm^2. It is made of water, which has similar total linear attenuation coefficients to fibrous breast tissue. X-rays leaving the breast at the lower surface were scored as primary or scattered photons. Scatter-to-primary ratios were then calculated for air gaps of 1,11,21,31 and 41 cm. In all cases these ratios were averaged over the central area in the shadow of the field-of-view. That is, over a region for which the dimension in the scanning direction was equal to the field width (i.e. 15cm) and the dimension perpendicular to the scanning direction was the smaller of 2cm and the field length. For example for a 1cm wide field width, f, the S/P was found over a central region 15×1cm^2; for a 4cm field width the S/P was found over a central region 15×2cm^2. This method is a balance between that used by experimental workers where S/P is measured by a detector, typically placed in the centre of the field, and the method used by Dance and Day 1984 who measured S/P averaged over the entire shadow of the breast in order to achieve data with reasonable statistical quality without using unreasonable computer processing time.

(S_o/P_o) and δ_S were then calculated using the method of Sorenson, described above. $\sqrt{P_o/S_o}$ and δ_S were calculated for a wide range of input parameters:

- Patient widths from 2cm to 6cm (the patient is modelled as a block of water)

- Values of x from 30 to 150cm

- X-ray energies (monoenergetic x-ray sources were used) from 18keV to 120 keV

- Field sizes from 15cm x 0.1cm to 20cm x 20cm

Empirical formulae have been fitted to model the variations in $\sqrt{P_o/S_o}$ and δ_S, and these have been compared with published results.

5.3.3 Monte Carlo results

Typical Monte Carlo results for (S_o/P_o) and δ_S are shown in figures 3(a) and 3(b). The empirical formulae used to describe variations in (S_o/P_o) and δ_S are:

$$\delta_S = k_1 + (1 - e^{-k_2 f})(k_3 + k_4 e^{-k_5 E^{k_6}}) + k_7(x_p - 30)$$

Equation 5-8

$$\frac{S_o}{P_o} = \frac{S_o'}{P_o'}\left(1 - e^{-k_8 f}\right)$$

Equation 5-9

where (S_o'/P_o') is the scatter to primary ratio at the exit plane of the patient for a field width of 10cm, and k_1-k_8 are constants, the values of which are dependent on the phantom thickness. The values of the constants, and the differences between the empirical fits and the Monte Carlo results for different breast thicknesses are shown in Table 5-1. Variations in (S_o'/P_o') with energy for different breast thicknesses are given in Table 5-2.

(a)

(b)
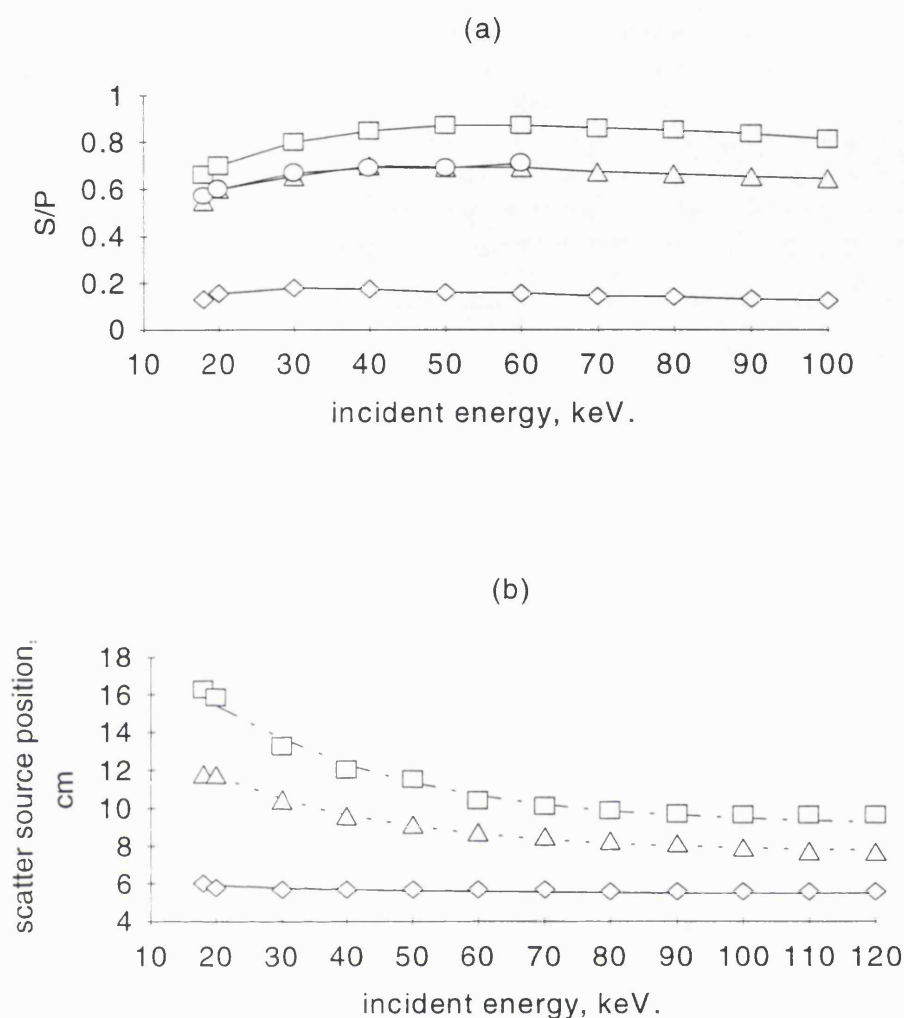
Figure 5-4(a) Monte Carlo results for scatter to primary ratios for a 6cm thick breast phantom for three different field sizes, compared with the results of Chan and Doi for a 5cm thick semi-infinite block of water, and (b) Comparison of Monte Carlo results (points), and predictions of equation 15 (lines) for a 6cm thick breast phantom. In (a) and (b) the field sizes are: 10cm (•), 5.5cm (Δ) and 0.5cm (◊). The results of Chan and Doi are indicated by O.

Variations in (S_O/P_O) with x_p were found to be negligible compared with statistical variations in the Monte Carlo results. The fractional errors between the Monte Carlo results and empirical formulae for S/P are largest for small field widths, and sometimes approach 75%., although the absolute error at these small field widths is small. This

does not affect the quality of the optimisations; firstly because of the optimisation technique used (i.e. the use of trends) and secondly because the effect of scatter on the SNR for small slot widths is negligible compared to other effects that are described further below. It should also be noted that the Monte Carlo results are at their least reliable for small fields: firstly, the amount of detected scatter is low, so the statistics are poor; secondly, the majority of detected scatter at low angles is coherent scatter, the amount of which is affected by the independent atoms assumption stated earlier.

L cm	k_1 cm	k_2 cm^{-1}	k_3 cm	k_4 cm	k_5 keV^{-k6}	k_6	k_7	k_8	max. error on δ %	max. absolute error on S/P
2.0	3.00	0.113	7.67	12.00	0.015	1.175	0.01	0.95	5	0.06
4.2	4.80	0.130	7.50	17.00	0.028	1.100	0.04	0.40	9	0.06
6.0	5.20	.082	6.85	20.00	0.023	1.094	0.07	0.34	4	0.08

Table 5-1 Empirical ESPS constants and associated prediction errors for three different phantom thicknesses

Incident energy, keV	18	20	30	40	50	60	70	80	90	100
S_o/P_o (L=2cm)	0.24	0.29	0.32	0.38	0.38	0.37	0.34	0.32	0.31	0.30
S_o/P_o (L=4.2cm)	0.42	0.48	0.60	0.63	0.62	0.62	0.58	0.54	0.52	0.50
S_o/P_o (L=6cm)	0.66	0.70	0.80	0.85	0.87	0.87	0.86	0.85	0.84	0.81

Table 5-2 Variation of measured So/Po with incident energy

5.3.4 Evaluation of the Monte Carlo model

Numerous authors have published data showing the effects of patient size, incident x-ray energy and field-size on the detected scatter-to-primary ratio. A comparison of the (S_o/P_o) values found here for a 6cm thick phantom, with those of Chan and Doi 1985 for a 5cm thick semi-infinite slab of water can be seen in Figure 5-4. Various published results are given in Table 5-3. An 'order of magnitude' comparison shown that the

scatter-to-primary ratio results of this study compare well with all the results, except those of Dance and Day 1984, whose values of S/P are all lower than those reported here.

The Monte Carlo analysis of Dance and Day 1984 used a more realistic mammography model which included effects like scatter from the patients body and, more importantly, scatter from the perspex breast compression plate. Their data showed an increase in (S_O/P_O) at low energies due to photons which were not aimed at the breast, but were scattered towards the detector by the end of the compression cone. This source of scattered photons, is neglected in this work as its significance is much reduced for smaller fields; for larger fields it is implicitly assumed in this work that the x-ray field is 'shaped' to suit the breast. The fact that the ratios of Dance and Day 1984 are generally lower than those found here can be partly attributed to their method of averaging the ratios over the entire field-of-view. The scatter contribution can be significantly less at the edge of the field of view than at the centre, and therefore reduce the average scatter-to-primary ratio.

The effects of the input parameters on δ_S have received much less attention than the scatter to primary ratios. The range of δ_S values found in this study agree broadly with those used by Muntz et al, who experimentally found $\delta_S = 7\text{cm}$ and $\delta_S = 8$ or 9cm for 5 and 8cm thick water phantoms (10cm diameter) respectively.

Author	Details (exp=experimental, MC=Monte Carlo study)	Comments	L, cm	Incident x-ray energy	S/P
Barnes & Brezovich 1978	14cm diameter radiation field, lucite phantom, S/P measured in centre of field (exp)	data showed no consistent change with energy, form 27kVp to 42kVp	3 4 5 6	27-42kVp	0.4 0.55 0.71 0.85
Chan & Doi 1985	Pencil ray incident on water phantom. Scatter collected over all exit plane of the phantom (MC)	Bernstein & Muntz used the extensive data in this study to model scattered radiation transfer	5	>60keV	0.7
Kalender 1991	water phantom, scatter detected in centre of field (MC)	Results are for 4cm air gap Italicised S/P refers to estimated result using δ=9cm.	5 *5*	60keV *60keV*	0.24 *0.33*
Dick et al (in Barnes 1979)	Monoenergetic beam, polystyrene phantom, 10.4cm diam field (exp)		5	17.4keV 32.0keV	0.49 0.69
Dance and Day 1984	Realistic study using standard breast (MC)	Low energy results include significant contribution from photons not originally aimed at the breast which are scattered in the end of the compression cone	2 4 6	20keV 40keV 20keV 40keV 20keV 40keV	0.275 0.228 0.428 0.414 0.544 0.676

Table 5-3 Comparison of published scatter to primary ratios

5.3.5 The energy of scattered radiation

Scattered radiation, produced by a mono-energetic x-ray beam incident of a slab of material, has a spectrum of energies, dependent on the incident x-ray energy and on the scattering angle. In this work, all scattered x-rays (for a mono-energetic spectrum) are assumed to have some effective (average) energy Es. This has been measured using Monte Carlo methods detailed above; the results are shown in Figure 5-5 for a phantom thicknesses of 4.2cm.

The approach used by Muntz, and repeated in the optimisations described below, is to use the approximation:

$$E_x = 0.95 E_p$$

Equation 5-10

which is also shown in Figure 5-5, and can be seen to give a reasonable estimate of the average scattered energy.
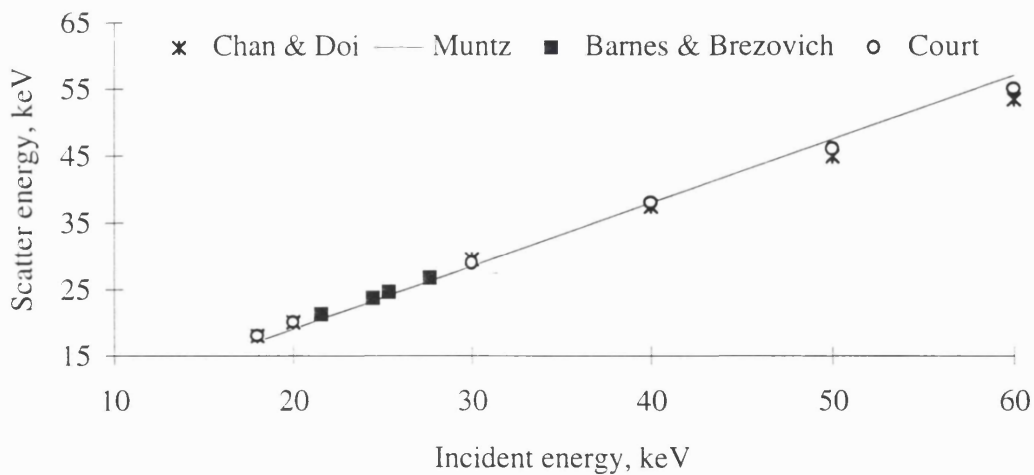
Figure 5-5 Energy of scattered radiation

Validation of the Monte Carlo model is provided, in part, by a comparison of its predictions with the Monte Carlo predictions of Chan and Doi 1985 and with some experimental results of Barnes and Brezovich 1978, which are also shown Figure 5-5. The work of Chan and Doi 1985 is for 5 and 10cm thick semi-infinite blocks of water; the results of Barnes and Brezovich 1978 were obtained using a 6cm thick lucite phantom 14cm in diameter.

5.3.6 Discussion of the implications of the scatter-to-primary ratio results

The small values of δ_S found for small field sizes demonstrates the fact that, as a smaller value of δ_S means a faster fall off of scatter flux with air gap, the use of an air gap to remove scatter is particularly effective when used with a small field. Equation 5-8 and Equation 5-9 can be used to show that equivalent values for S/P can be obtained with various combinations of slot sizes and air gaps. As an example, for a 0.5 x 15 cm^2 field with no air gap the predicted scatter-to-primary ratio is 0.136 for a 4.2 cm thick water phantom; this is the same as that achieved with a 2 x 15 cm^2 field and a 12 cm air gap. The optimum combination of field size and air gap depends not only on the scatter to primary ratio, but on a number of technical/technological constraints; this is discussed further in the optimisation below.

The use of a water phantom, rather than a 'standard breast', will affect the estimations of scatter flux. The use of trends in the optimisation means that this is not important, provided that the estimations are of the correct order of magnitude and that trends as the field-width is increased are adequately modelled.

5.4 Model of a mammography system

Signal to noise ratio

This model is based on the schematic of Figure 5-3. The width of the collimating slot dictates whether the system is a scanning or full area system. After Muntz 1979, the SNR^2 of such a system can be written as:

$$SNR^2 = \frac{\left(\int \varphi_{75} \frac{75^2}{(d_s + L_T)^2} \Delta I \eta_{E_p} E A_T \, dE \right)^2}{\int \left(\frac{\varphi_{75} 75^2}{x_p^2} e^{-\mu_{breast} L} \right) \left(\frac{\eta_{E_p} E_p^2}{M_{exit}^2} + \frac{(S_o/P_o)\eta_{E_s} E_s^2 \delta_s^2}{(A + \delta_s)^2} \right) A_I \, dE}$$

<div align="right">Equation 5-11</div>

where

$$A_I = M_T^2 A_T + (M_T - 1)^2 A_{FS} + A_D$$

<div align="right">Equation 5-12</div>

$$\eta_E \approx 1 - e^{-\mu_D(E) t_{det}}$$

<div align="right">Equation 5-13</div>

and

$$\Delta I = (e^{-\mu_{breast}(L-D) - \mu_{target} D} - e^{-\mu_{breast} L}) \approx e^{-\mu_{breast} L} \mu_{target} D$$

<div align="right">Equation 5-14</div>

where φ_{75} is the x-ray photon flux a distance 75cm from the x-ray source (cm^{-2}), L, L_T, d_s and A are defined in Figure 5-3, x_p is the sum of d_s and L, M_{exit} and M_T are the magnification of the breast exit plane and target respectively, A_I, A_T, A_{FS} and A_D are the effective aperture areas of the image, target, focal spot and the detector respectively, μ_{breast}, μ_{target} and μ_D are the energy dependent linear attenuation coefficients of the breast tissue, target (i.e. calcification or lesion) and detector respectively, D is the effective thickness of the target, η_E is the fraction of incident photons of energy E absorbed in the detector, t_{det} is the detector thickness. E_p is the energy of primary photons, and E_s is the average energy of the scattered photons; these are approximately related by: $E_s \approx 0.95 E_p$ (Muntz 1985), δ_s is the effective scatter source distance, and (S_o/P_o) is the scatter to primary ratio at the exit plane of the patient. The complete proof of this model is given in Appendix D.

Photon flux rate

The photon flux rate (mA^{-1} s^{-1} cm^{-2}) at a distance 75cm from the x-ray tube is calculated using an algorithm of Birch and Marshall 1979, in which the attenuation of inherent and added filtration is calculated using the exponential attenuation law. That is,

$$\varphi_{75}(E) = \varphi_{75}^{0}(E)e^{-\mu_f(E)t_f}$$

<div align="right">Equation 5-15</div>

where $\varphi_{75}^{0}(E)$ is the flux rate before filtration (mA^{-1} s^{-1} cm^{-2}), μ_f is the linear attenuation coefficient of the filter and t_f is its total thickness. The inherent filtration is assumed to be equivalent to 0.3mm Al. Scatter from the filtration is neglected. There are some concerns about the quality of this algorithm, particularly in the calculation of the characteristic peaks, which are especially important for spectra from molybdenum targets. The use of trends when optimising the system (see below) should help overcome this problem although these concerns will reduce confidence when comparing x-ray tube target types using the theoretical spectra.

Total incident x-ray flux

The total incident flux (cm^{-1}) is approximated by:

$$\phi(E) \approx \varphi_{75}(E)\left(\frac{75}{d_s}\right)^{2}(I.t)\frac{f}{W}$$

<div align="right">Equation 5-16</div>

where f is the width of any collimating slot, W is the length of the breast to be scanned (assumed rectangular), $(I.t)$ is the product of the x-ray tube current and the exposure time (i.e. mAs), and d_s is the source to patient distance (SPD).

162

Patient dose

The average absorbed glandular dose is given by:

$$Dose = \int_E \phi(E)D(E)G(E)\,dE$$

Equation 5-17

where D(E) is the average absorbed dose per incident photon of energy E and G(E) is the fraction of this energy which contributes to glandular dose. The values of D(E) and G(E) used in this work have been calculated from Monte Carlo results. They are similar to the data of Dance 1980, giving agreement to within 5%. The mean dose to all tissues in the breast is estimated by setting G(E) equal to unity.

5.5 Assumptions made in the optimisation

The SNR of various targets have been optimised for a variety of input parameter, including exposure time and patient dose, using a simulated annealing algorithm described below. There are a number of assumptions made in the optimisation:

1. The observer and any automatic detection algorithms which could be used on the image are assumed to be ideal observers. That is, observers which integrate the noise over the image area. This assumption was used by Muntz 1979 in his description of a mammography system, and was found to give results which were reasonably consistent with experimental results (Muntz 1981).

2. It is assumed that the use of a relatively simple model of scatter will not strongly affect the trends seen in the optimisations. Similarly, it is assumed that the form of the relationship between focal spot size and tube loading capability dose not affect trends. It is accepted that these will affect absolute values - hence the advantage in using optimisation trends.

3. The optimum system is dependent of the size of the target being visualised (Muntz et al 1985). It is assumed that large targets have a sufficiently high SNR, that it is sufficient to optimise the system for smaller targets with lower contrast.

4. Increasing the SNR of a given target beyond a certain value does not necessarily increase its detectability. That is, if the SNR is sufficiently high that the target in question can already be detected, there is no advantage in further increasing the SNR. However, since for low contrast objects SNR $\propto$ (target thickness), it can be assumed that further increasing the SNR has the effect of bringing thinner calcifications into view. It is, therefore, assumed that optimising the SNR increases the detectability of low contrast targets.

5. It is assumed that neglecting the spatial frequency dependent nature of the detector's noise transfer characteristics, as described by a frequency dependent detective quantum efficiency, DQE(f), will not strongly affect the trends seen in the optimised system. It has been shown, however, that the presence of a secondary quantum sink caused by an inefficient optical system (for the example of a scintillating phosphor optically coated to a digital detector) can dominate at non-zero spatial frequencies and can significantly degrade the image (Cunningham et al 1994a and Cunningham et al 1994b). Although not experimentally proven, when applying the optimisation results to detectors with poor high spatial frequency noise characteristics it may be necessary to treat the detector as having a lower resolution than that which would be derived from its MTF. More experimental or simulation work is needed to evaluate the influence of this.

It should also be noted that the optimisation is for detail SNR and does not explicitly include reference to the system resolution as determined from its MTF, although resolution is included in terms of the effective apertures. Statutory resolution requirements may impose some restrictions on the chosen configuration.

5.6 Function Optimisation

There has been considerable interest in developing effective methods for optimisation. These techniques can be divided into two general classes (Pannatier 1990):

- local optimisation, where the neighbourhood of a starting solution is explored in the search for an optimal solution (iterative improvement methods, e.g. hill climbing)

- global optimisation, where the search for the optimal solution is carried out over all space.

The first class of optimisation technique tends to get trapped in the first local minima (or maxima) encountered, the position of which depends on the starting point of the algorithm, as can be understood from the graph below. This can be overcome by repeating the search with a large number of initial conditions, but this can soon result in unrealistic computation times. Alternatively, the algorithm could be allowed to move, in some limited way, in a direction which initially appears to be away from the minimum (i.e. moving in an uphill direction). In this way the algorithm can move through a sequence of local minima in search of the global minimum. One technique, which has this ability to escape local extrema, is that of simulated annealing.
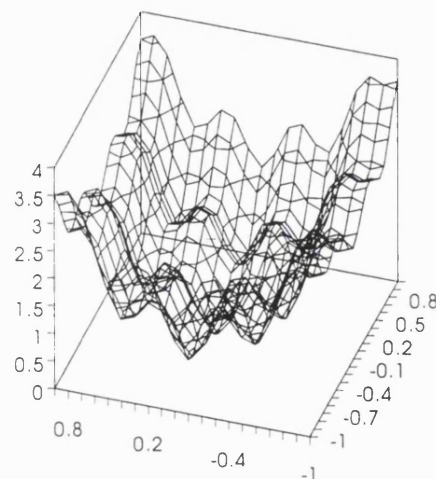
Figure 5-6 A function with various local minima

5.6.1 Simulated Annealing

Simulated annealing is a global optimisation algorithm which has been used for a variety of optimisation problems from planning radiotherapy dose distributions (Webb 1989) to investigating the classic travelling salesman problem (Szu 1987). It is based on the metallurgical process on annealing. When a molten metal is cooled its constituent atoms tend to move to relative lattice positions which minimise their potential energy. If the metal is cooled too quickly it is likely that, because of the large number of atoms and possible arrangements involved, the final state will only be a local energy minimum. If the metal is reheated and cooled at a slower rate it may move to a lower energy state - hopefully the global minimum.

The simulated annealing algorithm used in this work to minimise a function $F(x)$ with x restricted to membership of Ω, is given below. Note that a character in bold indicates a vector.

1. Set $T=T_{start}$, Select an arbitrary starting point x from Ω

2. Evaluate point x to give $F(x)$

3   Pick an adjacent point, x^*, at random

4. If $x^* \notin \Omega$ go to step 3, otherwise evaluate it and set $\Delta F=F(x^*) - F(x)$

5. Select x^* with probability $\exp(-\Delta F/T)$

6. Go to step 3 and repeat the cycle k times

7. Set $T=\alpha T$

8. If $T>T_{min}$ go to step 3

9. Finish

The starting point is chosen randomly and the objective function, which could be potential energy or patient dose, is calculated. A randomly chosen adjacent point is then evaluated, and the move accepted with a probability p. Again, this is for a *minimisation* problem, and shows that moves which reduce the objective function are always accepted; moves which result in an increase in the objective function are accepted if a random number drawn from a uniform distribution between 0 and 1, is less than p. In this way,

the probability of accepting a detrimental increment is always greater than zero, and less likely for larger increments; the algorithm can move out of local (and global) minima. A new random point is then found, and the process in repeated. The temperature is gradually decreased (the metal is cooled), thus gradually reducing the probability of accepting decremental increments. This continues until the temperature reaches some predetermined level, T_{min}, where the search is terminated. The choice of initial temperature, T, step size, Δr, and cooling rate, α, depend on the properties of the objective function and on the desired accuracy and resolution; these can significantly affect the efficiency and reliability of the algorithm as discussed below.

5.6.2 Choosing the optimisation parameters

Deckers 1991 found that practical experience with simulated annealing algorithms, as well as analytical considerations, showed that a reasonable value of T should be such that $0.5 < \exp(-\Delta F/T) < 0.9$; Probabilities much below 0.5 require too many function evaluations to escape from a local minima, while probabilities too close to 1 mean that virtually every step is accepted, giving an inefficient search. In this work a value of $T_{start} = 0.1$ was used. This meant that the initial search was somewhat random, becoming more defined as the optimisation progressed.

Similarly, a reasonable step size was found to be such that escape from a local minima is possible in 2-3 steps. The method of choosing an adjacent point used here is that of Bohachevsky et al 1986: If the number of variables in the optimisation is n, then n independent random numbers, $Y_1...Y_n$, are chosen in the range (-1,1) and the components of an n-dimensional position vector U are found:

$$U_i = \frac{Y_i}{\sqrt{\sum_{j=1}^{n} Y_j^2}}$$

Equation 5-18

167

The next point, **x***, to be tested is given by:

$$\mathbf{x^*} = \mathbf{x_o} + \Delta r \mathbf{U}$$

<div align="right">Equation 5-19</div>

where **x₀** is the current point and Δr is the step size. Some variables have more significant effects on F(x) than others. For example, a 1keV change in the x-ray tube potential has be a more significant effect than an increase in the filtration of, say, 1μm. For this reason Equation 5-19 was adapted such that the next point in direction i was then found from

$$x_i^* = x_{i0} + \Delta r_i U_i$$

<div align="right">Equation 5-20</div>

Suitable values of Δr_i, found with some trial and error, are given in Table 5-4.

The cooling program is also important. As in the real physical process, too fast a cooling rate can result in local rather than global optimisation. Cooling schedules of varying complexity have been proposed in the literature (Pannatier 1990), but the most common cooling law is the relatively simple decrement function first proposed by Kirkpatrick 1983:

$$T_t = \alpha T_{t-1} = \alpha^t T_0 \qquad t = 1, 2, 3, \ldots\ldots$$

<div align="right">Equation 5-21</div>

where alpha is a constant, usually such that $0.8 < \alpha < 1$. This has been found to perform reasonably well in practise, and is used here with a value of alpha of 0.9.

Symbol	Range	Typical value	Value used here	Description
T_{max}	Tmax>0	100	0.1	Starting temperature
T_{min}	Tmax>Tmin>0	0.1	0.001	Minimum temperature
α	0<r<1	0.9	0.9	Temperature decay rate
k	k>0	100	300	Time per temperature

Table 5-4 Typical parameters used in optimisation by simulated annealing

5.6.3 Testing and validation of the optimisation algorithm

The SNR of Equation 5-11 has been maximised for constant glandular dose using the constraints discussed above using the simulated annealing algorithm with the parameters given above. For a very limited selection of these optimisations the search was repeated using a very unintelligent (and calculation intensive) maximum search algorithm, which tested all points in a digital solution space for the maximum. These results were then compared to the simulated annealing results and found to give good agreement. Occasionally the simulated annealing algorithm was found to wander away form the maximum SNR, but the technique of looking at trends (as described below) meant that it was obvious when this had happened, and either a new estimate was made, based on the surrounding values and trends, or the optimisation was repeated.

Variable	Allowed values	Δr_i	Description
kVp	kVp>0	1 kV	X-ray tube potential
SPD	SPD>30	0.1 cm	Source to patient distance
M_T	such that air gap>0	0.01	target magnification
L_f	L_f >0	0.01 mm Al or 1μm Mo	thickness of filtration

Table 5-5 Step sizes used in optimisation by simulated annealing

5.7 Optimisation results

5.7.1 Optimisation of a 200μm calcification keeping magnification constant

In the first instance, consider the optimisation of the detail SNR of a 200μm calcification in a 4.2cm thick 'standard' breast, with the mean glandular dose restricted to a maximum of 0.5mGy. The composition of the calcification is taken as $Ca_5(PO_4)_5OH$. The x-ray tube has a tungsten target, 0.3mm Al inherent filtration, and a 300μm focal spot. The detector's response and resolution is approximately equivalent to a 100μm thick CsI phosphor screen (A_{det}=36000μm², equivalent to a Gaussian standard deviation of 54μm) and the image magnification is set to 1.4 to optimise the system's spatial resolution. This assumption of a 100μm thick CsI screen is close to the thickness used in this work (43μm. 67μm and 120μm, see chapter 3). The variables for this optimisation - tube voltage, thickness of added aluminium filtration and the source to patient distance (SPD) - are allowed to vary to optimise the SNR for a range of exposure times and detector widths. The results are shown graphically in Figure 5-7. Although the detector widths do not go as far as needed for a full area detector, the trends have already been established. Figure 5-7(a) shows the variation of optimum SNR with exposure time and

detector width. (b), (c) and (d) show the conditions of tube potential, filtration and source to patient distance needed to give the optimum SNR respectively. Figure 5-7(e) indicates the limiting factors for the various exposure time/detector width configurations.

It can be seen from Figure 5-7 that for a given detector width, the optimum SNR increases with exposure time. This is purely a consequence of the increase in total available x-ray flux, an effect which is most noticeable for small detector widths, as they only use a small fraction of the available x-rays. Conversely, the effect is relatively small for large detector widths, which use much more of the available flux and are consequently much less affected by the rate at which the x-ray tube can produce x-rays. The optimisation results are further explained by setting the exposure time to, say, 2s. As the detector width is increased, the SNR also increases as more and more of the available x-ray flux is used, and the image is less affected by the tube loading limitations. For a larger exposure time of 10s, flux limitations are less of a problem, and, as the detector width is increased from 0.4cm, the SNR is quickly seen to rise to a maximum, where it starts to be limited by factors like patient dose and, particularly, scattered x-ray degradation of the SNR. As the detector width continues to increase, the SNR falls slightly as the amount of scattered x-rays reaching the detector increases. The interactions between the processes involved are made clearer by examining the values of the optimisation variables (tube potential, filtration, SPD) which are needed to give this optimum SNR. For small detector widths and short exposure times Figure 5-7(b) shows the tube potential at a maximum value, as this increases both the available tube current, and the rate of production of x-rays, in an attempt to address the limitations

–
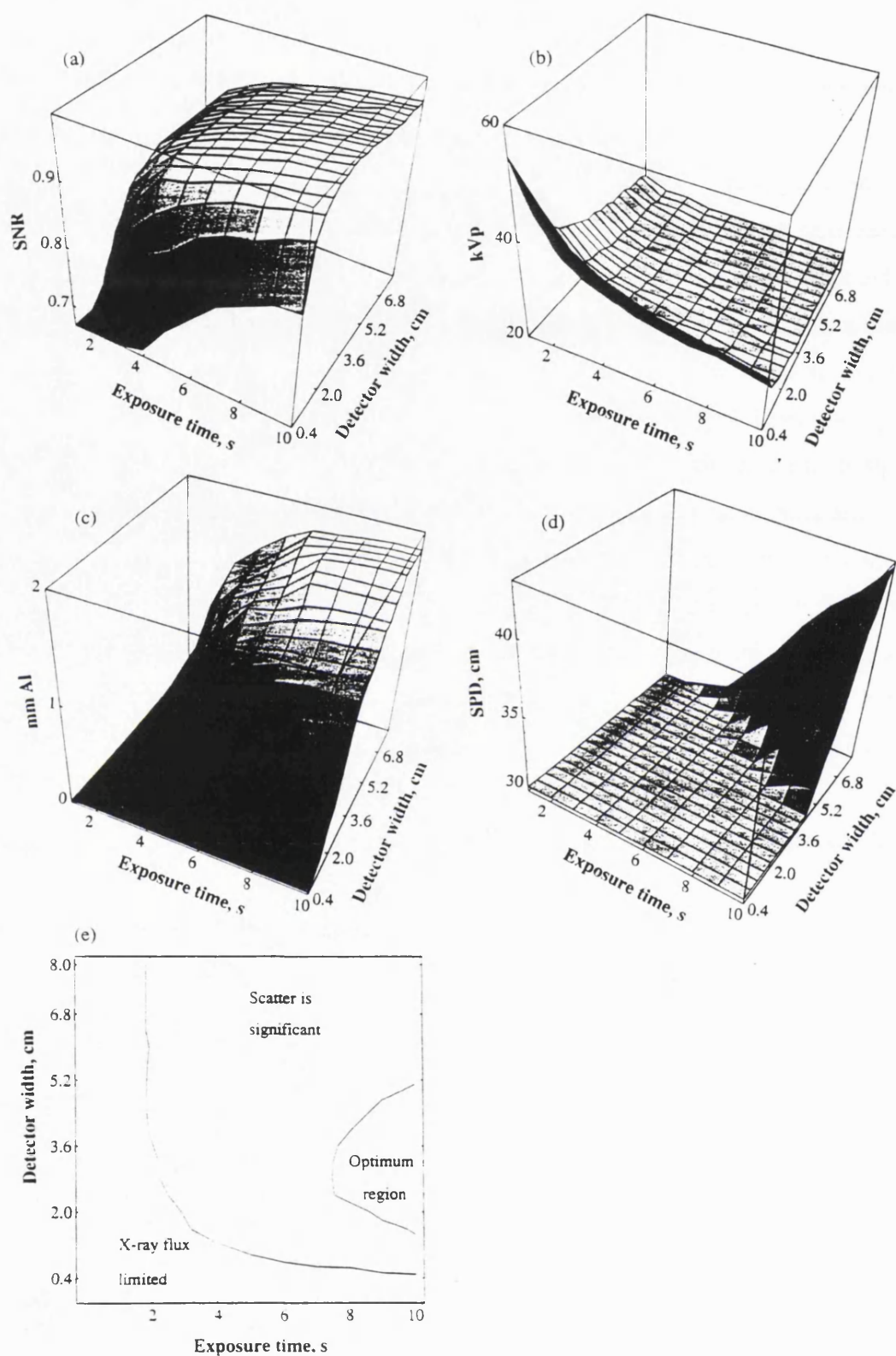
Figure 5-7 Results of the optimisations with magnification kept constant. See text for further details.

on SNR imposed by x-ray tube constraints. In this case, this is somewhat unsuccessful, and the SNR still drops dramatically for small detector width/short exposure time combinations. The significance of this can be reduced by using a tube with a higher power rating, as provided by, for example, a larger focal spot (the use of larger focal spots is discussed in section 4.2). As the detector width and/or exposure time is increased, the optimum tube potential drops rapidly towards a plateau region where, in this case, it has a value of 24kVp, where the x-ray flux limit is no longer the most significant factor. While the tube potential is at its peak value of 55kVp, the optimum solution has no added filtration, as shown in Figure 5-7(c) (although the inherent filtration is unaffected), in another attempt to maximise the number of available x-rays. As the detector width and/or the exposure time are increased and the x-ray flux becomes less of an issue, the amount of filtration therefore increases to better optimise the x-ray spectra. That is, more Al is added to impede low energy x-rays, which cannot get through the patient but simply serve to increase the patient dose. For most of the exposure time/detector width combinations shown the source to patient distance (SPD) stays at its imposed minimum of 30cm. However, as mentioned previously, for large detector widths/exposure times the influence of scatter of the detail SNR becomes a more significant factor. In this initial optimisation the magnification is fixed , so the air gap between the patient and the detector can be increased by making a corresponding increase in SPD. The optimised solution is seen to take this approach to increase the patient-detector air gap and so reduce the scatter flux reaching the detector, as shown in Figure 5-7(d). It is also worth noting that the rate of increase of added filtration with increasing detector width and/or exposure time slows significantly at the point where scatter becomes an important problem, and SPD starts to increase. This is because increasing the SPD, for a given exposure time and detector width, reduces the available x-ray flux; the filtration increase therefore reduces to accommodate this. For reduced magnification constraints (say 1.1), scatter becomes significant for smaller detector widths, and the SPD therefore begins to increase for smaller detector widths and shorter exposure times.

The results of this initial optimisation are summarised in Figure 5-7(e). It shows a reasonably distinct region which is flux limited and should, therefore, be avoided,

although, to some extent, increasing the tube potential, reducing the filtration and SPD do help maintain the SNR at the borders of this region. Figure 5-7(e) also shows a less distinct region for which scattered radiation has a significant effect on the SNR. The significance of scatter in this region is kept to a minimum by increasing the SPD. The optimum region is a compromise between efficient use of the available x-ray flux, efficiency of scatter reduction/rejection and the best x-ray spectrum. It should be noted that in this example the optimum region is not very distinct. For example, reducing the exposure time from 10s to 4s for a 2cm wide detector reduces the optimum SNR by less than 5%.

5.7.2 Optimisation of a 200µm calcification with magnification as a variable

In the second optimisation example, the system is essentially the same as that described above, but the exposure time is set to an arbitrary 4s, the magnification is treated as a variable - i.e. it is allowed to vary in the search for the optimum SNR - and now the optimisations are repeated for a range of detector widths and focal spot sizes. The results of this optimisation are shown graphically in Figure 5-8, with the optimum SNR shown in Figure 5-8(a) and the conditions of magnification, tube potential, filtration and source to patient distance needed to achieve this optimum SNR being illustrated in (b), (c), (d) and (e) respectively. Figure 5-8(f) gives a graphical summary of the results.

The trends in the results of this optimisation can be compared with those that have been seen before: increasing the detector width increases the efficiency of the use of the available x-ray flux, but eventually results in the detection of more scattered x-rays which can degrade the detail SNR; increasing the focal spot size, like increasing the exposure time, increases the amount of available x-ray flux, until for an 800µm focal spot, the x-ray flux limitation is no longer a problem, even for the smallest detector widths. For the larger detector sizes where the scatter x-ray flux can be important, once the focal spot is large enough that the available flux is not an issue, the optimised SNR is found to decrease with further increase in the focal spot size, as illustrated in Figure 5-8(a). This is because of the intimacy between system resolution and SNR: for a given magnification, as the focal spot is increased the system resolution is degraded and the
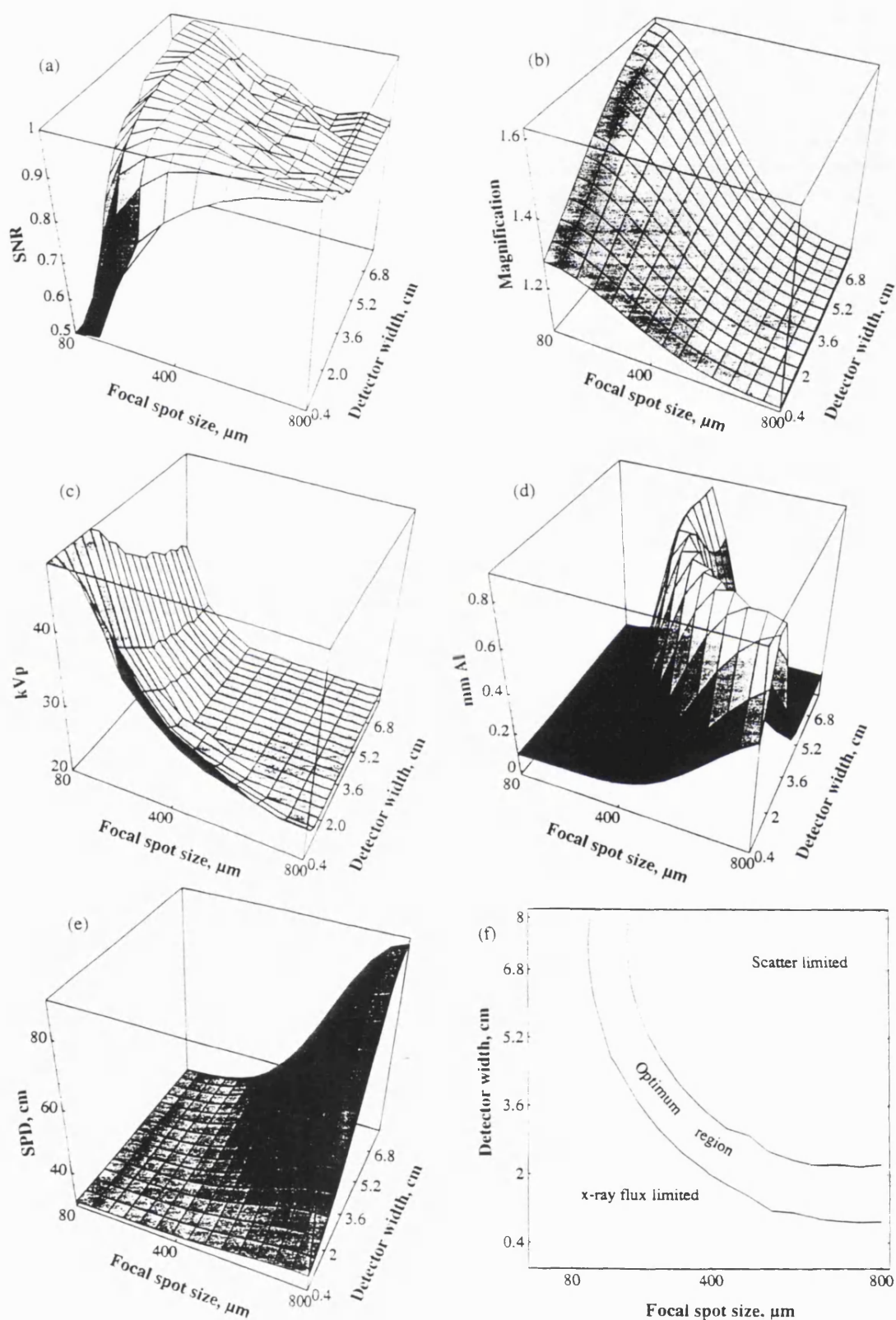
Figure 5-8 Results of the optimisation with magnification as a variable. See text for details.

signal is spread out over a larger area, increasing the amount of background noise. The SNR is then maximised by reducing the magnification, thus reducing the importance of the focal spot in the system resolution.

For the larger detector widths shown here, approximately 30% of this background noise comes from scattered x-rays. Reducing the detector width reduces this contribution and for larger focal spot systems (i.e. those for which less severe power limitations) a consequent increase in SNR is seen. As in the previous optimisations, Figure 5-8(c) shows that the tube potential has a high value for small detector widths in an attempt to increase the available x-ray flux. Where previously the tube potential was seen to peak for short exposure times, here it is seen to peak for small focal spot sizes which have a lower load capability and hence cannot produce as much x-ray flux as their larger counterparts. As the focal spot and/or detector width increases, the tube potential moves towards its plateau region; however, for the smallest focal spot sizes, flux remains a problem for all detector widths and the optimum tube potential is still 34kVp for an 8cm wide detector (4s exposure).

The trends of the image magnification are shown in Figure 5-8(b). As would be expected from resolution considerations, for large focal spot sizes the optimum magnification approaches unity and decreasing the focal spot size results in an increase in the optimum magnification. It is interesting, however, that these changes in optimum magnification are dependent on the width of the detector with a larger increase seen for the large area detectors than for slot scanning systems. To appreciate the significance of the detector width it is necessary to simultaneously describe the changes in added filtration and source to patient distance (SPD), as illustrated in Figure 5-8(d) and (e) respectively. Starting with the 800μm focal spot and 15x8cm detector the optimum magnification is found to be 1.05. Scatter, however, is a problem for such a large detector, and the optimum solution attempts to address this by increasing the SPD to a relatively large 85cm giving an air gap of 4.5cm. Such an increase in SPD could, alternatively, allow a simultaneous decrease in magnification but, in this case, the scatter reduction properties of an increased air gap is more important. If the detector width is decreased, the amount of detected scatter is also decreased, so the optimum solution

moves from the extreme of large amounts of scatter reduction towards optimising the spectrum by increasing the amount of added filtration, as shown in Figure 5-8(d). The SPD is simultaneously reduced to increase the available x-ray flux to help account for that removed by the filtration Eventually, when the SPD is at its imposed minimum of 30cm, the amount of available x-ray flux used does become a problem, and the amount of added filtration must be reduced to increase the available x-ray flux. A slight increase in tube potential is also seen.

For the 0.4cm detector a reduction in the focal spot size results in a reduction in the available x-ray flux. Added filtration is already virtually at zero, as shown in Figure 5-8(d), and Figure 5-8(e) shows the SPD to be at its minimum 30cm., so the only way to increase the available flux is to increase the tube potential. Increasing the magnification would result in slightly less efficient use of the available x-ray flux, and, therefore, is not initially an attractive solution. As the focal spot is further reduced, the advantages of increasing the magnification eventually overcome the disadvantage of the reduction in the efficiency of use of the available x-ray flux, and a small increase in image magnification is seen. Larger detectors (say 2cm wide) experience this swap over in priorities earlier on, and the magnification is found to increase for smaller focal spot sizes as the focal spot is decreased. For the largest detectors considered, increased magnification also offers a way of reducing the scatter flux at the detector.

It should be noted that statutory resolution requirements may impose added restrictions on the choice of system configuration. For example, an 800μm focal spot may give insufficient resolution and may therefore not be the appropriate choice.

5.7.3 The influence of the x-ray flux limitations on the optimum magnification

The influence of the available x-ray flux on the optimum magnification was further illustrated by carrying out optimisations both with and without limits on the x-ray flux. Figure 5-9(a) shows the optimum magnification for a system with 500μm pixels in which there are no x-ray tube power limitations, as might be experienced if the exposure time is infinitely long. The optimum magnification is seen to increase dramatically for small

focal spots. In this case the magnification for optimum SNR is similar to the magnification which maximises the system resolution. Figure 5-9(a) should be compared with Figure 5-9(b), which shows the optimum magnification for a system in which the flux is limited by a 4s exposure. Here, flux limitations have reduce the optimum magnification to 10% of the unlimited case. This shows that it is not sufficient to set the optimisation to that predicted on the basis of resolution assumptions alone. It also indicates that scanning systems are not ideally suited to magnification techniques.
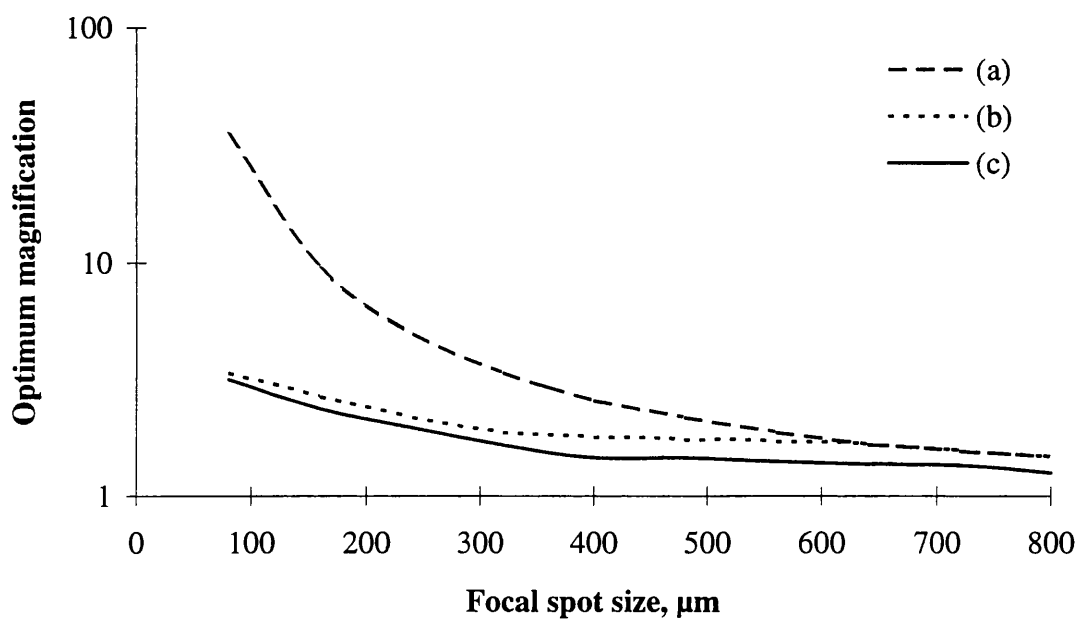
Figure 5-9 Influence of flux limitations of the optimum magnification. (a) no limitations, (b) 8cm detector width, 4s exposure, (c) 0.4cm detector width, 4s exposure

5.7.4 Optimisation of a full area detector

As shown above, even for the 8cm detector the optimum magnification can be severely restricted by the x-ray flux limitations. In this section the results of an optimisation in which the area of the detector is determined by the magnification are described. This means that any change in the magnification does not effect the efficiency of the use of the available x-ray flux, but results in an increase in detector size. The x-ray tube and other conditions are generally as given in section 5.7.1. The only differences are the effective

178

aperture of the detector is taken as $0.0002cm^2$ and a perfect grid is placed between the patient and the detector. The use of a perfect grid and its influence on the optimum configuration is discussed in section 5.7.6. The optimisations were repeated for a range of focal spot sizes and exposure times. The results of these optimisations are shown graphically in Figure 5-10, with the optimum SNR shown in (a) and the conditions of magnification, tube potential and filtration shown in (b), (c) and (d) respectively.

Many of the trends seen in the results of this optimisation can be compared with those that have been seen before. Increasing the exposure time results in an increase in SNR as the available x-ray flux increases and allows the system spectrum to be better optimised. For small focal spot sizes and short exposure times the tube potential increases and the amount of added filtration decreases in an attempt to overcome the x-ray tube flux limitations. As seen in Figure 5-10, this is only partially effective. In this set of optimisations increasing the magnification is not effected by the available x-ray flux and, therefore, an unhindered increase in magnification is seen as the focal spot decreases in size, giving an optimum magnification very similar to that predicted from resolution considerations. The amount of magnification is seen to increase as the focal spot size and/or exposure time increases. In this optimisation the SPD always remained at its imposed minimum as the presence of an anti-scatter grid between the patient and detector meant that there was no need to increase to reduce x-ray scatter.

This optimisation gives a good example of the advantages of using trend surfaces to display the results. Figure 5-10(a) shows that the optimum SNR increases by just over 10% when a small focal spot is used in a magnification configuration rather than a larger focal spot with no magnification. Considerations in the system design not included in the optimisation include resolution limits and storage space required for the image. With regards to the storage space the designer may consider a x4 magnification to give too large an image and may choose the low magnification option, even though this will result in a 10% decrease in optimum SNR. The designer will also have to consider the system resolution requirements if opting for the larger focal spot option.
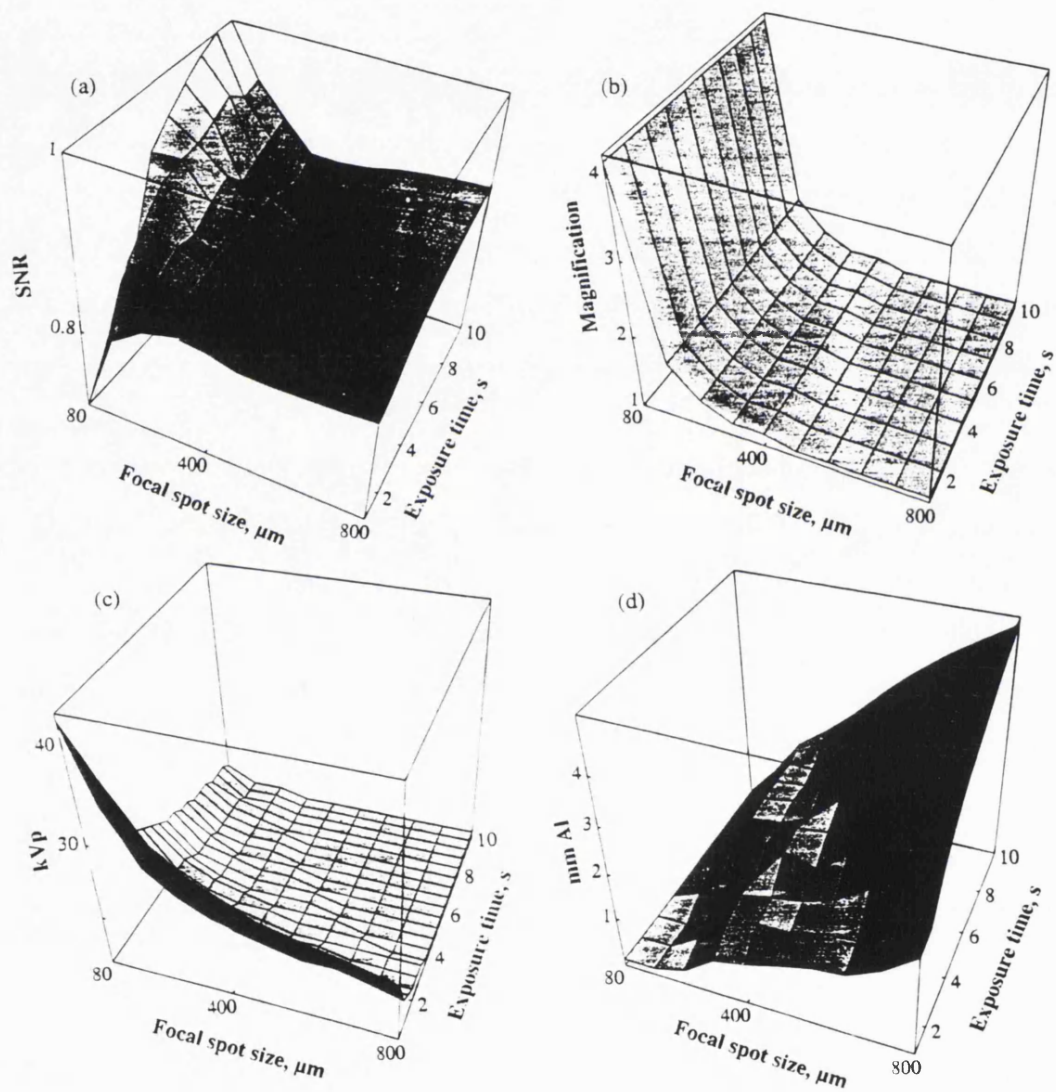
Figure 5-10 Results of the optimisations for a full area detector. See text for details

5.7.5 Effect of detector resolution and noise on the optimum system configuration

Detector resolution has a significant effect on the optimum magnification. For slit scanning systems this relationship is somewhat confused by the relationship between magnification and the efficiency of use of the available x-ray flux, as illustrated in section 5.7.3., whereas for large area devices added confusion is provided by the influence of scattered x-rays, and the possible need to provide an air gap to reduce the scatter flux reaching the detector. Noise density, in terms of detector noise per unit detector area can also affect the optimum magnification. These effects can be understood by considering four contrasting situations: slit detector with excellent resolution, slit detector with poor resolution, large area detector with excellent resolution and large area detector with poor resolution. The target magnification used with a detector with excellent resolution is typically close to unity as this minimises the blurring due to the focal spot. For a slit scanning system this small magnification is ideal as it also makes optimum use of the available x-ray flux. Very few scattered x-rays are detected and, therefore, it is not important that the detector is placed so close to the patient. For a slit detector with poor resolution, as illustrated above, the optimum magnification is very dependent on the available x-ray flux. If noise density of the detector can not be considered insignificant, then this also serves to reduce the optimum magnification as this reduces the image area. Detector noise is generally not significant in a slit scanning system, where x-ray flux limitations can be severe and dominate the system design, but is more significant for large area devices. For a particularly noisy large area device with poor resolution (say 500μm pixels), where 10% of the background signal is made up from equivalent detector signal, such as dark current in a CCD, then the optimum magnification can be 10% less than that of a noise-free optimisation. This reduction in magnification for noisy detectors is typically accompanied by an increase in SPD of a few centimetres to increase the air gap to offset the reduction in efficiency of scatter reduction caused by the reduction in air gap when the magnification was decreased. In the last example of a large area detector with good resolution the resolution is optimised for a magnification close to unity. In this case the optimum magnification when SNR is considered may be increased because of the degradation effect of scattered x-rays on the image. Typically, however, it was found that the optimum solution kept the magnification small, but not minimised,

such that an increase in SPD gave an increase in air gap. Different results were found when an alternative anti scatter mechanism, such as an anti scatter grid, were used.

5.7.6 Effect of an anti-scatter grid on the optimum system configuration

The influence of an anti-scatter grid placed between the patient and the detector or, equivalently, a series of collimating slits on the above optimisations was calculated by repeating the optimisations with the scatter flux set to zero. It was assumed that the grid was perfect and, therefore, allowed all primary photons to pass through to the detector, whilst stopping all scattered photons. There are two primary motivations for assuming a perfect grid, rather than using the well published characteristics of conventional grids. The first is that this can be treated as a multiple slit assembly (see, for example, Barnes et al 1976): such a system will allow all primary photons to pass through, but still have excellent scatter rejection characteristics. In this way, a 3cm detector can be considered as equivalent to a series of six 0.5cm detectors. The second justification for assuming a perfect grid is that the use of an air gap between the patient and detector, as is often the case for poor resolution large area detectors, allows the use of very deep thin septa, which will have characteristics very close to those of a perfect grid. It was found that the use of a perfect grid had no significant effect on the optimum x-ray tube voltage, but did effect the optimum magnification, filtration and source to patient distance. The effect for small detector/small exposure time/small focal spot combinations was negligible as scatter is already insignificant compared with other factors for these combinations. For large detector/long exposure times/large focal spot combinations where x-ray flux limitations are not important and scatter is often the dominant noise source, the effects on the optimum configuration were significant. The SPD was found to stay at its minimum of 30cm, and, where previously the filtration either virtually stopped increasing or even decreased, the amount of filtration continued to increase as the focal spot size, exposure time or detector width was increased, and the x-ray spectrum became progressively more optimised. For most system combinations the use of a collimating grid had little effect on the optimum magnification; the only exception to this was for a large area detector with excellent resolution, where there is no longer any need to increase the magnification as a means to increase the air gap and, therefore, help reduce

scatter. The most significant difference in SNR was found for large area good resolution detectors, where an increase of 10% was found. Large area detectors used in a magnification configuration also experienced increases in SNR, but the air gap already present meant that increased scatter rejection gave a less significant increase in SNR.

5.7.7 Effect of dose restrictions on the optimum system configuration

In all the studies described above the maximum mean glandular patient dose has been set to 0.5mGy. Broadly speaking, if the above optimisations are repeated for different doses, the same trends in the system parameters are seen, but the rates of change can vary significantly. The absolute values of SNR vary approximately as the square-root of the dose, although increasing dose for a slit scanning system has a lower increase in SNR than might be expected. This is simply because of the x-ray tube power limit problems already experienced with these systems - increasing the allowed dose tended to either result in a very high tube potential and very little filtration, which gives a far from ideal spectrum, or, eventually, the patient dose which gave the optimised image was not as high as the maximum allowed. Also, for an allowed patient dose of 2mGy, the relative importance of scattered x-rays on the optimum system was much reduced and only really became important when the detector width reached that equivalent to a full area detector. For a significantly reduced allowed patient dose of 0.2mGy, except for very small focal spots/short exposure time/very thin collimating slit combinations, power limits are no longer important. The amount of added filtration quickly reaches higher values of 3-4mm Al and the SPD starts to increase much sooner as the detector width and exposure times are increased. Slit detectors are, therefore, more efficient for low dose examinations than for high ones, as more suitable values of tube potential etc. can be used. For this reason, these detectors showed a lower reduction in SNR with reduced dose than predicted by a square root of patient dose relationship. It is also interesting to compare the optimum system for total and glandular dose situations. The optimisations described in section 5.7.2. were repeated using 1mGy total dose instead of 0.5mGy glandular dose. The main difference between the two dose optimisations was found in the amount of added filtration, as shown in Figure 5-11; a slight difference in tube potential was also experienced. For the total dose optimisation the amount of added

filtration is significantly higher than for the glandular dose optimisation. This is in response to the standard breast model used in this work which has an outer 0.5cm thick layer of fat. Many of the low energy x-rays are absorbed in this layer and, therefore, do not contribute to the glandular dose. They do, however, contribute to the total dose. The result of this is that a greater emphasis is placed on removing low energy x-rays from the incident spectrum for total dose models than for glandular dose models. This is accompanied by a slightly higher tube potential for the total dose optimisations - this is partly in response to the slightly higher average x-ray energy needed for the total dose optimisation and also to increase the average x-ray flux to account for the higher energy x-rays removed by the extra filtration.
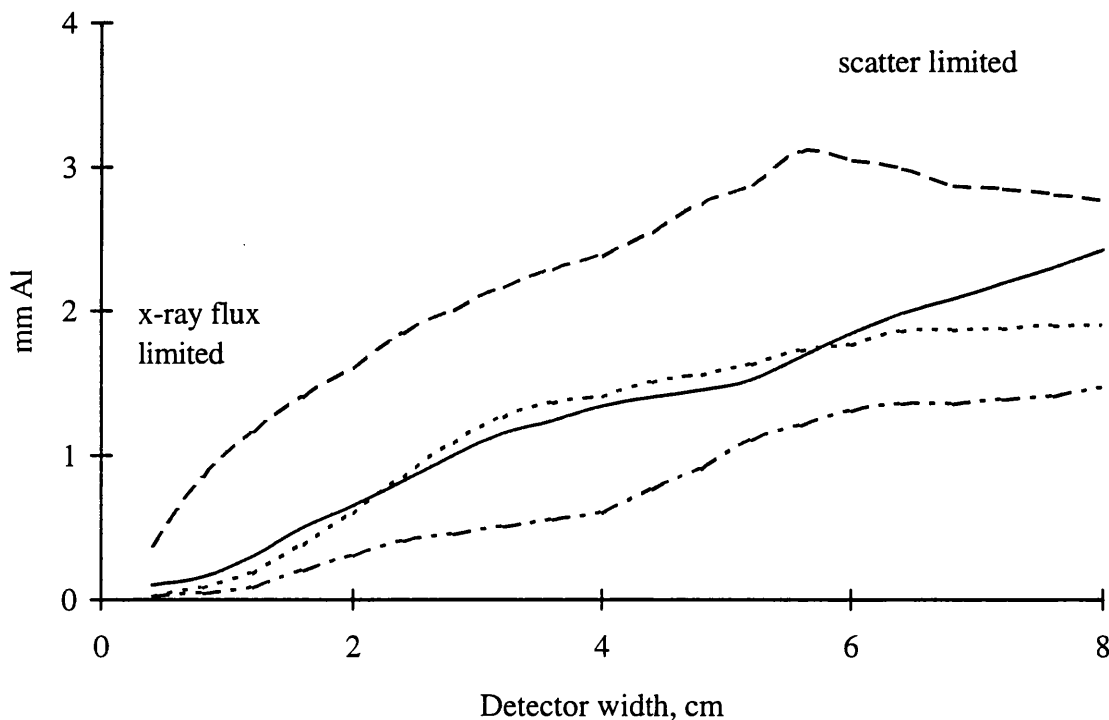
Figure 5-11 Effect of dose restriction on optimum amount of added filtration

5.7.8 The effect of breast thickness on the optimum system configuration

If thicker breasts are considered then the trends are all as discussed above. The main difference is the need for a more penetrating x-ray spectrum, which results in higher tube potentials and more. The increase in breast thickness from 4 to 6cm is known to increase

the scatter-to-primary ratio at the exit plane of the patient by approximately 50% (see section 5.3.3). The influence of this on, for example, SPD and air gap was found to be quite small because of the simultaneous need to better filter the incident x-rays, and is insignificant for poor resolution detectors where the air gap is already reasonably large.

5.7.9 The choice of x-ray tube target

Finally, the relative merits of tungsten, molybdenum and rhodium targets should be discussed. This has been the subject of much work over the last 20 years (Marshall 1975, Jennings 1981, Maidment et al 1993....). Some modern film-screen mammography units use a dual metal anode such that different spectra can be used for different breast thicknesses and/or compositions. The first target is molybdenum, with the second target being either tungsten or rhodium. In general, the spectrum of a molybdenum target with molybdenum filtration has been considered to be the choice for the thinner breasts (less than, say, 5cm) with a harder spectrum such as that produced with a tungsten target with aluminium filtration being more suited for thicker breasts (see, for example, Marshall 1975). Additional considerations include the range of intensities experienced at the exit plane of the patient, which can be larger for molybdenum than tungsten spectra thus requiring a larger detector dynamic range (Maidment et al 1993), although shaped filters may alleviate this problem. The most important factor for scanning systems has been shown above to be the power rating of the tube. Typically, tungsten tubes have a higher power rating than molybdenum tubes and are thus more suited for scanning systems, even for thinner breasts. This was found to be the case in the optimisations carried out for this work but this was not always the case if a hypothetical increase in power rating was used for the molybdenum tube. As well as the assumed power ratings other factors which affect these comparisons include the limitations of the Birch and Marshall algorithm (Birch and Marshall 1979). In spite of these notes of caution the argument for using a tungsten target with scanning systems is supported in the literature, including the theoretical optimisations of Fahrig et al who used an alternative spectra model, and the experimental results of Maidment et al who found that a scanning mammography system using a tungsten target x-ray tube gave comparable image quality to conventional systems. Indeed, even for a large area system for which power rating has been shown to

have a reduced significance, Jennings showed that film-screen and xeromammography techniques can be performed optimally with a tungsten x-ray tube and appropriate filtration (Jennings et al 1981). There is a argument for using rhodium, or some other K-edge, filtration with the tungsten target as this takes advantage of the power rating of the tungsten anode while providing a spectrum with a relatively low average energy. Although this combination is not described here, the trends detailed above are applicable to the design of such a system.

5.8 Conclusions

A large number of multidimensional optimisations have been described for different digital mammography configurations and requirements, with the aim of maximising the image quality. These optimisations have been used to demonstrate the relative importance of factors like the amount of detected scatter and x-ray tube power limits on the image quality for different system designs. They have illustrated possible solutions to various mammography imaging problems. For example combinations of a larger focal spot/increased slit widths/low magnification/increased tube potential/reduced added filtration/increased exposure time and low SPD have been shown to be useful in overcoming flux limitations for scanning systems. It has been shown that x-ray tube power limitations can have a strong limitation on the optimum magnification, particularly for scanning systems, with the result that poor resolution detectors are not suited for use in scanning systems. This is because an increase in magnification gives a reduction in the efficiency of use of the available x-ray flux and, therefore, can give a reduction in SNR. It is, therefore, not always appropriate to optimise the magnification based on resolution assumptions alone. Large focal spot/high resolution detector combinations have been shown to be particularly useful for scanning systems. For a system in which the detector size is limited by, for example, the area of a CCD, it may be possible to significantly reduce x-ray flux problems by using a relatively large focal spot together with a high resolution scintillator. For full area systems these limits are less of a problem and instead some constraint on the magnification may be imposed by detector noise although, if detector noise is neglected, the optimum magnification is similar to that calculated from

optimum resolution assumptions alone. In this case, unlike for scanning systems, there in no disadvantage in using small focal spots - providing that the power limits are not too restrictive, as can be the case for very small focal spots - as, when used with image magnification the improvement in resolution gives an associated increase in SNR. It has been demonstrated that, in many cases, appropriate optimisation can reduce the influence of using seemingly inappropriate system configurations, such as large focal spot sizes or detector widths, so that the detail SNR is reduced by less than 5-15%. This is significant as it allows the designer to consider other problems such as resolution, image storage space, cost and the availability of equipment.

Other factors which have been described above include the influences of allowed patient dose and type of dose (i.e. total or glandular).

Application of the optimisation results to a TDI CCD digital mammography system

The CCDs used in this work (EEV CCD15-11) are approximately 7mm wide in the scanning direction. The optimisations above indicate that the optimum system will have the following configuration, probable values are given in italics:

- Tungsten target x-ray tube
- Relatively large focal spot   *800μm*
- Relatively high x-ray tube voltage   *35kVp*
- Relatively low amounts of added filtration   *0.5mmAl total*
- Small source to patient distance   *30cm*
- Minimal patient magnification   *close to unity*

The main emphasis is in overcoming x-ray tube power limitations. The influence of scattered x-rays on the optimum system is negligible.

6. EVALUATION OF PHANTOM IMAGES

The theoretical analysis of chapter 5 is useful for predicting the optimum configuration of a digital mammography system, for indicating probable sources of degradation of the detail SNR, and for indicating possible methods of overcoming these degradations. This analysis may not always be sufficient and some experimental 'fine tuning' may be necessary to fully optimise the system. Reasons for this include differences in predicted and real x-ray fluxes. In this chapter it is shown that many of the effects described in chapter 5 can be demonstrated experimentally. These include the degrading effect of scattered radiation on the image quality and the use of increased tube voltage or reduced SPD to reduce x-ray tube power limitations. One of the aims of this chapter is to provide a reasonably simple quantitative method of experimentally evaluating the system's image quality and to show how the theory of chapter 5 can help explain the experimental results.

This chapter, therefore, begins by describing some alternative methods of evaluating image quality, most of which are subjective and require either a large number of viewers, a large number of images or a combination of both. Two alternative qualitative techniques for image evaluation are then discussed, followed by some experimental results. The use of the theoretical optimisations to help provide a strategy for the experimental optimisation of a given digital mammography system is then described. Finally, optimised system configurations are evaluated in a subjective manner to allow comparison with typical current of film-screen based systems.

6.1 Methods of evaluating image quality

Some of the difficulties in connecting ideal observer performance with real human performance have recently been discussed by Metz et al 1995. The DQE(f) provides a full description of the transfer of both signal and noise through the detector and,

therefore, contains information relating to the image quality for a range of targets. For example, the high frequency DQE(f) indicates how well the detector can image the shape and structure of microcalcifications. Unfortunately, the link between DQE(f) and image quality is not trivial and an alternative method of evaluating image quality is needed to provide an evaluation of the potential diagnostic quality of the system in a less ambiguous fashion.

The diagnostic accuracy of an imaging technology can be defined as the "extent to which radiologists (or physicians) image-based diagnoses agree with patients' actual states of health or disease" (Metz 1995). A useful measure of diagnostic accuracy is provided by receiver operating characteristic (ROC) analysis (Metz 1978) which separates differences in discrimination capacity. Eventually, when a clinical digital mammography system is available an ROC study must be carried out to compare its performance with conventional systems, in the same way the use of 'Fuji plates' has been evaluated in Leeds. These studies, however, can be time consuming and are not always suitable for evaluating prototype systems or for experimentally optimising a given system, and other methods must be found. Possible alternatives include threshold-contrast detail-detectability (TCDD) tests and phantom scoring, both of which are carried out in a subjective manner with observers viewing a suitable test phantom containing various objects and scoring the number of visible objects. Although these techniques are appropriate for use with phantoms and can be used to give a comparison of different imaging systems, where a higher phantom score might indicate a better imaging system, they suffer from a number of problems. Firstly, their subjective nature means that, as with ROC analysis, they can be time consuming and are not suitable for experimental optimisation of the system. Secondly, they rely on the phantom to give changes in score which are realistically and sensitively related to diagnostic quality. When comparing system scores evaluated with different phantoms, there is also some concern regarding the variable quality of the phantoms, such that the same objects in one phantom may be easier to detect than the same objects in another phantom (Chakraborty and Eckert 1995). For quality control tests on a given system phantoms are adequate and a reduction in score will generally indicate a reduction in image quality caused by, for example, a degradation in the x-ray tube output. Here, these concerns are neglected and

it is assumed that commercial phantoms are reasonably realistic, with the provision that it may be appropriate to design a phantom exclusively for optimisation work some time in the future.

Two phantoms are used in this work: The "Barts" phantom, described by White and Tucker 1980 and the TOR[MAX] phantom developed by FAXIL at Leeds. The "Barts" phantom, shown in Figure 6-1, consists of low contrast cylinders, cubes and filaments embedded in a 50:50 fat:water substitute material. It also contains a step wedge and simulated calcifications. It is acknowledged that this phantom is probably not sufficiently sensitive for comparison of modern mammographic systems (IPSM 1989), but was found to be sufficiently sensitive to tube voltage and amount of added filtration to be used in this work. The TOR[MAX] phantom, illustrated in Figure 6-2, consists of a thin plate containing high and low contrast resolution gratings and various low contrast objects. Many other phantoms are available, seven of which were evaluated by Faulkner and Law 1994, who concluded that no single phantom was clearly superior to all the others.
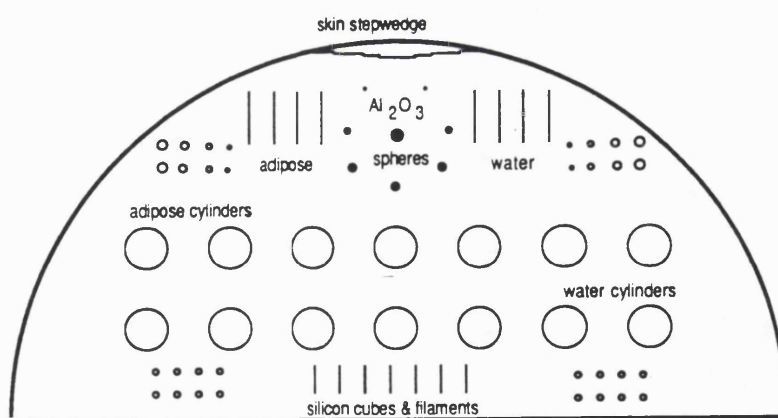
Figure 6-1 Main details of the White and Tucker ("Barts") phantom
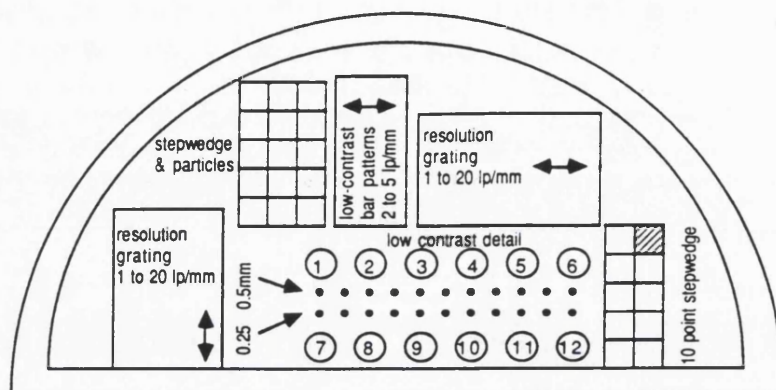
Figure 6-2 Main details of the TOR(MAX) phantom, after Cowen et al 1989

6.2 Quantitative evaluation of phantom images

The signal to noise ratio (SNR) of an object is known to be related to its detectability One method of evaluating an image, therefore, is to measure the SNR of the objects within that image. In this work two methods have been used to evaluate the SNR of given objects. The first, and simplest, method is appropriate for use with objects which give shadows which are large compared with the effective aperture of the imaging system. That is, with large objects for which the system resolution does not have a significant influence on the SNR. The second method is used for small objects for which the system resolution does degrade the SNR. Other quantitative methods for evaluating mammography phantom images have recently been discussed by Chakraborty and Eckert 1995 who devised a technique which gave good correlation with subjective scoring. Their method is not appropriate for use here, however, as the quantitative score must first be fitted to the subjective scores. This also means that their results are specific to the phantom type used.

6.2.1 Method 1: Evaluation of the SNR of large objects

For a single image of the selected object, the signal from six regions of interest (ROIs) in the object and from six ROIs in the background were used to calculate the mean signal levels, S_O and S_B and standard deviations, σ_O and σ_B.
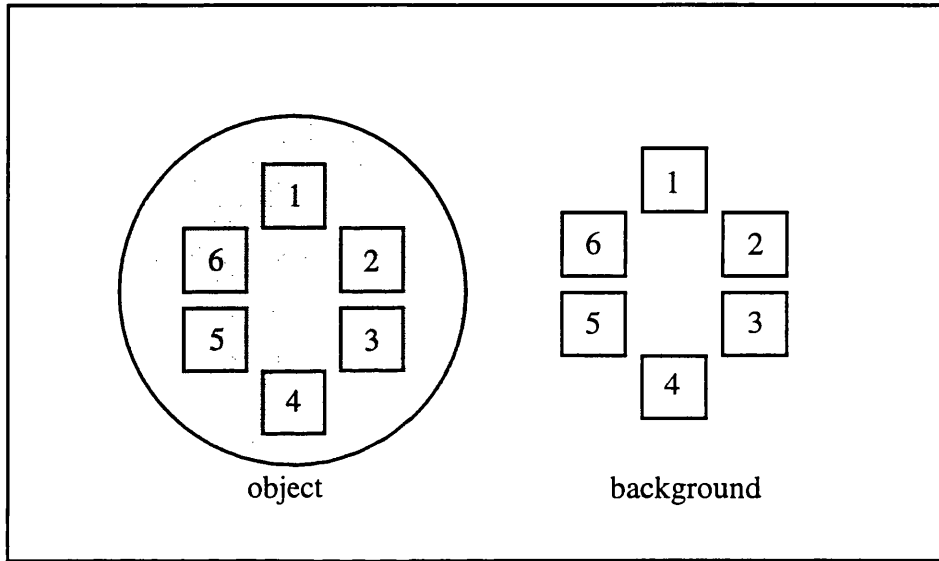
Figure 6-3 Schematic of ROIs used in SNR calculation

The SNR is then calculated using

$$SNR = \frac{S_o - S_B}{\sqrt{\sigma_o^2 + \sigma_B^2}}$$

Equation 6-1

This method is illustrated in Figure 6-3.

6.2.2 Method two: Evaluation of SNR of small objects

The SNR of relatively small objects can be significantly influenced by the system resolution as it spreads the signal out to cover an increased area. The method described above is not appropriate for these objects as it is not sensitive to these changes.

If the area over which the noise should be integrated is taken as the area of the shadow of the object, as in the theory of chapter 5 and appendix D, then the first step in calculating the SNR is to find this area. Noise in the image means that this is not a trivial task and simple techniques such as thresholding can not be used. The algorithm found to work best makes the assumption that the object is circular, and searches for the central coordinates for which the smallest circle can be drawn which gives the same signal as a much larger circle, where the signal is defined as the average signal in six ROIs in the background subtracted from the signal in the circle surrounding the object. If the circle is too small or if its centre is displaced from the centre of the object shadow it will not enclose all the signal. This is illustrated in Figure 6-4(b) and (c). To increase the accuracy of this technique, several images were added together to reduce the image noise, typically using an effective mean glandular dose of 20mGy. Once the position and area of the object shadow is known, an image with realistic dose (1mGy) is taken. The signal in the object area is calculated, and subtracted from the average signal from six ROIs of equal area in the background to give the effective signal. The background noise, σ_B is calculated from these six ROIs. This is repeated for six images and the SNR found using Equation 6-1, with the variance being the average variance from the six images and the effective signal being the average effective signal from the six images. It is assumed that σ_O is equal to σ_B. The variance was averaged (i.e. not summed) over the images to remove effects due to image-to-image variations in the incident x-ray flux. Although image-to-image variations were not generally significant for the molybdenum target x-ray tube, they were found to be significant for the tungsten target x-ray tube.
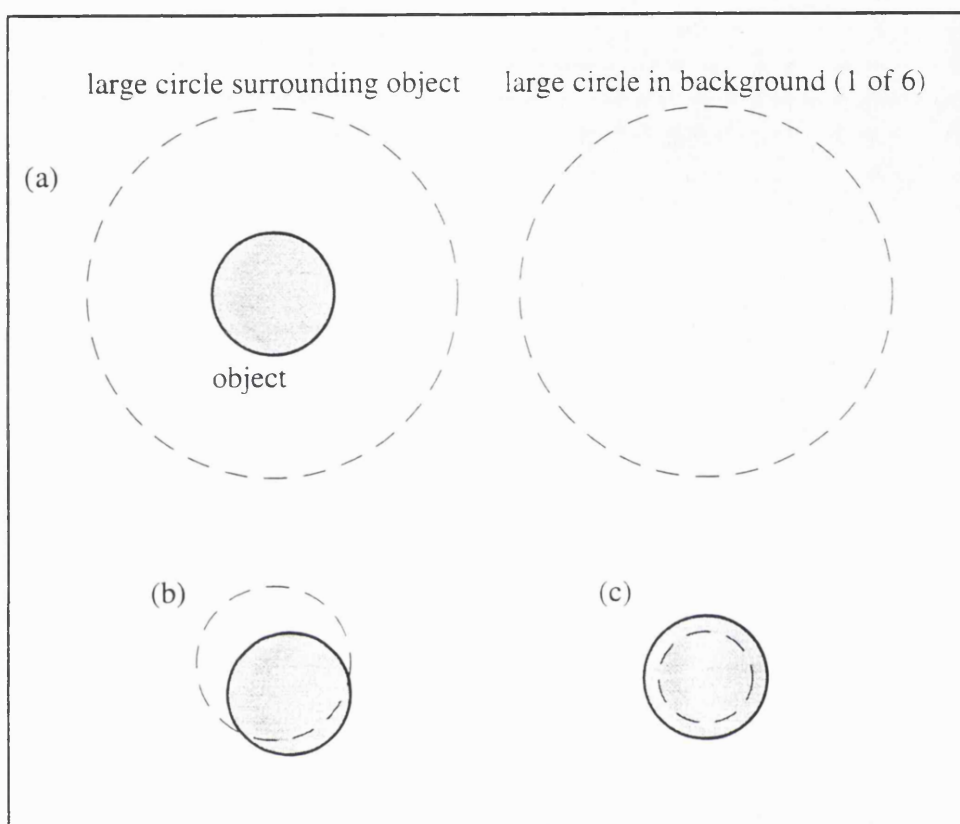
Figure 6-4 Schematic of algorithm to estimate object area

An example of an image where the object area has been identified using this technique is shown in Figure 6-5.
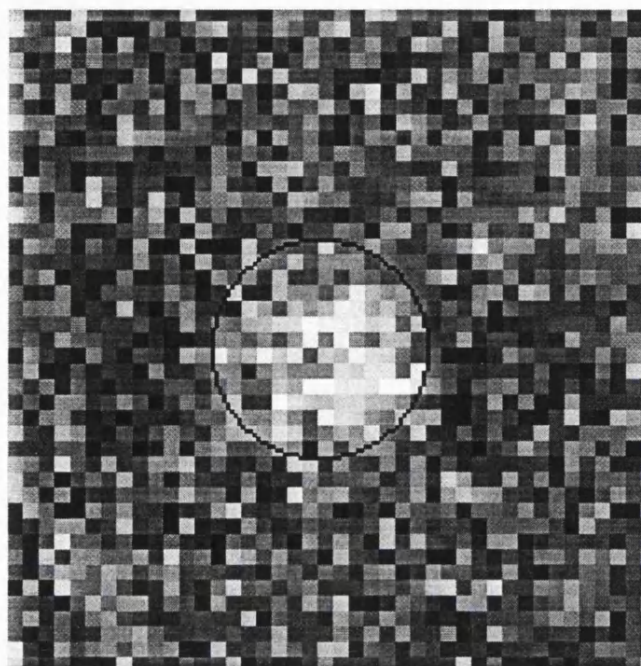
Figure 6-5 Image with object identified using algorithm described in text
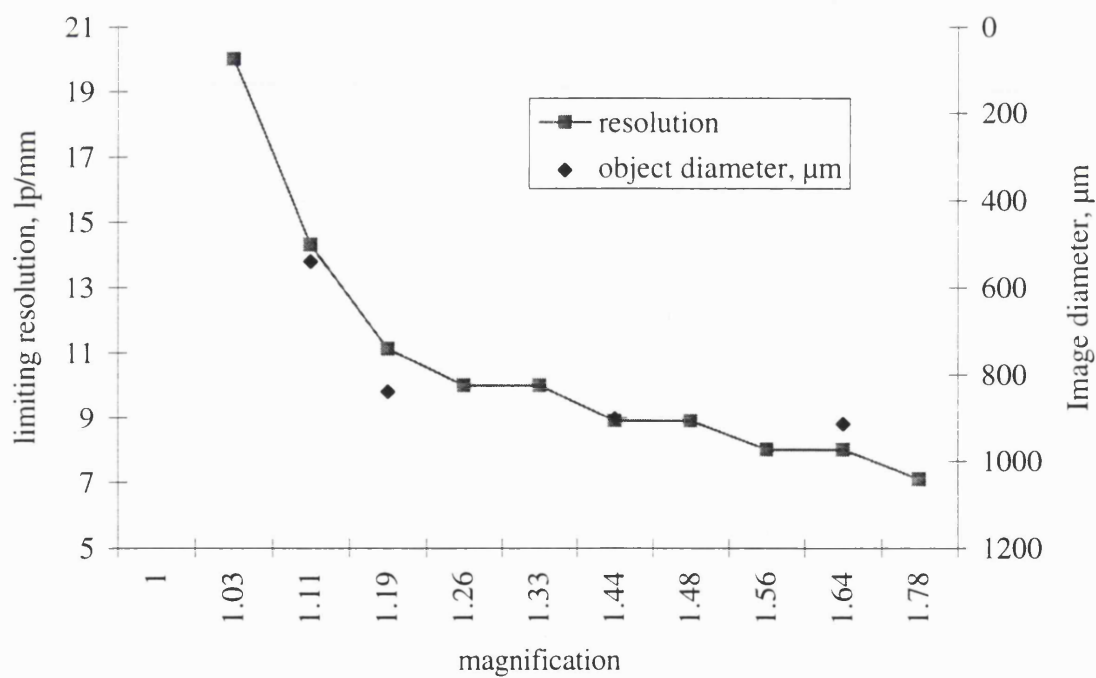
Figure 6-6 Variation of resolution and object diameter with magnification

The system resolution for CCDb (43μm CsI coating), found using bar patterns in the TOR[MAX] phantom, is compared with the estimated image object area (expressed in the object plane) in Figure 6-6 for a range of target magnifications. The object used is the 500μm detail in the TOR[MAX] phantom with the highest contrast. It can be seen that the estimated image diameter follows the same trends as expected from the limiting resolution measurements. The areas are, however, larger than might be expected from the limiting resolution measurements if the Point Spread Function was Gaussian. This difference is attributed to the shape of the system PSF, which can have large tails. This also applies to the individual focal spot and detector PSFs. Figure 6-7 shows an experimental LSF for CCDb (43μm CsI coating). The measurement technique is described in chapter 4.

distance, pixels
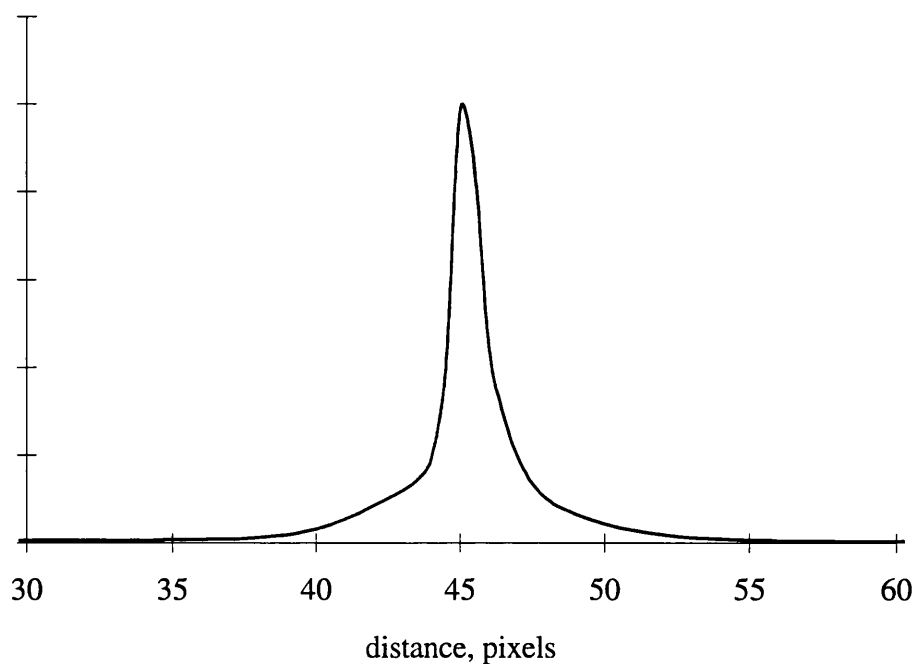
Figure 6-7 LSF measured for 43μm CsI coated CCD

6.3 Experimental details for the evaluation of phantom images

6.3.1 Patient dose

Average glandular dose can be calculated from the phantom incident air kerma without back scatter using conversion factors calculated by Dance 1990. The conversion factors are dependent on breast thickness, and half value layer (HVL). The breast thickness was taken as 4.5cm. The HVL and incident kerma was measured for both tubes for all values of tube voltage and added filtration using the standard method described in Johns and Cunningham 1983. If K_{100} is the air kerma at 1m and g the conversion factor of Dance 1990 the mean glandular dose for the standard phantom, D_{glan} is given by

$$D_{glan} = gK_{100}\left(\frac{100}{SPD}\right)^2 It$$

<div align="right">Equation 6-2</div>

where It is the mAs. When the influence of a collimating slot is included the mean glandular dose of Equation 6-2 is multiplied by a factor (f/W) where W is the length of the breast to be scanned and f is the slot width.

When using the tungsten tube which has a constant tube current, the SPD is adjusted such that the incident kerma gives the required patient dose. With the molybdenum tube, and the CCD operated in stationary mode, a value of SPD is selected and the mAs adjusted appropriately. The only restriction is that the exposure time is less than approximately 2s, as increased integration times are associated with excessive dark current.

6.3.2 Correcting the image

For Equation 6-1 to give correct and self consistent results it is important that all fixed pattern type noise sources are either removed or corrected for. It has already been shown that fixed pattern noise due to pixel to pixel response and dark current variations can dominate the image noise for large fluxs or exposure times (see chapter 3). This source of noise is reasonably easy to remove using the flat fielding algorithm of chapter 1. Another source of noise experienced with the slot scanning system was a slow variation in x-ray tube current with time, giving a variation in intensity across the image. In this case it was found that this source of noise could generally be adequately removed by fitting the pixel values along a column for the rows which match the object position to a straight line, using a least-squares-fit algorithm, and then correcting the image to give a constant level. A straight line is only appropriate for corrections over small distances (e.g. the 0.5cm of the object) - a higher order polynomial may be more appropriate when correcting an entire image.

6.4 Experimental results of experiments to quantitatively evaluate phantom images

6.4.1 Influence of air gap on SNR

The influence of the size of the air gap between the patient and the detector on the SNR was investigated using method 1, described above, with the CCD system in stationary mode using the molybdenum target x-ray tube with inherent molybdenum filtration, 28kVp and mean glandular dose of 1mGy. The SPD was set to 60cm. The object for which the image SNR was calculated was the adipose cylinder with maximum contrast in the "Barts" phantom. The source-to-patient distance (SPD), air gap and mAs were varied to keep a constant target magnification of 1.42. The results are shown in Figure

6-8 where they are compared with theoretical results using Equation 5-11 of chapter 5 (with $\delta_s= 13$, $S_0/P_0=0.6$, see chapter 5 for further details).

The theoretical results are multiplied by an arbitrary constant. As expected, the SNR increases with increasing air gap as less scattered radiation reaches the detector. This results is far from new, but this experiment shows that the effect is simple to measure using a single image of a single object and points the way for a simple quick strategy for experimental optimisation of the system. The errors on the experimental results are ± 1, calculated by repeating the 15cm air gap results 5 times.
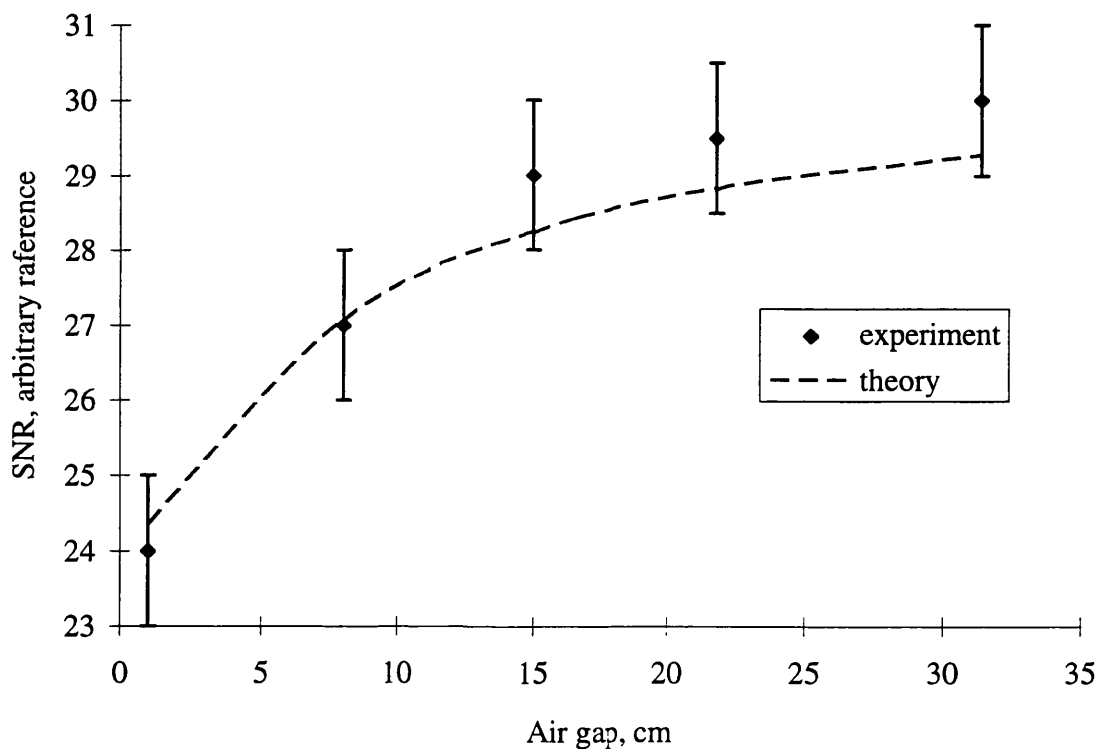
Figure 6-8 Comparison of measured and theoretical variations in SNR with air gap

6.4.2 Influence of tube voltage on SNR

The influence of tube voltage was investigated using method 1, using the slot scanning system with the tungsten target x-ray tube. Two experiments were carried out, one with a minimum SPD of 50cm and one with a minimum SPD of 30cm. If the dose calculations required a lower SPD that the minimum permitted, the SPD was set at the minimum. These points, therefore, have a lower dose than the maximum allowed dose (1mGy). The results of this experiment are given in Figure 6-9, where they are compared with theoretical results, normalised to the experimental results for 40kVp. The SPD necessary to give a 1mGy dose never reaches 30cm, and, therefore, a minimum SPD of 30cm has no effect on these results. The SNR can be seen to increase as the tube voltage decreases. Although the same shape is seen for the theoretical results, the increase in SNR with decrease in tube voltage is seen at significantly lower values of tube voltage. This disparity between theoretical and experimental results, which was not experienced when the measurements were repeated with the molybdenum target x-ray tube, is attributed to differences between the theoretical and real tungsten spectra. The main cause of this is the type of rectification used. i.e. the generator used here uses full-wave rectification with little or no smoothing, while the theoretical spectra is based on a constant tube voltage. The variation in peak voltage with time for this x-ray tube measured from the spectrum using a Keithley kV divider is shown in Figure 6-10 for a set tube voltage of 100kVp. Note that the minimum voltage measurable with this meter was 40kV.

The offset in voltage between the theoretical and experimental results (at 36kVp) is approximately 9kV. If the tube voltage is taken to vary as the modulus of a sine wave then the average tube voltage is $(2/\pi)$ times the peak voltage (kVp), giving an expected offset between theory and experiment of 13kV (at set tube voltage of 36kVp). This extra difference between theoretical and observed offset is attributed to smoothing at lower tube voltages not shown in Figure 6-10.
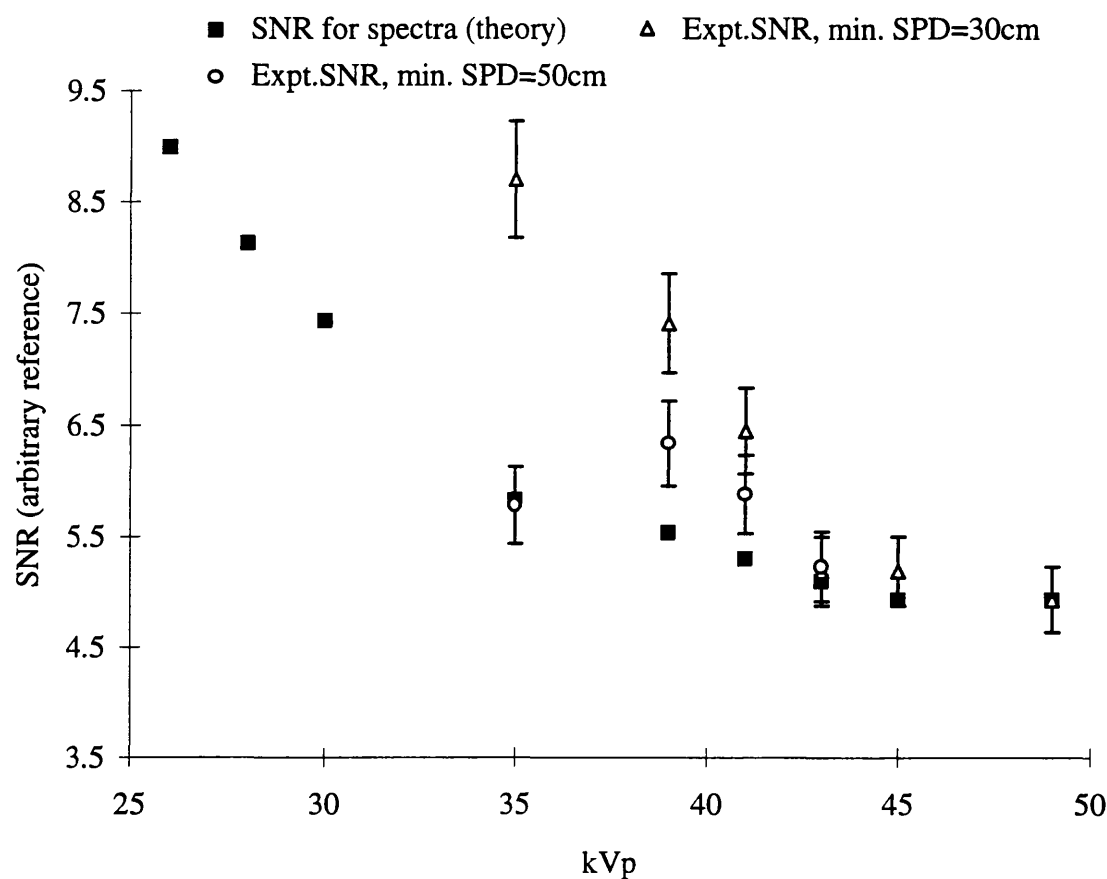
Figure 6-9 Influence of tube voltage on SNR
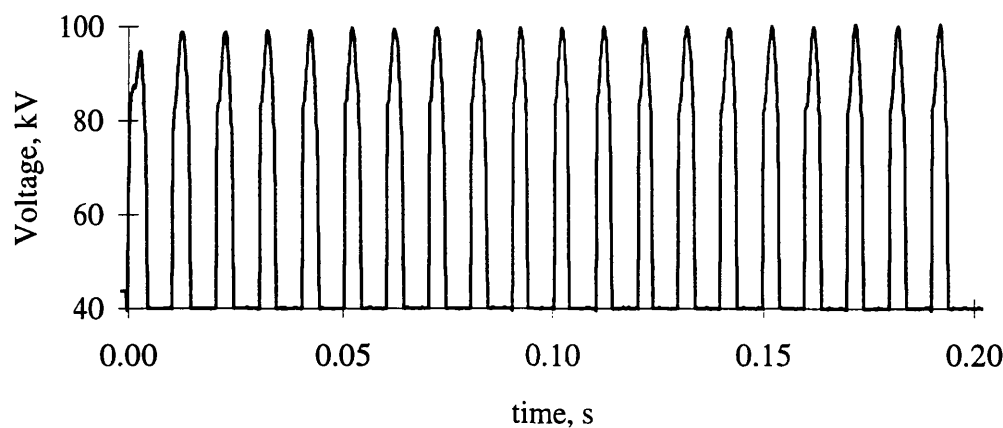
Figure 6-10 Variation of tube voltage with time

At high values of tube voltage (above approximately 48kVp) the experimental SNR for a minimum SPD of 50cm is the same as that for a minimum SPD of 30cm. As the tube voltage is decreased eventually the x-ray tube cannot move close enough to the patient to provide enough x-rays and an associated decrease in SNR is seen.

6.4.3 Influence of added filtration on SNR

The above experiment was repeated, again using method 1, for a range of thicknesses of added filtration for 36kVp and 40kVp. Figure 6-11 shows the measured effect of adding filtration.
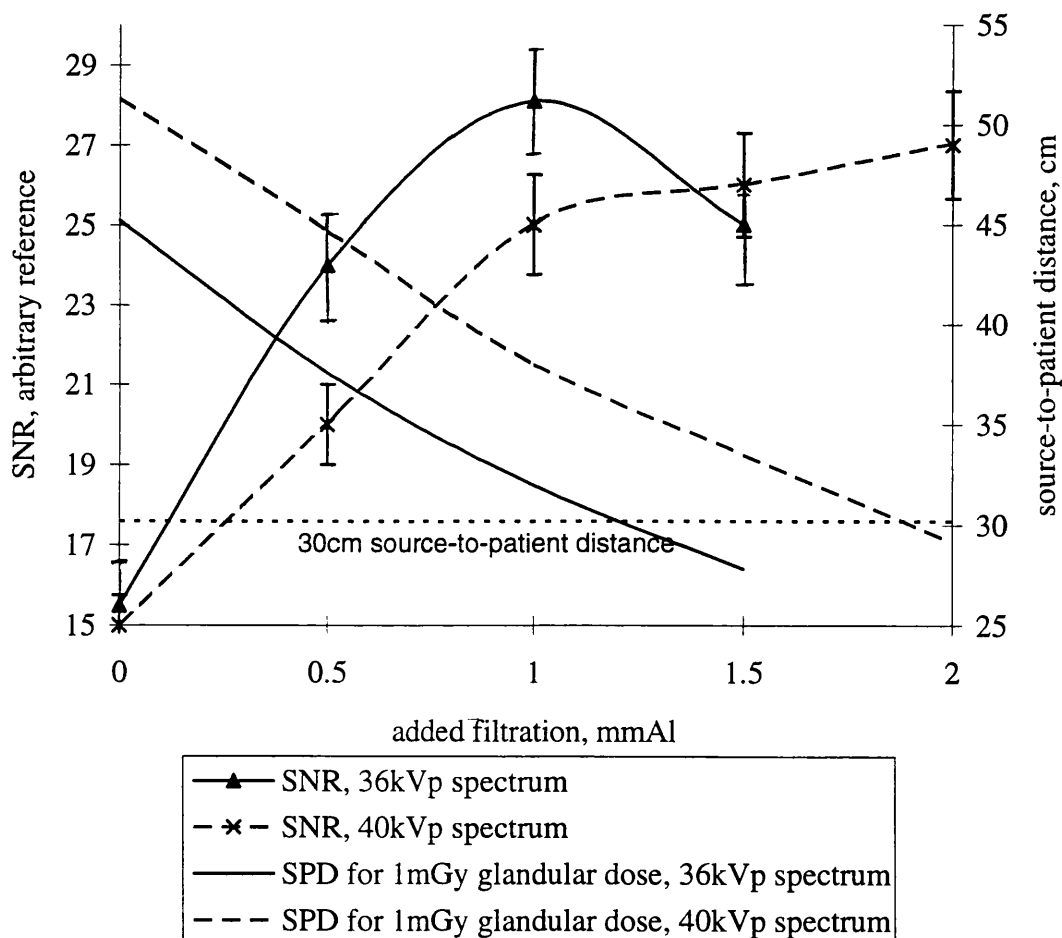
Figure 6-11 Effect of adding filtration on SNR

It also shows the source-to-patient distances needed to give the 1mGy mean glandular dose. Initially, for both 36kVp and 40kVp the SNR can be seen to increase as filtration is added. This is expected, as the filtration removes more and more of the low energy photons which tend to increase the dose without adding much to the detected signal. For 36kVp once 1mmAl added filtration is exceeded the SPD needs to move closer to the patient than the 30cm allowed to overcome the reduction in flux caused by the added filtration. A reduction in SNR is, therefore, found, giving an optimum amount of added filtration of approximately 1mm (36kVp).

6.4.4 Influence of magnification on SNR

The influence of the magnification on the SNR of the 250μm object (highest contrast) in the TOR[MAX] phantom was investigated using method 2, as detailed above, for a large area imaging configuration with no collimation between the x-ray tube and the phantom and also with a 7mm lead slit between the x-ray tube and the phantom to simulate the use of the system in slot scanning mode. The first configuration is a high scatter case, the second in nearly scatter free. The results of these are given in Figure 6-12, where they are compared with the theory of chapter 2, with δ_s=13cm and S_0/P_0=0.6 (zero for the no-scatter case). The theoretical results has been multiplied by an arbitrary constant to fit the experimental values.

It can be seen that the trends in the experimental results follow those of the theory and, therefore, this method can be assumed to give a reasonable estimation of the object SNR, although the large errors mean that this conclusion must be treated with some caution For the no-scatter configuration the SNR is seen to decrease as the system resolution decreases (magnification increases). For the non-collimated configuration there is an initial increase in SNR as the magnification (and air gap) is increased as this results in a reduction in detected scattered radiation. Eventually the two configurations move close together as the influence of scattered radiation becomes negligible.
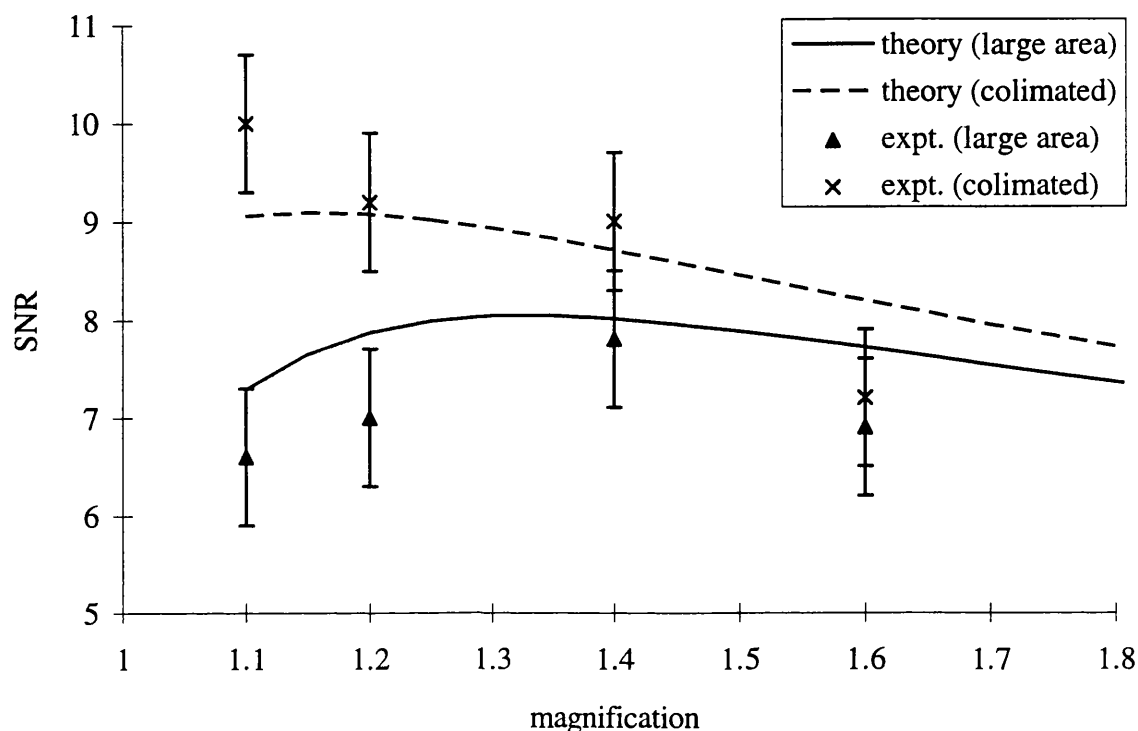
Figure 6-12 Influence of magnification on SNR of a small object

This method (i.e. method 2) has a number of drawbacks. The main one is the difficulty in estimating the area of the object shadow, even when several images are averaged together. This was found to be the main source of error on the results. The need to take several (say 10) images before the object area can be adequately estimated also reduces the advantages of this method over the subjective techniques described above. It should also be noted that the optimum magnification for the large area case is dependent on the size of the object, making the results somewhat ambiguous. As described below, the situation is generally simplified by the removal of scattered radiation either by a slot for the scanning system or a grid for the large area system.

6.5 Discussion on the quantitative evaluation of phantom images

The above experimental results have shown that it is possible to quantitatively measure the influence of factors such as air gap, tube voltage, filtration and magnification on the SNR. The first method, which is appropriate for use with large objects is particularly useful as it only requires a single image of a single object. The second method has some limitations as it requires several images to be taken for each configuration tested and, therefore, is not necessarily any more useful in optimising the system than the qualitative techniques described above. That is, there may be no saving in time and also reasonably large errors on the final results. The results are, however, quantitative. If sufficient collimation is used such that scattered radiation can be neglected then it may not be necessary to use method two in optimising the system, and method 1 may be sufficient. For example, as described in chapter 5, the optimum configuration for a slot scanning system involves a high resolution detector and a relatively large focal spot. For this configuration it is already known that the magnification should be kept close to unity and it should, therefore, be sufficient to optimise the kVp and filtration using method 1. With the exception that a smaller focal spot may be used, this is also the case for large area detectors when used with an anti-scatter grid. If a grid is not used then it may be necessary to use method 2, although power constraints are no longer a problem and the results of section 6.4.4 indicate that the theory of chapter 5 can give adequate predictions of the optimum geometry.

6.6 Subjective evaluation of phantom images

6.6.1 Method of subjective evaluation of phantom images

The digital mammography system was evaluated using the TOR[MAX] phantom with 4.5cm perspex. Two scores were evaluated: the number of 500μm details unambiguously seen (out of a total of 11), and the total number of 6mm circular details

objects unambiguously seen (out of a total of 12). This was repeated for a film-screen system to allow comparison between the digital mammography system built here and a conventional mammography system.

Two experimental configurations were used: the first configuration uses the tungsten target x-ray tube with a tube voltage of 36kVp and 1 mm Al (for 1.4mGy mean glandular dose) or 0.5mmAl (for 2mGy glandular dose) added filtration (inherent filtration is approximately 0.8mm); the second configuration uses the molybdenum target x-ray tube at 28kVp with molybdenum filtration In both cases lead collimation was used, giving a slit width of 0.7cm. The source-to-patient distance was set up at 30cm, with the CCD operated in integration mode. The effect of the SPD on the scores was evaluated by repeating the molybdenum target measurements for an SPD of 60cm and this effect was found to be negligible (no power constraints). Therefore, only the results for an SPD of 30cm are reported. In all cases the air gap between the detector and the phantom was approximately 1cm to give space needed by projecting components on the CCD camera board. The experiments were carried out with the protective glass coating in front of the CCD removed as this reduces the x-ray flux by approximately 20% and 55% for the tungsten and molybdenum target spectra respectively.

The results for two CCD/phosphor combinations are given in Table 6-1 for the maximum permitted mean glandular dose of 2mGy. The results for a mean glandular dose of 1.4mGy are also shown, which can be directly compared with results of a film-screen system taken using a mammography unit in current clinical practice (Mammomat 3). The film-screen combination used was Kodak MRE film and Kodak Min-R2 screen. The relationship between the scores and minimum observable contrast is shown in Table 6-2, which is reproduced from the TOR(MAX) manual (Cowen et al 1989). Note that these are the contrasts for a specified spectrum produced with a molybdenum target x-ray tube and molybdenum filtration and a tube voltage of 28kVp.

Detector arrangement	X-ray tube	Mean glandular dose, mGy	Number of 500μm objects detected	Number of 6mm objects detected
CCDa	Mo	2	3	2
CCDb	Mo	2	6	4
CCDa	W	2	3	2
CCDb	W	2	5	4
CCDa	Mo	1.4	2	2
CCDb	Mo	1.4	5	3
CCDa	W	1.4	2	2
CCDb	W	1.4	5	3
film-screen	Mo	1.4	7	5

Table 6-1 Subjective phantom scores for various detector/x-ray tube/dose combinations

Number of 500μm objects detected	Minimum detectable contrast, %	Number of 6mm objects detected	Minimum detectable contrast, %
1	37	1	8.5
2	33	2	5.5
3	24	3	3.8
4	20	4	2.6
5	16	5	2.0
6	8.3	6	1.6
7	5.4	7	1.2

Table 6-2 Relationship between phantom scores and minimum detectable contrast

6.6.2 Discussion of subjective evaluation of phantom images

Detectability scores were similar for the molybdenum and tungsten target x-ray tubes, with the system managing to detect contrasts down to 11% and 2.6% for the small and large objects respectively with a mean glandular dose of 2mGy. For a mean glandular

dose of 1.4mGy the CCD based system detected the 500μm and 6mm objects down to 16% and 3.8% respectively, compared with 8.3% and 2.0% for the film-screen system. Examination of Table 6-2 shows that these results are accurate to within approximately 25%. These results show that the system built in this project does not perform as well as current film-screen systems.

These disappointing results reflect the low values of DQE found in chapter 4, where it was shown that removal of the direct x-ray interactions with the CCD should significantly improve the DQE. The detectability scores are sufficiently close to the film-screen systems that it is likely that improvements to the system will bring the image quality of the CCD system to that of film-screen systems. The similarity of the results with both x-ray tube targets indicates that tungsten will be a suitable target of choice once power considerations are included.

6.7 Conclusions

A number of techniques for the subjective and quantitative evaluation of phantom images have been demonstrated. It has been shown that quantitative measurements of SNR agree broadly with the theory of chapter 5 and that, at least for large objects, it is reasonably easy to experimentally optimise the tube voltage and amount of added filtration. Evaluation of the SNR of small objects was found to be more difficult, particularly if trying to show the influence of resolution on the SNR. It is, therefore, convenient that the theory of chapter 5 gives a reasonable prediction of the measured SNR and, also, that for many applications the optimum magnification is already known. For example, it has been demonstrated both experimentally and theoretically that the magnification of a scanning system should be minimised. This maximises the efficiency of the use of the x-ray flux and also allows the use of a relatively large focal spot size. Once the magnification is set, the optimisation of the tube potential and amount of added filtration should be adequate to give an optimised system, although the attenuation coefficients of the object concerned may have an important effect on this. It may,

therefore, be appropriate to build a phantom with large area objects with contrast and attenuation properties similar to calcifications such that the parameters can, if required, be easily optimised for these objects.

Subjective comparison of various x-ray tube/detector combinations has shown that some improvement to the system is needed before it can compete with film-screen combinations. The uncertainty in the subjective scores are fairly large (20-25%) and it seems that a more sensitive phantom may be needed. The results indicate that the improvements needed are not enormous and a new system should be able to compete with conventional film-screens on the basis of the test carried out here. These improvements are discussed further in chapter 8.

7. DIGITAL STEREO-MAMMOGRAPHY

7.1 Introduction

This chapter discusses the possible use of the prototype TDI CCD digital mammography system for digital stereo-mammography. It details the basic theory of stereoscopic imaging, followed by the design of a stereo-mammography system. Finally initial results on the depth resolution of this system are given, together with typical images.

7.2 Stereoscopic x-ray imaging

Stereoscopic x-ray imaging was first used in radiology by MacKenzie Davidson in 1898, only three years after the discovery of x-rays by Roentgen. It soon became so popular that a review by Jarre and Teschendorf in 1933 stated that "no American Roentgenologist doubts the advantages to be derived from the study of sterio-Roentgenograms.". Increased concerns about patient dose, however, led to the decline in the use of stereoscopic x-ray imaging. More recently, the use of stereoscopic x-ray imaging has been investigated for use in routine screening of freight by HM. Customs and Excise (Evans 1993). The possible benefits of stereo-radiography in breast imaging have recently been studied by Hsu et al 1994 and 1995 using computer generated images. Their results indicated that digital stereo-mammography may allow easier detection of certain tissue abnormalities compared with 'mono-mammography'. In addition, Seemann 1968 claimed that "a stereo pair is especially advantageous where superimposed structures form an intricate image". It, therefore, seems that the advent of digital detectors with characteristics suitable for use on mammography may lead to the introduction of digital stereo-mammography systems.

Many breast screening centres routinely take two views of each breast at a given screening session and, therefore, it should be possible to take a stereo image with no

increase in breast dose. This may mean abandoning one of the views currently used, which may not be acceptable to many radiologists. Alternatively, since the eye/brain combination of the observer superimposes the two images it may be adequate to use a reduced dose for each of the two images used for the stereo-mammogram and retain the second view with little on no increase in breast dose.

7.3 Theory of stereoscopic imaging

Okoshi 1976 states that an observer uses up to ten cues for depth perception: Occlusion, shadows and shading, linear perspective, texture gradient, retinal image size, areal perspective, binocular parallax, monocular movement parallax, accommodation and convergence. The first six of these are psychological cues which can all be deduced from a two-dimensional image such as a photograph but are generally of little use when interpreting a conventional radiograph. The other four cues for depth perception are physiological and are not available with a two dimensional image. Binocular parallax is considered to be the most robust of these and requires the eyes to be focused and converged on to a point. This point occupies corresponding positions on the retina of each eye. Other points in the image, however, do not focus onto corresponding positions on the retina, the relative displacement of these points is related to the depth on the objects (binocular parallax). The eye/brain combination uses these disparities to give a sensation of depth in a process known as stereopsis.

In this work it is assumed that the three-dimensional x-ray visualisation system must give an orthoscopic image. That is, there must be a 1:1 correspondence in relative depths and sizes in both the image capture and image display processes. That is,

$$L_e = ML_x \quad (all\ P)$$

Equation 7-1

where Le, Lx and P are illustrated in Figure 7-1 and M is the image capture to image display magnification.

Image capture
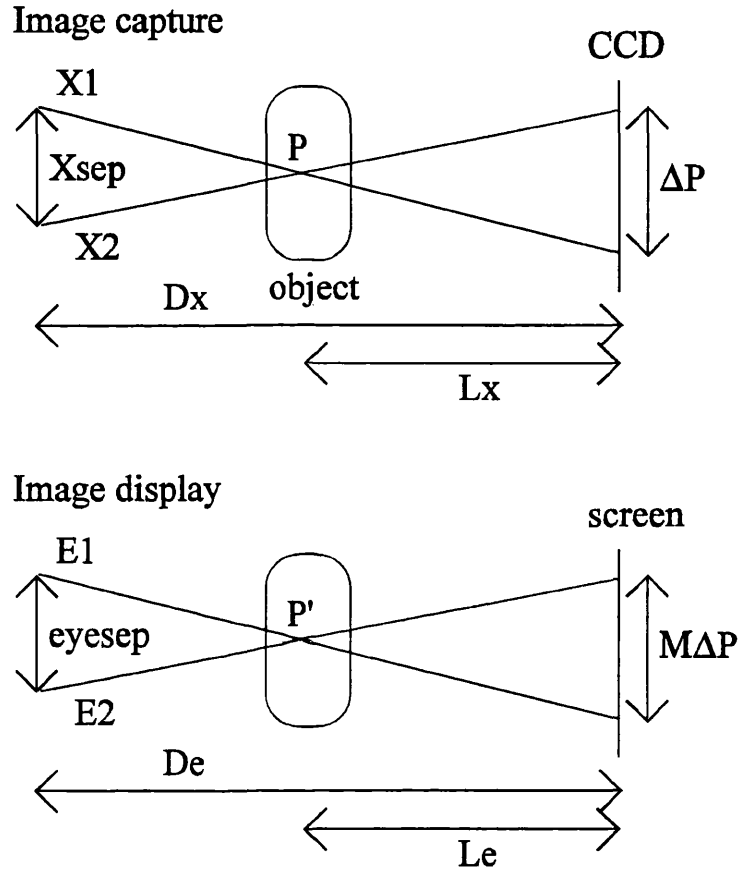
Image display

Figure 7-1 Schematic of stereoscopic image capture and display stages

From Figure 7-1 we have:

$$\frac{\Delta p}{L_x} = \frac{X_{sep}}{(D_x - L_x)}$$

Equation 7-2

and

$$\frac{M\Delta p}{L_e} = \frac{E_{sep}}{(D_e - L_e)}$$

Equation 7-3

This gives

$$\left(\frac{L_x}{D_x - L_x}\right)X_{sep} = \Delta p = \frac{1}{M}\left(\frac{L_e}{D_e - L_e}\right)E_{sep}$$

<div align="right">Equation 7-4</div>

which leads to

$$(D_e - ML_x)X_{sep} = (D_x - L_x)E_{sep}$$

<div align="right">Equation 7-5</div>

This must be true for all P. Therefore,

$$D_e = MD_x$$

<div align="right">Equation 7-6</div>

If the displacement, Δp is known then the depth can be calculated from

$$L_x = \frac{\Delta p D_x}{(X_{sep} + \Delta p)}$$

<div align="right">Equation 7-7</div>

The accuracy with which the depth of a given point identified on the left and right images can be predicted is given by

$$\delta L_X = \frac{D_X \Delta p}{(X_{sep} + \Delta p)^2}\delta(\Delta p)$$

<div align="right">Equation 7-8</div>

214

7.4 Design of an Orthoscopic stereo mammography system

The system is based on the scanning mammography system already described. Various requirements and optimum design configurations of scanning systems have already been discussed, including the need to use a small source to patient distance. With this in mind the system was set up with a source to detector distance of approximately 40cm, and an assumed viewer to screen distance of 60cm, giving the image capture to image display magnification as 1.5, and X_{sep} as $(1/1.5)E_{sep}$. Eye separation varies between viewers with a two standard deviation range of 40-71mm (Pimentel and Texeria 1993). Taking a typical value as 60mm this gives X_{sep} as 40mm. The natural range of eye separation distances means that the value of X_{sep} is not critical. The entire image is displayed on a Silicon Graphics Indigo workstation which has 1280 x 1024 pixels (15x11inches).

7.5 Depth resolution

The depth resolution was measured by taking stereo images of a 50μm diameter wire placed a known distance from the CCD. The position of this wire was controlled using a Digiplan stepper motor and controller (800 steps per mm). Equation 7-7 was then fitted to the experimental results to give more precise values of D_x and X_{sep}. In this way Dx and Xsep were measured at 422.7mm and 39.4mm respectively. A comparison of the experimental results with the predicted depths using Equation 7-7 is shown in Figure 7-2.

The depth resolution was estimated by evaluating the standard deviation in the differences between the experimental and predicted depths to be less than 200μm. Equation 7-8 shows that the resolution is depth dependent and, therefore, this value of 200μm is an average over the depths tested. This is in reasonable agreement with the predictions of Equation 7-8 which, for an assumed disparity resolution equivalent to a pixel width, gives a depth resolution of 180-280μm for depths of 90-5mm.

Note that this is the resolution on the depth of a point which has been identified in both left and right images. It is not the same as the resolution to which depth can be

estimated by an observer when viewing the images stereoscopically. This will inevitably be dose dependent. It is not measured here, and should be the subject of future work.
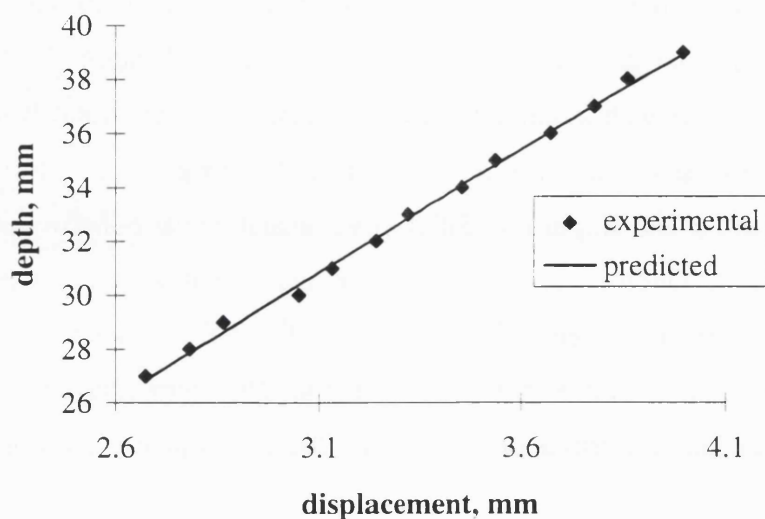
Figure 7-2 Evaluation of the depth resolution of a stereo-mammography system

7.6 Example stereo images

Stereo images were taken of a three dimensional phantom, are shown in Figure 7-3 and Figure 7-4. The first phantom consisted of 5 objects at increasing depths. From Figure 7-3 it can be seen that the disparity between the objects positions is largest at the top of the image and smallest for the bottom object, corresponding to objects at the top of the image being further from the detector than objects closest to the detector.
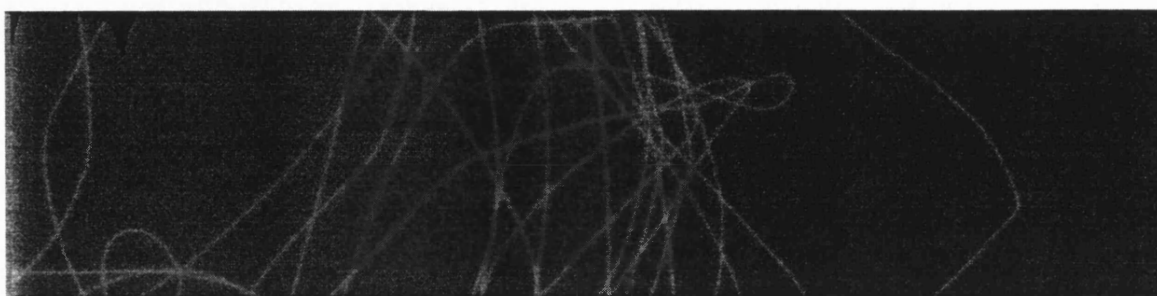
Note that for Figure 7-3 the x-ray tube displacement was orthogonal to that used for Figure 7-4.
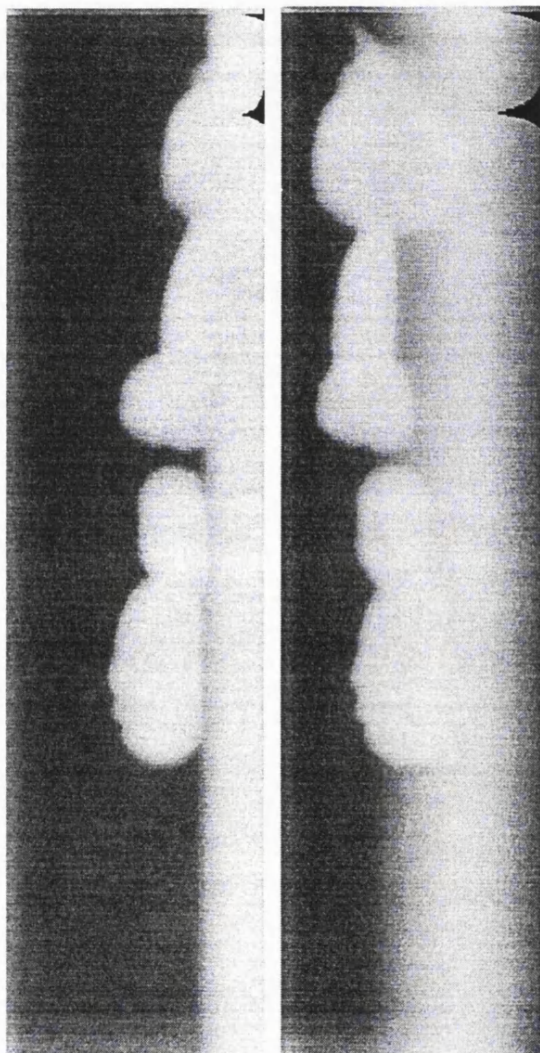
Figure 7-3 Left and right stereo images of a three dimensional phantom
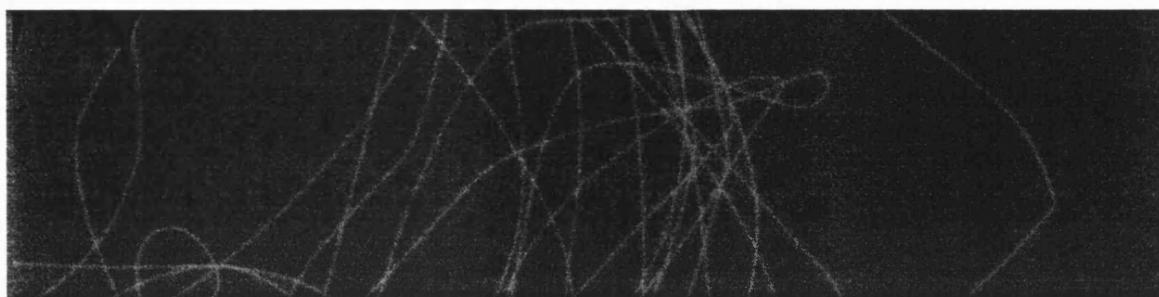
Figure 7-4 Left and right images of a wire phantom

When displayed in stereo it was possible to see that these overlapping objects were at different depths. Similarly with the second phantom, which is essentially a bundle of wires of 50μm diameter, it was possible to determine which wires were closest to the detector.

7.7 Conclusions

Stereo-mammography is an extremely exciting future development. Computer simulations have shown that this technique may permit easier detection of certain tissue abnormalities (Hsu et al 1995) and the experimental work above has experimentally demonstrated the use of such a system. The depth resolution of this system was measured at 200μm. Of course, this work is only preliminary. More detailed investigation required specially constructed phantoms and will include work to investigate the visual depth resolution (i.e. the depth resolution as measured by an observer) rather than that found when mathematically calculating the depth of a given point.

8. CONCLUSIONS

This thesis has discussed the design, theoretical optimisation, construction and evaluation of a digital mammography system based on Charge-Coupled Device (CCD) technology. The emphasis throughout was on using the CCDs in Time Delay and Integration (TDI) scanning mode to overcome the size mismatch between CCDs and the breast, although the optimisation of a full area detector was discussed in chapter 5, and the effect of scattered radiation on the optimum geometry was experimentally demonstrated for both scanning and full area systems in chapter 6.

A subjective evaluation found that the prototype system built in this project produces images of inferior quality compared with a conventional film-screen combination (chapter 6). The subjective image scores are close enough to those of conventional film-screen combinations, however, that a second generation system should be able to compete with film-screen combinations.

The main source of degradation of the image quality is attributed to the x-ray detection stage. The need to remove the direct x-ray interactions with the silicon of the CCD is highlighted in chapter 4, where the significance of this effect in degrading the spatial frequency detective quantum efficiency, DQE(f) is illustrated. It is interesting that these interactions give an improved high frequency response in the MTF, although the accompanying increase in noise means that consideration of the MTF alone gives a false impression of the image quality of the system. It was shown in chapter 3 that the use of a fibreoptic stud with high lead content-between the phosphor and the CCD is one method for reducing these interactions. Others include using suitable optics between the phosphor and the CCD to bring the CCD out of the direct path of the x-rays.

Once these direct x-ray interactions have been removed the system performance can still be improved. The exposure time is currently limited by the maximum readout rate of the CCD15-11 to approximately 5s for a 10cm scan. The recent replacement for the CCD15-11, the EEV CCD30-11, which has a similar imaging format but a readout rate

three times that of the CCD15-11, the use of which would bring the exposure time closer to the 1 or 2 second limit indicated in chapter 1. The use of a CCD with even faster output circuitry would allow the resolution degradation due to clocking waveforms to be reduced (see chapter 4), thus bringing the resolution closer to that achieved with a stationary CCD. A CCD with faster readout rate is, therefore, advantageous provided that other factors such as readout noise do not become significant.

Another major drawback of the current system is the small size of the images produced. Although the images were of a sufficient size to allow evaluation of characteristics such as Modulation Transfer Function, MTF, and Noise Power Spectrum, NPS, it made any comprehensive evaluation of image quality difficult and time consuming. This drawback is reasonably easy to overcome with increased investment.

Further improvements in this system relate to the available x-ray tubes and associated high voltage generators. Evaluation of a properly optimised x-ray detection system, which takes into account the discussion above as well as the theoretical optimisations of chapter 5, will require a versatile x-ray unit, probably with a variable focal spot size. It would also be useful and, as indicated in chapter 2, reasonably simple to interface the detection system with the x-ray tube.

A second generation system could also improve on the mechanical arrangement currently used. This could include rotating the x-ray tube to follow the detector in an arc, similar to the technique used by Maidment et al 1993 (see chapter 1).

The optimum thickness of the CsI layer is still unclear as the direct interactions of the x-rays with the silicon of the CCD somewhat confused the issue in this work. As with all phosphor screens increased thickness gives and increase in responsivity but also reduces the resolution. The results of chapter 4 indicate that the columnar structure of the CsI screen is not helpful in channelling light towards the CCD. Although numerous guidelines exist regarding the image quality in mammography (see chapter 1), the exact requirements of a mammography system are still unclear. An extremely interesting future piece of work would be to investigate the relationship between DQE(f) and image

quality in mammography and also in other examinations. For example, what is the optimum compromise between quantum efficiency and high spatial frequency response? This would involve extensive Receiver Operator Characteristic (ROC) analysis, but would be invaluable in producing an optimum x-ray detection system.

This discussion has described various ways of improving the current system. A question which must be asked before embarking on such an upgrade is whether a CCD based scanning system is the way forward for digital mammography. Such a system can definitely compete in image quality with current film-screen systems. There are, however, other digital detectors which should be considered, such as amorphous silicon thin-film arrays. Initial concerns regarding the use of these arrays in digital mammography included the fill factor problem and the relatively large pixel sizes currently available. Although reduced fill factor will reduce the optical coupling efficiency between the scintillator and the CCD and will, therefore, increase secondary quantum noise, this is unlikely to be a problem if CsI (Tl) is used as the phosphor because of the large amount of light produced (see chapter 3 for details regarding the x-ray to electron gain when using CsI(Tl) with CCDs). The theoretical optimisation results of chapter 5 indicate that the use of such a detector with a reduced focal spot size and with increased magnification may give equivalent image quality to a scanning detector. An investigation into the necessary pixel size could be included in the research regarding the necessary DQE(f) work mentioned above, as this issue is still unclear (see chapter 1). The choice between large area and scanning systems may then be simplified to practicalities such as possible geometries and relative costs.

The theoretical optimisations of chapter 5 were presented in such a way that they should be helpful in designing any second generation system, whether it is a large area detection system or a scanning system. The experimental optimisation techniques presented in chapter 6 may also be useful for optimising the image quality once the system is built.

Having indicated that large area detectors are equally useful in digital mammography as a scanning system, a very exciting future development of mammography should be discussed. That is, the possible use of the scattered radiation leaving the breast as an aid

to diagnosis in, so called, Diffraction Enhanced Breast Imaging, DEBI, currently being investigated at UCL (G Kidane, Medical Physics Department, UCL, personal communication 1995). If tumours and healthy breast tissue can be identified by their diffraction pattern then the 30% of x-rays which leave the breast but are not currently used may contribute to the diagnosis. A scanning system, such as the one developed here, is ideal for modification such that diffraction patterns from well defined regions of the breast can be collected.

Another possible technique for improving diagnosis is the use of stereo-mammography, as described in chapter 7. This is also an exciting development although the need for special viewing conditions may hinder its use in a screening context. It may, however, be useful for examining mammograms from referred patients. The extra image needed for stereo viewing means that before the introduction of this technique as a serious contender for digital mammography systems much work is needed into its use, including dose reduction techniques and an investigation into the minimum dose required for stereo viewing.

APPENDIX A: THE MODULATION TRANSFER FUNCTION

Background theory

The resolution properties of an imaging system which is linear and shift-invariant, can be found from the output of an input delta function. This output, once normalised - the Point Spread Function (PSF) in two dimensions, or the Line Spread Function (LSF) in one dimension - can be Fourier transformed to give the Optical Transfer Function (OTF). Strictly speaking the conditions of linearity and particularly spatial invariance are not always satisfied, but they can usually be approximated. Digital systems are generally linear, but they can never be spatially invariant because of the finite pixel size. The OTF can be separated into two parts: the modulation transfer function (MTF) and the phase transfer function (PTF), which describe the modulus and phase of the complex OTF respectively. In an analogue system the LSF can be obtained from the image of a narrow slit. The OTF is then found from:

$$OTF(u) = \int_{-\infty}^{+\infty} LSF(x)e^{-j2\pi ux}dx$$

Equation A - 1

where

$$\int_{-\infty}^{+\infty} LSF(x)dx = 1$$

Equation A - 2

Alternatively the OTF can be obtained from the image of an edge. The image of an edge
gives the edge response function, ERF(x), which is related to LSF(x) by:

$$LSF(x) = \frac{d}{dx} ESF(x)$$

Equation A - 3

For a rotationally invariant system the full two-dimensional MTF can be characterised by
a single measurement but, if the system is not isotropic then, in principle, all possible
orientations of the LSF should be considered. In practice it is considered sufficient to
measure two orthogonal LSFs - for example, the LSF in the x- and y- directions.

The detector OTF, and hence a slit image, is degraded by a number of factors described
below, the product of which gives the analogue pre-sampling OTF (Giger and Doi
1984). The slit image is then sampled at discrete intervals of the sampling distance Δx.
This is equivalent to a multiplication of the analogue signal by a 'comb' function, as
illustrated in Figure A - 1, where the signal, (a), is multiplied by a sampling comb, (b), to
given a digital signal, (c). In the frequency domain this is equivalent to convolution of the
frequency response with a comb function, also illustrated in Figure A - 1, where the
frequency spectrum of the signal, (d), is convolved with the frequency sampling comb,
(e) to give the frequency response, (f). The spectrum of a sampled signal is, therefore,
periodically repeated. The period centred at zero frequency is known as the base band,
and the other periods are called side bands (Sones 1984).

The distance between the periods in the frequency domain is related to the sampling
interval, Δx by $\Delta f=1/\Delta x$. This means that if Δx is increased then Δf decreases and the
periods move closer together, and eventually overlap - a process known as aliasing, as
illustrated in Figure A - 1(g). The Whittaker-Shannon sampling theorem states that
when the bands overlap it is impossible to uniquely recover the original signal from its
samples (Ganzales and Wintz 1987). This occurs when the signal contains frequencies
above $f_N=(2\Delta x)^{-1}$, known as the Nyquist frequency.
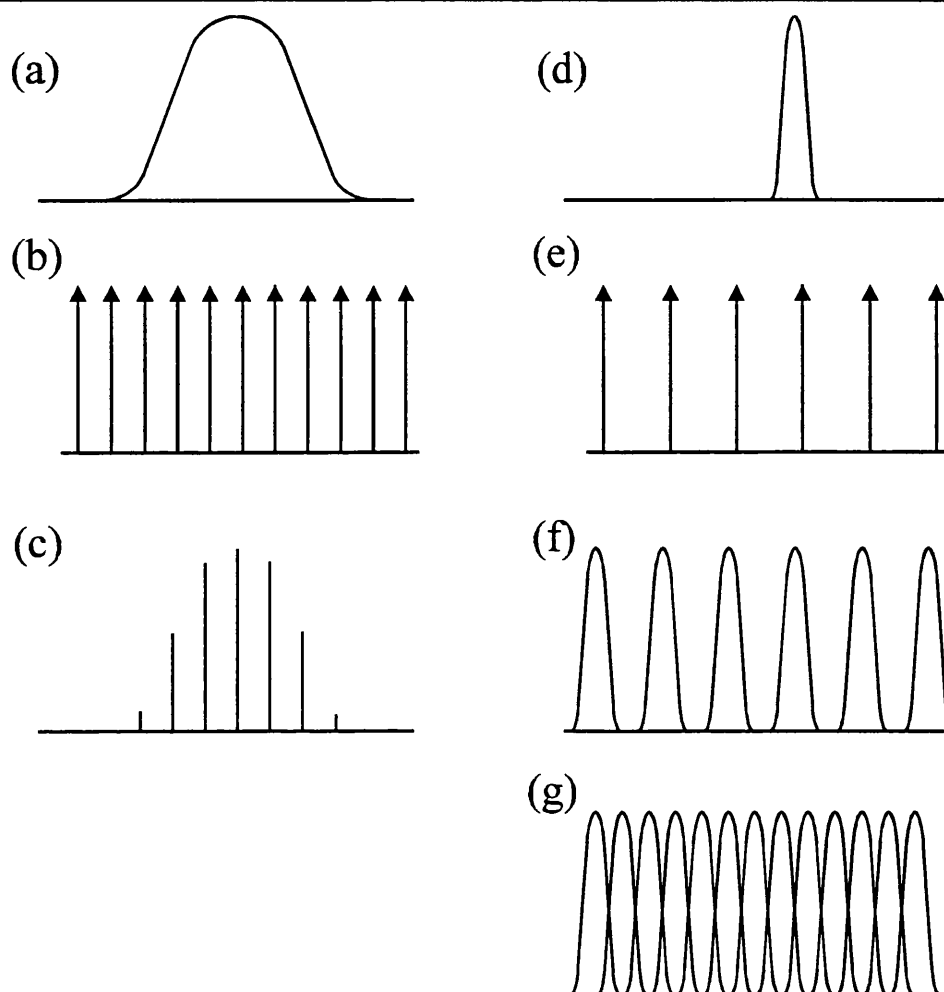
Figure A - 1 Schematic of the sampling process. (a) - (d) are in real space, (d)-(g) are in frequency space

Aliasing is not a significant problem when characterising the response of an analogue film-screen system, where the continuous image of a slit or knife edge is scanned and sampled with a microdensitometer, as the sampling rate, and hence the separation of the periods in the frequency domain, can be appropriately controlled. Digital systems, however, are typically designed to undersample as, in practice, sufficient sampling can only be obtained with a design that causes excessive blurring (Reichenbach 1991). Unless care is taken, the measured MTF of digital systems may include a false response due to aliasing (see, for example, Giger et al 1984). Another complication is caused because digital systems are not shift invariant and two extremes of alignment exist: in the first, the slit is positioned in the centre of the pixel and in the second, the slit is positioned one half the sampling distance away form the pixel centre. Fujita et al 1985 showed that

by measuring the OTF for various shifted slit positions it is possible to estimate the average pre-sampling OTF even at frequencies higher that the Nyquist frequency. Various other methods have been proposed to overcome the measurement uncertainties caused by aliasing, including measurements on images of cyclic bar patterns (Droege et al 1985) and images of more complicated phantoms which consist of accurately spaced arrays of wires (Sones 1984). Possibly the simplest method is similar to the original method of Fujita et al 1984 but, instead of only using a few (2 or 3) slit alignments, it uses many (say, 20) alignments to give a highly sampled image. This technique, described below, has apparently been independently described by a number of authors, including Reichenbach et al 1991 and Fujita et al 1992, as well as Judy 1976.

Use of an angled slit to determine the presampling MTF

This method uses a slit (or edge) positioned at a slight angle (usually <2 degrees) to the scan direction, as shown in Figure A - 2 (note that, for illustration purposes, the slit angle is exaggerated).
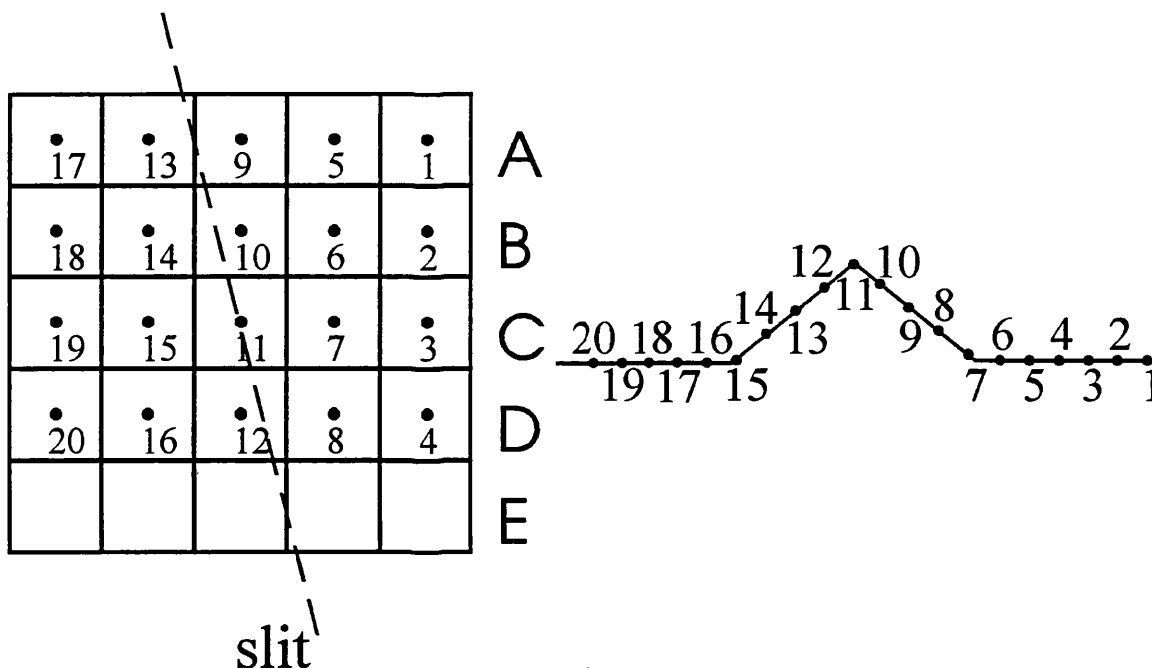
Figure A - 2 Schematic of the angled slit technique

The slight angle means that the LSF at each location A, B, C and D correspond to different alignments of the slit relative to the sampling co-ordinate (Fujita et al, 1992) with A and E being separated by one complete pixel. The data from these individual LSFs can then be combined in the order 1,2,3,... to generate a finely sampled LSF, also called a super-resolution scan (Reichenbach et al 1991), with a smaller effective sampling than the individual LSFs. This super-resolution LSF is the Fourier transformed to obtain the presampling OTF.

The effective sampling distance is given by $\Delta x'=\Delta x/(n+1)$, where n is the number of pixels between two different centre alignments. In the example illustrated in Figure A - 2 n=3 and $\Delta x'=0.25\Delta x$.

APPENDIX B: THE NOISE POWER SPECTRUM

The Wiener Spectrum of the fluctuations of a stationary[+] ergodic[#] process is given by (Dainty and Shaw, 1974)

$$W(u,v) = \lim_{X,Y \to \infty} \left\langle \frac{1}{2X}\frac{1}{2Y} \left| \int_{-X}^{X} \int_{-Y}^{Y} \Delta D(x,y) e^{-i2\pi(ux+vy)} dx\, dy \right|^2 \right\rangle$$

<div align="right">Equation B - 1</div>

where $\Delta D(x,y)$ describes the spatial noise variations from a zero mean and $\langle\rangle$ denotes the ensemble average.

A related function is the autocorrelation function, $C(\xi,\eta)$, which describes the spatial structure of the image noise in spatial, rather than frequency, terms:

$$C(\xi,\eta) = \lim_{X,Y \to \infty} \frac{1}{2X}\frac{1}{2Y} \int_{-X}^{X} \int_{-Y}^{Y} D(x,y) D(x+\xi, y+\eta) dx\, dy$$

<div align="right">Equation B - 2</div>

where $D(x,y)$ describes the spatial image intensity variations.

The Wiener-Khintchin theorem states that the Wiener spectrum and the auto-correlation function are Fourier transform pairs (Dainty and Shaw 1974). For a Gaussian process, both of these functions give a complete description of the random process.

[+] A statistically stationary process is one for which the statistics are the same over all areas and are not influenced by a shift in origin.

[#] An ergodic process is a random process for which all the statistics can be identified from a single realisation.

It can be shown that the experimentally measured auto-correlation function is equal to the actual auto-correlation function convolved twice with the measuring system's point spread function (PSF) (Dainty and Shaw 1974, Barrett and Swindell 1981). In spatial frequency terms, this is equivalent to the multiplication of the actual Wiener spectrum by the square of the modulation transfer function (MTF) of the measuring system, T(u,v). The actual Wiener spectrum is, therefore, easily recovered from the measured Wiener spectrum:

$$WS(u,v) = \frac{WS_M(u,v)}{|T(u,v)|^2}$$

Equation B - 3

where the subscript M denotes the measured value.

Experimentally, it is possible to measure a one-dimensional spectrum $W'_M(u)$, which is related to the two dimensional spectrum by

$$W'_M = \int_{-\infty}^{\infty} W(u,v)|T(u,v)|^2 \, dv$$

Equation B - 4

For a slit of length L and width a the MTF of the measuring system is given by

$$T(u,v) = sinc(au)sinc(Lv)$$

Equation B - 5

If this slit is long enough that W(u,v) can be considered constant over the spatial frequency range where $sinc^2(Lv)$ is non-zero, then

$$W'(u) = sinc^2(au)W(u,0) \int_{-\infty}^{\infty} sinc^2(Lv)dv$$

$$W'(u) = \frac{sinc^2(au)}{L}W(u,0)$$

Equation B - 6

In a digital system, the Wiener spectrum is multiplied by the absolute square of the aperture spatial frequency response, $OTF_s(u,v)$, to give an analogue "pre-sampling" Wiener spectrum (Giger et al 1984).

A slit can be simulated by averaging pixels along a slit length. That is,

$$\Delta D(y) = \frac{1}{M} \sum_{x=0}^{M-1} \Delta D(x,y)$$

Equation B - 7

where M is the length of the slit, in number of pixels. The measured Wiener spectrum is then given by:

$$WS_M(u) = \lim_{N \to \infty} \left[\frac{1}{N\Delta x} \left| \sum_{y=0}^{N-1} \Delta D(y) e^{-i2\pi yu/N} \Delta x \right|^2 \right]$$

Equation B - 8

where Δx is the pixel size. The actual pre-sampling Wiener spectrum is then found by multiplying WS_M by the length of the slit, $L=M\Delta x$.

The total noise power spectrum can be expressed as the sum of the uncorrelated noise sources (Nishikawa and Yaffe 1990):

$$W_T(u) = W_Q(u) + W_{SQ}(u) + W_D(u)$$

<div align="right">Equation B - 9</div>

where $W_T(u)$ is the total noise power spectrum. $W_Q(u)$ is the NPS due to x-ray detection, $W_{SQ}(u)$ is the NPS due to secondary quantum fluctuations and $W_D(u)$ is the NPS due to inherent detector system output fluctuations. $W_D(u)$ can be measured by acquiring images without illumination and $W_{SQ}(u)$ can be measured by illuminating the detector with a uniform light field and subtracting $W_D(u)$ form the measured NPS. Similarly, $W_Q(u)$ can be evaluated by uniformly irradiating the CCD with x-rays and subtracting $W_D(u)$ and $W_{SQ}(u)$ from the measured results. The detection system used here has an additional contribution to the NPS due to direct hits.

The NPS due to x-ray detection, $W_Q(u)$ which includes the effect of light spreading in the phosphor can be theoretically modelled as (Barrett and Swindell 1981):

$$W_Q(u) \propto \int_0^{d_s} |MTF_z(u)|^2 dz$$

<div align="right">Equation B - 10</div>

where $MTF_z(u)$ is the MTF due to an x-ray interaction at depth z in the phosphor and d_s is the total phosphor thickness. As noted by Barrett and Swindell 1981, this shows that the frequent assertions in the literature that $W_Q(u) = constant.|MTF(u)|^2$ is not correct. This sort of comparison is, however, useful for approximate comparisons.

APPENDIX C: THE DETECTIVE QUANTUM EFFICIENCY

The spatially dependent detective quantum efficiency, DQE(f) is defined as

$$DQE(f) = \frac{SNR_{out}^2(f)}{SNR_{in}^2(f)}$$

<div align="right">Equation C - 1</div>

where SNR$_{out}$(f) and SNR$_{in}$(f) are the output and input spatially dependent SNR respectively. The spatial frequency dependent propagation of the signal is given by the MTF and the spatial frequency dependent propagation of the noise is given by the ratio of the output NPS, W$_T$(f) to the input NPS. Because the distribution of x-rays incident on the detector is random and if it is assumed that the x-ray absorption and the subsequent emission of light is localised to a region which is small compared to the resolution of the detector, the input NPS can be considered to be flat, with a magnitude determined by the x-ray quantum fluence, ϕ. The DQE(f) can then be given by

$$DQE(f) = \frac{\phi K^2 MTF^2(f)}{W_T(f)}$$

<div align="right">Equation C - 2</div>

where K relates the changes in incident fluence at zero spatial frequency to changes in detector output (Maidment and Yaffe 1994). For a film-screen system K is given by

$$K = G \log_{10} e / \phi$$

<div align="right">Equation C - 3</div>

where G is the gradient of the film-screen response curve (the H-D curve, see chapter 1) at the exposure given by fluence ϕ. For a linear detector this is simplified to

$$DQE(f) = \frac{MTF^2(f)}{\phi\, W_{\Delta z/z}(f)}$$

<div align="right">Equation C - 4</div>

where $W_{\Delta z/z}(f)$ is the noise power spectrum of the relative noise fluctuations. The transfer of signal and noise through a radiographic system which consists of several steps in the process of image formation can be analysed in terms of amplification and spatial scattering processes. The propagation of NPS through a series of stages has been approached by Rabbani et al 1987 and Cunningham et al 1994, with the latter using the results to obtain a generalised expression for the spatial frequency dependent DQE of an N-stage system with Poisson distributed input:

$$DQE(f) = \left[1 + \sum_{i=1}^{N} \left(\frac{1 + \varepsilon_{gi}|MTF_i(f)|^2}{P_i(f)} \right) \right]$$

<div align="right">Equation C - 5</div>

where

$$P_i(f) = \prod_{j=1}^{i} \overline{g_i}|MTF_i(f)|^2$$

<div align="right">Equation C - 6</div>

ε_{gi} is the Poisson excess factor of gain g, defined as

$$\varepsilon_{gi} = \frac{\sigma_{gi}^2}{\overline{g_i}} - 1$$

<div align="right">Equation C - 7</div>

g_i is the gain of stage I, $MTF_i(f)$ is the MTF of stage I and σ_{gi}^2 is the variance of gain g_i. The Poisson excess factor is introduced to account for the process in which the variance

<div align="right">233</div>

of g is not equal to the mean value of g. It is equal to the relative amount the variance is in excess of g. In the detection system here, neglecting direct x-ray interactions in the silicon of the CCD, the imaging process starts by binary selection in the CsI screen, followed by an amplification process due to the emission of visible photons, described by the mean number of visible photons, $\overline{m}$, and the Poisson excess factor of the screen, ε_m. The spreading of optical photons in the screen is described by the MTF together with losses due to optical coupling efficiency, η_{op}. Detection of the optical photons by the CCD is another binary selection process described by the efficiency η_λ. The DQE(f) is then given by:

$$DQE(f) = \eta_Q \left[1 + \frac{\varepsilon_m}{\overline{m}} + \frac{1}{\eta_\lambda \eta_{op} \overline{m} MTF(f)} \right]^{-1}$$

Equation C - 8

It should be noted that other, more comprehensive, models of DQE(f) exist, such as that of Nishikawa and Yaffe 1990. The treatment considered here is useful for initial prediction of DQE(f).

For large m, ε_m is related to the Swank factor, I_X, by

$$1 + \frac{\varepsilon_m}{\overline{m}} \approx \frac{1}{I_X}$$

Equation C - 9

The zero frequency DQE(f) is therefore given by

$$DQE(0) = \eta_Q I_X$$

Equation C - 10

The original motivation for using I_X was the same as that for the Poisson excess factor. That is, it was introduced to account for fluctuations in the number of photons emitted per absorbed x-ray, giving the output SNR for an input x-ray flux, $\phi_{x\text{-ray}}$, as

$$SNR_{out} = \sqrt{\phi_{x-ray} I_X}$$

Equation C - 11

APPENDIX D: MODEL OF A MAMMOGRAPHY SYSTEM

This appendix describes the derivation of the theoretical model of a mammography system used in the optimisations of chapter 5. It describes the signal to noise ratio, SNR, and contrast of an object in the breast, and includes consideration of the system resolution and scattered radiation. This formulation closely follows the work of Muntz 1979, Muntz 1981 and Jafroudi et al 1982, from where more details regarding the model may be found.

The geometry used in this model is that of figure 5-3 in chapter 5. The definitions of SNR and contrast are illustrated in Figure D-1. Contrast is defined as
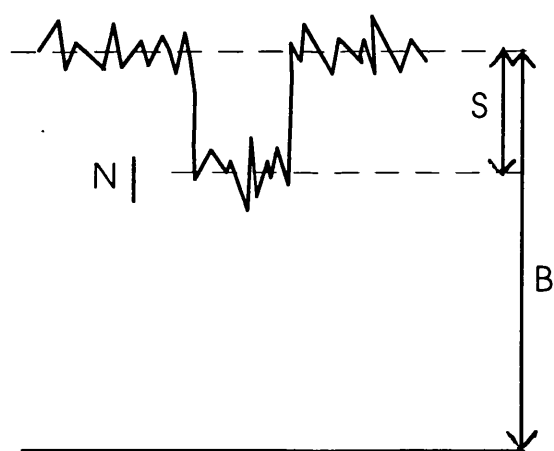
$$Contrast = \frac{Signal}{Background} = \frac{S}{B}$$

Equation D - 1

Signal to noise ratio is defined as

$$SNR = \frac{S}{N} \approx \frac{S}{\sqrt{B}}$$

Equation D - 2

Figure D - 1 Schematic showing signal, S, background level, B and noise, N

Using aperture theory, in which the resolution of each imaging element (i.e. the focal spot, the detector and the target) is represented by an effective aperture or area, and integrating the signal over its area gives the signal as

$$S = \int_{A_T} \varphi_{75} \left(\frac{75}{d_S + L_T} \right)^2 \Delta I dA_T$$

<div align="right">Equation D - 3</div>

where is the photon flux a distance 75cm from the x-ray source (cm^{-2}), d_s and $_{LT}$ are defined in figure 5-3 of chapter 5. ΔI is defined in equation 5:17 and describes the difference in x-ray intensity between the object shadow and the background level. A_T is the effective aperture of the target. Notice that the signal is independent of the object-detector distance. The reader is referred to Wagner 1974 for further details on aperture theory.

So far the responsivity of the detector and the influence of any anti-scatter grid between the patient and the detector has been neglected. If this is included then the signal is given by

$$S = \int_{A_T} \varphi_{75} \left(\frac{75}{d_S + L_T} \right)^2 \Delta I \, T_P \, E \eta_E \, dA_T$$

<div align="right">Equation D - 4</div>

where T_P is the transmission of primary photons through the grid. That is, if 80% of primary photons pass through the grid the T_P=0.8. η_E is the responsivity of the detector, expressed as a fraction. That is, if the detector absorbed 50% of the photons of energy E then η_E is 0.5. The factor E is included on the assumption that the signal size in the detector is proportional to the energy of the x-ray.

With the same assumptions as for the signal size, the background signal due to primary photons, $B_{primary}$, (i.e. not scattered photons) is given by

$$B_{primary} = \varphi_{75} \left(\frac{75}{x_p + A} \right)^2 e^{-\mu_{breast} L} T_P \, E \eta_E \, A_I$$

<div align="right">Equation D - 5</div>

where x_p is the source to exit plane of the patient distance, A is the air gap between the patient and the detector, μ_{breast} is the linear attenuation coefficient of the breast tissue and A_I is the effective area of the image, as calculated using aperture theory. This assumes that the background in constant throughout the area of the image.

Using the effective scatter source model described in chapter 5, the background signal due to scattered radiation is given by

$$B_{scatter} = \left\{ \varphi_{75} \left(\frac{75}{x_p} \right)^2 e^{-\mu_{breast}L} \left(\frac{S_o}{P_o} \right) \right\} \left(\frac{\delta_s}{\delta_s + A} \right)^2 T_S \, E_S \eta_{E_S} A_I$$

<div align="right">Equation D - 6</div>

where (S_o/P_o) is the scatter to primary ratio at the exit plane of the patient, T_S is the transmission of scatter photons through the grid, E_S is the average energy of the scattered photons and η_{E_S} is the responsivity of the detector to photons of energy E_s. δ_S is the effective scatter source distance, described in chapter 5. The first bracketed term gives the scatter flux at the exit plane of the patient. This is then converted to the scatter flux at the detector surface by the second bracketed term. The final terms describe the signal size. The total background, given by $B_{primary} + B_{scatter}$, After rearranging some of the terms in the background expression, the contrast can be written as

$$Contrast = \frac{\int_{A_T} \varphi_{75} \left(\frac{75}{d_S + L_T} \right)^2 \Delta I \, T_P \, E \eta_E \, dA_T}{\left\{ \varphi_{75} \left(\frac{75}{x_p} \right)^2 e^{-\mu_{breast}L} \left(\frac{S_o}{P_o} \right) \right\} \left(\frac{\delta_s}{\delta_s + A} \right)^2 T_S \, E_S \, \eta_{E_S} \, A_I}$$

<div align="right">Equation D - 7</div>

For an incident spectrum the denominator and numerator are integrated over the spectrum.

Making the assumption that photon shot noise is the dominant source of noise and also that the signal size per photon is constant the variance of the background signal is given by

$$\sigma^2_{background} = \sum_E W_E^2 N_E$$

<div align="right">Equation D - 8</div>

where W_E is the signal size per photon of energy E (proportion to E) and N_E is the number of detected photons of energy E. With this assumption the signal to noise ratio can be derived. Note that in this equation the effects of an anti-scatter grid are initially neglected (T_P and T_S taken as unity)

$$SNR^2 = \frac{\left(\int \psi_{75} \frac{75^2}{(d_s + L_r)^2} \Delta I \eta_{Ep} E A_T \, dE \right)^2}{\int \left(\frac{\psi_{75} 75^2}{x_p^2} e^{-\mu_{breast} L} \right) \left(\frac{\eta_{Ep} E_p^2}{M_{exit}^2} + \frac{(S_o / P_o) \eta_{E_s} E_s^2 \delta_s^2}{(A + \delta_s)^2} \right) A_I \, dE}$$

<div align="right">Equation D - 9</div>

Further assumptions regarding this model are given in chapter 5.

APPENDIX E: MONTE CARLO METHODS

Monte Carlo methods are probably the most common technique used for the study of radiation transport in medical radiation physics. They have been used for calculation of patient dose (Dance 1980), scattered radiation (Chan and Doi 1983) and for finding the optimal choices of detector parameters, such as composition and thickness (Bencivelli et al 1991, Boone 1992).

In this thesis all Monte Carlo simulations were developed using the Electron-Gamma Shower v.4 (EGS4) code system (Nelson et al 1985), which has been adapted using the method on Manito to include the incoherent scattering function. This is a general purpose package for the simulation of transport of electrons and photons in a user defined geometry. It consists of a set of subroutines links to user-written routines. It is possible to follow each particle on its path through the user defined geometry until it reaches a pre-determined energy cut-off point or a geometrical boundary, as defined by the user. The particles can be labelled and scored according to descriptors such as the interactions that take place, the regions where these interactions take place. The energy deposited can also be accurately scored. Correct energy scoring was ensured by including the Parameter Reduced Electron-Step Transport Algorithm (PRESTA) as developed by Bielajew and Rogers 1987 into the EGS4 code. This ensures the selection of appropriate electron-step sizes required to avoid energy scoring artefacts which can occur when working at relatively low energies.

Cross-sections used in the EGS4 simulations are prepared by a stand alone data pre-processing code (PEGS4) using cross section data taken from Storm and Israel 1970. The assumptions made are discussed further in the Monte Carlo evaluation of scatter flux in chapter 5.

The pseudo-random generator used by EGS4 is based on an algorithm developed by Marsaglia et al 1990. This algorithm is also used in the user generated code. For example, for randomly selecting the emission angle for x-rays from an x-ray tube.

REFERENCES

AAPM (American Association of Physicists in Medicine) 1990 *Equipment requirements and quality control for mammography report 29* (American Institute of Physics: New York)

Alexander F E, Anderson T J, Brown H K, Forrest A P M, Hepburn W, Kirkpatrick A E, McDonald C, Muir B B, Prescott R J, Shepherd S M, Smith A and Warner J 1994 The Edinburgh randomised trial of breast cancer screening: results after 10 years of follow-up *Br. J. Cancer* **70** 542-548

Anderson L F 1994 Large-scale effort tests digital mammography's potential *J. Nat. Cancer. Inst.* **86** 580-581

Antonuk L E, Boudry J, El-Mohri Y, Huang W, Siewerdsen J and Yorkston J 1994 High-resolution, high-frame rate, flat-panel TFT array for digital x-ray imaging *Proc. SPIE* **2163** 118-128

Ballu Y 1980 High resolution spectroscopy *Applied Charged particle optics* Ed. Septier A 257-381

Barnes G T 1979 Characterisation of scatter, *Reduced Dose Mammography*, ed. Logan WW and Muntz E P (Mason: New York) 223-242

Barnes G T, Brezovich I A 1978 The intensity of scattered radiation in mammography *Radiology* **126** 243-247

Barnes G T, Cleare H M and Brezovich I A 1976 Reduction of scatter in diagnostic radiology by means of a scanning multiple slit assembly *Radiology* **120** 691-694

Barrett H H and Swindell W 1981 *Radiological imaging: The theory of image formation, detection and processing* Vols I and II (Academic Press: New York)

Bebcivelli W, Bertolucci E, Bottigli U, Del Guerra A, Mazzei D, Messineo A, Nelson W R, Randaccio P, Rosso V, Russo P and Stefanini 1991 Use of EGS4 for the evaluation of the performance of a silicon detector for x-ray digital radiography *Nucl. Inst. Meth. Phys. Res.* **A305** 574-580

Bernstien H and Muntz E P 1986 Experimental verification of a technique for predicting scattered radiation transfer: Application to low photon energies *Med. Phys.* **13** 836-842

References

Beynon J D E and Lamb D R 1980 *Charge Coupled Devices and their Applications* (McGraw-Hill: New York)

Bielajew A F and Rogers D W O 1987 PRESTA: The parameter reduced electron-step transport algorithm for electron Monte Carlo transport *Nucl. Inst. Meth.* **B18** 165-181

Birch R and Marshall M 1979 Computation of Bremsstrahlung x-ray spectra and comparison with spectra measured with a Ge(Li) detector *Phys. Med. Biol.* **24** 505-517

Birch R and Marshall M and Ardran G M 1979 *Catalogue of spectral data for diagnostic x-rays* (The Hospital Physicists Association: London)

Blouke M M, Janesick J R, Elliot T, Hall J E, Cowens M W and May P J 1987 Current status of the 800x800 charge-coupled-device image sensor *Opt. Eng.* **26** 864-874

Bohachevsky I O, Johnson M E and Stein M L 1986 Generalised simulated annealing for function optimisation *Techometrics* **28** 209-217

Boone J M, Siebert J A 1994 An analytical edge spread function model for computer fitting and subsequent calculation of the LSF and MTF *Med. Phys.* **21** 1541-1545

Boreman G D 1987 Fourier spectrum techniques for characterisation of spatial noise in imaging arrays *Opt. Eng.* **26** 985-991

Boyle W S and Smith G E 1970 Charge coupled semiconductor devices *Bell Sys. Tech. J.* **49** 587-593

Braun M 1979 Focal spots in the future of mammography *Reduced dose mammography* ed. Logan WW and Muntz EP (Mason: New York) 195-209

Brettle D S, McLeod G, Oddy R J, Parkin G S J and Cowen A R 1994 Automated microcalcification localisation using matched Fourier filtering *presented at the Second International Workshop on Digital Mammography, York U.K.*

Burke B E and Gajar S A 1991 Dynamic suppression of interface-state dark current in buried-channel CCDs *IEEE Trans. Elect. Dev.* **38** 285-290

Burt D J 1991 CCD performance limitations: theory and practice *Nucl. Inst. Meth. Phys. Res.* **A305** 564-573

CEC (Commission of the European Communities) *1990 Quality criteria for diagnostic radiographic images (2nd edition working document XII/173.90)* (Commission of the European Communities: Luxembourg)

CEC (Commission of the European Communities) 1995 *European protocol on dosimetry in mammography* Draft (Commission of the European Communities: Luxembourg)

Chakraborty D P and Eckbert M P 1995 Quantitative versus subjective evaluation of mammography accreditation phantom images *Med. Phys.* **22** 133-144

Chan H and Doi K 1983 The validity of Monte Carlo simulation in studies of scattered radiation in diagnostic radiology *Phys. Med. Biol.* **28** 109-129

Chan H and Doi K 1985 Physical characteristics of scattered radiation in diagnostic radiology: Monte Carlo simulation studies *Med. Phys.* **12** 152-165

Chan H P, Niklason L T, Ikeda D M, Lam K L and Adler D D 1994 Digitisation requirements in mammography: Effects on computer-aided detection of microcalcifications *Med. Phys.* **21** 1203-1211

Cowen A R, Coleman J and Workman A 1989 *Leeds mammographic test objects Instruction Manual* (The Radiological Imaging Group, Leeds)

Cowen A R, Workman A and Price J S 1993 Physical aspects of photostimulable phosphor computed radiography *Br. J. Radiol.* **66** 332-345

Cox J D and Williams D W 1994 Direct x-ray sensing CCD array for intraoral dental x-ray imaging system *Proc. SPIE* **2163** 284-297

Craigmyle M B L 1984 *The Apocrine glands and the breast* (Wiley: New York)

Cunningham I A and Fenster A 1987 A method for modulation transfer function determination from edge profiles with correction for finite-element differentiation *Med. Phys.* **14** 533-537

Cunningham I A and Reid B K 1992 Signal and noise in modulation transfer determinations using the slit, wire and edge techniques *Med. Phys.* **19** 1037-1044

Cunningham I A, Westmore M S and Fenster A 1994 A spatial-frequency dependent quantum accounting diagram and detective quantum efficiency model of signal and noise propagation in cascaded imaging systems *Med. Phys.* **21**

Cunningham I A, Westmore M S and Fenster A 1994 Visual impact of the nonzero spatial frequency quantum sink *Proc. SPIE* **2163** 274-283

Dainty J C and Shaw R 1974 *Image Science* (Academic Press: New York)

Dance D R 1980 The Monte Carlo calculation of integral radiation dose in xeromammogrpahy *Phys. Med. Biol.* **25** 25-37

Dance D R 1988 Diagnostic radiology with x-rays *The Physics of Medical Imaging* ed. Webb S (Adam Hilger: Bristol)

Dance D R 1990 Monte Carlo calculation of conversion factors for the estimation of mean breast dose *Phys. Med. Biol.* **9** 1211-1219

Dance D R 1994 Radiographic films and screens *Medical radiation detectors - fundamental and applied aspects* ed. Kember N F, (IOP Publishing, Bristol) 57-74

Dance D R 1994 Storage phosphor plates and xerox receptors *Medical radiation detectors - fundamental and applied aspects* ed. Kember N F, (IOP Publishing: Bristol) 75-88

Dance D R and Day G J 1981 Simulation of mammography by Monte Carlo calculation - the dependence of radiation dose, scatter and noise on photon energy *Proceedings on patient exposure to radiation in medical x-ray diagnosis - possibilities for dose reduction* ed. Drexler G, Eriskat H, Schibilla H (Commission of the European Communities: Luxembourg) 227-243

Dance D R and Day G J 1984 The computation of scatter in mammography by Monte Carlo methods *Phys. Med. Biol.* **29** 237-247

Davis D H and Dance D R 1992 The automatic computer detection of subtle calcifications in radiographically dense breasts *Phys. Med. Biol.* **36** 1385-1390

Day G J and Dance D R 1983 X-ray transmission formula for antiscatter grids *Phys. Med. Biol.* **28** 1429-1433

Deckers A and Aarts E 1991 Global optimisation and simulated annealing *Math. Prog.* **50** 357-393

Department of Health 1989 *Guidelines of the establishment of a quality assurance system for the radiological aspects of mammography used for breast screening* (Pritchard report) Report of a Sub-Committee of the Radiological Advisory Committee of the Chief Medical Officer (Dept. Health: London)

Department of Health 1990 *Revised Guidance notes for health authorities on mammographic x-ray equipment requirements for breast cancer screening* Medical Devices Directorate report STD/90/46 (Dept. Health: London)

Droege R T and Rzeszotarski M S 1985 An MTF method immune to aliasing *Med. Phys.* **12** 721-725

EEV Ltd 1993 *CCD15-11 Series Scientific Image Sensor* EEV Ltd, Chelmsford, Essex

EEV Ltd 1995 *CCD30-11 Series Scientific Image Sensor* EEV Ltd, Chelmsford, Essex

Evans J P O 1993 *Development of a 3-D x-ray system* Thesis, The Nottingham Trent University

Everhart T E and Hoff P H Determination of kilovolt electron energy dissipation vs penetration distance in solid materials *J. Appl. Phys.* **42** 5837-5844

Fahrig R, Maidment A D A and Yaffe M J 1992 Optimisation of peak kilovoltage and spectral shape from digital mammography *Proc. SPIE* **1651** 74-83

Faulkner K and Law J 1994 A comparison of mammographic phantoms *Brit. J. Radiol.* **67** 174-180 Chakraborty D P and Eckert P 1995 Quantitative versus subjective evaluation of mammography accreditation phantom images *Med. Phys.* **22** 133-143

Feig S A 1987 Mammography equipment: Principles, features, selection *Radiol. Clin. N. America* **25** 897-911

Feltz J C 1990 Development of the modulation transfer function and contrast transfer function for discrete systems, particularly charge-coupled devices *Opt. Eng.* **29** 893-904

Fife I 1991 The physical dimensions of the compressed breast *Brit. J. Radiol.* **64** 73-74

Fitzgerald M, Dance D R, Fisher K, Lawinski C P and Ramsdale M L *1989 The Commissioning and routing testing of mammographic x-ray systems* Institute of Physical Sciences in Medicine Report 59

Fitzgerald M, Dance D R, Fisher K, Lawinski C P and Ramsdale M L *1994 The Commissioning and routing testing of mammographic x-ray systems* Institute of Physical Sciences in Medicine Report 59 2nd ed.

Forrest P 1987 *Breast cancer screening: report to the Ministers of Health of England, Wales, Scotland and Northern Ireland* (HMSO)

References

Freedman M, Steller D, Jafroudi H, Benedict S C, Zuurbier R A, Katial R, Hayes W, Wu Y C, Liu J S, Steinman R, Tohne W and Mun S K 1995 Digital mammography: Trade-offs between 50 and 100µm pixel size *Proc. SPIE* **2432** 114-125

Fu T and Roehrig H 1984 Noise power spectrum, MTF and DQE of photoelectronic radiographic systems *Proc. SPIE* **454** 377-386

Fujita H, Doi K and Giger M L 1985 Investigation of basic imaging properties in digital radiography. 6. MTFs of II-TV digital imaging systems *Med. Phys.* **12** 713-720

Fujita H, Tsai D, Doi K, Morishita J, Ueda K and Ohtsuka A 1992 A simple method for determining the modulation transfer function in digital radiography *IEEE Trans. Med. Imaging* **11** 34-39

Giger M L and Doi K 1984 Investigation of basic imaging properties in digital radiography. 1. Modulation transfer function *Med. Phys.* **11** 287-295

Giger M L, Doi K and Fujita H 1986 Investigation of basic imaging properties in digital radiography. 7. Noise Wiener spectra of II-TV digital imaging systems *Med. Phys.* **13** 131-138

Giger M L, Doi K and Metz C E 1984 Investigation of basic imaging properties in digital radiography. 2. Noise Wiener spectrum *Med. Phys.* **11** 797-805

Goldman L W 1992 Fluoroscopic performance tests using a portable computer/frame grabber: Wiener spectra measurements *Med. Phys.* **19** 45-52

Gonzales R C and Wintz P 1987 *Digital Image Processing*, 2nd ed. (John Wiley: New York)

Haus A G 1990 Technologic improvements in screen-film mammography *Radiology* **174** 628-637

Holdsworth D W, Gerson R K and Fenster A 1990 A time-delay integration charge-coupled device camera for slot-scanned digital radiography *Med. Phys.* **17** 876-885

Hopkinson G R 1983 Charge diffusion effects in CCD x-ray detectors 1: theory *Nucl Inst Meth* **216** 423-429

Hopkinson G R 1987 Analytical modelling of charge diffusion in charge-coupled device imagers *Opt. Eng.* **26** 766-772

Hospital Physicists' Association 1977 *The physics of radiodiagnosis* Scientific Report Series **6**

Hsu J, Chelberg D M, Babbs C F, Pizlo Z and Delp E 1995 Pre-clinical ROC studies of digital stereomammography *IEEE Trans. Med. Im.* **14** 318-325

Hubbell J H, Veigele W J, Briggs E A, Brown R T, Cromer D T and Howerton R J 1975 Atomic form factors, incoherent scattering functions and photon scattering cross sections *J. Phys. Chem. Data* **4** 474-513

Jafroudi H and Muntz E P 1984 The sensitivity to technological innovations of the dose delivered by optimised mammography systems *Proc. SPIE* **454** 175-182

Jafroudi H, Muntz E P, and Bernstein H 1982 Multiparameter optimisation of mammography *Proc. SPIE* **357** 75-83

Janesick J R and Elliot T 1991 History and advancements of large area array scientific CCD imagers *Astron. Soc. Pac. Conf. Series 1991*

Janesick J R, Elliot T, Collins S, Daud T and Campbell D 1987 Charge-coupled device advances for x-ray scientific applications in 1986 *Opt. Eng.* **26** 156-166

Jennings R J, Eastgate R J, Siedband M P and Ergun D L 1981 Optimal x-ray spectra for screen-film mammography *Med. Phys.* **8** 629-639

Jiang Y, Nishikawa R M, Giger M L, Doi K, Schmidt R A and Vyborny C J 1992 Method of extracting signal area and signal thickness of microcalcifications from digital mammograms *Proc. SPIE* **1778** 28-38

Johns H E and Cunningham J R 1983 *The Physics of Radiology* 4th ed. (Charles C. Thomas: Illinois)

Johns P C and Yaffe M J 1983 Coherent scatter in diagnostic radiology *Med. Phys.* **10** 40-43

Johns P C and Yaffe M J 1987 X-ray characterisation of normal and neoplastic breast tissue *Phys. Med. Biol.* **32** 675-695

Judy P F 1976 The line spread function and modulation transfer function of a computed tomography scanner *Med. Phys.* **3** 233-236

Kalender W 1981 Monte Carlo calculations of x-ray scatter data for diagnostic radiology *Phys. Med. Biol.* **26** 835-849

Karssemeijer N, Frieling J T M, Hendriks J H C L and Henriks H C L 1993 Spatial resolution in digital mammography *Invest. Radiol.* **5** 413-419

Kirkpartick A E and Law J 1987 A comparative study of films and screens for mammography *Brit. J. Radiol.* **60** 73-38

Knoll G F 1989 *Radiation detection and measurement* 2nd ed. (John Wiley: New York)

Law J 1991 A new phantom for mammography *Brit. J. Radiol.* **65** 116-120

Law J 1993 The influence of focal spot size on image resolution and test phantom scores in mammography *Brit. J. Radiol.* **66** 441-556

Lefebvre F, Benali H, Gilles R, Kahn E and Paola R D 1995 A fractal approach to the segmentation of microcalcifications in digital mammograms *Med. Phys.* **22** 381-390

Lumb D H, Chownaietz E G and Wells A 1987 X-ray measurements of charge diffusion effects in EEV Ltd. charge-coupled devices *Opt. Eng.* **26** 773-778

Mackenzie Davidson J 1898 Remarks on the value of stereoscopic photography and skiagraphy: records of clinical and pathological appearances *Brit. Med. J.* 1669-1671

Madiment A D A, Yaffe M J, Plewes D B, Mawdsley G E, Soutar I C and Starkoski B G Imaging performance of a prototype scanned-slot digital mammography system *Proc. SPIE* **1896** 93-103

Maidment A D A and Yaffe M J 1990 Scanned-slot digital mammography *Proc. SPIE* **1231** 316-326

Maidment A D A, Fahrig R and Yaffe M J 1993 Dynamic range requirements in digital mammography *Med. Phys.* **20** 1621-1633

Maidment D A and Yaffe M J 1994 Analysis of the spatial-frequency-dependent DQE of optical coupled digital mammography detectors *Med. Phys.* **21** 721-729

Marsaglia G, Zaman A and Tsang W W 1990 Toward a universal random number generator *Stat. and Prob. Lett.* **8** 35-39

Marshall M, Peaple L H J, Ardran G M and Crooks H E 1975 A comparison of x-ray spectra and outputs from molybdenum and tungsten targets *Brit. J. Radiol.* **48** 31-39

Martinez-Davalos A 1994 *An investigation of the imaging performance of new digital x-ray* Doctoral thesis The University of London

Metz C E 1978 Basic principles of ROC analysis *Sem. Nucl. Med.* **8** 283-298

Metz C E 1989 Some practical issues of experimental design and data analysis in radiological ROC studies *Invest. Radiol.* **24** 234-245

Metz C E, Wagner R F, Doi K, Brown D G, Nishikawa R M and Myers K J 1995 Toward consensus of quantitative assessment of medical imaging systems *Med. Phys.* **22** 1057-1061

Motz J W and Danos M 1978 Image information content and patient exposure *Med. Phys.* **5** 8-22

Muntz E P 1979 Analysis of the significance of scattered radiation in reduced dose mammography, including magnification effects, scatter suppression and focal spot and detector blurring *Med. Phys.* **6** 110-117

Muntz E P 1981 On the comparison of actual and calculated improvements in the imaging of calcifications using magnification mammography *Med. Phys.* **8** 496-501

Muntz E P, Bernstein H and Jafroudi H 1984 Calculating Radiological Images *Proc. SPIE* **454** 36-40

Muntz E P, Jafroudi H, Jennings R and Bernstein H 1985 An approach to specifying a minimum dose system for mammography using multiparameter optimisation techniques *Med. Phys.* **12** 5-12

Nab H W, Karssemeijer N, Van Erning L J T H O and Hendriks J H C L 1992 Comparison of digital and conventional mammography: a ROC study of 270 mammograms *Med. Inform.* **17** 125-131

NCRP (National Commission on Radiation Protection) 1986 Mammography Report No 65 (NCRP Publications, 7910 Woodmont Avenue, Bethesda, MD 20814 USA)

Neitzel U 1992 Grids or air gaps for scatter reduction in digital radiography: A model calculation *Med. Phys.* **19** 475-481

Nelson R S, Barbaric Z, Bassett L W and Zach R Digital slot scan mammography using CCDs 1987 *Proc. SPIE* **767** 102-108

Nelson W R, Rogers D W O and Hirayama H 1985 *The EGS4 code system* Stanford Linear Accelerator Center Report SLAC-265

Nishakawa R M and Yaffe M J 1985 Signal-to-noise properties of mammographic film-screen systems *Med. Phys.* **12** 32-39

Nishakawa R M and Yaffe M J 1990 Effect of various noise sources on the detective quantum efficiency of phosphor screens *Med. Phys.* **17** 887-893

Nishikawa R M and Yaffe M J 1990 Model of the spatial frequency dependent quantum efficiency of phosphor screens *Med. Phys.* **17** 894-904

Nishikawa R M, Jiang Y, Giger M L, Doi K, Schmidt R A, Vyborny C J, Zhang W, Ema T, Papaioannou J, Wolverton D, Bick U, Nagel R and Mao Y 1994 Performance of automated CAD schemes for the detection and classification of clustered microcalcifications *presented at the Second International Workshop on Digital Mammography, York U.K.*

Nishikawa R M, Mawdsley G E, Fenster A and Yaffe M J 1987 Scanned-projection digital mammography *Med. Phys.* **14** 717-726

Okoshi T 1976 *Three-dimensional imaging techniques* (Academic Press: New York)

Pannetier J 1990 Simulated annealing: an introductory review *Inst. Phys. Conf. Ser.* **170** 23-44

Pappin P J and Huang H K 1987 A prototype amorphous selenium imaging plate system for digital radiography *Med. Phys.* **14** 332-329

Philips Medical Systems 1993 *Super rotalix metal. The dynamic solution* brochure 4512 - 158 14361/740 * 1993-02

Physik Instrumente 1993 *Products for micropositioning catalogue ed. E*

Pimentel K and Teiceira K 1993 *Virtual reality: through the looking glass* (Intel/McGraw-Hill: New York)

Press W H, Flannery B P, Teukolsky S A and Vetterling W T 1988 *Numerical Recipes in C* (Cambridge University Press: Cambridge)

Rabbani M, Shaw R, Van Metter R 1987 Detective quantum efficiency of imaging systems with amplifying and scattering mechanisms *J. Opt. Soc. Am.* A **4** 895-901

Regano L J and Sutton R A 1992 Radiation dose reduction in diagnostic x-ray procedures *Phys. Med. Biol.* **9** 1773-1788

Reichenbach S E, Park S K and Narayanswamy R 1991 Characterising digital image acquisition devices *Opt. Eng.* **30** 170-177

Robinson A and Underwood A C Scoring of image quality phantom films in mammography *Brit. J. Radiol.* **64** 640-641

Roebuck E J 1994 A personal view of the approach to breast cancer screening in UK *The Breast* **3** 60-68

Roehrig H Prototype performance of a high resolution x-ray imaging system for use in coronary angiography *Proc. SPIE* **914** 551-559

Roehrig H, Fajardo L L, Yu T and Schempp W S 1994 Signal, noise and detective quantum efficiency in CCD-based x-ray imaging systems for use in mammography *Proc. SPIE* **2163** 320-332

Roehrig H, Ovitt T W, Dallas W J, Lamoreaux R D, Vercillot R and McNeill K M 1987 Development of a high resolution x-ray imaging device for use in coronary angiography *Proc. SPIE* **767** 144-153

Rowlands J A, Hunter D M and Araj A 1991 X-ray imaging using amorphous selenium: A photoinduced discharge readout method for digital mammography *Med. Phys.* **18** 421-431

Russo J and Russo O H 1987 Development of the human mammary gland *The Mammary Gland* ed. Neville M C and Daniel C W (Plenum Publishing: New York) 67-93

Sanada S, Doi K, Yin F and Giger M L 1991 Comparison of imaging properties of a computed radiography system and screen-film systems *Med. Phys.* **18** 414-420

Schiebel U, Conrads N, Jung N, Weibrecht M, Wieczorek H and Zaengel T 1994 Fluoroscopic x-ray imaging with amorphous silicon thin-film arrays *Proc. SPIE* **2163** 129-140

Seeman H E 1968 *Physical and photographic principles of medical radiography* (Wiley: New York)

Seib D H 1974 Carrier diffusion degradation of modulation transfer function in charge coupled imagers *IEEE Trans. Elect. Dev.* **ED-21** 210-217

References

Sickles E A 1982 Mammographic detectability of breast microcalcifications *Am. J. Roent.* **139** 913-920

Sones R A and Barnes G T 1984 A method to measure the MTF of digital x-rays systems *Med. Phys.* **11** 166-171

Sorenson J A and Floch J 1985 Scatter rejection by air gaps: An empirical model *Med. Phys.* **12** 308-316

Spiekerman A J G and Staalenburg J C 1994 Phosphor-covered junction CCD x-ray sensor for dental imaging *Proc. SPIE* **2163** 366-374

Storm E and Israel H I 1970 Photon cross-sections from 1 keV to 100MeV from elements Z=1 to 100 *At. Data and Nucl. Tables* **7** 565-681

Suckling J, Dance D R, Moskovic E, Lewis D J and Blacker S G 1995 Segmentation of mammograms using multiple linked self-organising neural networks *Med. Phys.* **22** 145-152

Swank R K 1973 Calculation of modulation transfer functions of x-ray fluorescent screens *Applied optics* **12** 1865-1870

Szu H 1987 Fast simulated annealing *AIP Conf. Proc. Neural networks for computing, Snowbird, UT, April 1986* 420-425

Tabar L 1990 Control of breast cancer through screening mammography *Radiol.* 655-656

Tabar L and Dean P B 1985 *Teaching Atlas of Mammography*, 2nd ed (Georg Thieme Verlag: Berlin)

Thorne D J, Waltham N R, Newton G M, Breda I G, Fisher m and Rudd P J 1990 CCD guidance system for the Williams Herschel telescope *Proc. SPIE* **1235** 400-412
Tzannes A P and Mooney J M 1993 Toward the characterisation of infrared cameras *Proc. SPIE* **2020** 472-481

Vaile M S B, Calnan M, Rutter D R and Wall B 1993 Breast cancer screening services in three areas: uptake and satisfaction *J. Pub. Health Med.* **15** 37-45

Wachsmann F and Drexler G 1976 *Graphs and tables for use in radiology* (Springer-Verlag: Berlin)

Wagner L K, Cohen G, Wong W H and Amtey S 1981 Dose efficiency and the effects of resolution and noise detail perceptibility in radiographic magnification *Med. Phys.* **8** 24-32

Wagner R F 1977 Toward a unified view of radiological imaging systems, Part II: Noisy images *Med. Phys.* **4** 279-296

Wagner R F, Barnes G T and Askins B S 1980 Effect of reduced scatter on radiographic information content and patient exposure: A quantitative demonstration *Med. Phys.* **7** 13-18

Wagner R F, Weaver K E, Denny E Q and Bostrom R G 1974 Toward a unified view of radiological imaging systems, Part 1: Noisless images *Med. Phys.* **1** 11-24

Wald N, Frost C and Cuckle H 1991 Breast cancer screening: the current position *Br. Med. J.* **302** 845-855

Webb S 1989 Optimisation of conformal radiotherapy dose distributions by simulated annealing *Phys. Med. Biol.* **34** 1349-1370

Westmore M S and Cunningham I A 1993 Analysis of the detective quantum efficiency of coupling a CCD to a scintillating phosphor for x-ray microtomographic imaging *Proc. SPIE* **1896** 82-92

Workman A, Cowen A R and Brettle D S 1994 Physical evaluation of computed radiography as a mammographic x-ray imaging system *Brit. J. Radiol.* **67** 988-996

Yin F F, Giger M L, Doi K 1990 Measurement of the presampling MTF of film digitisers using a curve fitting technique *Med. Phys.* **17** 962-966